



UNIVERSITY OF
CAMBRIDGE

MULTISTABLE SHELL STRUCTURES

Paul Maximilian Herbert Sobota

Corpus Christi College

This dissertation is submitted for the degree of
Doctor of Philosophy

June 2019

Declaration

The work described here was carried out in the Department of Engineering at the University of Cambridge between January 2015 and March 2019 and contains approximately 47,000 words and 60 figures. The author declares that, except for commonly understood and accepted ideas, or where specific reference is made to the work of others, the content of this dissertation is his own work and includes nothing that is the outcome of work done in collaboration. Parts of the research described in chapter 5,6 and 7 were published by the author in scientific articles¹; in all of them, he is the first author without collaborators except for his supervisor, Prof. Keith Seffen. This dissertation has not been submitted previously, in part or in whole, to any university institution for any degree, diploma, or other qualification.

Cambridge, 04/10/2020

Paul Sobota

¹ List of relevant publications:

- [1] Sobota, P. M. & Seffen, K. A. Multistable slit caps. *Proceedings of the International Association for Shell and Spatial Structures (IASS)* (2016). ‘Spatial Structures in the 21st Century’, Tokyo, Japan , Madrid, Spain: IASS.
- [2] Sobota, P. M. & Seffen, K. A. Effects of boundary conditions on bistable behaviour in axisymmetrical shallow shells. *Proceedings of the Royal Society of London A* 473, 20170230 (2017)
- [3] Sobota, P. M. & Seffen, K. A. Nonlinear Growing Caps. *Proceedings of the International Association for Shell and Spatial Structures (IASS)* (2018). ‘Creativity in Structural Design’, Boston, USA , Madrid, Spain: IASS.
- [4] Sobota, P. M. & Seffen, K. A. Bistable polar-orthotropic shallow shells. *Royal Society Open Science* (2019) (in print)

Abstract

Multistable Shell Structures by Paul M. Sobota

Multistable structures, which possess by definition more than one stable equilibrium configuration, are capable of adapting their shape to changing loading or environmental conditions and can further improve multi-purpose ultra-lightweight designs. Whilst multiple methods to create bistable shells have been proposed, most studies focussed on free-standing ones. Considering the strong influence of support conditions on related stability thresholds, surprisingly little is known about their influence on multistable behaviour. In fact, the lack of analytical models prevents a full understanding and constitutes a bottle-neck in the development process of novel shape-changing structures. The relevance becomes apparent in a simple example: whilst an unsupported sliced tennis ball can be stably inverted without experiencing a reversion, fixing its edge against rotation erodes bistability by causing an instantaneous snap-back to the initial configuration. This observation reveals the possibility to alter the structural response dramatically by a simple change of the support conditions.

This dissertation explores the causes of this behaviour by gaining further insight into the promoting and eschewing factors of multistability and aims to point out methods to exploit this feature in optimised ways. The aforementioned seemingly simple example requires a geometrically nonlinear perspective on shells for which analytical solutions stay elusive unless simplifying assumptions are made. In order to capture relevant aspects in closed form, a novel semi-analytical Ritz approach with up to four degrees of freedom is derived, which enforces the boundary conditions strongly. In contrast to finite element simulations, it does not linearise the stiffness matrix and can thus explore the full solution space spanned by the assumed polynomial deflection field. In return, this limits the method to a few degrees of freedom, but a comparison to reference calculations demonstrated an excellent performance in most cases.

First, the level of influence of the boundary conditions on the critical shape for enabling a bistable inversion is formally characterised in rotationally symmetric shells. Systematic insight is provided by connecting the rim to ground through sets of extensional and rotational linear springs, which allows use of the derived shell model as a macro-element that is connected to other structural elements. It is demonstrated that bistability is promoted by an increasing extensional stiffness, i.e. bistable roller-supported shells need to be at least twice as tall compared to their fixed-pinned counterparts. The effect of rotational springs is found to be multi-faceted: whilst preventing

rotation has the tendency to hinder bistable inversions, freeing it can even allow for extra stable configurations; however, a certain case is emphasised in which an increasing rotational spring stiffness causes a mode transition that stabilises inversions.

In a second step, a polar-orthotropic material law is employed to study variations of the directional stiffness of the shell itself. A careful choice of the basis functions is required to accurately capture stress singularities in bending that arise if the radial Young's modulus is stiffer than its circumferential equivalent. A simple way to circumvent such singularities is to create a central hole, which is shown not to hamper bistable inversions. For significantly stiffer values of the radial stiffness, a strong coupling with the support conditions is revealed: whilst roller-supported shells do not show a bistable inversion at all for such materials, fixed-pinned ones feel the most disposed to accommodate an alternative equilibrium configuration. This behaviour is explained via simplified beam models that suggest a new perspective on the influence of the hoop stiffness: based on observations in free-standing shells, it was thought to promote bistability, but it is only insofar stabilising, as it evokes radial stresses; if these are afforded by immovable supports, it becomes redundant and even slightly hindering.

Finally, combined actuation methods in stretching and bending that prescribe non-Euclidean target shapes are considered to emphasise the possibility of multifarious structural manipulations. When both methods are geared to each other, stress-free synclastic shape transformations in an over-constrained environment, or alternatively, anticlastic shape-changes with an arbitrary wave number, are achievable. Considering nonsymmetric deformations offers a richer buckling behaviour for certain in-plane actuated shells, where a secondary, approximately cylindrical buckling mode as well as a 'hidden' stable configuration of a higher wave number is revealed by the presented analytical model.

Additionally, it is shown that the approximately mirror-symmetric inversion of cylindrical or deep spherical shells can be accurately described by employing a simpler, geometrically linear theory that focusses on small deviations from the mirrored shape.

The results of this dissertation facilitate a versatile practical application of multistable structures via an analytical description of more realistic support conditions. The understanding of effects of the internal stiffness makes it possible to use this unique structural behaviour more efficiently by making simple cross-sectional adjustments, i.e. by adding appropriate stiffeners. Eventually, the provided theoretical framework of emerging actuation methods might inspire novel morphing structures.

Acknowledgements

I am deeply grateful to all the wonderful people who made this PhD journey a real journey and who were with me in the UK, but also in Greece, Italy, the Czech Republic, in several places in Germany, Gran Canaria, across South America, the Netherlands, and last but not least Isla Providencia, and who taught me so many life skills.

Thanks, Robin, for the kick-started warm welcome in Cambridge. Thanks to G, Mel and Marcel for so many unforgettable moments. Thanks, Mel Jay, for bringing a hometown-vibe to Cambridge. Thanks, Laura, I miss our deep conversations on Saturdays. Thanks to my dear Limeys, Ali, Ananya Angel, Charlotte, Christoph, Jono, Laura, Marcin, Marina, Martin, Max - I hope to meet all of you very soon again. Thanks, Alex not only for submitting the dissertation for me, but for being a great friend. Xie, xie Karla-san not for being an amazing MCR president, but for being the warm-hearted, positive, charismatic social butterfly you are. Thanks, Yin, for being with me all the time until the very last moment in the UK. Many thanks to Johannes for creating this wonderful place under the flamboyant tree - it really made me feel like home, and I often remember this wonderful place where I wrote the main part of this dissertation. Many thanks to Daniel for leaving your room to us - working on my dissertation would have been tough otherwise. Thanks, Birgit (and Dinu), for making the goodbye to Europe even more dramatic. Ein grosses Dankeschöen auch an Jakob Grave: Voller Inbrunst unterstützte er mich stetig bei meiner Promotion. Danke, Jakob! Danke! And, of course, I am eternally grateful to Tez for so many reasons - listing them would certainly fill several pages.

A debt of gratitude is owed to the friendly and supportive staff in the library and the service desk office, the wonderful people in the canteen, the cleaners, and also to Ian Smith, whose hard work was not always valued as much as it should have been. Thanks to Karen for enriching this place so much. You were always honest, human in the best possible way, and caring. Thanks to Phil for helping me with the milling - and for being the amazing, authentic and true person you are! I am also grateful to the Language Unit - possibly the most wonderful place in our department, who supports our international community in understanding each other a little bit better, coming closer, and making bonds that last.

I am also grateful to my colleagues in INO 27 - we laughed together, we suffered together in this shady 'office', but it was a great time. Thanks, Georgios and Alessandra,

for taking care of the students' needs and triggering a change that lasts. Thanks to my direct neighbours, Martin and Tim, I enjoyed the discussions with you all the time - our group would not have been the same without you. Thanks to Isi, who for the first time in almost 10 years goes another way in life. I wish you all the best and hope to see you very soon close by! Thanks, Anjali, for always having a joke or a photoshopped picture at hand.

While many people were involved in the greater context of this dissertation, nobody had as much influence on the content, as you, Keith. I would like to thank you wholeheartedly for being this passionate, talented, yet humble teacher and researcher, who values the principles of good academic work. Our discussions were inspiring and broadened my perspective of the wonderful, multi-faceted theory (and philosophy!) of shell structures.

I am thankful to Prof. Allan McRobie for several inspiring discussions about buckling theory and for being this spark of creativity and enthusiasm in our department. Thanks to Prof. Jeremy Baumberg and Laura Brooks for discussing the potential application in the field of nanophotonics and for inspiring this research idea. Thanks to Prof. Stefano Vidoli for kindly explaining your QVC method to me at the beginning of my studies. Thanks to Dr. Fumiya Iida and Josie Hughes from the Robotics Lab for their support with 3D-printing the moulds for the cast rubber-shells. Thanks also to Alistair Ross for his advice with respect to prototyping. I am grateful to the proof-readers: Dad, Georg, Leonid, Marcel, Mel, Robin and Tez. I would also like to express my gratitude to Dr. Fehmi Cirak as well as Professor Chris Calladine for their support.

Financial support was received from the Friedrich-Ebert-Foundation (FES) and Corpus Christi College in the form of a research studentship and travel grants. Additional travel grants were provided by the Centre national de la recherche scientifique (CNRS) and the Engineering Department. I would also like to express my gratitude to the team of the FES, in particular Simone Stoehr and Sohel Ahmed, for being involved in the continuous improvement of the non-material studentship.

Special thanks to Horst, Eva and Dad, for being there for me when I did not expect it at all. Thanks, Mom, for being the wonderful, sometimes quirky, but always loving, selflessly supporting person you are.

– *in memoriam Herbert, Marianne et Stepanka* –

List of Symbols

Abbreviations

BC	Boundary conditions
CAD	Computer-Aided Design
DOF	Degree of freedom
FEA	Finite element analysis
FEM	Finite element method
FvK	Föppl-von Kármán
QVC	Quadratically varying (Gaussian) curvature

Greek Symbols

α	Opening angle of a shell, see Fig. 4.2
β	Polar-orthotropic ratio $\beta = E_\theta/E_r = \nu_{\theta r}/\nu_{r\theta}$
γ	Angular defect; see §2.1
Γ	Boundary of Ω
Γ_D	Boundary with imposed displacement condition (Dirichlet condition)
Γ_N	Boundary with imposed stresses (Neumann condition)
δ	Variation
δ_{ij}	Kronecker Delta
δh	Horizontal displacement in deep shells, see Eqn (4.29)
η_i	Degree of freedom
∇	Nabla operator
$\bar{\epsilon}$	Strain tensor: $\bar{\epsilon} = [\epsilon, \kappa] = [\epsilon_1, \epsilon_2, \epsilon_{12}, \kappa_1, \kappa_2, \kappa_{12}]$
ϵ_{ij}	Membrane strains in i -direction acting on a surface normal to j -direction
$\varphi, \bar{\varphi}$	Meridional variable and reversed value, $\bar{\varphi} = \alpha - \varphi$, see Fig. 4.2
φ_r	Radial gradient of deflection field, see Eqn (5.5)
Φ	Airy stress function
κ_{ij}	First order curvatures (indices as in ϵ_{ij})
λ	Shell slenderness parameter introduced in Eqn (4.31): $\lambda^2 \approx R\mu^2/2$
λ_c	Cylinder slenderness parameter introduced in Eqn (4.39)
μ	Shell slenderness parameter introduced in Eqn (4.19): $\mu = Et/D - \nu^2/R^2$
ν	Isotropic Poisson's ratio, except for §6, where $\nu = \nu_{\theta r} = \beta\nu_{r\theta}$
Π_B, Π_S, Π	Bending, stretching and total strain energy, respectively
ρ, ρ_c	Dimensionless planform radius variables: $\rho = r/a$ and $\rho_c = r/c$
σ_{ij}	Membrane stress resultant per unit length (indices as in ϵ_{ij})
τ	Time
Ω	Mid-plane domain

Latin Symbols

a	Outer planform radius
A_i	i^{th} constant of integration
\mathbf{A}	Stretching rigidity matrix
b	inner radius of a planform annulus in §5 and §6
\mathbf{B}	Coupled stretching-bending rigidity matrix
c	Connection point between two shells, see §5.2.3
C_i	i^{th} constant of integration
\mathbb{C}	Material tensor (4^{th} order tensor)
\mathbb{C}	Set of complex numbers
dS	Infinitesimal area
dV	Infinitesimal volume
D	Flexural rigidity = $Et^3\beta/[12(\beta - \nu^2)]$
\mathbf{D}	Bending rigidity matrix
E	Young's modulus
\mathbf{E}	Material tensor (2^{nd} order tensor)
f^0, f	Arbitrary polynomial functions introduced in Eqn (5.4)
g	Change in Gaussian curvature, = $K - K^0$
δh	Horizontal displacement in deep shells, see Eqn (4.29)
H	Mean curvature
\mathbf{H}	Hessian matrix of stiffness defined in (5.20)
k_u, k_U	Extensional spring stiffness and its dimensionless value: $k_U = ak_u/(Et)$
k_φ, k_ϕ	Rotational spring stiffness and its dimensionless value: $k_\varphi = ak_\phi/(Et^3)$
K	Gaussian curvature
L	Length
n_r	Radial external edge load
\mathbb{N}	Set of natural numbers (integer > 0)
m_{ij}	Bending moment resultant per unit length (indices as in ε_{ij})
p_T, p_N	Tangential and normal load
q_i	Shear force per unit length normal to i -direction
(r, θ, φ)	Spherical coordinates, see Fig. 4.2
(r, θ, z)	Cylindrical coordinates (also used in shallow shells)
r_0	Projected planform radius, see Fig. 4.2
R	Radius of curvature
\Re, \Im	Real and imaginary part of an expression, respectively
\mathbb{R}	Set of real numbers
t	Thickness of a shell or height of a cross-section
\mathbf{u}	Displacements vector of the respective coordinate system; $\mathbf{u} = (u, v, w)$ – note differences between configurations: $\mathbf{u}^0, \hat{\mathbf{u}}, \mathbf{u}$ and \mathbf{u}_A
U, V	Substituted variables introduced in Eqn (4.8)
V_i	i^{th} auxiliary term introduced in Eqn (4.22)
(x, y, z)	Cartesian coordinates

Indices

$(\cdot)^0$	Initial value
\hat{u}	Deviations from the mirror symmetric shape in §4, see Fig. 4.2
$(\cdot)^*$	Characteristic value: wave length in §4; stability threshold elsewhere
$(\cdot)_A, (\cdot)_E$	Distinction between imposed and elastic values, see Fig. 7.2
$(\cdot)^c, (\cdot)^h$	Reference to clamped or hinged subset in §5.2.1 only
$(\cdot)_h, (\cdot)_p$	Value calculated via homogeneous or particular solution only
$(\cdot)_M$	Midpoint value at $r = 0$; introduced in Eqn (5.36)
ω_I	Physical height of annular shell, $\omega_I = (1 - b^2/a^2)w_M/t$
$(\cdot)_\varphi/(\cdot)_\theta$	Reference to meridional and circumferential direction
$(\cdot)_r/(\cdot)_\theta/(\cdot)_{r\theta}$	Reference to radial, circumferential and shear direction

Contents

§1 Introduction	1
1.1 Motivation	2
1.2 Methodology	5
1.3 Scope and Objective	6
1.4 Outline of Dissertation	8
§2 Background Concepts	9
2.1 Fundamentals of Differential Geometry of Surfaces	9
2.2 Föppl-von-Kármán (FvK) Plate Equations	12
2.3 Two-Surface Perspective	14
2.4 Ritz Method	17
2.5 Summary	18
§3 State of the Art	21
3.1 Analytical Treatment of the FvK Equations	21
3.2 Methods to Achieve Bistability	24
3.2.1 Pre-Stressed or Pre-Strained Structures	26
3.2.2 Structures with Initial Gaussian Curvature	27
3.2.3 Bistable Structures Made from Anisotropic Materials	29
3.2.4 Displacement Boundary Conditions	31
3.2.5 Combinations and Further Manipulations	33
3.3 Actuation Methods in Shells	37
3.3.1 Actuators in Structural Engineering	37
3.3.2 Bioinspired and Natural Actuators	38
3.4 Summary	41
§4 Inversion of Deep Shells	43
4.1 Geometrically Linear Governing Equations	45

4.2	Simplification of the Governing Equations	48
4.3	Thin Shell Approximation	53
4.4	Inversion of Cylindrical Shells	54
4.5	Linear Shallow Shell Theory	56
4.6	Results	58
4.6.1	Finite Element Modelling	58
4.6.2	Inversion of Cylindrical Shells	61
4.6.3	Inversion of Spherical Shells	62
4.7	Summary	69
§5	Nonlinear Shell Theory: Inversion of Shallow Shells	71
5.1	Derivation of an Analytical Model: General Solution	73
5.2	Particular Solutions	79
5.2.1	Particular Solution of a Hole-Free Shell	80
5.2.2	Initially Curved Shells with Annular Planform	85
5.2.3	Interaction of Two Shells	87
5.2.4	Simplification to a Beam Model	89
5.3	Results	90
5.3.1	Finite Element Modelling	90
5.3.2	Centrally Fixed Examples	92
5.3.3	Spherical Cap with Extensional Spring Supports	96
5.3.4	Dual Spring-Supported Nonuniformly Curved Shell	99
5.3.5	Extension for Shells with Annular Planform	104
5.3.6	Multishell Coupling	107
5.3.7	Limitations	111
5.4	Summary	112
§6	Bistable Polar-Orthotropic Shells	115
6.1	Geometrically Linear Bending of a Plate	117
6.2	Nonlinear Solution for Shallow Caps	120
6.3	Nonlinear Solution for Shallow Planform Annuli	122
6.4	Results	123
6.4.1	Qualitative Influence of Stiffeners on Bistable Inversion	123
6.4.2	Quantitative Analysis: Inverted Shapes and Corresponding Stress Resultants	124
6.4.3	Minimum Apex Height Required for Bistable Inversion	127

6.4.4	Beam Analogy	129
6.4.5	Bistable Inversion of Planform Annuli	130
6.5	Summary	131
§7	Combined Actuation Methods	133
7.1	Analytical Model	135
7.1.1	Growth Modes of Constant Positive Gaussian Curvature . . .	138
7.1.2	Higher-Order Growth Modes Including $g < 0$	140
7.2	Results	145
7.2.1	Finite Element Modelling	145
7.2.2	Synclastic Cases ($g > 0$)	146
7.2.3	Anticlastic Cases ($g < 0$)	150
7.3	Summary	155
§8	Conclusions and Future Work	157
	References	161
§A	Isotropic Nonlinear Shell Model	169
§B	Polar-Orthotropic Nonlinear Shell Model	173
§C	Actuation	177

List of Figures

1.1	Illustration of a bistable shell	2
1.2	Structural colour	3
1.3	Micro-cavities	4
1.4	Interference Lithography	5
2.1	The concept of Gaussian curvature	11
2.2	Two-surface perspective	15
3.1	Structural concept of elasticity	25
3.2	Pre-stressed bistable shells	26
3.3	Bistable shells with initial Gaussian curvature	28
3.4	Orthotropic bistable shells	31
3.5	Tristable shells	33
3.6	Neutrally stable shells	34
3.7	Pentstable shells	35
3.8	Morphing metal	36
3.9	Motor organ of the <i>Mimosa Pudica</i>	39
3.10	Nonlinear actuation in 3D printed hydrogels	40
3.11	Anisotropic nonlinear actuation via ‘4D’ printing	40
3.12	Baromorphs	41
4.1	Inversion of a deep shell	43
4.2	Spherical coordinate system and definition of stress resultants	45
4.3	Inversion of cylinders	55
4.4	Sequence of inversion of a cylindrical shell	59
4.5	Sequence of inversion of a spherical shell	60
4.6	Inversion of cylinders: analytical predictions vs FEA	61
4.7	Inversion of a deep thin shell: analytical predictions vs FEA	63
4.8	Inversion of a deep thick shell: analytical predictions vs FEA	64

4.9	Inversion of a relatively shallow shell: analytical predictions vs FEA	67
4.10	Inversion of a deep thin shell: analytical predictions vs FEA	68
5.1	Inversion of shallow shells: the influence of support conditions	72
5.2	Overview of analytical methodology: Ritz approach	74
5.3	Overview of analytical methodology: subdivision of displacement fields	81
5.4	Example of a coupled shell	87
5.5	Overview of overseeing Python script	91
5.6	Inversion of a relatively shallow shell: nonlinear predictions	93
5.7	Bistable threshold of a cap: predictions vs FEA and literature	94
5.8	Stress resultants of an inverted shell: the suitability of lower order models	96
5.9	Lower order model's predictions of the bistable threshold	97
5.10	The influence of horizontal supports on the bistable threshold	98
5.11	Convergence of higher-order models	100
5.12	Bistable threshold of a dual spring-supported nonuniformly curved cap	100
5.13	Mode changes due to an increased rotational stiffness in shells	102
5.14	Mode changes due to an increased rotational stiffness in beams	103
5.15	Inverted shapes of shells with annular planform	104
5.16	Bistable threshold of shells with annular planform	105
5.17	Alternative self-stressed state of shells with annular planform	106
5.18	Benchmark test: coupled shells	108
5.19	Experimental observation: quadstable shells	109
5.20	Analytical prediction of the stability diagram of quadstable shells	110
6.1	Overview: inversion of polar-orthotropic shells	116
6.2	Effective cross-section of stiffened shells	124
6.3	Inverted shapes of polar-orthotropic shells	125
6.4	Stress resultants: analytical predictions vs FEA	126
6.5	Logarithmic plot of stress singularities for $\beta < 1$	127
6.6	Bistable thresholds: fixed-pinned and roller-supported shells	128
6.7	Bistable thresholds of fixed-pinned and roller-supported annular shells	130
7.1	Non-Euclidean geometries in nature	134
7.2	Distinction between initial shape, target shape and resulting shape	136
7.3	Illustration of applied boundary conditions	140
7.4	Elliptic and anticlastic assumed mode shapes	143

7.5	Displacement diagram of synclastic in-plane actuated shell	149
7.6	Post-buckled shapes of different nonlinear in-plane actuated shells . .	151
7.7	Strain energy predictions for nonlinear in-plane actuated shells	152
7.8	Displacement diagram of anticlastic in-plane actuated shell	153
7.9	Secondary buckling due to in-plane actuation	155

Chapter 1

Introduction

Most structures are designed to be stiff, strong and stable to resist versatile loading cases without undergoing larger deformations. However, in living organisms a different behaviour is often observed: to avoid direct exposure to load, leaves and grass stalks adapt by large changes of their shape. The first design is predominant in man-made structures, because it spares engineers from distinguishing between an initial and deformed state, which drastically simplifies statical calculations and provides a powerful tool suitable for the unique planning process of each building. With the development of more efficient calculation methods and the requirement to save costs and materials, engineers began to adapt the latter, nonlinear designs. Even though grass stalks are not a suitable blue print for skyscrapers, the idea to use the advantage of more elastic structures has become common in the structural engineering community [1]. In tunnel design, for instance, material usage is minimised by taking a certain amount of deformations into account to activate the self-supporting capabilities of the overlaying soil [2].

More advanced, well-behaving nonlinearities can be found in recent developments in aerospace engineering, where the increased analytical effort of ultra-lightweight designs is economical due to a more controllable manufacturing environment, bulk production and concomitant fuel savings during the life cycle. These developments motivated engineers to create adaptable structures with multiple purposes that include controlled shape changes geared to a certain type of usage. An example is a morphing wing-tip that transforms according to changing flight conditions in order to reduce drag [3]. Such structures are often inspired by nature, where some of the most fascinating structural phenomena occur. The Venus Fly Trap, for instance, is able – despite

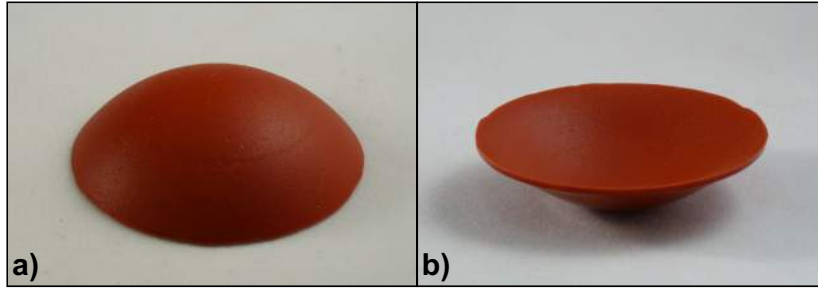


Figure 1.1: a) A spherical cap in its initial configuration; b) the same cap turned inside-out; it rests in this alternative equilibrium configuration in the absence of other loads than self-weight.

the lack of muscles – to ensnare its prey within 50 ms due to a triggered propagating instability known as snap-through buckling [4]. A similar mechanism is employed by one of the fastest moving animals, the hummingbird. When hunting fruit flies, it opens and over-stretches its beak just to let it snap back during the closing process, where the movement exceeds velocities explainable by muscle force alone [5].

These examples emphasise an important difference: whilst the Venus Fly Trap relies on an external stimulus of the prey, hummingbirds actively use muscle force to cull their targets. The related philosophical difference between a tragic accident and a ruthless murder is also reflected in a structural perspective: the reaction to load changes characterises *passive* systems, whereas the employment of actuators defines *active* structures. While the latter grants an increased flexibility that may, for example, be employed to damp an excitation from an earthquake, they also require an energy source to exert the desired effect. This may be problematic, since extreme scenarios, like the aforementioned earthquake, are often concomitant with a power cut. In contrast, *bistable* passive systems are fail-safe and remain in one equilibrium position unless they are forced into an alternative stable configuration. An illustration of a bistable structure - though without a particular application - is a spherical cap that can be turned inside out, cf. Fig. 1.1. While shape-changing structures have many different applications, a particular one initially inspired this research project.

1.1 Motivation

This research project aims to enable novel applications of bistable structures for nano-scale surface texturing. While the changing shape itself may not be visible for the naked eye, the effect of it becomes apparent, when used for structural colouring.

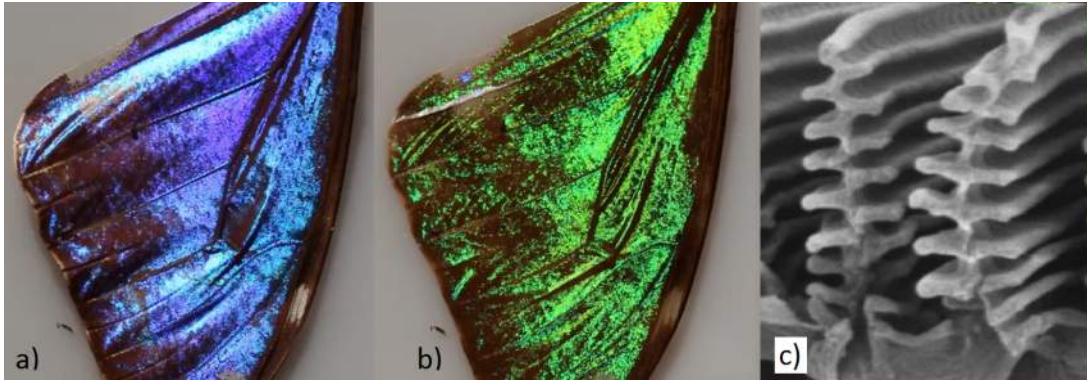


Figure 1.2: Example of structural colour: a) the dry wing of a morpho-butterfly; b) when immersed in isopropanol, it unveils the real colour of its pigments: green; c) SEM image of the wing shows the undulated surface structure [6].

Structural colour is a well-known surface effect that can be observed in several biological structures such as the wings of Morpho butterflies, whose surface is textured with repeated undulations, see Fig. 1.2(c). Since the gaps in between each ‘ridge’ are just a few hundred nanometres wide, they interfere with waves in the visible spectrum. For Morpho butterflies, the distance corresponds to the wave length of yellow light so that this wavelength gets filtered out by getting lost in the ‘valleys’. Hence, the wings of Morpho butterflies appear in their famous brilliant blue. However, once a liquid gets spilled over the wing, the valleys get flooded and the effect shifts to a different, non-visible spectrum; hence, it appears in its *real* colour, green, cf. Fig. 1.2(b).

In order to reproduce this example of a colour-changing structure in artificially created smart materials, it is desirable to be able to control this effect. One approach is to produce sheets with nano-cavities like in Fig. 1.3, and coating them with a thin layer that can be actively controlled, say by magnetic attraction. While such an active method seems suitable in general, passive structures are advantageous since they do not require energy to sustain the deformation. Thus, the colour change of a passive structure persist, until it is forcefully altered.

In order to derive a mechanical model of a passive (=bistable) structure, let us start with choosing a relatively simple structure of a uniformly curved cap mounted on top of one of the aforementioned micro-cavities. This example points towards the following questions which will be addressed in this dissertation:

1. Existing research has mainly focussed on free-standing shells. By mounting a shell on a substrate, horizontal as well as rotational spring supports are added.

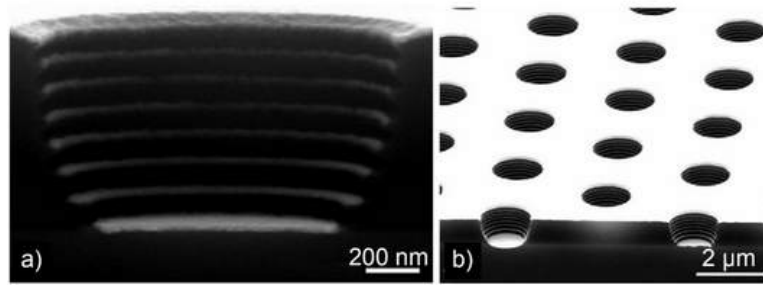


Figure 1.3: Substrate with micro-cavities : a) cross section of a single cavity; b) substrate with several, periodically arranged cavities [7]

While an additional horizontal constraint is expected to support a bistable inversion of spherical shells, an additional rotational spring stiffness at the edge is likely to hamper a bistable response. So, is it more likely that a shell on a substrate possesses an alternative stable state? In order to estimate the influence on bistability, it is important to quantify these effects separately.

2. While the diameter of the cavities is prescribed by the frequency of the optical branch, the thickness of the shell depends mainly on current manufacturing methods. Even modern methods currently lead to relatively thick shells with span-to-thickness ratios of approximately 15. Hence, it is desirable to find ways to reduce the required height for a bistable response.
3. A sharp kink in between the mounted shell and the flat substrate is not desirable. More suitable shapes possess smooth transitions in order to avoid stress concentrations. Thus, the mechanical model, which is going to be developed here, should be capable to cover more complex shapes than just uniformly curved caps.
4. The manufacturing methods have to be taken into account: in order to manufacture doubly-curved structures on the micro- and nanoscale, most commonly interference lithography is used. The effect is, in principle, similar to a photography, where the energy of impacting photons triggers a chemical reaction of a photoresist, see Fig. 1.4(a)-(d) . In a second step, either the product or the reagent is dissolved in order to get the positive or negative structure, respectively. While a single laser suffices for 2D structures, multiple, interfering lasers are required to create more complex 3D structures. However, creating plain surfaces is non-trivial, since concomitant refraction-, reflection- and absorption processes in

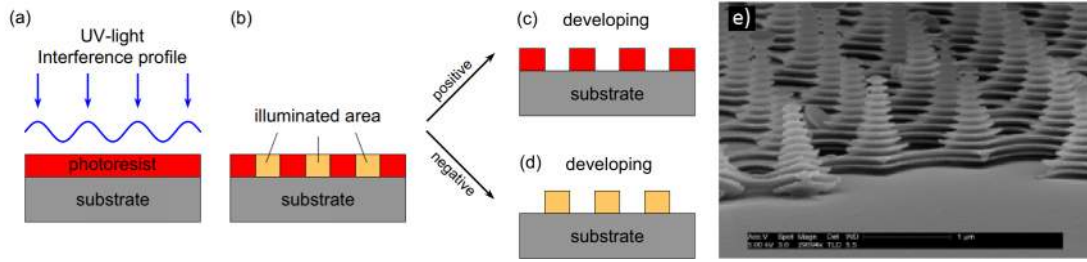


Figure 1.4: (a) - (d): Manufacturing via interference lithography: a) UV-light transmits energy into a photoresist; b) in areas with high energy input, a chemical reaction was triggered; hence, either the previously illuminated area is dissolved (c) or remains (d). e) Nano-pillars with undulations caused by refraction, reflection and adsorption. Rearranged from [8]

the material cause undulations, as exemplified in the nano-pillars in Fig. 1.4(e). The obvious questions are: how will such undulations affect the structural response, in particular, the shells bistable properties? Can they even be used in beneficial ways?

5. If such bistable structures are produced, they may initially be convex. Once popped through, they take a concave shape, but how can they be transformed back to their initial shape? Several options do exist: the trigger could be pressure-related, or alternatively, caused by swelling and shrinking. The latter consideration leads to a rich field of advanced structural manipulations. We could, for instance, create shells that are bistable in a, say, dry environment, but temporarily lose this property in a humid environment. Hence, high humidity would trigger the transformation towards their initial shape.

The first three points will be addressed when developing a mechanical nonlinear model for shallow shells in §5. The undulations caused by interference lithography are considered via a polar-orthotropic material law in §6. Alterations by swelling and the use of actuators are analysed in §7.

1.2 Methodology

Numerical approaches like the finite element method (FEM) are predominantly used for nonlinear analysis of shell structures. Unfortunately, such methods are not able to explore the cause of a structural response and require tedious numerical parameter

studies to analyse influencing factors. This lack of understanding constitutes a bottleneck in the development of novel smart structures [9]. In response to this, the central goal of this dissertation is to gain insight into the structural behaviour and identify the promoting and eschewing factors of multistable shell structures. This may inspire novel applications or improve existing ones by increasing the versatility of bistable structures, using less material and/or increasing their efficiency.

In contrast to commonly employed bistable beam structures, shells offer a more versatile and often advantageous behaviour that makes use of their unique geometrical interaction of bending and stretching. The challenge of this research project is that the advantages of shells come at a cost: the mathematical complexity of the governing equations, especially in the nonlinear domain, is so intricate that closed-form solutions are notoriously difficult to obtain. The aim is to develop a theory that is simplifying the governing equations enough to capture certain bistable properties in closed-form, without affecting the accuracy significantly.

For this purpose, a novel semi-analytical model based on the Ritz method is developed. It is capable of describing a shell's post-buckling behaviour and detecting when a certain structure becomes bistable. A geometric restriction to initially rotationally symmetric shells, which do not necessarily deform in the same manner, is imposed to make the problem amenable to an analytical treatment.

1.3 Scope and Objective

The questions outlined in §1.1 shall be addressed within the following framework:

In order to analyse also non-shallow bistable shells, it will be shown that - despite their more complex geometry - their mathematical treatment is in fact simpler: for cylinders as well as deep and thin spherical shells, which buckle into an approximately mirror-symmetric stable form, a particular simplification is possible, where geometrically linear theories suffice to predict the in fact small deviations from the mirrored shape. The limits of applicability of this simplification are also analysed in this study.

For the more intricate case of shallow shells analytical solutions are scarce and restricted to particularly simple geometries, since nonlinear approaches are required. A semi-analytical model of a shell connected to ground or other structural elements in all kinds of ways is developed in order to analyse the boundary interaction. Considering

the ubiquity of this problem and that (horizontal) support conditions are an indispensable requirement to produce bistable beam structures, surprisingly little is known about their effects on the bistable behaviour in shells. Hence, a systematic analysis of the influence of various support conditions is conducted. Furthermore, new light is shed on how existing methods for the achievement of bistability interact with varying support conditions:

- First, the bistable performance of rotationally symmetric, doubly curved shells with in-plane as well as rotational edge supports is considered, which allows approximation of familiar boundary conditions of hinged, clamped, and self-evidently free edges via the limits of a vanishing or infinite spring stiffness. Since these may introduce additional complexity to the deflection field, a refined approach with superior accuracy is required.

The analytical model is employed to investigate the minimum height of shallow shells required to cause a bistable inversion, where the focus is on manipulating this threshold in beneficial ways by variations in support conditions and shape. The coupling of multiple shells is then analysed in order to explore ways to create structures with more than two stable equilibrium configurations.

- Another aspect concerns the domain of a shell itself rather than its boundary in order to address the aforementioned interference patterns. While it is known that a certain hoop-stiffness of caps assists their bistable inversion, the exact quantity and possible limits are unknown. By employing a polar-orthotropic constitutive law, the effects of variations of a shell's stiffness on their bistable behaviour is analysed in detail. This enables engineers to enhance and control a shell's bistable performance as well as its inverted shape by adding appropriate stiffeners or cutting out less relevant areas to save material as it is common in other structural disciplines. By analysing the limits of the orthotropic ratio, the commonalities and differences between bistable shell and beam structures are explored, where the presence of horizontal supports plays a vital role. Furthermore, methods to prevent concomitant stress singularities that arise directly from the employed material law are investigated.
- Eventually, an analytical framework for spatially nonlinear actuation methods is developed, which allows to model complex swelling and shrinkage processes. Emerging actuators are capable of imposing in-plane strains not only at certain

points, but continuously distributed over an area. An employment in a layered build-up makes it also possible to induce a strain gradient through the thickness. The combined actuation in stretching and bending allows for novel multifarious structural manipulations and the related design space is explored.

In particular it is investigated if the presence of additional supports prevents a structure from morphing into different shapes without evoking changes of the strain energy when precisely matched actuation patterns are employed. In a final step, possibilities are explored to use nonlinear in-plane actuation patterns in order to trigger versatile shape changes by symmetry-breaking buckling.

1.4 Outline of Dissertation

The layout of this dissertation is as follows: in §2, background concepts that are essential in this dissertation are presented. In order to introduce the reader to contextual research, relevant literature about multistable shell structures and their actuation methods is reviewed in §3. An accurate description for a broad range of deep shells is given in §4, where the suitability of linear theories to predict approximately mirror-symmetric post-buckling shapes of spherical shells is evaluated and the limits of applicability are analysed. In order to overcome demonstrated linear shortcomings in shallow shells, a geometrically nonlinear analytical model is developed in §5 to study the effects of different support conditions on the existence of alternative stable configurations. Then follows an extension for polar-orthotropic materials in §6, where the effects of directional stiffness variations on bistable thresholds are analysed. In §7 the interaction of spatially nonlinear in-plane and out-of-plane actuation methods are investigated. Finally, a summary and conclusion are given in §8.

Chapter 2

Background Concepts

The analysis of shells has a long-standing history with rewarding outcomes, such as the realisation of structures with unprecedented slenderness ratios. The source of their high efficiency is their inherent static indeterminacy that causes an interaction of bending and stretching, which simultaneously adds a mathematical complexity.

For the sake of clarity, this chapter outlines fundamental concepts that are relevant in the context of this dissertation: a key factor for a shell's efficiency is the underlying geometric relations of surfaces, as described in §2.1, from which the shell kinematics can be derived. In over a century, several shell theories have been developed, see [10] for a historic review. The most widely used theory for the analysis of bistable shells is based on the geometrically nonlinear Föppl-von-Kármán (FvK) shallow shell theory, which is introduced in §2.2. Aspects of the duality of stretching and bending are then outlined in §2.3, and finally, the Ritz method is addressed in §2.4.

2.1 Fundamentals of Differential Geometry of Surfaces

First, the fundamental aspects of the geometry of surfaces required to quantify bending and stretching deformations of a surface are given. An arbitrarily shaped surface, S , in a Euclidean space can either be described in convective coordinates within its plane as a two-dimensional object embedded in a three-dimensional space, or in a fixed three-dimensional coordinate system. Let us refer to the first as an intrinsic description, since it can be imagined as a coordinate system that is carved into the surface and thus,

it describes the surface from *within*; the latter characterises an extrinsic perspective, since it refers to an *external* observer.

The shape of this surface can be completely described by two measures of curvature: the mean curvature, H , and the Gaussian curvature, K . The former is the semi-sum of the principal curvatures, $H = (\kappa_1 + \kappa_2)/2$. Since it can only be observed from outside the plane, it is an extrinsic measure. The mean curvature does not contain information about the distortion of the *metric* of a surface: for example, a sphere of radius R ($\kappa_1 = \kappa_2 = 1/R$) and a cylinder of half its radius ($\kappa_1 = 2/R, \kappa_2 = 0$) have the same mean curvature, but only the latter is developable.

In order to describe such internal distortions, the *Gaussian curvature*, K , needs to be considered. It can be used to judge a surface's developability and distinguishes Euclidean ($K = 0$) from non-Euclidean geometries ($K \neq 0$). The Gaussian curvature can be derived independently of a coordinate system and is invariant under coordinate transformations, see [11, 12] for details. Due to its central role in structural mechanics, a recapitulation following the concept of Calladine [13] is given: for each point on a differential surface element dS on \mathcal{S} that is bounded by $d\Gamma$, a unit normal vector, \mathbf{n} , can be defined. In order to measure the subtended solid angle by $d\Gamma$, which is defined as $d\gamma$, it can be mapped onto a unit sphere via a *Gauss map*, see Fig. 2.1 for an illustration: by shifting the initial point of each unit normal vector from the surface (right) towards the centre of a unit sphere (left), all vectors are preserved during the mapping process and the mapping function gives every normal vector a unique representation on the sphere; however, multiple points on the surface can have coinciding surface normal vectors. By mapping all normal vectors on the boundary $d\Gamma$, the measurement of angles on curves is generalised to a measurement of angles subtended by a differential surface element dS . The enclosed surface area on the unit sphere, dA , is equal to the subtended dimensionless solid angle on the sphere, $d\gamma = dA/R^2$, since the sphere's radius is '1'. This local quantity can be interpreted as an angular defect of an infinitesimal planar element; it is, for instance, found in a cone that is constructed by cutting a certain angle, $d\gamma$, out of a sheet and gluing the free edges together. The Gaussian curvature is defined as the ratio of this solid angle and the differential surface element dS , and in the limit of $dS \rightarrow 0$, we obtain:

$$K = \frac{d\gamma}{dS}. \quad (2.1)$$

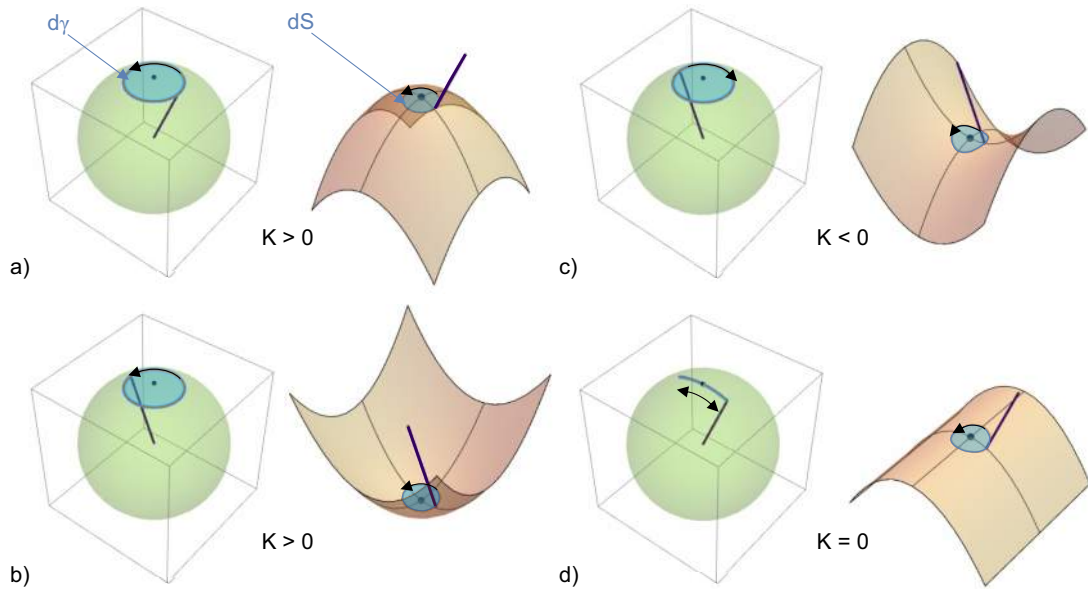


Figure 2.1: Surfaces (right) and their corresponding Gauss map (left): when both centres of the principle radii of curvature lie on the same side of a surface, it has positive Gaussian curvature, see (a); in contrast to the mean curvature, the value of Gaussian curvature does not depend on the spatial orientation of the surface, *cf.* (b). Negative Gaussian curvature arises, when the centres' orientations lie on opposite sides of the surface, *cf.* (c). In this case a clockwise path on the surface causes a counter-clockwise projection on the unit sphere of the Gauss map. If one principal direction of curvature is zero, the surface is developable and the spherical projection of the normal does not enclose any area.

Points with positive Gaussian curvature are called *elliptic*, negative ones are *hyperbolic*, and points with $K = 0$ are either planar ($\kappa_1 = \kappa_2 = 0$) or parabolic otherwise. Surfaces that contain only elliptic points are called *synclastic*, while their entirely hyperbolic counterparts are known as *anticlastic* surfaces. The four examples in Fig. 2.1 illustrate relevant curvature characteristics: in a doubly curved surface with principal directions that lie on the same side of the surface, the Gaussian curvature is positive, see (a). This intrinsic property does not depend on the orientation of the surface, *cf.* the mirror image of (a) in (b); note that their mean curvature, however, has an opposing sign. Negative values of Gaussian curvature are caused by centres of principal curvature on opposing sides of the surface, see (c); note that the negative sign arises because a counter-clockwise rotation on $d\Gamma$ causes a clockwise rotation in the Gauss map. If one principal curvature is zero, the mapping degenerates to a line, see (d), since all normals on any generator line are identical, and thus, the enclosed area is zero. For planar dS the mapped area reduces to a point on the sphere (not shown). Note that

the Gaussian curvature at a cone's apex is undefined and zero elsewhere; however, the surface integral is well defined via a Dirac δ -function and recovers the solid angle, $d\gamma$.

It can easily be shown that the Gaussian curvature's extrinsic definition is the product of principal curvatures, $K = \kappa_1 \kappa_2$. A compact generalisation of this equations for non-principal directions of curvatures reads:

$$K = \kappa_1 \kappa_2 - \kappa_{12}^2. \quad (2.2)$$

where the lower indices '1' and '2' now denote orthogonal in-plane coordinates and '12' the twisting curvature. Relations to other curvature definitions include that K is the dot product of the Ricci curvature tensor and the metric tensor or the double dot product of the Riemann curvature tensor with the metric tensor.

The 'remarkable' characteristic of Gauss Theorema Egregium (Latin for 'remarkable theorem') is that the Gaussian curvature is an *intrinsic* measure and thus, the angular defect can be expressed in terms of in-plane quantities only. It allowed the inventor, Carl Friedrich Gauss, who was inspired by his work as surveyor, to determine the curvature of the earth based on his measurements of length and angles in triangulated meshes on its surface. In contrast to Gauss, structural engineers usually know the measurements of the objects they analyse, but they aim to quantify deformations to calculate concomitant stresses and strains. Hence, rather than the Gaussian curvature, K , itself, the *change* in Gaussian curvature, g , is of particular interest. Its intrinsic definition expressed in terms of in-plane strains, ε , reads:

$$-g = \frac{\partial^2 \varepsilon_{22}}{\partial x_1^2} - 2 \frac{\partial^2 \varepsilon_{12}}{\partial x_1 \partial x_2} + \frac{\partial^2 \varepsilon_{11}}{\partial x_2^2}. \quad (2.3)$$

In contrast to Eqn (2.2), this equation has a linear relation between the strains. This result is not only of fundamental importance in differential geometry but has a direct physical interpretation in shell theories, as described in the following section.

2.2 Föppl-von-Kármán Plate Equations

The complexity of the mathematical treatment of shells required mathematicians, physicists and engineers to use reasonable simplifications to make this field of mechanics amenable to an analytical treatment. In the following an outline of the Föppl-von

Kármán (FvK) equations and its implied assumptions is described in Euclidean space and Cartesian coordinates, (x, y, z) .

Von Kármán's motivation was to extend Love's theory [14] for the bending of flat plates to the geometrically nonlinear domain. Love's linear theory neglects all higher-order displacement terms since all of them are regarded as small compared to the plates in-plane dimensions in the xy -plane, L_x and L_y . Since the thickness of a plate, t , is by definition small compared to L_x and L_y , it was additionally assumed by Love that plates under transversal loading deform by bending in a way that avoids stretching entirely. This assumption requires $g = 0$ and is justified by differing scaling laws of the stretching and bending rigidity. Love's theory is accurate in the range of small deflections of up to $w = 0.2t$, but for $w \gtrsim 0.3t$, the load-bearing behaviour changes, since concomitant stretching of the mid-plane significantly increases the stiffness, and for $w \approx t$, the stretching energy is of the same order of magnitude as the bending energy for common dimensions [15].

The Föppl-von-Kármán equations stretch these assumptions by distinguishing between in-plane and out-of-plane displacements. Even though all displacements u, v and w in x, y and z -direction, respectively, are small compared to the planform dimensions, the deflection, w , is significantly larger than the other two displacements and may exceed the thickness of the plate ($\{L_x, L_y\} \gg \{w, t\} \gg \{u, v\}$). In order to overcome the shortcoming of Love's theory whilst preserving the possibility of an analytical treatment at the same time, the FvK strain definition incorporates the nonlinear deflection term, but neglects higher-order gradients of u and v :

$$\varepsilon_x = \frac{\partial u}{\partial x} + \frac{1}{2} \left(\frac{\partial w}{\partial x} \right)^2 \quad \varepsilon_y = \frac{\partial v}{\partial y} + \frac{1}{2} \left(\frac{\partial w}{\partial y} \right)^2 \quad \text{and} \quad \varepsilon_{xy} = \frac{\partial u}{\partial y} + \frac{\partial v}{\partial x} + \frac{\partial w}{\partial x} \frac{\partial w}{\partial y}. \quad (2.4)$$

Note that these original equations are derived for a flat plate without an initial deflection in their stress-free state, w^0 , and thus, the deflection, \hat{w} and the resulting shape $w = \hat{w} + w^0$ coincide; suitable extensions for considering initially shallow shells and such with imposed strains are introduced in the respective chapter in which they are needed. Since this strain definition is not invariant under rotations, it includes the assumption of a shallow shell with shallow gradients:

$$\left| \frac{\partial w}{\partial x} \right| \ll 1 \quad \text{and} \quad \left| \frac{\partial w}{\partial y} \right| \ll 1. \quad (2.5)$$

Despite considering moderate deflections, small strains are assumed, and thus it is admissible to approximate the energy integral via the original surface area. The Kirchhoff assumptions, which assume the absence of shear deformations, plane cross-sections and a vanishing through-thickness stress are retained, and other common kinematic assumptions, such as neglecting higher-order curvatures are implied.

The FvK equations [16] consider the interaction of bending and stretching by combining Love's bending theory with Föppl's membrane theory [17]. For linear elastic isotropic homogeneous materials, the resulting nonlinear and coupled system of partial differential equations reads:

$$D\nabla^4 w - t \left(\frac{\partial^2 \Phi}{\partial y^2} \frac{\partial^2 w}{\partial x^2} - 2 \frac{\partial^2 \Phi}{\partial x \partial y} \frac{\partial^2 w}{\partial x \partial y} + \frac{\partial^2 \Phi}{\partial x^2} \frac{\partial^2 w}{\partial y^2} \right) = p_N \quad (2.6a)$$

$$\frac{1}{E} \nabla^4 \Phi + \left(\frac{\partial^2 w}{\partial x \partial y} \right)^2 - \frac{\partial^2 w}{\partial x^2} \frac{\partial^2 w}{\partial y^2} = 0, \quad (2.6b)$$

where D , ∇ , Φ , p_N and E denote the flexural rigidity of $D = Et^3/[12(1 - \nu^2)]$, the nabla operator, the Airy stress function, a pressure loading and the Young's modulus, respectively. Eqn (2.6a) is an equilibrium equation, in which Love's term from plate bending, $\nabla^4 w$, is extended by a nonlinear term that accounts for the diverted in-plane force due to the plate's deflection. The second equation ensures the compatibility of bending and stretching deformations by equating the intrinsic definition of the Gaussian curvature with its extrinsic counterpart.

The constants of integration arising from the solution for w and Φ are required to satisfy boundary conditions, which can be either Dirichlet, Neumann or mixed type conditions: whilst the first concern a prescribed displacement condition, for instance by a clamped edge, the second impose stresses on the boundary, *e.g.* by an edge-load. Mixed type conditions exist, for instance, at spring-supported boundaries, where the reaction force of the spring is coupled with a certain displacement via the spring stiffness, k .

2.3 Two-Surface Perspective

The compatibility equation, Eqn (2.6b), highlights a fundamental geometric effect in shells around which several shell theories have developed: the interaction between bending and stretching. Love's plate theory assumed isometric deformations with

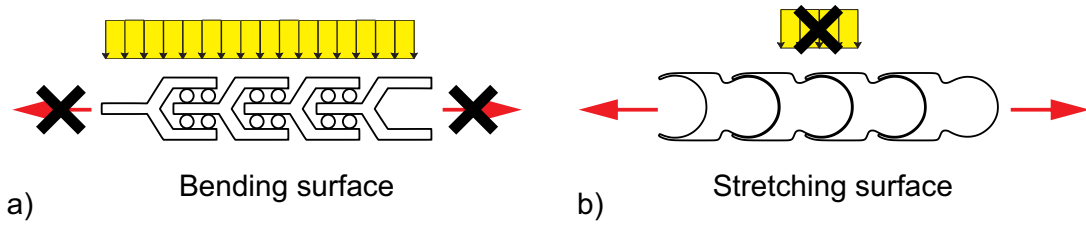


Figure 2.2: Two-surface perspective [13]. (a) Cut view of a surface without stretching rigidity; (b) cut view of a surface without bending rigidity.

$g = 0$ to avoid a consideration of stretching effects of the mid-plane, and thus only considers bending within the aforementioned limits of small deflections. Föppl's membrane theory takes into account that the bending rigidity scales with the thickness's third power, while the rigidity against stretching scales linearly and concludes that a consideration of the latter is sufficient for *very* thin shells.

In contrast to plates, shells possess double curvature, but their bending rigidity is generally non-negligible. Nevertheless, certain incompatible loads can create very stiff and efficient membrane responses during which the full cross-section experiences a constant stress over the height, and thus, the material can be used to its full capacity. While similar constructions can also be achieved by beams of a particular shape, the defining characteristic of shells is that they may react to *several* load cases with a pure membrane response. These bending-free configurations enable engineers to create highly efficient shell structures with slenderness levels that are unprecedented in beam structures. However, a pure membrane response is only possible for certain support conditions, and practicable solutions commonly include a bending disturbance at the edge which fades away at a certain distance of the centre.

Hence, a distinction between these two fundamentally different load-bearing behaviours is advantageous to understand under which conditions the one or the other apply, see Calladine [13] for details. In this context the concept of the *two-surface perspective* [18], which is elaborated next, is relevant. We may understand a shell as a construction as depicted in Fig. 2.2, where a bending surface, (a), and a stretching surface (b) bear the load like two parallel springs. The first possesses a finite bending rigidity, but is free to expand in-plane and the latter one is free to rotate, but has a finite stretching stiffness. A shell can now be thought of as such two surfaces of different stiffness that are spatially overlapping and glued together. Thus, the final response of the shell must be compatible everywhere with respect to their Gaussian curvature. This com-

patibility equation extends the well-known duality of form and force to shells with non-isometric deformations and the similarity is also reflected mathematically in the governing equations: consider an initially stress-free but curved shell with in general differing principal radii of curvature, R_1 and R_2 , respectively. The behaviour of each surface is governed by a single potential function of the Airy stress function, Φ , and the displacement field, w , which are related to the in-plane and out-of-plane response, respectively. While the first potential is related to in-plane stresses, σ , the latter describes the change of curvatures, κ :

$$\sigma_x = \frac{\partial^2 \Phi}{\partial y^2}, \quad \sigma_{xy} = -\frac{\partial^2 \Phi}{\partial x \partial y} \quad \text{and} \quad \sigma_y = \frac{\partial^2 \Phi}{\partial x^2}, \quad (2.7a)$$

$$\kappa_x = -\frac{\partial^2 w}{\partial x^2}, \quad \kappa_{xy} = -\frac{\partial^2 w}{\partial x \partial y} \quad \text{and} \quad \hat{\kappa}_y = -\frac{\partial^2 w}{\partial y^2}. \quad (2.7b)$$

The curvature relation arises directly from geometric considerations, whereas the former potential was designed in such a way that the in-plane equilibrium equations are fulfilled for arbitrary choices of Φ . The duality between the term of a pressure loading and the Gaussian curvature become apparent, when the compatibility equation and the transversal equilibrium equations of each surface in a shallow shell are considered [18]:

$$\frac{\sigma_x}{R_1} + \frac{\sigma_y}{R_2} = p_N \quad (2.8a) \quad \nabla^4 \frac{\Phi}{E} = \frac{\partial^2 \varepsilon_y}{\partial x^2} - \frac{\partial^2 \varepsilon_{xy}}{\partial x \partial y} + \frac{\partial^2 \varepsilon_x}{\partial y^2} = -g \quad (2.8c)$$

$$\frac{\kappa_x}{R_1} + \frac{\kappa_y}{R_2} = g \quad (2.8b) \quad \nabla^4 w = \frac{\partial^2 m_x}{\partial x^2} - \frac{\partial^2 m_{xy}}{\partial x \partial y} + \frac{\partial^2 m_y}{\partial y^2} = -p_N, \quad (2.8d)$$

where m and ε denote bending moments and membrane strains as before. The first equation describes the equilibrium in normal direction, whilst the resembling Eqn (2.8b) expresses the change in Gaussian curvature due to changes of the curvatures κ_x and κ_y . Similarly, the two equations on the right, Eqn (2.8c) and Eqn (2.8d), describe the corresponding other quantity after applying the biharmonic operator; isotropy is assumed here. The identical differential operators reveal how a change in Gaussian curvature acts as a ‘forcing term’ and suggest that a pressure loading on the bending surface can be transferred to the stretching surface via such a change and vice versa.

The two-surface concept also illustrates for which load cases interactions are expected: the uniform heating of a centrally fixed plate for example will cause stretching without any bending-interactions, since $g = 0$ according to Eqn (2.3), whilst a uniform

through-thickness gradient will change the metric, *cf.* Eqn (2.2). It also elucidates how any change of the shell's metric can be interpreted as a 'forcing-term' that causes an interaction with the other surface. The perspective is particularly helpful in cases of combined actuation in stretching and bending, which allow, for instance, shape changes without evoking strain energy; such transformations are discussed in detail in §7.

So far, the governing equations were discussed, but due to the coupled and nonlinear nature of the FvK equations, analytical solutions are notoriously difficult to achieve. An eminently successful approach to obtain semi-analytical solutions, which will also be applied in the context of this dissertation, is discussed next.

2.4 Ritz Method

The principle of Ritz was developed to give further insight into the experiments of Chladni [19] who discovered the mesmerizing sand patterns that form on vibrating plates in 1787. The problem arose significant interest and inspired several advancements in the field of elastic plate theory with contributions from Lagrange, Poisson, Germain and Kirchhoff, among others, see Meleshko [20] for a historic review. However, it took more than a century to find a satisfying answer to the geometrically linear problem of arbitrarily shaped vibrating plates and the related biharmonic equation. Noteworthy contributions that eventually lead to Ritz's method are an approximation by Wheatstone, the work of Voigt [21] and later Rayleigh's approach [22], which was refined and corrected more than 30 years later by Ritz [23].

The key idea is to approximate a solution to a differential equation by using trial functions and applying Hamilton's principle of stationary action instead of finding a solution directly to the equation itself. It requires the Lagrangian, \mathcal{L} , which is defined as the difference between kinetic energy and potential energy, $\mathcal{L} = T - \Pi$, to be constant over time, τ :

$$\delta \int_{t_0}^{t_1} \mathcal{L} d\tau = 0 \quad (2.9)$$

where δ indicates the variation. It follows that the action in a system is stationary. Ritz argues that by applying a variational formulation the differential equation arises and a stationary solution is found. However, since it is known that the energy functional is

stationary in a specific problem, arbitrary test functions can be chosen to achieve an approximated solution [23].

In the absence of dynamic effects, $T = 0$ and, thus, the integral simplifies for shells into an integral over the domain, Ω , which is described in terms of the mid-plane coordinates x_k and x_l :

$$\delta \int_{\Omega} \Pi \, dA = 0 \quad (2.10)$$

For a mechanical system it is reasonable to assume a deflection field

$$w = \sum_{i=1}^n \eta_i w_i(x_k, x_l) \quad (2.11)$$

which consists of a summation of n weighting factors, η_i , multiplied by a trial function of the deflection, w_i , that satisfies the boundary conditions. The potential energy, Π , of the system is calculated and stationary values, for which a structure is at equilibrium, are identified via

$$\frac{\partial \Pi}{\partial \eta_i} = 0. \quad (2.12)$$

However, these equations do not contain information about the stability. If every possible perturbation of an equilibrium configuration causes an energy increase, it is stable, and this condition requires the stiffness matrix, $\partial^2 \Pi / \partial \eta_i \partial \eta_j$, to be positive definite. Ritz demonstrated the suitability of his principle by calculating the solution of vibrating strings and was able to approximate the first natural frequency with a error of $3e^{-9}$ by employing only three polynomial terms. Such a variational approach ensures that the best possible fit within the assumed deflection fields is found and thus, the choice of a suitable pair of basis functions is crucial. The method is particularly useful to gain insight into observed experimental data, where the measured deflection can be used to identify and quantify the influence of relevant terms.

2.5 Summary

This chapter discussed established theories that are essential in the context of this research. The fundamental concepts of differential geometry allow readers to familiar-

ise themselves with relevant quantities and jargon in non-Euclidean geometry, such as the Gaussian curvature. These mathematical concepts find an engineering application in the Föppl-von-Kármán equations, which provide the theoretical framework to describe the geometrically nonlinear deformations of thin-walled structures under certain, well-defined assumptions. The importance of geometry in shell theories was emphasised by the *two-surface* perspective, which grants further insight into the interplay between bending and stretching for non-isometric deformations. Finally, the Ritz method provides an analytical, energy-based approach to approximate equilibrium. These theories are not only relevant for this dissertation, but also to understand key concepts of existing approaches in the literature, which are discussed next.

Chapter 3

State of the Art

The aforementioned background concepts have been applied in various differing morphing shell structures. This chapter reviews inventions in literature that are relevant in the context of this dissertation. Since the FvK equations provide a suitable framework to describe a broad range of bistable structures, methods of their analytical treatment are discussed first in §3.1. In §3.2 follows an overview of advances in the field of transformable shell structures that possess at least one stable alternative equilibrium configuration. Finally, §3.3 discusses existing actuation methods in structural engineering and nature.

3.1 Analytical Treatment of the FvK Equations

Due to their coupled and nonlinear nature, the Föppl-von-Kármán equations are rarely amenable to pure analytical methods, and hence, closed-form solutions are elusive. For the particular case of a flat circular plate, Way [24] introduced an infinite power series, that solely depends on two coefficients that have the physical interpretation of the in-plane stresses and the curvature at the centre of the plate. In order to obtain analytical solutions in other cases, several simplifying approaches have been proposed.

Simplification of the Governing Equations

Berger [25] decouples the FvK equations by neglecting the second invariant of the in-plane strain tensor based on his observations of available data. Banerjee & Datta [26] however point out that inaccuracies in Berger's equations exist for certain support

conditions of initially flat plates ($w^0 = 0$), since his simplification ignore a term related to the radial stresses,

$$\sigma_r = \frac{E}{1 - \nu^2} (\varepsilon_r + \nu \varepsilon_\theta) = \frac{E}{1 - \nu^2} \left[\frac{du}{dr} + \frac{1}{2} \left(\frac{dw}{dr} \right)^2 + \nu \frac{u}{r} \right], \quad (3.1)$$

where ν , r , u , and w denominate the Poisson's ratio, the polar radial variable, the radial mid-plane displacement and the transversal displacement, respectively. Within the limit of shallow gradients, $|dw/dr| \ll 1$, Berger's method provides a fair approximation for fixed-pinned supports, and even better results for clamped edges, but the theory is not applicable in roller-supported shells, where the nonzero edge displacement of u significantly affects the structural behaviour. Based on this observation, Sinharay & Banerjee [27] proposed an alternative method to decouple the FvK equations that holds also for movable supports: by substituting a nonlinear displacement term in the strain energy functional of shallow shells with an initial out-of-plane deflection, w^0 , via

$$\left(\frac{u}{r} \right)^2 \approx \frac{\lambda_{BC}}{1 - \nu^2} \left[\frac{1}{2} \left(\frac{dw}{dr} \right)^2 + \frac{dw}{dr} \frac{dw^0}{dr} \right], \quad (3.2)$$

it becomes possible to adjust the parameter λ_{BC} by an approximation that depends on the support conditions, which ultimately leads to an improved accuracy.

Ritz Approaches

The most prevalent approach does not simplify the governing equations – it strictly speaking violates them. Inspired by the approximately uniformly curved shape, several investigators employed a *uniform curvature* (UC) approach, by assuming the following deflection field with three degrees of freedom, η_1, η_2, η_3 , according to Ritz's method:

$$w = \eta_1 x^2 + \eta_2 y^2 + \eta_3 xy. \quad (3.3)$$

The concomitant drastic simplification of the problem gives compact closed-form solutions that are in fair agreement with finite element (FE) simulations as well as experimental results. This seems insofar surprising, as several aspects are contradictory or seed uncertainty:

- (i) *The edge moment does not vanish:*

The assumption of a deflection field of uniform curvature is not capable of mod-

elling the boundary conditions of a vanishing edge moment at the outer edge in free standing or hinged shells. It is often justified by the argument that this concerns a boundary layer problem that is rapidly damped out so that the overall structural behaviour is not strongly affected [28]. This statement will be analysed in detail in §4 and §5.

(ii) *Polynomial basis function cannot exactly satisfy the equilibrium equation:*

Sobota & Seffen [29] point out that the choice of polynomials basis functions cannot exactly satisfy the equilibrium equations, since a dimensional mismatch exists: for any polynomial of order p the first term of the equilibrium equation in Eqn (2.6a) is of order $p - 4$, whilst the second (mixed) terms order is $p - 2 + \deg(\Phi'')$, where the primes indicate a partial second derivative. Thus, for matching orders, the Airy stress function requires a logarithmic component to match the deflection term of the highest order. However, in closed shells, such a component in the stress function evokes inadmissible in-plane stress singularities that would cause an infinite strain energy. This incompatibility cannot be overcome by increasing the number of terms, since every additional term also requires an additional correction term, and a mismatch will always remain. In contrast to the equilibrium condition, matching orders can easily be achieved in the compatibility equation (2.6b), where the quadratic nature of the nonlinear displacement terms in the mid-plane strain definition is reflected by the fact that $\deg(\Phi) = 2 \cdot \deg(w)$. Since equilibrium has the same axiomatic nature as work, the equilibrium equation, (2.6a), is ignored and a deflection is assumed instead to find an approximate *yet* accurate solution via energy minimisation.

(iii) *Reliability of the Ritz method:*

The quality of the results when employing the Ritz method strongly depends on the suitable choice of the basis functions that span the solution space. In geometrically linear problems, it is straightforward to employ a large number of degrees of freedom to approximate the real solution, for instance with an infinite Fourier series [13, 30]. However, geometrically nonlinear problems require considering the interaction of degrees of freedom, and without a linearisation the energy functional becomes too complex to solve when more than a few degrees of freedom are used. Thus, the question arises if a Ritz approach is suitable to describe buckling problems. While the shape observed in reality constitutes the energetically most favourable, the approximation will always overestimate the

strain energy in static problems. Thus, in the analysis of the natural frequency, for instance, a Ritz approach yields an upper limit; however, the same cannot be stated for buckling problems, since the *ratio* of the bending-to-stretching energy is the decisive factor. Additionally, even slight deviations of the shape may cause significant errors of the buckling threshold, since instabilities are imperfection sensitive [31]. Unfortunately, some researchers do not see the requirements to validate their approximated results with other methods, which leaves a range of uncertainty, see *e.g.* [32–34]. This, however, ignores Ritz’s intention, since he developed his method to gain insight into the underlying structural mechanics of experimental problems to which solutions would stay elusive otherwise; hence, a validation of results obtained by Ritz’s method is crucial. Interestingly, even simple UC approaches have been demonstrated to represent experimental results in several occasions, *e.g.* [28, 35–44] adequately. Thus, the Ritz method can be regarded as a useful tool to explore design spaces and to understand the structural behaviour better.

Recent developments overcame the uniform curvature assumption by introducing additional degrees of freedom that are used to satisfy the boundary conditions precisely. These *higher-order models* are advantageous due to their capability to depict more complex structural behaviour and having increased accuracy compared to their uniformly curved counterparts [45]. The additional degrees of freedom allow for an increased flexibility that is required to depict a wider range of shapes, versatile loading cases, or more intricate geometric constraints.

3.2 Methods to Achieve Bistability

In the context of this dissertation, multistability is defined as: *the existence of at least one alternative stable equilibrium configuration under unchanged loads to which a transition within the elastic limit can be marshalled*. Note that this definition permits shape manipulations via imposed inelastic strains, *e.g.* through actuators, as long as the transition between two stable states is purely elastic. The term ‘unchanged loadings’ is interpreted in such a way that it does include constant pressure loadings since one might argue that the load itself stays unchanged even though the direction of the resulting force might change in consequence of a deformation of the structure.

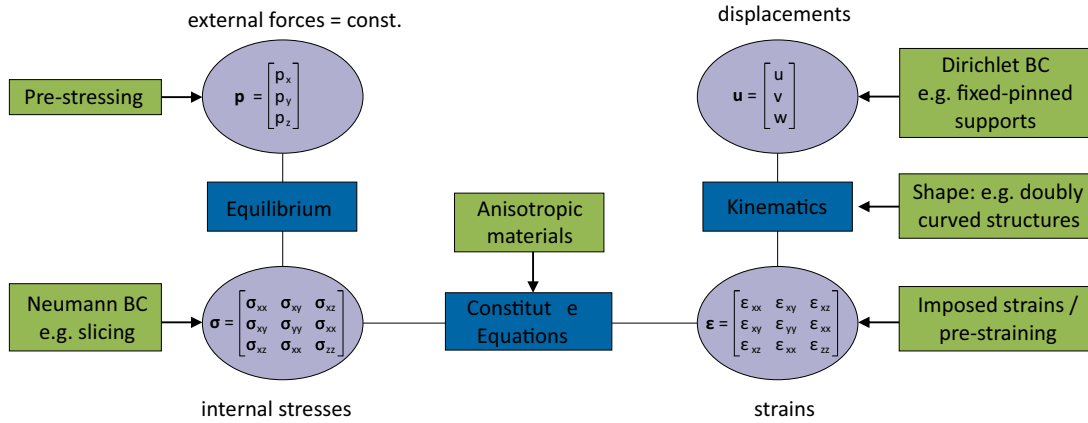


Figure 3.1: Structural concept of elasticity (blue) and possible ways to create bistable structures (green).

In order to create bistable structures, an energy barrier that prevents them from bending back to their initial configuration has to be put in place; this may lock the inverted configuration at a higher energy level by making the *transition* to the lower level energetically even more costly. The fact that this energy barrier must be a *stretching* barrier becomes apparent, when one considers that alternative isometric embeddings only exist for a 2D object in a 3D space, but not for 3D objects [46]. Hence, it is possible to find an alternative embedding for the stretching surface, where all lengths are preserved, and no stretching energy arises. However, it is not possible to find an alternative configuration of the bending surface in which the bending energy vanishes – presuming that the structure is continuous and does not contain hinges.

In general, structural manipulations to create a stretching barrier can be undertaken on all structural levels, *cf.* Fig. 3.1. The lack of a clear categorisation of methods to achieve bistability in literature is owed to the variety of multifaceted approaches that often combine more than one method, and thus, often there is no sharp distinction. In particular, a distinction between external loads and pre-stressing is somewhat arbitrary because, in general, both can cause the same stress-patterns; similarly, pre-stressing and pre-straining are often tantamount, since one is concomitant with the other and there is a causality dilemma. Additionally, imposing bending *and* mid-plane strains in a coordinated manner can also alter the stress-free natural shape, but this special case is treated separately, and it is discussed in detail in §7. The author believes that a categorisation is nevertheless helpful and thus, distinguishes in the following between structures:

- (i) that are pre-stressed or pre-strained,
- (ii) that possess globally non-isotropic material laws,
- (iii) with initial Gaussian curvature or that require non-Euclidean deformations, and finally,
- (iv) structures with additional displacement boundary conditions.

Where multiple methods are used, the most relevant part of each invention is chosen and where an interaction plays a vital role, a separate description is given.

3.2.1 Pre-Stressed or Pre-Strained Structures

A broad class of bistable structures are manufactured by pre-stressing uniaxially curved shells or by imposing inelastic strains, *e.g.* by heating. Any of such impositions can ultimately lead to out-of-plane buckling. For instance, an initially flat plate may buckle under a radial edge load [47, 48], where the sign of the resulting out-of-plane displacement is theoretically indeterminate and depends in practice on imperfections. The buckling threshold also marks the point of bistability, since the structure can either move upwards, or downwards, and if an elastic transition between those two stable states is marshalled, the structure will remain in one of them without requiring additional energy to sustain it.

Kebadze *et al.* [38] showed that coiling a cylindrical panel outwards in longitudinal direction creates a suitable pattern of residual bending stresses to promote a bistable response. By assuming uniform and inextensional deformations, two stable configurations are identified: an extended and a coiled one (see Fig. 3.2). Each of them is cylindrical, and thus, possesses one preferred direction of curvature. Due to the inextensional assumption the only path in between the two configurations involves twisting,



Figure 3.2: (a) Extended configuration, (b) oppositely bent unstable transitional shape, and (c), coiled configuration resulting from (b). [38].

and whilst the isotropic twisting rigidity is usually not sufficient, the bending moment aids to create an additional local minimum in the strain energy landscape.

Bistability through pre-straining frequently occurs in shells exposed to a thermal through-thickness gradient or multi-layered structures with a differing thermal expansion coefficient. A related problem in which a circular substrate is attached to a mismatching top layer was investigated by Freund [36]: by taking a geometrically nonlinear deformation profile into account, he derives a buckling criterion of an imposed normalised curvature of $\kappa_{rA} a^2/t \geq 8 \sqrt{1/(1+\nu)}$.

The bistable behaviour evoked by spatially nonlinear thermal profiles or tantamount growth patterns has been analysed by Seffen & Maurini [49] via a uniform curvature approach. The study considers in-plane as well as out-of-plane actuation pattern and explores a wide range of design spaces of nonlinear actuation patterns within the limits of constant changes of Gaussian curvature throughout the shell's domain. Other actuation methods using the piezo-effect [50–52] or employing shape memory alloys *to impose strains* [53] have been successfully demonstrated and may be extended by other actuation methods described in §3.3.

3.2.2 Structures with Initial Gaussian Curvature & Structures That Require Non-Euclidean Deformations

An isotropic *centrally fixed* cylindrical panel will always bend back to its initial configuration, since it is developable and thus has an initial Gaussian curvature of $K^0 = 0$. During the inversion process there is a smooth isometric transition where the panel is bend in such a way that it flattens out and then bends into the opposite direction, and hence, a change of Gaussian curvature that would cause a stretching barrier is not observed. However, if an initial positive Gaussian curvature exists, say in a cap as depicted in Fig. 3.3, a uniform transformation between the initial and inverted state requires both principal curvatures, κ_1 and κ_2 , to change sign. Thus, the Gaussian curvature – initially $K^0 = \kappa_1 \kappa_2$ – diminishes and rises again in the inverted configuration which can ultimately prevent the cap from reverting due to the involved changes in the metric.

Several studies analyse the critical shape at which a structure becomes bistable directly or indirectly: Wittrick *et al.* [35] extend the work of Timoshenko & Woinowsky-Krieger [54] on beams to shallow shells and analyse the critical temperature and geometry at which uniformly heated bimetallic caps buckle. The analysis focusses in

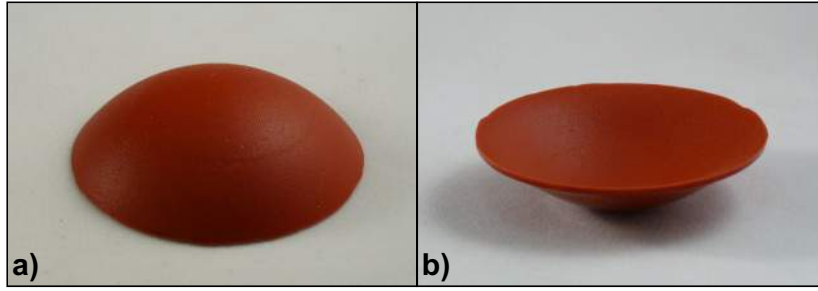


Figure 3.3: Initially doubly curved, but stress-free shell in (a) as well as its stable inversion in (b) in the absence of other loads than self-weight.

particular on the critical initial central rise, w_M^{0*} , at which the cap becomes bistable. By employing a nonlinear shell model this threshold is found to slightly more than four times the thickness – the exact value depends on the Poisson’s ratio, but not the Young’s modulus. As expected, this result closely resembles the findings of Freund [36] in the pre-strained case. Seffen [55] employed a uniform curvature approach to calculate the bistable threshold of initially curved elliptic and in general orthotropic disks of constant thickness, which simplifies for isotropic shells with circular planform to a minimum required initial midpoint displacement of

$$|w_M^0| \geq \frac{4t}{\sqrt{1-\nu}}, \quad (3.4)$$

where t denotes the thickness and ν the Poisson’s ratio. The study shows that initial twisting curvature, which is for shallow shells the only way to cause negative Gaussian curvature in the bending surface, diminishes bistability, and hence, an isotropic saddle is never bistable. An intuitive explanation for the latter example is that the inverted configuration can be reverted by a rigid body rotation of 90° around the normal at the centre, and since such a rotation is isometric, no stretching barrier is formed.

Mansfield [56] analysed bistable properties of uniformly curved shells with an elliptic planform and a lenticular cross-section. The latter form was chosen to find an exact solution that avoids a conflict with the edge condition of a vanishing edge moment through a vanishing thickness at this location. The keystone in his derivation is the proportional relation between the Airy stress function and the bending stiffness, which varies in the same way due to the chosen thickness profile. The analysis provides an elegant exact nonlinear solution and states that bistability occurs if the initial central

rise of a disk of circular planform exceeds:

$$|w_M^0| \geq \sqrt{\frac{14 + 2\nu}{1 - \nu}} t. \quad (3.5)$$

Further insight into the transition in between two stable configurations was provided by Gomez *et al.* [57], who considered the Donnel-Mushtari-Vlasov equations that resemble the FvK equations but contain an additional term that accounts for an initial curvature explicitly. They employ a numerical solution scheme that is accompanied by a leading order term analysis to revise Pogorelov's problem of propagating mirror buckling [58] and distinguish between seven spatial regions in which the shell behaves fundamentally different. A consecutive study dealt with a secondary, symmetry-breaking bifurcation that is observed in deeper shells [59].

The work of Brinkmeyer *et al.* [60] considered caps made from viscous materials and identified the narrow range of geometric parameters under which these show a 'pseudo-bistable' behaviour where the material damping causes a belayed, self-actuated reversion process.

An interesting bistable structure is presented in Walker & Seffen [61]: despite not possessing any *initial* Gaussian curvature, an isotropic metallic strip with a longitudinal crease is bistable, when it is deformed by opposite side bending. It was shown that the driving factor is not plastic yielding, but a localisation effect caused by non-isometric deformations that evoke changes of the metric.

Two other examples of developable structures that possess a stable inversion are a cone and a cylinder: whilst the first structure's Gaussian curvature is undefined at the centre and zero elsewhere, its angular defect is well defined. However, the latter example elucidates that this is not the key to bistability: a second equilibrium state becomes possible as soon as the reversion process requires a change of Gaussian curvature. In the case of circumferentially closed structures like a cone and a cylinder, the only path for reversion is bending the initially uncurved longitudinal axis, where the involved double curvature causes a stretching barrier.

3.2.3 Bistable Structures Made from Anisotropic Materials

Instead of causing a change in the metric, the constitutive relations of the material can assist to stabilise an alternative equilibrium configuration. The material law relates

the stress tensor $\bar{\sigma} = [\sigma, m] = [\sigma_1, \sigma_2, \sigma_{12}, m_1, m_2, m_{12}]$ to the work conjugated strain tensor $\bar{\varepsilon} = [\varepsilon, \kappa] = [\varepsilon_1, \varepsilon_2, \varepsilon_{12}, \kappa_1, \kappa_2, \kappa_{12}]$ – both expressed in Voigt notation – via a tensor of fourth order, \mathbb{C} :

$$\bar{\sigma} = \mathbb{C} \bar{\varepsilon} \quad \text{with } \mathbb{C} = \begin{bmatrix} \mathbf{A} & \mathbf{B} \\ \mathbf{B}^T & \mathbf{D} \end{bmatrix}. \quad (3.6)$$

The $(-)$ -quantities distinguish the total strain components from the decomposed mid-plane quantities $\sigma = [\sigma_1, \sigma_2, \sigma_{12}]$ and $\varepsilon = [\varepsilon_1, \varepsilon_2, \varepsilon_{12}]$. The 3×3 sub-tensors \mathbf{A} , \mathbf{D} and \mathbf{B} denote the stretching rigidity, bending rigidity and the coupled bending-stretching rigidity; the latter arises only in fully anisotropic materials, *e.g.* unsymmetrically layered laminates, since the pre-integration of a symmetrically layered material tensor in thickness direction gives:

$$\int_{-t/2}^{t/2} z^2 dz = 0.$$

Hence, using composite materials gives rise to various manipulations of the constitutive equations that favour bistable responses. Strengthening \mathbf{A} compared to \mathbf{D} will increase the stretching barrier, and the stretching-curvature coupling gives even more elaborate opportunities: when producing non-symmetric laminates at high temperatures, Hyer [37] observed that these take bistable cylindrical shapes after cooling down to room temperature. However, classical linear lamination theory predicted a contradictory saddle-shape, and the problem was resolved by a geometrically nonlinear Ritz approach for shallow shells that confirmed the experimental observations.

A study of Eckstein *et al.* [44] considers initially uniaxially curved but stress-free laminated plates and explores the design space for bistability with respect to their initial curvature and temperature via a uniform curvature approach. Pirrera *et al.* [62] and also [63] analyse the bistable response of heated fibre-reinforced composite plates in a numerical higher-order path-following Ritz approach and conclude that the displacement fields are well resolved by a 5th order approximation, but that higher-order functions are required to capture details of the snap-through process.

Instead of employing fully anisotropic materials, orthotropic materials, in which the ratio between \mathbf{A} and \mathbf{D} is unchanged by definition, also offer the opportunity to create multistable structures. Guest & Pellegrino [28] showed that cylindrical panels with



Figure 3.4: Cylindrical panel from Guest & Pellegrino [28] with two stable configurations made from a composite material: initial configuration (left) and deformed configuration (right).

$\kappa_1 \neq 0$ and $\kappa_2 = 0$ can exhibit an extra stable configuration as depicted in Fig. 3.4, if

$$(D_{12})^2 \left(2 \frac{D_{33}}{D_{11}} + 2 \frac{D_{12}}{D_{11}} - 2 \frac{D_{22}}{D_{12}} \right) > 0. \quad (3.7)$$

This implies that even *isotropic* cylindrical panels, where $D_{22}/D_{11} = 1$, $D_{12}/D_{11} = \nu$ and $D_{33}/D_{11} = (1 - \nu)$, can be bistable: while common materials with $\nu > 0$ are monostable, auxetic materials ($\nu < 0$) are bistable. The physical interpretation of this equation is that the twisting mode plays an essential role. Guest & Pellegrino [28] first derived the results under the assumption of inextensible deformations, and thus, a mode involving twisting via $\kappa_1 \kappa_2 - \kappa_{12} = 0$ is the only transition between the two configurations that show a distinct major axis of bending. Hence, a strong twisting rigidity, D_{33} , is essential to create the required energy barrier. This does not change when the inextensibility assumption is relaxed since a refined analysis revealed that the results are unchanged if $\mathbf{B} = \mathbf{0}$; otherwise the values have to be substituted by $\tilde{\mathbf{D}} = \mathbf{D} - \mathbf{B}^T \mathbf{A}^{-1} \mathbf{B}$, which causes only slight deviations in common materials.

Applications of such systems are commonly encountered in aerospace structures, such as deployable storable extensible members (STEM), [64, 65], morphing aerofoils [66], and are also part of novel nanotube manufacturing methods [67].

3.2.4 Displacement Boundary Conditions

Dirichlet boundary conditions are well-known to have a vital influence on multistability. The presumably simplest continuous structure that exemplifies the nature of this

problem is a fixed-pinned shallow arch with a central rise of at least $w_M^0 = 1.1 t$, which was first described by Timoshenko [68]. This problem exemplifies that the support conditions can be crucial: as soon as horizontal reaction forces are absent, beams will always bend back to their initial configuration. If the supports are present, they become stiffer and build up additional stretching energy before buckling; its release during the snap-through stabilises the inverted configuration against the reverting endeavour of the bending component. Timoshenko's criterion quantifies the critical geometry at which arches become too shallow to cause a sufficient stretching barrier that could prevent a snap-back to the initial configuration.

However, if an arch is too deep, the horizontal reaction forces become large enough to cause asymmetric buckling modes of higher order; an upper bound of this load is the second critical Euler load. Such modes diminish the stretching barrier and Qiu *et al.* [69] showed that such an unwanted response can be overcome by preventing the rotation at the centre. Alternatively, buckling into higher-order mode shapes can be prevented by allowing for some horizontal displacements by employing in-plane springs, rather than fixed-pinned supports. An even simpler problem than an arch is the 'von Mises truss', but it is not considered here, since the central hinge allows the structure to rotate without bending. This, however, eradicates the competition between bending and stretching and, thus, trivialises the problem.

Despite these well-known examples that elucidate the vital influence of the support conditions in stability problems, their effect on the *bistable* response of shells has not been investigated in detail. Existing analytical studies in this context are scarce and confined themselves to unsupported shells with a single fixed edge: Brunetti *et al.* [70] analysed the design space of initially stress-free, orthotropic, cantilever-like shells. In a higher-order Ritz approach, alternative stable configurations of initially pseudo-conical shaped shells were found to possess a strongly nonuniform curvature; the findings were in fair agreement with finite element analysis and experimental results [71]. The nonuniform shape highlights that the clamped support condition introduces an additional complexity that cannot be tackled with conventional UC approaches. While these more intricate structures demonstrate, that fixing rotations can enrich the solution, the opposite is also possible, since a uniformly curved cap with clamped edges was never observed to be bistable [29].

3.2.5 Combinations and Further Manipulations

The categories mentioned above showed general ways to create bistable structures. In several cases that are presented in the following, these methods can be combined to create structures with advantageous characteristics.

Tristability in Orthotropic Doubly Curved Shells

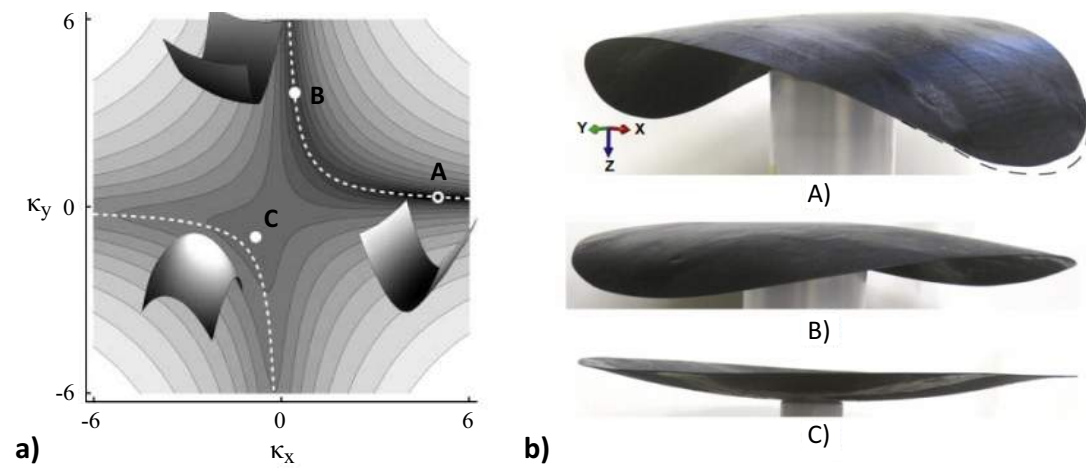


Figure 3.5: (a) Energy landscape according to a higher-order model for a tristable shell taken from [40]. An initially doubly curved shell with $\kappa_x > \kappa_y$, (A), has two stable inverted configurations: mode (B) is separated by a twisting barrier and shows one dominant direction of curvature, while (C) is approximately uniformly curved. The contour plot indicates energy levels where dark $\hat{=}$ low and white $\hat{=}$ high. (b) Related experiment that demonstrates the practical feasibility [41].

By manufacturing initially doubly curved shells from orthotropic materials, continuous shells with three stable equilibrium states can be created, see Fig. 3.5. Such tristable structures offer different modes of structural adaptation for multiple loading cases and thus, a broader field of potential application. The initially stress-free structure is orthotropic *and* doubly curved but possesses one dominant curvature direction. The double curvature is required to cause a stretching barrier that stabilises configuration (C) in Fig. 3.5 – similar to the previously discussed example of a cap, *cf.* §3.2.2; the orthotropic material introduces a twisting barrier as in Fig. 3.4 that favours one principal direction of bending. Analytical studies investigated the required curvature ratios and material properties to manufacture such tristable shells by employing a non-

linear shallow shell approach under the assumption of uniform Gaussian curvature [40] and, more recently, by implementing a ‘reduced’ higher-order model [45], where the term ‘reduced’ indicates that only a few terms are employed in the Ritz approach. The experimental feasibility of these predictions was demonstrated by Coburn *et al.* [41] and Hamouche *et al.* [72], respectively.

Neutral Stability



Figure 3.6: Neutrally stable structure in [73]: for particular values of the twisting stiffness and fine-tuned bending pre-stressing in the longitudinal direction, neutrally stable behaviour is observed. The structure is stable in every depicted configuration and can be morphed effortlessly in between an extended and a coiled configuration via a zero-stiffness twisting mode. The top layer differs from the bottom layer by an opposing direction of applied twist.

Neutral stability describes an equilibrium state in which a structure can be transformed into several other states that possess the same strain energy, and thus, none of them is preferable to another; a common example is the self-equilibrating spring-linkage system of an Anglepoise lamp. A zero-stiffness *shell* made from an isotropic uniaxially pre-stressed cylindrical panel is depicted in Fig. 3.6. Interestingly, it is only achievable with isotropic materials, since the use of orthotropic materials causes a bistable response instead [42].

The key factor is a precisely imposed pre-stressing bending moment: if it is too small only the extended configuration will be bistable, and if it is chosen too large, the structure buckles into a then stable coiled configuration. However, at the critical value of an outwards pointing bending moment of $R/D(1 - \nu)$, where R is the panel’s initial radius of curvature and D the flexural rigidity, a neutrally stable twisting behaviour as

depicted in Fig. 3.6 with an infinite number of equilibrium solutions is observed [42]. An additional finding showed that particular caps can even be bistable *and* neutrally stable at the same time, since they may possess a stable inversion in addition to their zero-stiffness twisting mode.

The unusual behaviour of neutral stability inspired several inventions such as morphing wind-turbine blades [74], morphing aerofoils [75] and a discrete twistable I-beam structure [76, 77]. A concept of an actively controllable zero-stiffness structure was shown by Hamouche *et al.* [52] who created a gear-less motor by attaching several individually controllable Macro-Fibre-Composite actuators on the top of a shell to induce the required pre-stressing. After the imposition of plastic deformations, the shell can be twisted with the help of actuators at a vanishingly low energetic cost.

Pentastability by Slicing

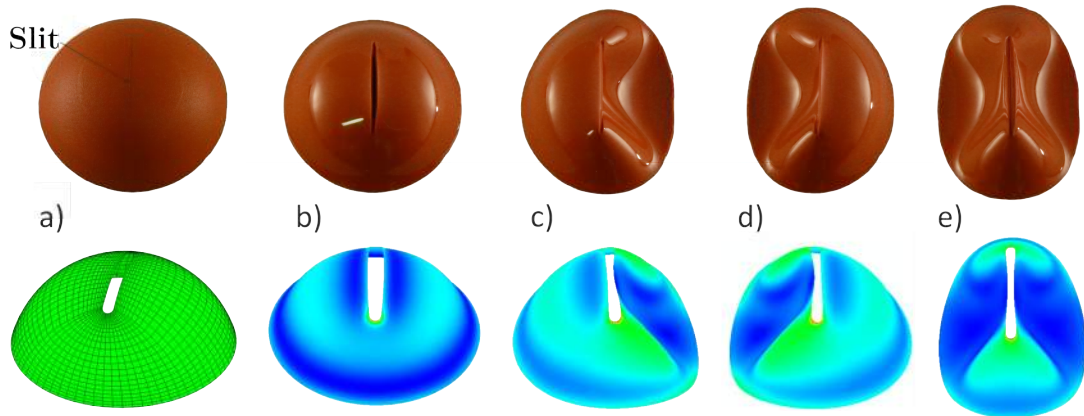


Figure 3.7: Sliced shell structure with five stable configurations [78]: experimental results (top) and finite element simulation (bottom) of an initially uniformly curved spherical cap with a slit, (a), that can be inverted into (b); additional stable configurations include a partial reversion, which can be triggered separately as in (c)-(d) or in combination, (e).

The multistable response of a doubly curved shell may be enhanced by adding slits or slots to a shell, as shown by Sobota & Seffen [78]. This imposes additional free-edge boundary conditions that loosen constraints in the shell by allowing for rotation and stopping bending from propagating. Thus, a shell may partially invert without directly affecting the other part of the structure. The example in Fig. 3.7 shows in total five stable configurations, and is thus *pentastable*: the initially stress-free state, depicted

ted in (a), inverts in an approximately mirror-symmetric manner in (b). The inverted shape shows strong resemblance to the one of a shell of the same initial geometry but without a slit. The presence of a sufficiently large slit allows for additional stable configurations, in which the shell partially reverts, *cf.* (c-e). Since these can be controlled independently on each side of the slit, they allow for three additional stable configurations. It is notable that similar semi-inversions are not stable before the shell was inverted; an FE analysis confirmed that the inversion acts similar to pre-stressing, since it builds up bending energy and its release during a semi-reversion in (c-e) stabilises those configurations. An analytical model of this structure is currently under investigation.

Macrostructures with Bistable Unit Cells: Morphing Metal

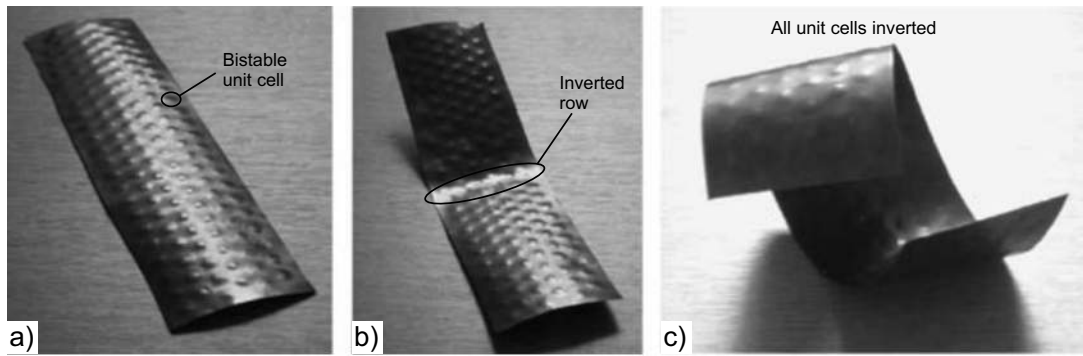


Figure 3.8: Morphing metal adopted from [79]: (a) initial configuration, (b) inverting one row locally induces curvature into the macrostructure, (c) inverting all cells imposes an approximately uniform curvature throughout the shell's domain.

When multiple bistable unit cells are placed on an array, a multistable morphing macrostructure is created, where the inversion of a single cell affects the neighbouring substrate [79]. By inverting different patterns, the global shape can undergo dramatic shape transformations, see Fig. 3.8. Since each shell can be inverted individually, a structure with n dimples has in theory 2^n stable configurations. The expected shape changes have been predicted by tedious finite element simulations but gaining analytical insight into the structural behaviour is nontrivial: the manufacturing process involves plastic deformation that impose residual stresses in the dimple; however, these are not essential for the bistable behaviour of the unit cell since it is governed by the

initial Gaussian curvature. Hence, the results of this dissertation may provide further insight into the interaction of unit cells in the future.

Whilst ways to create bistable shells were discussed in this section, actuation methods that may trigger the transition between stable configurations are presented next.

3.3 Actuation Methods in Shells

In contrast to passive systems that rely on a stimulus from a certain load-case, active structures can transform at any desired point in time by using actuators. Several different methods have been developed and their particular application depends on the scale, environment and preferred form of usage. Here, structural engineering applications are presented before bioinspired actuators are discussed.

3.3.1 Actuators in Structural Engineering

Engineers frequently employ pre-stressing to increase the resistance of large-scale structures against self-weight or as an economic manufacturing method to produce doubly curved surfaces [80]. In order to vary the amount of pre-stress and regulate the structural response to variable loads like excitations from earthquakes and wind loads, active-control mechanisms have recently enjoyed an increased interest within the structural engineering community. The possible gains in structural efficiency are crucial when realising ultra-lightweight designs, and in addition, actuation mechanisms provide a momentous component in morphing structures. The first actively controlled large scale structure was realised by Neuhäuser *et al.* [81], who used linear pneumatic actuators at four corner points that react to external loads and provide active damping against vibrations. Senatore *et al.* [82] placed such actuators in a truss structure that encloses a volume to minimise the sum of embodied and operational energy in the structure's life cycle.

Rather than using actuators at certain points, continuous Macro Fiber Composite (MFC) actuators can be employed for a directional in-plane actuation using the inverse piezoelectric effect that induces strain proportional to an applied electric current; such actuators can trigger snap-through buckling [83], damp a shells vibration [84] or control its periodic movement [52], or – by using the direct piezoelectric effect instead of its inverse – harvest energy from vibrations [50, 51]. By using a layered build-up,

these actuators are also capable of directly inducing curvatures in shells. Alternatively, a constant bending deformation throughout a shell's domain is commonly caused by the uniform heating of bimetallic strips [35], a pre-strained top-layer [36], or a temperature through-thickness gradient [85] in a homogeneous shell.

A novel manufacturing method of 'printed magnetisation' gives rise to a highly non-linear actuation by offering the possibility to magnetize materials in almost arbitrary patterns [86, 87]. Thus, in addition to the spatial variations of the magnetised pattern, the magnetic actuation force itself depends on the displacements. While elaborated magnetisation patterns have not yet been employed in bistable structure, a recent study of Seffen & Vidoli [88] captured the magnetically initiated snap-through buckling of a cap with constant magnetisation analytically.

3.3.2 Bioinspired and Natural Actuators

Biological bodies are by definition smart structures since they are capable of sensing, controlling and actuating; in fact, engineers often took inspiration from flora, fauna and fungi, and Cao *et al.* [89] describes smart structures even as a their 'primitive analogue'. In nature, we find elaborated mechanisms that allow plants to undergo dramatic shape changes: they grow from small seeds to trees, track the solar movement with their leaves, develop flowers and transform back to an energy preserving mode before winter.

Due to the lack of a nervous system, plants cannot react consciously to stimuli, but show nevertheless complex ways to react to them. Seeds, for instance, sense gravity to find the upwards growth orientation [90], and the directional growth of tendrils along a supporting structure [91] requires pressure-sensing. Similarly, the growth process of plants as well as bones is highly dependent on the stress state. The former vary the wood's cellulose-concentration to alter the material strength and show increased growth rates in highly stressed areas to optimize themselves [92, 93]. Floral actuators, which are required to perform such structural transformations, are usually based on changes of *turgor pressure* due to osmosis or on the accretion of material [94]. In general, the actuation patterns in biological shell structures exist in stretching as well as in bending. The growth of leaves is an example of in-plane actuation, while the motor organ (*pulvinus*) in the *Mimosa Pudica* or other solar tracking plants induces a curvature through an ex-centric expansion, see Fig. 3.9. A purer form of out-of-plane

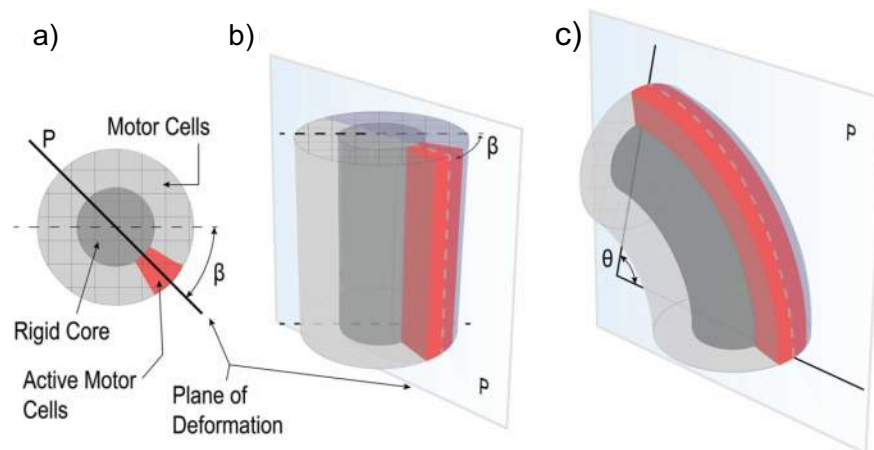


Figure 3.9: Floral bending actuation in a motor organ taken from Charpentier *et al.* [94]: (a) top view of the motor organ that surrounds a rigid core. (b) undeformed configuration with highlighted active motor cells (red). (c) the in-plane expansion of the ex-centric motor cells deform the stem predominantly in bending.

actuation in plants is the humidity-dependent opening of a pine-cone [95] that involves rotations of approximately 50° .

These observations in nature have inspired scientists from different disciplines to create actuators that resemble the pine-cone [95], muscular contraction [96], and an adaptation of the Venus fly trap was employed as a shading device [97]; shape changes can for instance be triggered by variations in humidity [95], pH [98, 99], light intensity [100] or temperature [85, 101].

In contrast to engineering applications, spatially non-Euclidean actuation and growth patterns are common in floral shell structures, since evolution favoured these doubly curved shapes due to their high stiffness. They can be realised experimentally by an established method of Klein *et al.* [101] in which gels of different thermal expansion coefficients are mixed to produce a very thin disk with a nonuniform expansion coefficient, see Fig. 3.10(a). When these are exposed to a uniform heating, these will transform into non-Euclidean shapes that remarkably resemble floral ones, see Fig. 3.10(b). The resulting shapes were predicted without considering the shell's bending rigidity, and thus, the problem was transformed into an entirely geometric one of finding the three-dimensional embedding, *i.e.* the target shape, of a nonlinear in-plane actuation pattern.

More recently, Gladman *et al.* [102] manufactured structures with programmable, anisotropic expansion coefficients by 3D-printing layers of composite hydrogels that

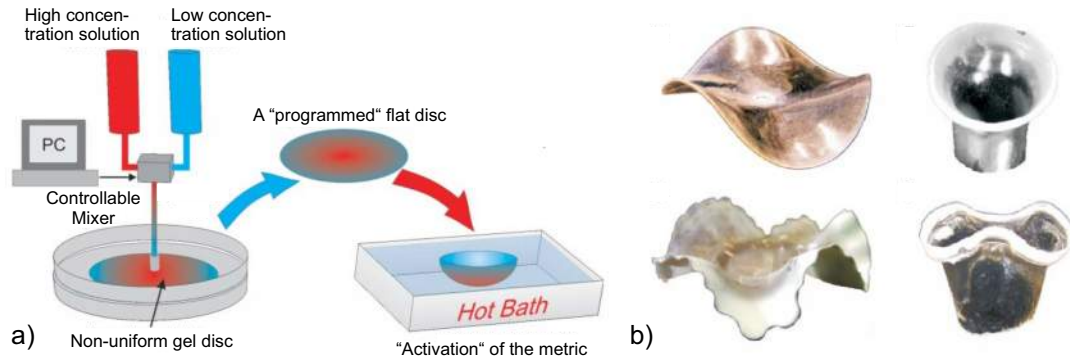


Figure 3.10: (a) Manufacturing of a spatially nonlinear in-plane actuated shell by mixing hydrogels with differing expansion coefficients and printing a 'programmed' structure [101]. Swelling is triggered by immersing the structure into hot water, which creates shapes of double curvature depicted in in (b); shapes in (b) arose from a flat disk (left) and a cylinder (right).

are reinforced with cellulose fibres to control the expansion behaviour. This enabled them to manufacture bioinspired structures resembling a blossom that opens up when immersed in water, see Fig. 3.11.

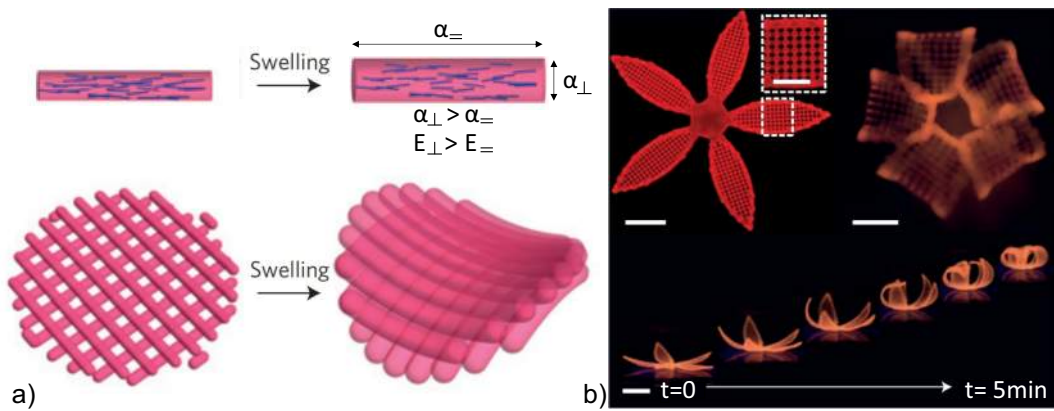


Figure 3.11: (a) Manufacturing of anisotropic nonlinear actuated shells: by 3D-printing layers with a varying cellulose fibre density, the effect expansion coefficient can be tailored in every region of the shell. (b) Petals curve after the immersion in water and mimic a closing blossom [102].

Another kind of actuated structures, so called *baromorphs* [103], use internal pressure to cause a shape transformation by inflation: they consist of networks of elastic tubes that – when pressurized – undergo significantly larger cross-sectional expansions, and thus, directional growth paths can be predefined by a particular pattern of chan-

nels, see Fig. 3.12. This actuation method offers the possibility to impose stretching strains – and when layered also curvatures – on rubber materials. This is promising, since a very flexible material with a relatively high ultimate tensile strength becomes suitable for spatially nonlinear actuation methods. As shown in (c), this allows engineers to impose deformations with positive or alternatively negative Gaussian curvature.

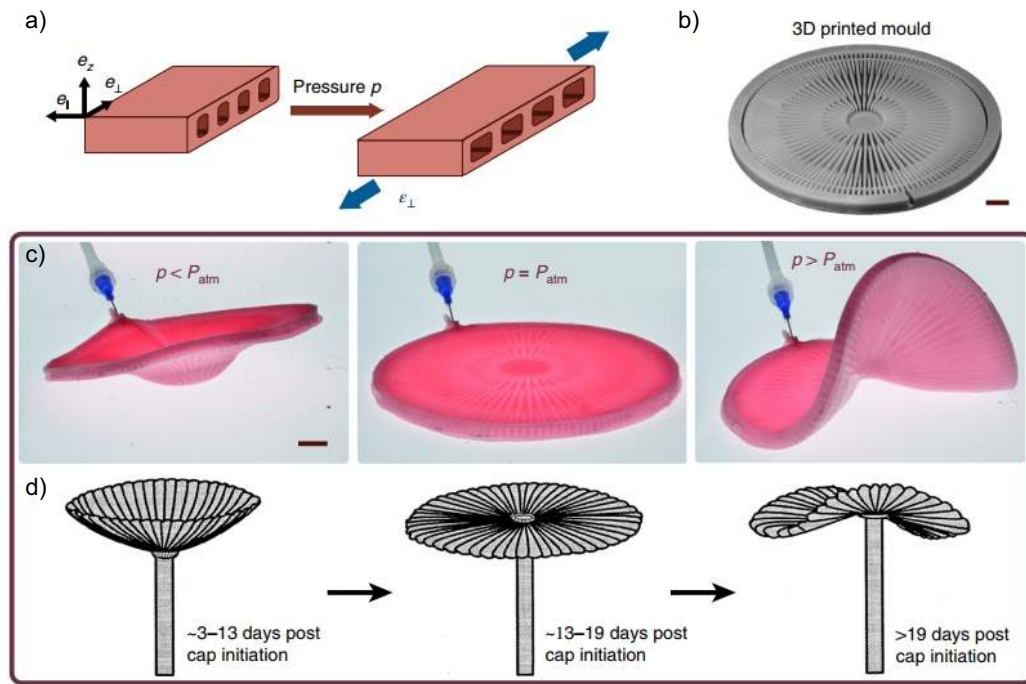


Figure 3.12: Baromorphs [104]: (a) When the depicted plate with hollow inclusions is pressurised, the lateral expansions exceed the longitudinal ones; this creates a similar directional expansion as in Fig. 3.11. (b) Mould in which plates with pre-defined pattern of inclusions are cast. (c) Transformation of a plate with radial channels: when the pressure is reduced, an elliptic geometry forms, whereas an increased pressure transforms the initially flat plate into a hyperbolic mode. The bioinspired nature of this actuation method is illustrated by a comparison to the observed growth modes of the *Acetabularia* alga in (d). Figure taken from Siéfert *et al.* [104].

3.4 Summary

This chapter first reviewed relevant literature around shell structures that possess more than one stable equilibrium configuration and categorised different methods to create

them. Besides ‘pre-stressing and pre-straining’, ‘the use of non-isotropic materials’, and ‘structures with non-Euclidean deformations’, a barely explored, fourth category, ‘adding displacement boundary conditions’, was presented. Throughout this dissertation the combination of the latter category with the former ones will be systematically analysed.

The second part of this chapter focussed on novel actuation methods, which can be used to impose nonlinear strain patterns continuously throughout a shell’s domain. Such methods are employed in §7 in order to expand the analysis from passive to active structures.

Even though it was pointed out that nonlinear approaches are usually required to model bistable behaviour, the suitability and limitations of simpler, linear methods for shells with approximately mirror symmetric inverted shapes are explored next.

Chapter 4

Inversion of Deep Shells

When structures made from highly elastic materials buckle, they do not necessarily fail: an isotropic rubber cap of radius R as shown in Fig. 4.1, for instance, becomes unstable under a critical downwards pointing load and thereby transforms from a strongly compressed structure into a more efficient one in tension that stiffens under additional loading. The transition process may involve a secondary, asymmetric buckling mode [57, 105, 106], since large bending deformations become energetically favourable compared to predominant deformations in stretching, but the resulting, inverted shape gains rotational symmetry again. Provided that the shell is deep and thin enough, it stays inverted even when the applied load is removed, and interestingly, the resulting configuration takes approximately an isometric shape of mirror symmetry. The focus of this chapter is to predict this shape and concomitant stresses precisely in deep spherical shells and cylinders.

An isometric shape minimises stretching at the expense of large bending deformations with changes of both principal curvatures of $\hat{\kappa}_1 = \hat{\kappa}_2 = -2/R$, which come at



Figure 4.1: (a) Initial configuration, (b) inverted configuration, (c) sketch of both profiles: the inverted shape shows slight deviations from a mirror image of the former.

a much lower energetic cost in these structures of low bending rigidity. The evoked bending stresses of $m_1 = m_2 = -2D(1+\nu)/R$ in such an ideal state are, however, incompatible with the boundary condition, since the meridional edge moment must vanish, and thus, an opposing edge moment of the same magnitude has to be superposed to calculate the deviations from the mirrored shape. In order to model the inverted configuration, a geometrically linear approximation that assumes deflections within the limits of small deflection theory is presented in this chapter. Note that decreasing the depth or employing thicker shells increases the relative bending rigidity so that ultimately the edge bending moment may become large enough to trigger a reversion. This limiting state adds additional complexity since it requires a nonlinear analysis, which is presented in the subsequent chapter §5. The aim of this chapter is to identify the region, in which geometrically linear approximations are suitable. Since the exact solution involves a hypergeometric series that complicates the analytical treatment, several approximations are presented and compared.

The proposed methodology may seem paradox at first glance since the employed geometrically linear theory usually only quantifies the critical pressure but does not give any information about the post buckled shape. In addition, it is well-known that a discrepancy between observed and experimental values of the buckling threshold exist: Mandal & Calladine [107] elucidated that the linear critical axial compressive stress in cylindrical shells shows a dimensional mismatch that scales with the thickness via $t^{1.5}$. The causes of such erroneous predictions of linear theories that also affect spherical shells have long been debated [31, 107–111]. However, it turns out that these arguments are of limited relevance here: by considering only the deviations from the mirror-symmetric shape, the problem is transformed, and the post-buckled shape is predicted by considering the *pre-buckled* shape of a spherical cap loaded by a continuously distributed bending moment. This theoretical tweak is possible, since the resulting shape strongly resembles the initial one, and whilst linear theories are unable to describe the transition they become valid *again* in the inverted state. For analysis, the well understood linear shell theory based on the Kirchhoff assumptions is used, which include that (1) normals stay normal, (2) cross-sections remain plane and (3) small displacements. It is applied in the context of deep spherical shells, and additionally, an extension for inverted cylinders is presented.

The governing equations are given next. Hereafter, an asymptotic method for spherical shells is presented before a related method for cylindrical shells is described. A

second simplifying method for shallow spherical shells follows in §4.5. Subsequently, the predictions of the shape of inverted shells are compared to finite element results and the suitability with respect to their mathematical complexity and accuracy of the differing methods is evaluated. The chapter closes with a summary and conclusion.

4.1 Geometrically Linear Governing Equations

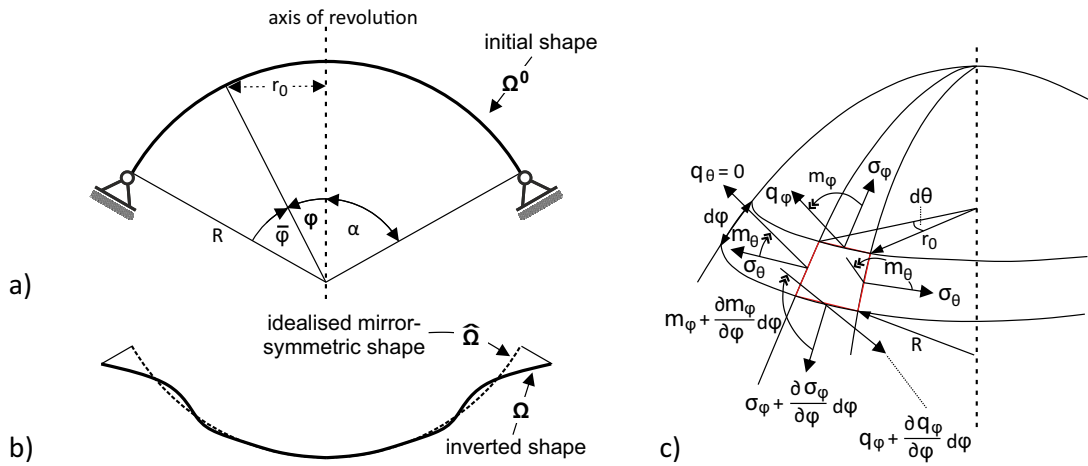


Figure 4.2: (a) Cut through $r\phi$ -plane of a spherical shell: illustration of the coordinate system; (b) resulting inverted configuration, Ω , and idealised mirror symmetric shape, $\hat{\Omega}$; (c) equilibrium at a differential element of the same shell.

Let us consider an isotropic, ideal elastic deep spherical shell of radius R with an opening angle α in spherical coordinates, (r, θ, ϕ) , as shown in Fig. 4.2(a). While linear theories usually spare us from distinguishing between different configurations, the current case differs since a small displacement theory is applied in the context of a large displacement problem. The mid-plane of the initial, stress-free configuration is denoted by Ω^0 , its mirror image by $\hat{\Omega}$, whereas the resulting, observable shape is indicated by Ω , cf. Fig. 4.2(b). Whilst the transition from the initial to the inverted state is described by the displacements $\mathbf{u}^0 = \hat{\Omega} - \Omega^0$, the additional small displacements that arise due to the edge effect are given by $\hat{\mathbf{u}} = \Omega - \hat{\Omega}$. The transformation from Ω^0 to Ω is thus described by $\mathbf{u} = (u, v, w) = \hat{\mathbf{u}} + \mathbf{u}^0$, where u, v and w describe the meridional, circumferential and outward normal displacement, respectively. Note that this notation differs from other chapters insofar as the displacement vector $\mathbf{u}^0 = (u^0, v^0, w^0)$

evokes bending stresses here, whereas elsewhere a small initial *stress-free* transversal displacement, w^0 , is taken into account to extend the FvK plate theory to the context of shallow shells.

Since linear theories allow the superposition of results, the governing equations are written in terms of the observable displacements, \mathbf{u} ; they can easily be adapted to a particular transformation by substituting all involved stresses, strains and displacements, *e.g.* using $\hat{\mathbf{u}}$ instead of \mathbf{u} , etc. Due to rotational symmetry, three of the linearised equilibrium equations are trivial, and the remaining in-plane equilibrium in the two tangential directions (φ and θ) as well as the balance of momentum in meridional direction require [112]:

$$\begin{aligned} \frac{d}{d\varphi} (\sigma_\varphi \sin \varphi) - \sigma_\theta \cos \varphi - q_\varphi \sin \varphi + p_T R \sin \varphi &= 0 \\ \sigma_\varphi \sin \varphi + \sigma_\theta \sin \varphi + \frac{d}{d\varphi} (q_\varphi \sin \varphi) + p_N R \sin \varphi &= 0 \\ \frac{d}{d\varphi} (m_\varphi \sin \varphi) - m_\theta \cos \varphi - q_\varphi R \sin \varphi &= 0. \end{aligned} \quad (4.1)$$

where p_T and p_N denote a meridional in-plane loading per unit area and a pressure loading, respectively. The shear stress in circumferential direction is absent due to rotational symmetry, and thus $q_\theta = 0$. The considered problem is statically indeterminate, since three equilibrium equations contain five unknowns: the meridional and circumferential in-plane stresses, σ_φ and σ_θ , respectively, the corresponding bending stress resultants, m_φ and m_θ , and the meridional shear force q_φ ; note that all stress resultants are pre-integrated in thickness direction and are thus expressed as force per unit length [N/m] or bending moment per unit length [Nm/m].

By making use of the kinematic relations and the material law, the in-plane and bending stress resultants can be rewritten as a function of displacements in the meridional and the outwards positive normal direction, u and w , respectively, to reduce the number of unknowns to three. While the kinematic relation of the mid-plane strains, ε , requires:

$$\varepsilon_\varphi = \frac{1}{R} \left(\frac{du}{d\varphi} - w \right) \quad \text{and} \quad \varepsilon_\theta = \frac{1}{R} (u \cot \varphi - w), \quad (4.2)$$

the geometric relation between the curvature changes and displacements is expressed by:

$$\kappa_\varphi = \frac{1}{R^2} \frac{d}{d\varphi} \left(u + \frac{dw}{d\varphi} \right) \quad \text{and} \quad \kappa_\theta = \left(u + \frac{dw}{d\varphi} \right) \frac{\cot \varphi}{R^2}. \quad (4.3)$$

Due to the isometry of the mirror image, no elastic in-plane strains are initially imposed ($\varepsilon_\varphi^0 = \varepsilon_\theta^0 = 0$), and thus $\varepsilon = \hat{\varepsilon}$. The constitutive law relates those strains to the stress resultants via

$$\begin{aligned} \sigma_\varphi &= \frac{Et}{1-\nu^2} (\varepsilon_\varphi + \nu \varepsilon_\theta), & \sigma_\theta &= \frac{Et}{1-\nu^2} (\varepsilon_\theta + \nu \varepsilon_\varphi), \\ m_\varphi &= D (\kappa_\varphi + \nu \kappa_\theta) & \text{and} & \quad m_\theta = D (\kappa_\theta + \nu \kappa_\varphi), \end{aligned} \quad (4.4)$$

where $D = Et^3/[12(1-\nu^2)]$ denotes the flexural rigidity.

These four stress resultants can be expressed in terms of displacements. By substituting the strain expressions with the kinematic relations in Eqn 4.2, the in-plane stresses transform to

$$\begin{aligned} \sigma_\varphi &= \frac{Et}{1-\nu^2} \left[\frac{du}{d\varphi} - w + \nu(u \cot \varphi - w) \right] \frac{1}{R} \\ \text{and} \quad \sigma_\theta &= \frac{Et}{1-\nu^2} \left[u \cot \varphi - w + \nu \left(\frac{du}{d\varphi} - w \right) \right] \frac{1}{R}, \end{aligned} \quad (4.5)$$

and a substitution of the curvatures via Eqn (4.3) in Eqn (4.4) converts the bending stresses to

$$\begin{aligned} m_\varphi &= -\frac{D}{R^2} \left[\frac{d}{d\varphi} \left(u + \frac{dw}{d\varphi} \right) + \nu \left(u + \frac{dw}{d\varphi} \right) \cot \varphi \right] \\ \text{and} \quad m_\theta &= -\frac{D}{R^2} \left[\nu \frac{d}{d\varphi} \left(u + \frac{dw}{d\varphi} \right) + \left(u + \frac{dw}{d\varphi} \right) \cot \varphi \right]. \end{aligned} \quad (4.6)$$

With these expressions at hand, the equilibrium equation (4.1) can be rewritten in terms of two displacements u, w and the shear force, q_φ :

$$\begin{aligned} \frac{Et}{R(1-\nu^2)} \left(\frac{d^2 u}{d\varphi^2} + \cot \varphi \frac{du}{d\varphi} - u (\cot^2 \varphi + \nu) - (1+\nu) \frac{dw}{d\varphi} \right) - q_\varphi + R p_T &= 0 \\ \frac{Et}{R(1-\nu)} \left(u \cot \varphi + \frac{du}{d\varphi} - 2w \right) + \frac{dq_\varphi}{d\varphi} + q_\varphi \cot \varphi + R p_N &= 0 \\ -\frac{D}{R^2} \left[\frac{d^2 u}{d\varphi^2} + \frac{d^3 w}{d\varphi^3} + \cot \varphi \left(\frac{du}{d\varphi} + \frac{d^2 w}{d\varphi^2} \right) - (\cot^2 \varphi + \nu) \left(u + \frac{dw}{d\varphi} \right) \right] - R q_\varphi &= 0. \end{aligned} \quad (4.7)$$

4.2 Simplification of the Governing Equations

The set of three equilibrium equations can be simplified considerably to two second order differential equations by changing variables according to the methodology of [112–114] via:

$$V = \frac{1}{R} \left(u + \frac{dw}{d\varphi} \right) \quad \text{and} \quad U = R q_\varphi, \quad (4.8)$$

where V has the physical interpretation of the angle of rotation around the axis of the circle of latitude, θ . A substitution of first expression into Eqn (4.6) simplifies the bending stresses to

$$m_\varphi = -\frac{D}{R} \left(\frac{dV}{d\varphi} + \nu \cot \varphi V \right) \quad \text{and} \quad m_\theta = -\frac{D}{R} \left(\nu \frac{dV}{d\varphi} + \cot \varphi V \right). \quad (4.9)$$

In order to establish a relation between the newly introduced variables and the in-plane force σ_φ , the first two equilibrium equations in Eqn (4.1) can be used: by multiplying the first with $\sin \varphi$ and the second with $\cos \varphi$, the two equations may be added and σ_θ cancels out. Integrating this expression then simplifies for shells without an opening at the top to:

$$\begin{aligned} \sin \varphi \left(\sigma_\varphi \sin \varphi + q_\varphi \cos \varphi \right) + R F(\varphi) &= 0 \\ \text{with } F(\varphi) &= \int_0^\varphi \sin \varphi \left(p_T \sin \varphi + p_N \cos \varphi \right) d\varphi. \end{aligned} \quad (4.10)$$

A second relation for σ_θ is obtained by substituting the previous result into the second equilibrium equation in Eqn (4.1), and eventually, both in-plane stress resultants can be expressed in terms of the shear force, or more conveniently U , via

$$\sigma_\varphi = -\frac{1}{R} U \cot \varphi \quad \text{and} \quad \sigma_\theta = -\frac{1}{R} \frac{dU}{d\varphi}. \quad (4.11)$$

The term of the force potential, $F(\varphi)$ has been omitted in this expression since only equilibria in the absence of (pressure) loadings are considered; the only relevant ‘forcing terms’ are the initial bending moments $m_\varphi^0 = m_\theta^0 = -2D(1 + \nu)/R$ and a counterbalancing edge moment. In order to establish a compatibility condition between U and V , the two previous equations are equated with Eqns (4.5) from which the following

simplification can be derived:

$$\begin{aligned} \frac{du}{d\varphi} - w &= \frac{R}{Et} [\sigma_\varphi(U) - \nu\sigma_\theta(U)] \\ \text{and } u \cot \varphi - w &= \frac{R}{Et} [\sigma_\theta(U) - \nu\sigma_\varphi(U)] . \end{aligned} \quad (4.12)$$

Now, w can be eliminated from these equations, and after differentiating the second equation, the term $du/d\varphi$ can be eliminated as well, and the compatibility equation is eventually obtained:

$$u + \frac{dw}{d\varphi} = \frac{1}{Et} \left[(1 + \nu) (\sigma_\varphi - \sigma_\theta) \cot \varphi - R \frac{d}{d\varphi} (\sigma_\theta - \nu\sigma_\varphi) \right] . \quad (4.13)$$

Substituting the displacement variables on the left-hand side with V and using Eqn (4.11) to express the stress resultants in terms of U , the following reduced equilibrium equation arises:

$$\frac{d^2 U}{d\varphi^2} + \cot \varphi \frac{dU}{d\varphi} - (\cot^2 \varphi - \nu) U = Et R V . \quad (4.14)$$

A second equilibrium equation in terms of U and V is obtained by substituting the expressions from Eqn (4.9) into the third equilibrium equation in Eqn (4.1), which reduces to:

$$\frac{d^2 V}{d\varphi^2} + \cot \varphi \frac{dV}{d\varphi} - (\cot^2 \varphi + \nu) V = -\frac{UR}{D} . \quad (4.15)$$

This gives the desired coupled set of two second order equilibrium equations. By introducing a differential operator,

$$L(\dots) = \frac{1}{a} \left[\frac{d^2(\dots)}{d\varphi^2} + \cot \varphi \frac{d(\dots)}{d\varphi} - \cot^2 \varphi (\dots) \right] , \quad (4.16)$$

the two preceding equations can be written more compactly as:

$$\begin{aligned} L(U) + \frac{\nu}{R} U &= Et V \\ \text{and } L(V) - \frac{\nu}{R} V &= -\frac{U}{D} . \end{aligned} \quad (4.17)$$

In order to decouple these equations, the first is substituted into the second equation. Hence, a single expression that relates U and V is obtained:

$$L(V) = \frac{\nu}{EtR} \left(L(U) + \frac{\nu}{R} U \right) - \frac{U}{D}. \quad (4.18)$$

By applying the above defined differential operator on both sides of the first equation of Eqn (4.17) and substituting Eqn (4.18), this system can be converted into a single differential equation of fourth order depending solely on U :

$$LL(U) + \mu^4 U = 0 \quad (4.19)$$

with $\mu^4 = Et/D - \nu^2/R^2$. This equation can finally be reduced to two *uncoupled* second order differential equations,

$$L(U) \pm i\mu^2 U = 0, \quad (4.20)$$

which are complex conjugates. Their solution is also a solution to Eqn (4.19) since applying the L -operator on Eqn (4.20) transforms it back into Eqn (4.18). For the sake of clarity, the two equations in Eqn (4.20) are explicitly rewritten in terms of q_φ :

$$\frac{d^2 q_\varphi}{d\varphi^2} + \cot \varphi \frac{dq_\varphi}{d\varphi} - \cot^2 \varphi q_\varphi \pm i\mu^2 R q_\varphi = 0. \quad (4.21)$$

Now, the solution, which was first obtained by Meissner [112], can be calculated using commercial mathematical software, such as *Mathematica* [115]. It reads for

shells with an opening angle of $\alpha < 90^\circ$:

$$\begin{aligned}
 q_\varphi &= \sin \varphi (\bar{C}_1 V_1 + \bar{C}_2 V_2 + \bar{C}_3 V_3 + \bar{C}_4 V_4) \\
 \text{with } V_1 &= {}_2F_1 \left(\frac{1}{4} (3 - \sqrt{5 - 4iR\mu^2}), \frac{1}{4} (3 + \sqrt{5 - 4iR\mu^2}); 2; \sin^2(\varphi) \right), \\
 V_2 &= {}_2F_1 \left(\frac{1}{4} (3 - \sqrt{5 + 4iR\mu^2}), \frac{1}{4} (3 + \sqrt{5 + 4iR\mu^2}); 2; \sin^2(\varphi) \right), \\
 V_3 &= \bar{G}_{2,2}^{2,0} \left(\sin^2(\varphi) \middle| \begin{array}{c} \frac{1}{4} (1 - \sqrt{5 - 4iR\mu^2}), \frac{1}{4} (1 + \sqrt{5 - 4iR\mu^2}) \\ -1, 0 \end{array} \right), \\
 V_4 &= \bar{G}_{2,2}^{2,0} \left(\sin^2(\varphi) \middle| \begin{array}{c} \frac{1}{4} (1 - \sqrt{4iR\mu^2 + 5}), \frac{1}{4} (\sqrt{4iR\mu^2 + 5} + 1) \\ -1, 0 \end{array} \right),
 \end{aligned} \tag{4.22}$$

and $\bar{C}_1, \bar{C}_2, \bar{C}_3, \bar{C}_4 \in \mathbb{C}$,

where ${}_2F_1$ denotes Gauss's hypergeometric function and \bar{G} the even more general Meijer G function [116]. When the analysis is additionally confined to closed shells, two constants of integration vanish ($\bar{C}_3 = \bar{C}_4 = 0$) to avoid stress singularities and indeterminate expressions at $\varphi = 0$.

The hypergeometric function is an infinite series that can be defined using the gamma function, $\Gamma(\cdot)$, via:

$${}_2F_1(a, b; c; z) = \sum_{k=0}^{\infty} \frac{\Gamma(a+k)\Gamma(b+k)\Gamma(c)}{\Gamma(a)\Gamma(b)\Gamma(c+k)} \frac{z^k}{k!}. \tag{4.23}$$

Its convergence rate depends mainly on μ and has a historic importance, since it was a decisive factor for the practical applicability that limited it to shells with a radius-to-thickness ratio of $R/t \lesssim 100$ [54, 117]. However, nowadays, increased computational performance easily allows the numerical analysis of slenderer shells, even though the series solution complicates an analytical treatment.

Since the solution was obtained by the consideration of two complex conjugate differential equations, the real and imaginary part of V_1 and V_2 may be separated to obtain two real functions:

$$I_1 = \frac{V_1 + V_2}{2} \quad \text{and} \quad I_2 = i \frac{V_1 - V_2}{2} \tag{4.24}$$

Hence, the constants of integration in Eqn (4.22) can be changed accordingly to obtain a real solution:

$$q_\varphi = \sin \varphi (C_1 I_1 + C_2 I_2) \quad \text{with } C_1, C_2 \in \mathbb{R}. \quad (4.25)$$

By using $U = Rq_\varphi$, the first equation in Eqn (4.17) gives V , which then allows the calculation of all stress resultants with the previously introduced substitutions in the Eqns (4.11) and (4.9). These are then used to satisfy the Neumann boundary conditions. The outer edge of a centrally fixed shell, for instance, requires the tantamount conditions of $\sigma_\varphi = q_\varphi = 0$ to be satisfied, and additionally a vanishing edge moment of $m_\varphi = \hat{m}_\varphi + m_\varphi^0 = 0$. Hence, the two constants of integration suffice to enforce the boundary conditions, but their values are not presented here due to a lack of compactness. Note that it is the balance of the bending moment that prevents a trivial solution of $C_1 = C_2 = 0$ and thus evokes the boundary layer effect. The resulting displacements u and w are obtained by considering both kinematic relations in Eqn (4.2): solving for the meridional displacement leads to the integral expression of

$$u = R \sin \varphi \left(\int \frac{\varepsilon_\varphi - \varepsilon_\theta}{\sin \varphi} d\varphi + C_5 \right), \quad (4.26)$$

and substituting this result into the latter equation gives the normal displacement:

$$w = R \cos \varphi \left(\int \frac{\varepsilon_\varphi - \varepsilon_\theta}{\sin \varphi} d\varphi + C_5 \right) - R\varepsilon_\theta. \quad (4.27)$$

The constant C_5 is used to satisfy a boundary condition, *e.g.* $u = w = 0$ at $\varphi = 0$ for the considered centrally fixed shell; it represents a rigid body mode that does not directly affect the strain energy. By substituting these two expressions into Eqn (4.8), the relation between the angle of rotation and in-plane strains is revealed:

$$V = \cot \varphi (\varepsilon_\varphi - \varepsilon_\theta) - \frac{d\varepsilon_\theta}{d\varphi}. \quad (4.28)$$

The horizontal displacement, which is of central importance in practical application since it transfers a shearing force to the subjacent walls, takes the particular simple form:

$$\delta h = R \sin \varphi \varepsilon_\theta. \quad (4.29)$$

Hence, all relevant quantities for a shell's design can be derived from U and V . Note that the expressions in Eqn (4.26) and Eqn (4.27) involve integrals of a hypergeometric series, which can be expressed via a *Meijer G* function. However, such series expressions add additional arduousness that makes analytical solutions elusive, and thus, simplifying methods are discussed next.

4.3 Thin Shell Approximation

The historic limitation to slenderness ratios of $R/t \lesssim 100$ for practical application led to a series of simplifications in the beginning of the 20th century, since lightweight shell constructions during that time encountered ratios of up to $R/t = 600$, which corresponds to $\mu \approx 45$ [117]. Blumenthal [118] analysed the accuracy of an asymptotic method and considers $\mu \rightarrow \infty$ to propose a solution that employs a series expansion with k terms for deep shells; he concludes that using four terms gives very accurate results since the error is approximately proportional to $(\mu^2)^k$ as long as φ does not take very small values. However, for most practical application the consideration of a single term suffices. In his approach, he first substitutes $z = q_\varphi \sqrt{\sin \varphi}$ and approximates Eqn (4.21) in its asymptotic limit. The substitution has the advantage that the term containing the first derivative of q_φ in Eqn (4.21) vanishes. It can be shown that for large values of μ , the derivative of the function will be large compared to the original function, and the same holds for higher derivatives. Thus, it is justified to neglect the function q_φ in (4.21), but not its derivatives, which then gives:

$$\frac{d^2 q_\varphi}{d\varphi^2} = Et V \quad \text{and} \quad \frac{d^2 V}{d\varphi^2} = -\frac{R}{D} q_\varphi, \quad (4.30)$$

and eliminating V results in:

$$\frac{d^4 z}{d\varphi^4} + 4\lambda^4 z = 0 \quad \text{with} \quad 4\lambda^4 = (1 - \nu^2) \left(1 + 12 \frac{R^2}{t^2} \right) \approx R^2 \mu^4. \quad (4.31)$$

For a more compact notation the variable of the opposing angle that is measured from the outer edge at $\varphi = \alpha$ is introduced: $\bar{\varphi} = \alpha - \varphi$; note that both variables, φ and $\bar{\varphi}$, are used to write the solution of Eqn (4.30):

$$q_\varphi = \frac{e^{-\lambda \bar{\varphi}}}{\sqrt{\sin \varphi}} [C_1 \cos(\lambda \bar{\varphi}) + C_2 \sin(\lambda \bar{\varphi})] + \frac{e^{\lambda \bar{\varphi}}}{\sqrt{\sin \varphi}} [C_3 \cos(\lambda \bar{\varphi}) + C_4 \sin(\lambda \bar{\varphi})]. \quad (4.32)$$

The variables of C_3 and C_4 are related to the non-decaying term and are zero in the considered case of closed shells. After calculating V via the second equation in Eqn (4.30), the in-plane and out-of-plane stress resultants are calculated according to Eqn (4.11) and Eqn (4.9), respectively, and finally, relevant displacements are obtained as before via Eqns (4.26)-(4.29). The free edge condition requires $\sigma_\varphi(\bar{\varphi} = 0) = q_\varphi(\bar{\varphi} = 0) = 0$, and thus, $C_2 = -C_1 \cot(\alpha\lambda)$, which reduces the previous expression in Eqn (4.32) to:

$$q_\varphi = C_1 e^{\lambda \bar{\varphi}} \frac{\sin(\lambda \varphi)}{\sin(\alpha \lambda) \sqrt{\sin \varphi}}. \quad (4.33)$$

A vanishing edge moment is ensured by taking into account that the inversion process applied a uniform bending moment of $m_r = -2(1 + \nu)D/R$ everywhere; thus, an edge moment of opposing sign is required. It follows:

$$C_1 = \frac{2E\lambda^2 t^3 \sqrt{\sin(\alpha)}}{3R^2(1 - \nu)[(1 - 2\nu) \cot(\alpha) - 2\lambda]}. \quad (4.34)$$

Substituting these constants into the equations of the stress resultants and displacements gives all results in closed form, where the only remaining variables are the geometric and material parameters.

A further simplification of these equations for shells with $\alpha = 90^\circ$ was presented by Geckeler [119], where the substitution of $z = q_\varphi \sin \varphi$ becomes negligible. The solution resembles a boundary problem in cylinders, and thus, it can also be applied for inverted tubes as described in the following for the sake of completeness.

4.4 Inversion of Cylindrical Shells

The equations of a cylinder of length, L , and mid-plane radius, R , in cylindrical coordinates, (r, θ, x) , can be considered as a special case of the equations of Meissner [112] for rotationally symmetric structures with in general two differing radii of curvature; when the meridional radius of curvature approaches infinity, the angular coordinate becomes the vertical axis, x . In inverted cylinders, a similar edge effect is observed, where – depending on the sign of the Poisson's ratio – the edge either rotates outwards ($\nu > 0$) or inwards ($\nu < 0$) around the circumferential axis, θ , see Fig. 4.3.

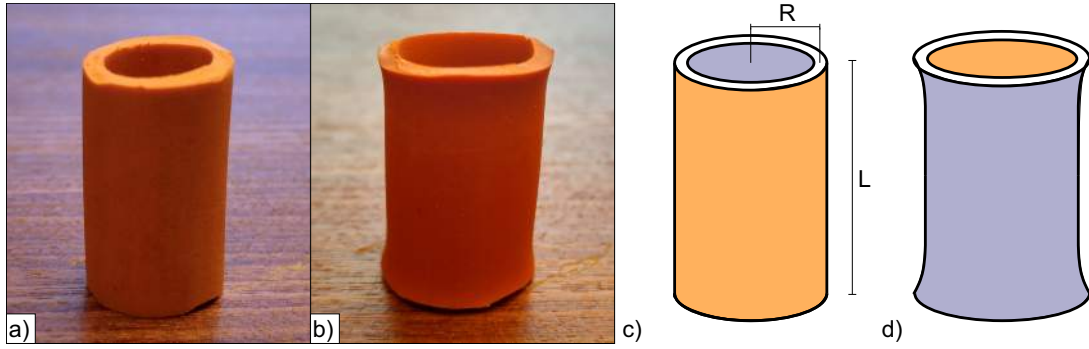


Figure 4.3: Initial stress-free cylinder, (a), and its inversion, (b). The corresponding sketches in (c) and (d) illustrate that the inversion forces the outer radius to become the inner radius and vice versa, which imposes a constant bending moment of $m_\theta = -2D/R$ on the mirror-symmetric shape. For positive Poisson's ratios, an outwards rotation of the edges is observed.

The kinematic relations in a cylinder with rotationally symmetric deformations read:

$$\varepsilon_x = \frac{du_x}{dx} \quad \text{and} \quad \varepsilon_\theta = \frac{w}{R}, \quad (4.35)$$

where w describes the outwards normal deflection [13]. The strains are related to forces as before, see Eqn (4.4) with $\varepsilon_\varphi \equiv \varepsilon_x$. It is assumed that the boundary condition $\sigma_x = 0$ for $x = 0$ and $x = L$ is also satisfied everywhere else in the boundary region since axial constraints are absent; hence, $\varepsilon_x = -\nu\varepsilon_\theta$. Rotational symmetry excludes variations in the circumferential direction from which follows $q_\theta = 0$. The balance of momentum requires $dm_x/dx = q_x$, and for the normal equilibrium of forces follows:

$$-\frac{d^2 m_x}{dx^2} + \frac{\sigma_\theta}{R} = 0. \quad (4.36)$$

The kinematics of curvatures simplify to:

$$\kappa_x = -\frac{d^2 w}{dx^2} \quad \text{and} \quad \kappa_\theta = -\frac{w}{R^2}. \quad (4.37)$$

Substituting the stress resultants in Eqn (4.36) with their expressions in terms of strain components according to Eqn (4.4), and using the kinematic relations in Eqn (4.37) and Eqn (4.35), respectively, gives the governing equation:

$$\frac{d^4 w}{dx^4} + \frac{\nu}{R^2} \frac{d^2 w}{dx^2} + \frac{Et(1-\nu^2)}{DR^2} w = 0. \quad (4.38)$$

Let us now consider the particular case of the small deflections from the mirror symmetric shape: the change in circumferential curvature of this configuration are negligible, $\hat{\kappa}_\theta \approx 0$, since $\hat{w} \leq t \ll R$, and thus, the term containing the second derivative in Eqn (4.38) vanishes:

$$\frac{d^4 \hat{w}}{dx^4} + 4\lambda_c^4 \hat{w} = 0 \quad \text{with} \quad 4\lambda_c^4 = \frac{12(1-\nu^2)^2}{R^2 t^2}. \quad (4.39)$$

Note the similarity to the method of [118] resulting in Eqn (4.31), where higher-order derivatives dominate the structural behaviour. The relevant terms of the solution of this simplified equation reads:

$$\hat{w} = e^{-\lambda_c x} (C_1 \sin \lambda_c x + C_2 \cos \lambda_c x). \quad (4.40)$$

The similarity to Geckelers solution is apparent, and the only difference is the parameter $\lambda_c \neq \lambda$. From the shear force boundary condition, $d^3 \hat{w}/dx^3 = 0$ at $x = 0$ follows $C_1 = -C_2$. In contrast to the spherical case, one principal curvature ($\kappa_x^0 = 0$) does not change during inversion, and thus, the continuously imposed bending moment in longitudinal direction is solely evoked by the Poisson's effect, $m_x^0 = -2\nu D/R$. Since $\kappa_\theta \approx \kappa_\theta^0 = -2/R$, the resulting longitudinal bending moment can be approximated via:

$$m_x \approx D(\hat{\kappa}_x + \nu \kappa_\theta^0) = -2\lambda_c^2 C_1 e^{-\lambda_c x} [\sin(\lambda_c x) + \cos(\lambda_c x)] + m_x^0 \quad (4.41)$$

and enforcing the vanishing edge moment gives the remaining constant of integration with the physical interpretation of the normal edge displacement:

$$C_1 = -\frac{\nu}{\lambda_c^2 R} = \nu \frac{t}{3(1-\nu^2)^2}. \quad (4.42)$$

This amplitude is a function of the Poisson's ratio and the thickness, only, and does not depend on the radius of the cylinder.

4.5 Linear Shallow Shell Theory

The simplification in §4.2 excluded cases of shallow shells where the angle φ is very small throughout the shell, and it can be shown [117] that the quality of the solution of

the method of Blumenthal [118] depends on the smallness of the value

$$\frac{\cot \varphi}{\sqrt{2R/t} [3(1 - \nu^2)]^{1/4}}. \quad (4.43)$$

The exact method, however, requires a high number of terms if the considered shell is very thin, and this leaves a theoretical gap of suitable methods for shells that are shallow *and* thin. In order to close it, a Taylor series expansion of the exact governing equations can be used to approximate $\cot \varphi$ via $1/\varphi$, which causes an error of not more than an 1.0% for $\varphi < 10^\circ$. The governing equations in Eqn (4.21) then become:

$$\frac{d^2 U}{d\varphi^2} + \frac{1}{\varphi} \frac{dU}{d\varphi} - \frac{1}{\varphi^2} U \pm i\mu^2 U = 0. \quad (4.44)$$

Using the same reasoning as for Eqn (4.21) and taking into account that the solutions are complex conjugates, it suffices to solve only one of these equations. Hence, the real (\Re) and imaginary (\Im) part can be separated to obtain:

$$\begin{aligned} U = & C_1 \Re [J_1 (\sqrt[4]{-1} \varphi \mu)] + C_2 \Im [J_1 (\sqrt[4]{-1} \varphi \mu)] \\ & + C_3 \Re [Y_1 (-\sqrt[4]{-1} \varphi \mu)] + C_4 \Im [Y_1 (-\sqrt[4]{-1} \varphi \mu)], \end{aligned} \quad (4.45)$$

where J_1 and Y_1 denote Bessel functions of the first order of the first and second kind, respectively. Meissner [112] pointed out that the hypergeometric function in Eqn (4.22) resembles the series representation of Bessel functions, which can be written as:

$$\begin{aligned} J_p(\varphi) &= \frac{(\varphi/2)^p}{\Gamma(p+1)} {}_0F_1 \left(; p+1; -\varphi^2/4 \right) = \sum_{k=0}^{\infty} \frac{(-1)^k \left(\frac{\varphi}{2}\right)^{2k+p}}{\Gamma(p+k+1) k!} \\ \text{and } Y_p(\varphi) &= \lim_{x \rightarrow p} \frac{J_p \cos(p\pi) - J_{-p}(\varphi)}{\sin(p\pi)}, \end{aligned} \quad (4.46)$$

where p denotes the Bessel function's order and ${}_0F_1(\dots)$ the generalized hypergeometric function. For closed shells, the constants C_3 and C_4 vanish, since Y_1 is singular at $\varphi = 0$. The solution of U is employed to find the corresponding expression V via the first equation of Eqn (4.17):

$$V = \frac{1}{Eha} \left[\frac{dU}{d\varphi^2} + \frac{1}{\varphi} \frac{dU}{d\varphi} - \frac{1}{\varphi^2} U \right], \quad (4.47)$$

and consequently all stresses in Eqn (4.8), Eqn (4.9) and Eqn (4.11) now read:

$$\begin{aligned} \sigma_\varphi &= -\frac{1}{\varphi} \frac{U}{R} \quad , \quad m_\varphi = -\frac{D}{R} \left(\frac{\nu}{\varphi} V + \frac{dV}{d\varphi} \right) \quad , \quad q_\varphi = R U \\ \sigma_\theta &= -\frac{1}{R} \frac{dU}{d\varphi} \quad \text{and} \quad m_\theta = -\frac{D}{R} \left(\frac{1}{\varphi} V + \nu \frac{dV}{d\varphi} \right) . \end{aligned} \quad (4.48)$$

The displacements are then calculated in the same manner as before in Eqn (4.26)-(4.29).

4.6 Results

In the following, the presented methods are evaluated and compared to finite element simulations. First, the simulation details are described, before the results of inverted cylindrical and spherical shells are evaluated in §4.6.2 and §4.6.3, respectively.

4.6.1 Finite Element Modelling

The geometrically nonlinear finite element simulations were computed with the commercially available code *LS-DYNA* [120]. The software was chosen, since it offers a wide variety of solution control parameters that turned out to be vital for a reliable calculation; similar attempts to produce accurate results in *ABAQUS* were not successful.

In order to produce a reference solution for analytical approaches, the inversion of cylindrical and spherical shells were studied. The first are relatively thick ($R/t = 20.5$) and approach the limit of the shear-neglecting shell theory of Love, whilst in the latter case thick and thin shells with $R/t = 20$ and $R/t = 100$, respectively, were analysed. In both cases, axisymmetric volume weighted solid elements were employed to model one side of a section. An implicit dynamic analysis was conducted to stabilise the finite element simulation when static stability is lost and to guarantee that a valid equilibrium is found after dynamic effects are rapidly damped out by a high mass and stiffness damping. The numeric time integration parameters of the Newmark method [121] were chosen to be unconditionally stable. The linear elastic material law was employed with $E = 10^7$, density equal to 0.05 and a varying positive Poisson's ratio; all values refer to SI units.

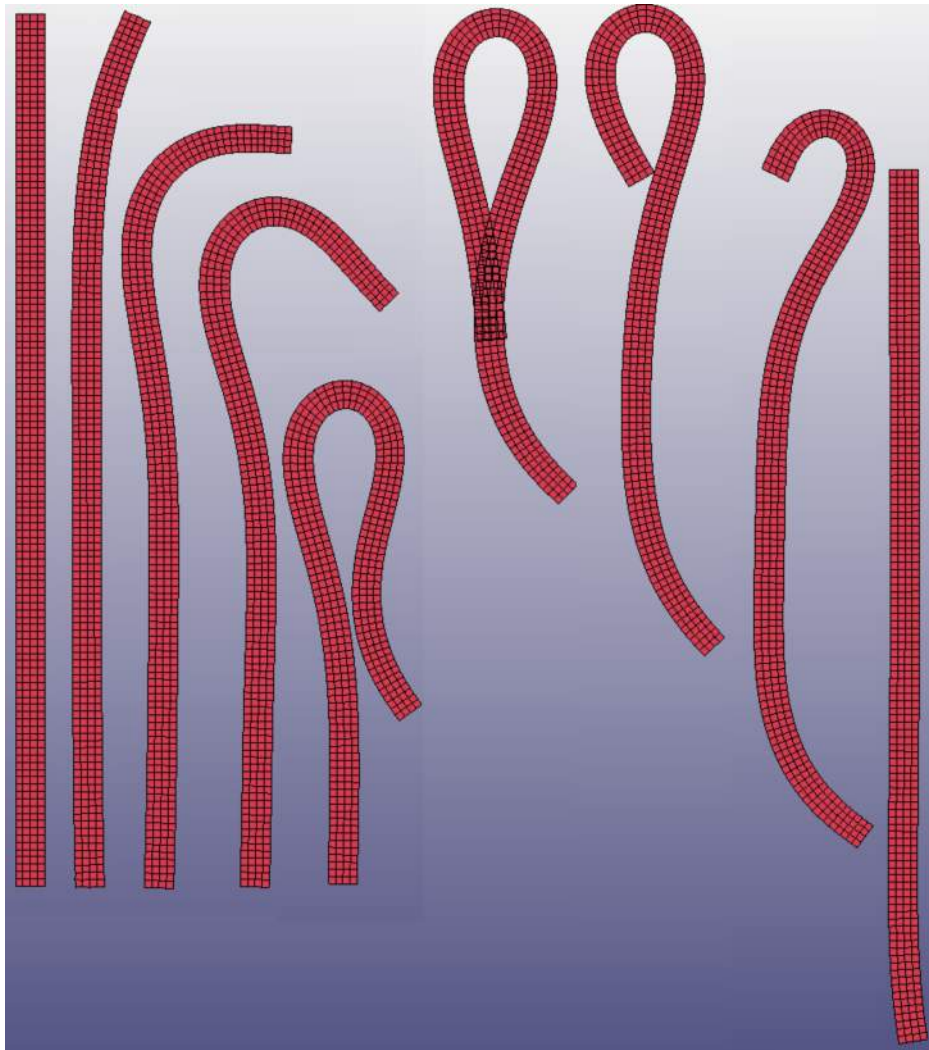


Figure 4.4: Sequence of the inversion of a cylindrical shell in LS-Dyna. Initial shape (left), followed by unstable transition modes, and finally, a stable inversion forms (right). Since the potentially non-symmetric transition is not of particular interest here, only a section with axial symmetry has been modelled.

Before the inversion process of the cylinder was initiated by a displacement controlled vertical movement of the mid-node, an outwards pointing force at the cylinder's top was applied temporarily to cause a sufficiently large eccentricity of approximately $1.5t$, see Fig. 4.4. Since only the resulting inverted shapes are compared, no contact was considered during analysis; this avoids the introduction of a potential error source to the implicit time integration scheme that is known to be prone to rounding errors. The model contained 120×4 elements in longitudinal and thickness direction, respectively.

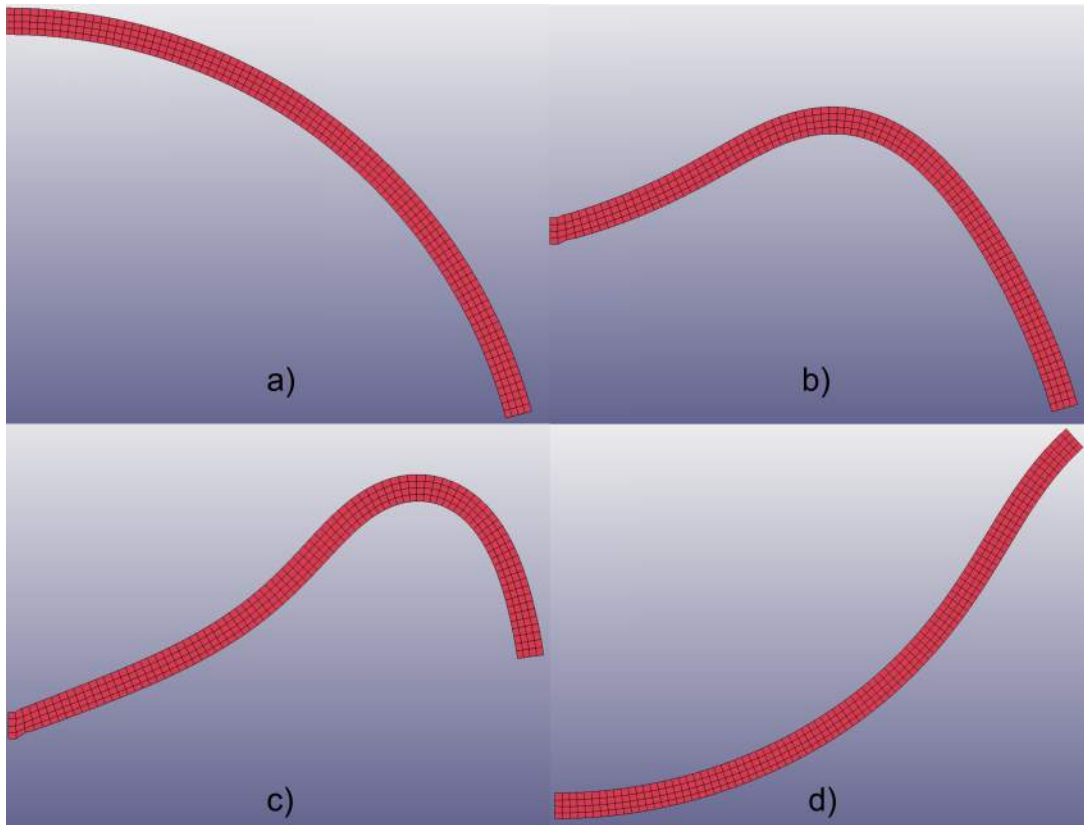


Figure 4.5: Sequence of inversion of a spherical shell with $\alpha = 75^\circ$ in LS-Dyna. Due to axial symmetry only a section has been modelled.

In the spherical case, at least 50×4 elements in meridional and thickness direction, respectively, were used. First, the horizontal and vertical movement of the most outer point was temporarily prevented before a prescribed displacement was imposed to all central nodes at the axis of revolution to ensure a smooth inversion process, see Fig. 4.5. The outer horizontal supports turned out to increase the stability of the analysis and were just released at the end of the inversion process (not depicted). The maximum time step size was chosen to 0.01 and the analysis was terminated after all oscillations were damped out.

A key factor to guarantee the stability of the analysis and to prevent inaccuracies is to control the solutions energy and displacement convergence tolerance and specifying an extremely small value of 10^{-14} , which self-evidently requires a double precision analysis. It is required since the stresses during the inversion process are extremely large compared to the only slightly stressed inverted shape, and thus, even slight devi-

ations during the inversion process may cause significant deviations in the alternative equilibrium state.

4.6.2 Inversion of Cylindrical Shells

The suitability of the presented analytical approach in §4.4 is evaluated by considering an example of an inverted cylinder with a midline-radius of $R = 10.25$, length $L = 20$ and thickness $t = 0.5$. The dimensionless outwards normal deflection, $\hat{\omega} = \hat{w}/t$, is shown for differing values of the Poisson's ratio in Fig 4.6. The analytical predictions (lines) for the amplitude as well as the wavelength show a very good agreement with FE simulations (dots) and confirm that the edge bending is solely caused by Poisson's effect.

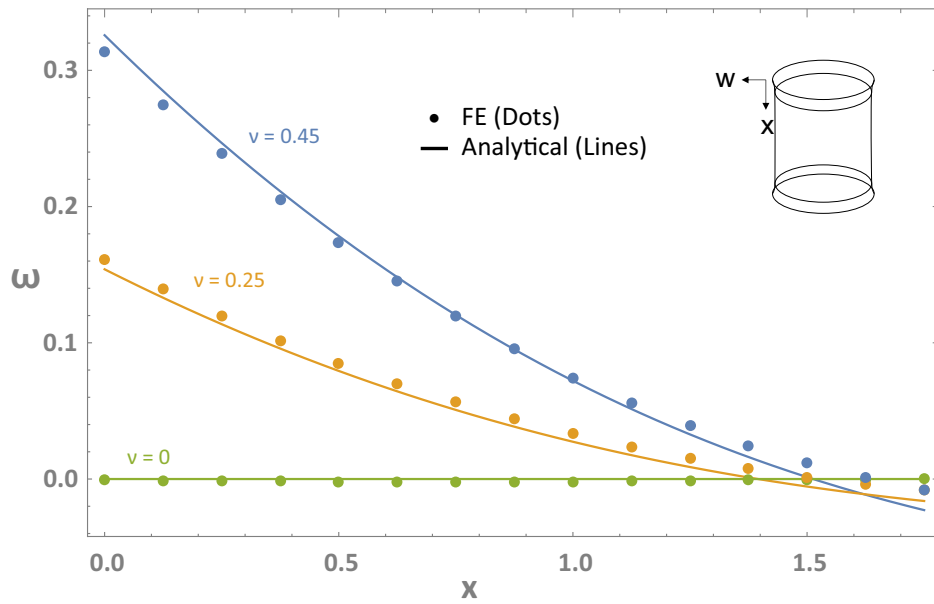


Figure 4.6: Normalised horizontal deflection, $\hat{\omega} = \hat{w}/t$, of an inverted cylinder with mid-plane radius, $R = 10.25$, $t = 0.5$ and $L = 20$ for variations in the Poisson's ratio. Dots represent FE-results, while lines denote analytical results.

Note that the amplitude,

$$\hat{w}(x=0) = \frac{\nu t}{\sqrt{3}(1 - \nu^2)}, \quad (4.49)$$

is independent of the radius of the cylinder. The deflection function

$$\hat{w} = \frac{\nu}{R\lambda_c^2} e^{-\lambda_c x} [\cos(\lambda_c x) - \sin(\lambda_c x)] \quad (4.50)$$

decays quickly and after the first, second and third zero, the maximum deflections do not exceed 21 %, 0.9 % and 0.04 % of the amplitude, respectively. Thus, the doubly curved boundary layer is predominantly hyperbolic for $\nu > 0$ and elliptic for $\nu < 0$. The position of the n th root of the displacement function is:

$$\hat{w} = 0 \quad \text{for} \quad x = \frac{\pi + 8(n-1)}{4\lambda_c} \quad \text{with} \quad n \in \mathbb{N}, \quad (4.51)$$

where \mathbb{N} denotes the set of natural numbers ≥ 1 . In contrast to the amplitude, the characteristic wavelength, l^* , which is here defined as the first zero, is directly proportional to the square root of the radius:

$$\frac{l^*}{R} = \frac{\pi}{4R\lambda_c} = \frac{\pi}{4} \sqrt{\frac{t}{\sqrt{3}R(1-\nu^2)}}. \quad (4.52)$$

4.6.3 Inversion of Spherical Shells

The suitability of the presented linear approaches is evaluated by considering three different cases: first, horizontal variations from the mirror-symmetric shape of thin shells in the range of $\alpha = 30^\circ$ and $\alpha = 75^\circ$ are evaluated. In a second step, the thickness is increased to analyse the changes in the amplitude and wavelength. Finally, a shell on the brink of being shallow ($\alpha = 20^\circ$) is chosen in which the effects of changes in the thickness are analysed to demonstrate the limits of linear theories.

The predictions of the horizontal displacement, δh ($= \hat{\delta}h$ due to mirror symmetry), are depicted in Fig 4.7 and compared to a finite element reference solution. The value of $\nu = 0.45$ increases the acting edge moment by the factor of $1 + \nu$ and causes displacements of the order of the thickness; despite pushing the limit of validity of small displacement theory, all predictions are in good agreement with finite element results: Blumenthal's method (*cf.* §4.3) as well as the shallow shell approximation (*cf.* §4.5) produce virtually indistinguishable results from the exact approach calculated with a series expansion up to 100^{th} order; the working precision in the calculations of the latter was set to 100 digits to prevent rounding errors of significant extent. The accuracy

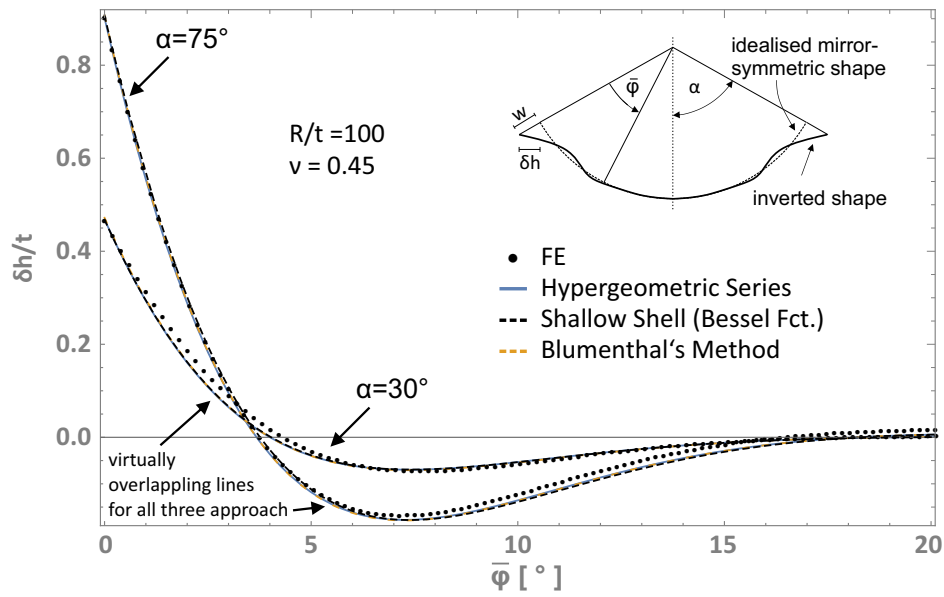


Figure 4.7: Horizontal displacement of two inverted spherical shells of slenderness $\lambda = 12.44$ with $\alpha = 75^\circ$ and $\alpha = 30^\circ$. Dots represent FE-results, while (dashed) lines denote analytical results; dashed lines were employed where necessary to better depict the resembling analytical predictions.

of the shallow shell approximation is insofar surprising, as the range of validity of the former is clearly violated. However, since it is applied to a boundary layer problem in which the edge perturbation rapidly fades out, the shell can be considered as *locally* shallow. Besides being computationally more efficient than the exact method, the shallow shell approach has the advantage that it does not require the user to specify an order of the series expansion; hence it can be calculated analytically without further simplification.

When relatively thick shells ($\lambda = 5.56$) are considered, the analytical predictions of the horizontal displacement are still in fair agreement with finite element results, see Fig. 4.8; the results are shown for opening angles of $\alpha = 75^\circ$ and $\alpha = 45^\circ$, where the latter value was chosen, because an equivalent thicker version of the shell in Fig. 4.7 with $\alpha = 30^\circ$ is not bistable any more according to finite element simulations. The accuracy levels of all analytical models evince only minor differences. This is insofar surprising, as Blumenthal's method is expected to deteriorate since the theory was based on the thinness and depth of a shell; in contrast to that, the exact solution's quality, which does not depend on such an assumption, is expected to stay the same or to even increase due to an increasing convergence rate of the hypergeometric series.

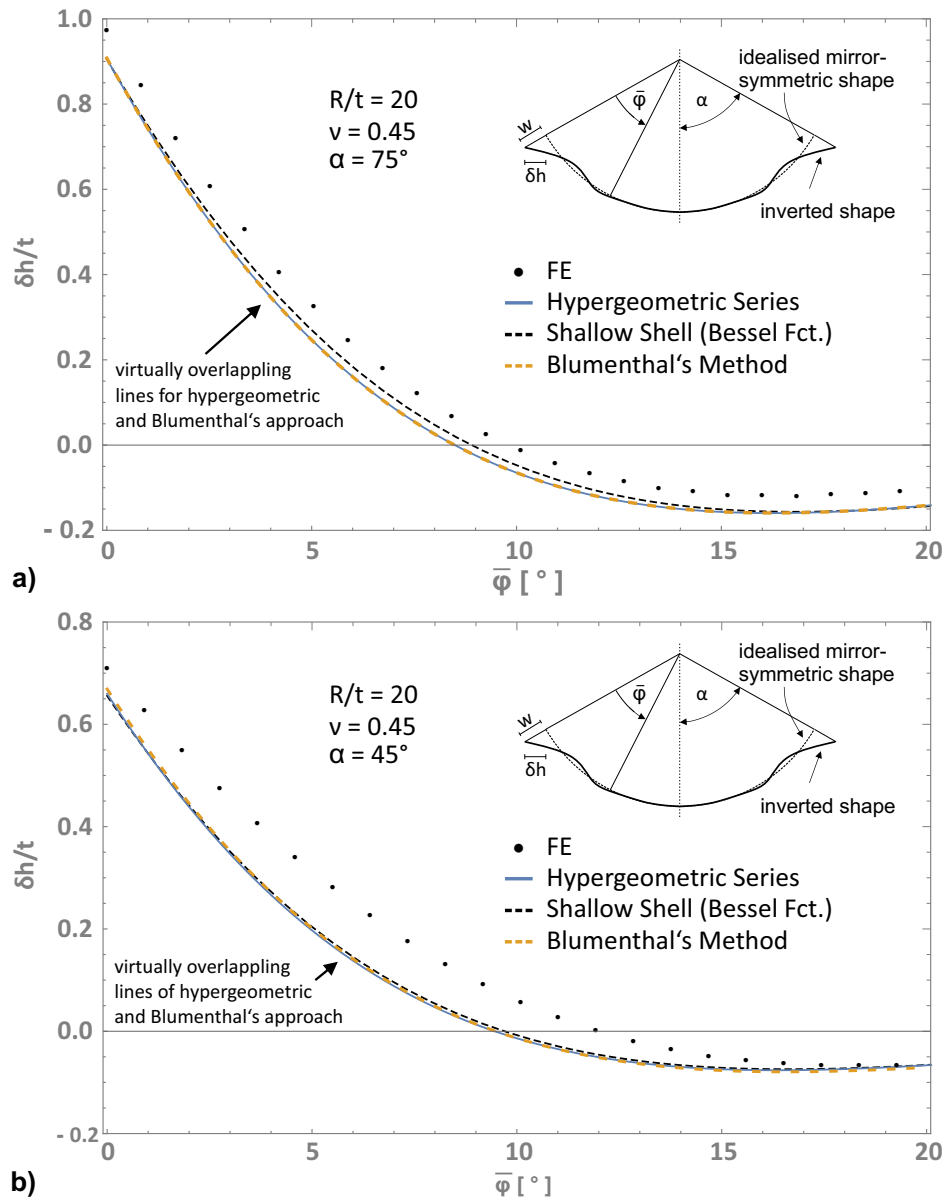


Figure 4.8: Horizontal displacement of two inverted spherical shells of decreased slenderness ($\lambda = 5.56$) with an opening angle of $\alpha = 75^\circ$ in (a) and $\alpha = 45^\circ$ in (b). Dots represent FE-results, while (dashed) lines denote analytical results; dashed lines were employed where necessary to better depict the resembling analytical predictions.

However, in *all* cases, the solution quality deteriorates slightly once the thickness is increased.

While neglected shear deformations become increasingly important in thicker shells, it can be deduced from equally shear-neglecting FvK approaches in literature that this factor is not decisive. More importantly, the bending rigidity increases disproportion-

ally, and thus, a stronger bending-stretching interaction is observed. This causes an increased wavelength that may become large enough to result in a reversion, and apparently this is the case for a shell that with $R/t = 20$ and $\alpha = 30^\circ$.

In order to estimate the wave length in closed form, the thin shell model of Blumenthal is used: The expression for the horizontal displacement in Eqn (4.29) can be rewritten as:

$$\delta h = \frac{R \sin \varphi}{Et} \left[\frac{dq_\varphi}{d\varphi} - \nu q_\varphi \cot \bar{\varphi} \right], \quad (4.53)$$

and substituting the solution of Eqn (4.33) into this equation gives:

$$\delta h = \frac{a\lambda C_1 e^{-\lambda \bar{\varphi}} \sqrt{\sin(\varphi)}}{Et} \left[\cos(\lambda \bar{\varphi}) - \sin(\lambda \bar{\varphi}) \left(1 - \frac{1+2\nu}{2\lambda} \cot(\bar{\varphi}) \right) \right]. \quad (4.54)$$

It can now be seen that the quantity containing the $\cot(\bar{\varphi})$ -term, which arises due to the νq_φ -term in Eqn (4.53), is negligible, since λ and φ were considered to be sufficiently large, and thus, the $\cot(\bar{\varphi})$ is small enough to apply the underlying assumption of $q_\varphi \ll dq_\varphi/d\varphi$ in this context. Using this approximation, the roots of this expression are readily determined to be:

$$\delta h = 0 \quad \text{for} \quad \varphi = \frac{\pi + 8n}{4\lambda} \quad \text{with } n \in \mathbb{N}, \quad (4.55)$$

where n denotes the n^{th} zero. This gives the characteristic wavelength of:

$$R\varphi^* = l^* = \frac{\pi R}{4\lambda} = \frac{\pi R}{\sqrt[4]{64(1-\nu^2)(1+12(R/t)^2)}} \approx \frac{\pi}{4} \sqrt{\frac{Rt}{\sqrt{3(1-\nu^2)}}} \quad (4.56)$$

Note that both, the methodology and solution closely resemble the cylindrical case: in Eqn (4.41), the small quantity of $\hat{\kappa}_\theta$ – that described the deviation from the mirror-symmetric shape – was neglected to obtain a wavelength in Eqn (4.52) that differs by the factor of $\sqrt[4]{(1-\nu^2)}$, since $\lambda_c \neq \lambda$. The factor arose through the consideration of $\sigma_x = 0$ at the cylinder's edge. An alternative derivation of the cylindrical equations with $u_x = \text{const.}$ would lead to identical characteristic wavelength; however, the violation of the support condition would deteriorate the quality of the cylindrical model and diminish the amplitude by more than 10 % for $\nu = 0.45$.

According to Blumenthal's method, the wavelength in spherical shells does not depend on the opening angle, which reveals the limits of this thin shell approximation: it was developed for practical applications in domes, where the lower part is usually of particular interest, since the highest stresses are observed here due to the induced perturbations to the membrane state that are evoked by the boundary conditions; alternatively, open domes can be calculated as long as the central hole is large enough. However, as a remnant of the neglected expressions containing $\sin \varphi$ -terms in the denominator, shallow angles are not approximated appropriately, and consequently, a singularity of the displacement function arises at the apex ($\varphi = 0 \rightarrow \bar{\varphi} = \alpha$). Thus, it is vital that any perturbation is damped out rapidly in closed shells so that it is reasonable to neglect the poorly approximated upper part.

A final example of relatively shallow shell ($\alpha = 20^\circ$) illustrates the limits of both theories: whilst the angle is kept constant, the thickness ratio varies between $R/t = 585$ and $R/t = 88.6$, which corresponds to slenderness ratios of $\lambda = 30.1$ and $\lambda = 11.7$, respectively. The first value was chosen since it represents common slender shells in practice, whereas the latter is an upper bound, since a further increase of the thickness prevented stable inversions. In order to facilitate a comparison with the results of the following chapter, the graphs are plotted over the projected planform radius, $r_0 = R \sin \varphi$; for the chosen parameters of $\alpha = 20^\circ$ and $R = 2.9238$, it follows that the outer planform radius is equal to one.

While all results of Blumenthal's method, shown in Fig. 4.9(a), are indeterminate at the apex of the shell, the neighbouring values for the two thickest shells with $R/t = 97.5$ and $R/t = 88.6$ are unphysical, since they do not approximate zero at the centre; thus, either a non-permissible large in-plane displacement gradient is required to enforce $u_\varphi = 0$, or the shell is predicted to be torn apart at the centre. The latter case, though, goes beyond the scope of the employed framework of linear elasticity and would require fracture mechanical considerations. This conflicting behaviour is concomitant with vanishing roots of the displacement function, and thus, an upper bound estimate for the opening angle at which Blumenthal's approximation becomes unsuitable is when the characteristic wavelength is longer than the opening angle: $\alpha < l^*/R$. Shells with high slenderness ratios, however, can extend their range of validity to such shallow angles and show a fair agreement with FE simulations, since a high λ values remediate some of the errors evoked by small values of φ , but ultimately, for even shallower angles, the theory becomes unsuitable even for very large values of λ .

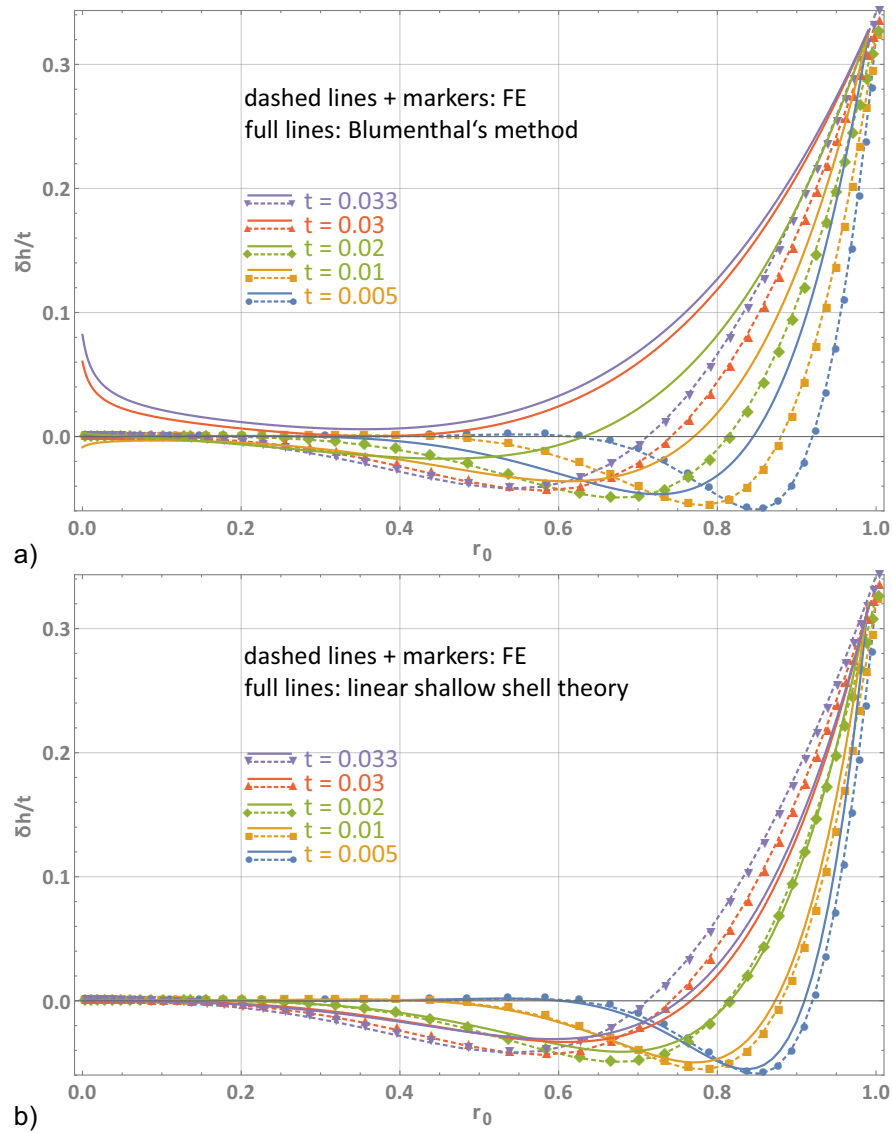


Figure 4.9: Predictions of the dimensionless horizontal displacement, $\delta h/t$, compared to FE simulations for shells of $\alpha = 20^\circ$ and $R = 2.9238$ and a variable thickness. The results are plotted over the coordinate of the projected planform radius, $r_0 = R \sin \alpha$. (a) Blumenthal's method, (b) linear shallow shell theory (cf. §4.5).

Unlike Blumenthal's method, the shallow shell approximation is expected to improve its performance in shallower regions for which it was derived. As depicted in Fig. 4.9(b), its approximation is superior since all boundary conditions are satisfied in all cases and the wavelength is still in fair agreement with finite element results. In contrast to Blumenthal's method, the horizontal displacement is now predominantly underestimated. While the normalised horizontal displacement, $\delta h/t$, at the outer

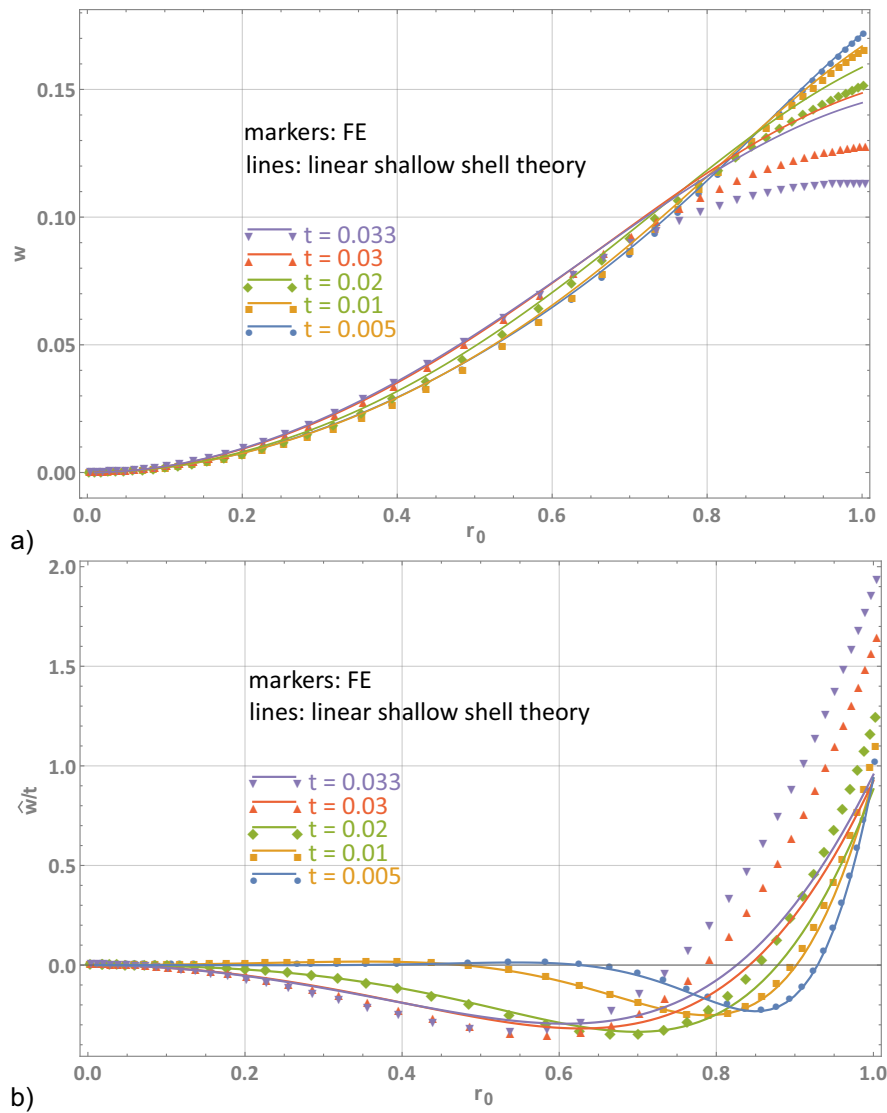


Figure 4.10: (a) Resulting inverted shape for the same geometric parameters as before: analytical predictions (lines) compared to FE results (markers) for differing thicknesses plotted over the projected planform radius, $r_0 = R \sin \alpha$. (b) Normal deviations from the mirror symmetric shape.

edge is almost constant in all cases, the normal displacement constantly increases, see Fig. 4.10, and as soon as the deflection rises above the value of $\hat{w}/t = 1$ the results significantly deteriorate. This indicates that geometrically linear theories exceed their range of validity. Since the pre-buckled shape already shows significant deviations that are not small, the results of a linear stability analysis are not expected to give meaningful results and are thus omitted here. In order to achieve an accurate description of

shells in this range, a geometrically nonlinear shallow shell approach is employed in the following chapter.

4.7 Summary

The inversion of cylindrical shells as well as deep spherical shells was investigated in this chapter. Even though this process involves large deflections, classical geometrically linear Kirchhoff-Love shell theory has been employed to drastically simplify the problem. The close resemblance of the initial and the inverted shape makes it possible to model the first by considering a uniformly imposed change in curvature of $-2/R$ throughout the shell and enforcing the free boundary condition of a vanishing bending moment. Thus, a linear theory was capable of capturing the small deviations from the mirror-symmetric, inverted shape in deep shells. The resulting boundary effect, which causes the observed deviations, has been analysed by using three different methods from literature for spherical shells: first, the exact method containing a hypergeometric series was presented; second, an asymptotic thin shell approximation according to Blumenthal was used; and finally, the suitability of a linear shallow shell theory was analysed. In addition, the cylindrical case was treated by deriving an approximated method that makes use of a small thickness-to-radius ratio.

While it was shown that Poisson's effect is the driving factor of the observed edge effect in cylinders, the spherical problem was found to also depend on the initial radius of curvature. Since the edge effect is damped out rapidly, the shallow shell approximation was found to show an excellent agreement even for clearly non-shallow shells with angles of up to 75° – and presumably even for angles beyond this value; in such shells, Blumenthal's method leads to almost identically accurate results. The mathematical simplicity of the latter made it possible to approximate the wavelength of the boundary value problem, which closely resembles the cylindrical result, in closed form. Differences in performance were observed, when the limits of linear theories were analysed: it was found that the predictive performance of the shallow shell theory exceeded Blumenthal's approximation in this region; however, since thicker shells experience a proportionally increasing normal displacement it eventually becomes larger than the thickness, and this ultimately requires a geometrically nonlinear approach.

In summary, linear approaches are suitable to describe the approximately mirror-symmetric, post-buckled shape of deep, thin shells, since the evoked rotation leads

to small changes of the radius's absolute value, which affect only a small portion of the shell; however, for thick shallow shells, linear shell theory is unsuitable, since the edge effect may decrease the already small curvatures significantly. In addition, the length of the boundary layer extends and begins to affect the whole shell, which may ultimately cause a reversion. Thus, the seemingly more complicated case of a deep shell can be treated with a simpler, linear theory, whilst shallow shells often require a more detailed, nonlinear analysis to model the long wave solution of the boundary layer accurately. Such a nonlinear approach is presented next.

Chapter 5

Nonlinear Shell Theory: Inversion of Shallow Shells

In order to establish a suitable framework for the analytical description of bistable shallow shells, a nonlinear approach is provided in this chapter to describe the behaviour of inverted shallow shells. The aim is to analyse and identify the critical geometry and related influencing factors at which alternative stable equilibria become possible. The accurate modelling of the inverted shape and concomitant stresses provides further insight into the governing factors and allows use of bistability in optimised ways. Whilst approaches in literature, *e.g.* [35, 36, 39, 45, 56, 72], focus on unsupported shells, the boundary conditions have recently been shown to be a vital factor: in an initial study Sobota & Seffen [29] point out that while a simply supported uniformly curved cap can be bistable, finite element analysis of a *clamped* cap for a wide range of parameters did not show any alternative stable configurations. Inspired by this observation, the influence of support conditions on bistability is analysed and quantified in a systematic way by employing linear elastic springs as edge supports. To the knowledge of the author, this aspect has not been studied before with the exception of the mentioned preliminary study [29] that was conducted in the context of this dissertation and of which some results are presented here. The findings are then applied to explore possibilities of further structural manipulations to produce bistable shells with annular planform. In a next step, the enriched solution space of two rotationally symmetric interacting shells is studied. In order to identify where the complex geometrical interaction of shells is required, and where simpler beam structures can be employed instead, a simplified beam model is derived for the purpose of comparison.

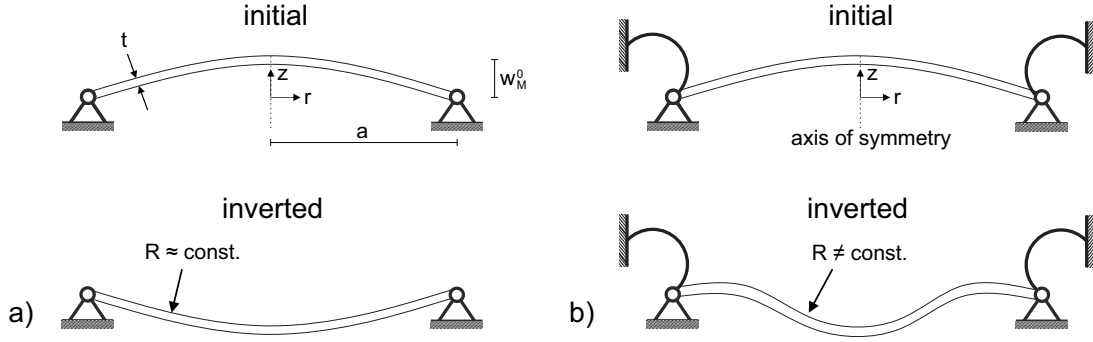


Figure 5.1: Illustration of the inverted configurations of: (a) a uniformly curved cap with fixed-pinned supports; (b) the same model with additional rotational spring supports that are soft enough to allow for a stable inversion. Whilst (a) is approximately uniformly curved, (b) possesses a more intricate deflection field with local variations in Gaussian curvature.

The higher-order FvK model developed here follows a Ritz approach that relates the assumed deflection field to the in-plane properties via Gauss Theorema Egregium and identifies stable inverted shapes via energy minimisation. This novel approach of higher order is required since existing models are not capable of describing the strongly nonuniformly curved deflections caused by the more elaborate supports, see Fig. 5.1. The model presented here overcomes the uniform curvature (UC) assumption, and since an increased number of degrees of freedom allows for additional latitude of the solution space, it can be applied to a wide range of different geometries. Without claiming to depict the details of the snap-through process, the employed approach aims to provide an accurate model of the resulting inverted shape.

This chapter is organised as follows: first, the mathematical framework of the analytical approach is developed and its general solution is described in §5.1. Several particular applications are then presented, of which the first in §5.2.1 considers a macro-element of an in general nonuniformly curved shell whose edges are supported by linear elastic rotational and in-plane springs. The following section, §5.2.2, deals with a changed topology of an annular planform, whereas §5.2.3 exemplifies the versatility of the presented methodology by considering two coupled shells, where a richer response is expected due to interaction. A brief simplification for corresponding beam structures is given in §5.2.4 to compare the behaviour of shells to their dimensionally reduced counterpart. Results are then presented in §5.3, followed by a summary.

5.1 Derivation of an Analytical Model: General Solution

In the framework of the employed shallow shell model, it is beneficial to employ a cylindrical coordinate system, (r, θ, z) , and to describe the shell in terms of its planform radius, a , and thickness, t , *cf.* Fig. 5.1. Whilst the original FvK equations consider a flat plate, it is straightforward to extend them for shallow shells by considering a small initial transversal displacement, w^0 , that does not evoke stresses. It is convenient to assume that this displacement is imposed without affecting the radial or circumferential displacement, u^0 or v^0 , respectively, so that the z component of Ω^0 is described by w^0 , whereas all its other displacement components are zero; note the difference to §4, where w^0 denoted the displacements towards the *mirror symmetric* configuration. The transition from Ω^0 to the deformed configuration is, as before, established via $\Omega - \Omega^0 = \mathbf{u} = (u, v, w)$ so that the transversal component of the current configuration is given by $w^0 + w$.

For uniformly curved shells, the geometric parameters of shallow shells are expressed in terms of the parameters of the previous chapter via

$$a = R \sin \alpha \quad \text{and} \quad w_M^0 = R(1 - \cos \alpha). \quad (5.1)$$

For $a \gg w_M^0$, the radius of curvature can be approximated by $R \approx a^2/2w_M^0$, and thus, the slenderness parameter transforms to $\lambda \approx a\sqrt{3(1-\nu^2)}/\sqrt{w_M^0}t$ for shallow shells. Instead of the angular coordinate, φ , its projection to the planform, $r = R \sin \varphi$, is used in the presented approach, which is outlined in Fig. 5.2. By assuming a deflection field, w , as a polynomial series with n degrees of freedom, η_i , two types of boundary conditions (BC) are satisfied on the boundary, Γ : these can either be Neumann conditions that specify stresses of σ_N on Γ_N , or impose certain displacements, u_D , on Γ_D via Dirichlet conditions. All related properties of the bending surface are derived from this and the coupling with in-plane stresses is realised by relating the changes in Gaussian curvature, g , to the Airy stress function, Φ , according to Gauss Theorema Ergregium. From Φ , the in-plane stresses and mid-plane strains, σ and ε , are derived in terms of the degrees of freedoms of the deflection field. The constants of integration that arise in Φ are employed to satisfy in-plane boundary conditions on Γ_N and Γ_D . By differentiating the strain energy functional, Π , which is the sum of the bending energy, Π_B ,

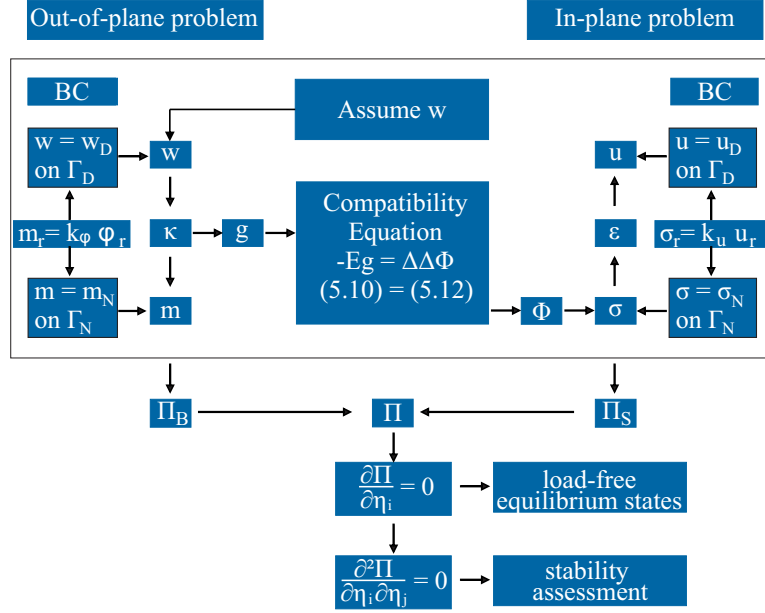


Figure 5.2: Overview of the coupled nature of the Föppl-von Kármán equations and the Ritz solution approach.

and the stretching energy, Π_S , with respect to the degrees of freedom, equilibria are approximated. Their stability is then assessed via the definiteness of the stiffness matrix. The general solution is outlined next, before particular applications are discussed.

Governing Equations

The nonlinear FvK strain definition of Eqn (2.4) reads for rotationally symmetric deformations in cylindrical coordinates:

$$\varepsilon_r = \frac{du}{dr} + \left(\frac{d(w^0 + w)}{dr} \right)^2 - \left(\frac{dw^0}{dr} \right)^2 \quad \text{and} \quad \varepsilon_\theta = u/r. \quad (5.2)$$

The considered shell is connected to ground along its circumference by linear elastic in-plane springs that may resist a radial expansion of u . Additionally, an edge rotation at $r = a$ may evoke a holding bending moment via attached rotational springs of stiffness k_φ . For a radial variation alone, the Föppl-von Kármán plate equations of Eqn (2.6) can be rewritten as [16, 17]:

$$D\nabla^4 w - \frac{t}{r} \frac{d}{dr} \left[\frac{d}{dr} (w^0 + w) \frac{d\Phi}{dr} \right] = p_N \quad (5.3a)$$

$$\frac{1}{E} \nabla^4 \Phi + \frac{1}{r} \frac{d}{dr} (w^0 + w) \frac{d^2}{dr^2} (w^0 + w) - \frac{dw^0}{dr} \frac{d^2 w^0}{dr^2} = 0, \quad (5.3b)$$

where ∇^2 denotes the familiar Laplacian operator in polar coordinates, equal to $d^2(..)/dr^2 + (1/r)d(..)/dr$. The external transverse pressure load is denoted by p_N , and the parameters D , E , and ν have the same meaning as in the previous chapters.

In order to decouple Eqns (5.3a) and (5.3b), the out-of-plane problem is solved first, and later a surjective and not injective stress function, $\Phi(w)$, is defined, which implies that a unique surjective inverse function, $w(\Phi)$, does not exist.

Out-of-plane curving

The initially stress-free shape is specified by a function $f^0(r) w_M^0$, where w_M^0 is the initial midpoint deflection. Since the focus is on finding load-free alternative equilibrium configurations, the load that is required to marshal the transition between two stable equilibria is not specified directly; instead, a ‘forcing term’ of the deflection is used:

$$w = f(r) w_M; \quad (5.4)$$

$f(r)$ and $f^0(r)$ are an arbitrary polynomial expression of order p , and both are specified when the particular solution of a problem is discussed. In axisymmetric structures, the change in gradient, φ_r , radial curvature, κ_r , as well as hoop-wise curvature, κ_θ , are related to the deflection via

$$\varphi_r = -\frac{dw}{dr}, \quad \kappa_r = -\frac{d^2 w}{dr^2} \quad \text{and} \quad \kappa_\theta = -\frac{1}{r} \frac{dw}{dr}. \quad (5.5)$$

The principal bending moments, m_r and m_θ , as well as the shear force, q_r , which do not depend on the stress-free initial configuration, read for shells made from linear elastic, isotropic materials:

$$m_r = D(\kappa_r + \nu \kappa_\theta), \quad m_\theta = D(\kappa_\theta + \nu \kappa_r) \quad \text{and} \quad q_r = \frac{dm_r}{dr} + \frac{m_r - m_\theta}{r}. \quad (5.6)$$

In-plane stretching

The Airy stress function, Φ , is a potential function that ensures in-plane equilibrium. The mid-plane stresses can be derived via

$$\sigma_r = \frac{1}{r} \frac{d\Phi}{dr} \quad \text{and} \quad \sigma_\theta = \frac{d^2\Phi}{dr^2}. \quad (5.7)$$

The corresponding strains are connected via an isotropic constitutive law,

$$\varepsilon_r = \frac{1}{E} (\sigma_r - \nu\sigma_\theta) \quad \text{and} \quad \varepsilon_\theta = \frac{1}{E} (\sigma_\theta - \nu\sigma_r), \quad (5.8)$$

which implies that no pre-stain is specified here, so that $\varepsilon_r^0 = \varepsilon_\theta^0 = 0$ holds. By using either the radial or circumferential strain definition in Eqn (5.2), the radial displacement is expressed either as a mixed formulation that includes an integral over in-plane strains as well as a nonlinear out-of-plane deflection term, or solely in terms of in-plane variables, respectively:

$$u = \int \varepsilon_r dr - \frac{1}{2} \int \left(\frac{d(w^0 + w)}{dr} \right)^2 - \left(\frac{dw^0}{dr} \right)^2 dr, \quad \text{or} \quad u = r \varepsilon_\theta. \quad (5.9)$$

Bending-stretching interaction

The coupling of in-plane and out-of-plane responses is achieved by equating the extrinsic definition of Gaussian curvature to its intrinsic counterpart according to Gauss's Theorema Egregium, recall §2.1. Since the Gaussian curvature of the bending and stretching surface has to equal in every configuration, the same holds for its *change*, g . The nonlinear nature of the extrinsic definition makes this change in Gaussian curvature also dependent on the initial shape:

$$g = K - K^0 = (\kappa_r^0 + \kappa_r)(\kappa_\theta^0 + \kappa_\theta) - \kappa_r^0 \kappa_\theta^0. \quad (5.10)$$

In contrast, the linear differential equation of the intrinsic definition,

$$g = \frac{1}{r} \frac{d\varepsilon_r}{dr} - \frac{1}{r} \frac{d^2(r\varepsilon_\theta)}{dr^2}, \quad (5.11)$$

does not show such a dependency. It is convenient to substitute Eqn (5.7) into Eqn (5.8) to express Eqn (5.11) in terms of the stress function,

$$g = -\frac{1}{E} \left[\frac{d^4 \Phi}{dr^4} + \frac{2}{r} \frac{d^3 \Phi}{dr^3} - \frac{1}{r^2} \frac{d^2 \Phi}{dr^2} + \frac{1}{r^3} \frac{d\Phi}{dr} \right], \quad (5.12)$$

since it reduces the description of the stretching surface to a single variable. Unlike in uniform curvature approaches where g is constant throughout the shell, this term is now a polynomial expression of order $2p - 4$ in r . In order to employ a series solution that sums the results of each polynomial degree, the coefficients α_i are introduced to sort g by order:

$$g = \sum_{i=0}^{2p-4} \alpha_i \left(\frac{r}{a} \right)^i. \quad (5.13)$$

Thus, it suffices to substitute the term ' $\alpha_i(r/a)^i$ ' of Eqn (5.13) into Eqn (5.12) and to integrate it with respect to r to obtain:

$$\Phi = E \sum_{i=0}^{2p-4} \frac{\alpha_i r^4}{(i+2)^2(i+4)^2} \left(\frac{r}{a} \right)^i + \frac{1}{2} C_1 r^2 + C_2 \log(r) + \frac{1}{2} C_3 r^2 \left[\log(r) - \frac{1}{2} \right]. \quad (5.14)$$

The relevant constants of integration C_1, C_2 and C_3 are determined by the boundary conditions, but before particular examples are discussed in §5.2, the general solution procedure is further outlined.

Boundary conditions

Boundary conditions can either be a Dirichlet, Neumann or mixed-type conditions. Whilst Dirichlet types impose displacements or rotations on a boundary Γ_D , Neumann boundary conditions prescribe generalised stresses on Γ_N . When springs are connected to the boundary, these conditions are coupled, and the specific stresses (either in-plane forces or bending moments) are related to an in-plane displacement or rotation via the spring stiffness, k_u or k_φ , respectively, by

$$-t\sigma_r = k_u u \quad (5.15a) \quad \text{and} \quad -m_r = k_\varphi \varphi_r. \quad (5.15b)$$

The minus sign in both expressions accords a resistive force or bending moment for positive directions of u and φ_r . By employing springs of arbitrary stiffness, the complete range of physical supports can be described by combining two out-of-plane

boundary conditions and one additional in-plane condition as follows:

$$\text{free edge:} \quad q_r = 0, \quad m_r = 0, \quad u = 0 \quad (5.16a)$$

$$\text{roller support:} \quad w = 0, \quad m_r = 0, \quad \sigma_r = 0 \quad (5.16b)$$

$$\text{hinged support:} \quad w = 0, \quad m_r = 0, \quad t\sigma_r = -k_u u \quad (5.16c)$$

$$\text{fixed-pinned support:} \quad w = 0, \quad m_r = 0, \quad u = 0 \quad (5.16d)$$

$$\text{clamped support:} \quad w = 0, \quad \varphi_r = 0, \quad u = 0 \quad (5.16e)$$

$$\text{dual spring support:} \quad w = 0, \quad m_r = -k_\varphi \varphi_r, \quad t\sigma_r = -k_u u \quad (5.16f)$$

These are later applied in several examples of §5.3. Note that the term ‘hinged support’ does not contain any information about the in-plane stiffness, while the terms ‘roller support’ and ‘fixed-pinned support’ refer to a vanishing horizontal force and radial displacement, respectively. The dual spring-supported case is a generalisation that unifies all of the conditions in Eqn (5.16): the free edge condition as well as roller supported case require $k_\varphi = k_u = 0$ and allow for an unrestricted displacement; in shells with rotationally symmetric deformations, both conditions are equivalent, since neither a rigid body movement nor a constant term of the shear force affects the strain energy. Fixed-pinned supports and clamped supports in Eqn (5.16d) and (5.16e), respectively, require a theoretically infinite spring stiffness and can be modelled by setting k_u and k_φ to large values in Eqns (5.16c) and (5.16f). In addition, dual spring supports allow to specify intermediate values in order to analyse the transition between idealised conditions.

In order to determine the three arising constants in Eqn (5.14), three equations are required: these are provided by the in-plane boundary condition at the inner and outer edge, and an additional equation that enforces the geometric compatibility of the two expressions of the radial displacement in Eqn (5.9). For closed shells, the inner boundary at $r = 0$ has to ensure that the surface stays smooth and does not intersect itself, which requires:

$$\varphi_r = 0, \quad \text{and} \quad u = 0. \quad (5.17)$$

The latter condition can be transformed to $\sigma_r = \sigma_\theta$ at the limit of $r \rightarrow 0$ [122].

Identifying stable configurations

After all constants are determined, these are substituted into the expressions of the stress and strain resultants to calculate the strain energy functional, $\Pi = \Pi_B + \Pi_S$, that solely depend on geometric parameters and the degrees of freedom. The bending and stretching energy components, Π_B and Π_S respectively, which include the spring contributions, can be calculated via:

$$\begin{aligned}\Pi_B &= \frac{1}{2} \int_{\Omega_0} (\kappa_r m_r + \kappa_\theta m_\theta) dS + \pi a k_\varphi \varphi_r^2 \Big|_{\rho=1} = \pi \int_0^a (\kappa_r m_r + \kappa_\theta m_\theta) r dr + \pi a k_\varphi \varphi_r^2 \Big|_{\rho=1}, \\ \Pi_S &= \frac{t}{2} \int_{\Omega_0} (\varepsilon_r \sigma_r + \varepsilon_\theta \sigma_\theta) dS + \pi a k_u u^2 \Big|_{\rho=1} = \pi t \int_0^a (\varepsilon_r \sigma_r + \varepsilon_\theta \sigma_\theta) r dr + \pi a k_u u^2 \Big|_{\rho=1}.\end{aligned}\tag{5.18}$$

These integrals are solvable since all expressions are derived from polynomials. The integral over the initial rather than the deformed domain is a valid approximation in the framework of the FvK equations since they include the assumptions of small strains as well as moderate rotations. Load-free equilibria are identified via stationary points of Π :

$$\nabla_\eta \Pi = 0, \tag{5.19}$$

where ∇_η denotes the nabla operator applied in the solution space spanned by the n degrees of freedom, η_i . These equilibria are stable if, and only if, all eigenvalues of the strain energy function are positive, which is guaranteed by a positive definite Hessian matrix of stiffness, \mathbf{H} , where

$$H_{ij} = \frac{\partial^2 \Pi}{\partial \eta_i \partial \eta_j}. \tag{5.20}$$

5.2 Particular Solutions

The generality of the presented methodology makes it a suitable tool for a wide range of inversion problems. However, a solution to a particular problem requires to consider a given initial shape of w^0 as well as a suitable set of basis functions in w . These are problem specific and depend on the shape as well as the support conditions (*cf.* Fig. 5.1). Here, three particular classes of shell structures are discussed; each pursues

the objective to preserve as much generality as possible. The first class considers a closed cap with dual spring supports as defined in Eqn (5.16f), which allow the analysis of a wide range of initial shapes. Another class deals with the topologically differing case of a uniformly curved shell with annular planform subjected to in-plane spring supports, for which a different set of basis function is required, since a central hole loosens some constraints of the deflection field. Finally, both methods are eventually combined by considering the coupling of shells, where two separate deflection fields are assumed – one for a central closed shell and another one of the surrounding annular shell. In addition, the simplification to a beam model is briefly discussed in order to compare the results for shells to their lower dimensional equivalent.

5.2.1 Particular Solution of a Hole-Free Shell

Whilst the initial shape can in general have the form of any arbitrary polynomial expression, two approximations of very well-known examples are chosen for evaluation in §5.3:

$$w^0 = (1 - \rho^2) w_M^0 \quad (5.21a) \quad \text{or} \quad w^0 = (1 - \rho^2)^2 w_M^0, \quad (5.21b)$$

where ρ denotes the dimensionless radius r/a and the lower index ‘M’ refers to the midpoint value at $\rho = 0$. The first shape describes a uniformly curved shallow cap and is inspired by a study of initially curved bistable beams [68] using a half cosine-wave; the latter represents a full cosine wave akin to the deflection field of a plate with a clamped edge[54, 122], where the gradient is zero.

Out-of-plane bending

In order to describe the transverse deflections of a shell bounded by rotational springs, the deflection, w , is subdivided into two fields: one satisfies a ‘hinged’ deflection field, w^h , while the other is fixed with regards to rotations, w^c . The first field is a polynomial series with n degrees of freedom, η_i , which by itself is the solution for simply supported cases where the boundary of shell is free to rotate for all time. The rotational spring equation, Eqn (5.15b), guarantees the compatibility between these two fields and is later employed to express the clamped midpoint deflection, w_M^c , in terms of the n degrees of freedom, *cf.* Eqn (5.31). Correspondingly, the total deflection, $w = w^h + w^c$,

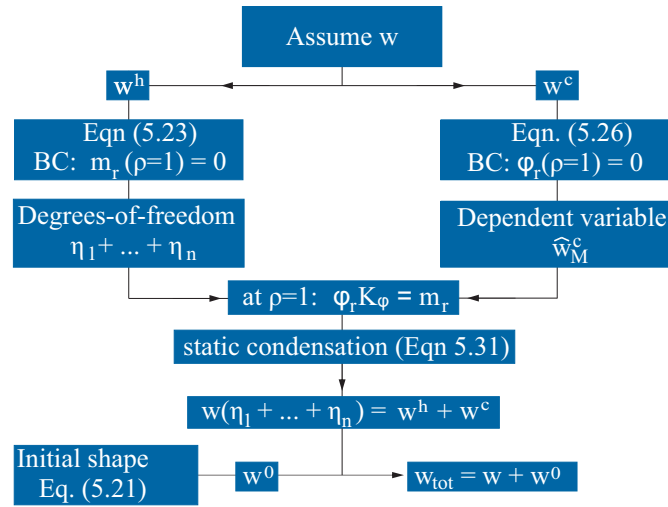


Figure 5.3: Schematic of the formulation of the deflection field components.

is obtained by summing both deflection components. A detailed derivation of each deflection field according to the scheme in Fig. 5.3 is given next.

Hinged subset (w^h):

The hinged subset has to satisfy the boundary conditions of a vanishing bending moment and deflection at $\rho = 1$. In order to ensure this, Eqn (5.5) is combined with Eqn (5.6) and a polynomial series of even powers is chosen for the radial bending moment:

$$D \left[-\frac{d^2 w^h}{d\rho^2} - \nu \frac{1}{\rho} \frac{dw^h}{d\rho} \right] = \frac{D}{a^2} \sum_{i=1}^n [1 - \rho^{2i}] \eta_i. \quad (5.22)$$

The solution of this differential equation is of order $p = 2n + 2$ and gives the hinged deflection field:

$$w^h = \sum_{i=1}^n \frac{1}{2} \left[\frac{1 - \rho^2}{1 + \nu} - \frac{1 - \rho^{2i+2}}{(i+1)(1 + 2i + \nu)} \right] \eta_i, \quad (5.23)$$

where the constant of integration enforces a zero edge displacement, $w^h|_{\rho=1} = 0$. Accordingly, the changes in curvatures read:

$$\kappa_r^h = \sum_{i=1}^n \left[\frac{1}{1 + \nu} - \frac{1 + 2i}{1 + 2i + \nu} \rho^{2i} \right] \frac{\eta_i}{a^2} \quad \text{and} \quad \kappa_\theta^h = \sum_{i=1}^n \left[\frac{1}{1 + \nu} - \frac{1}{1 + 2i + \nu} \rho^{2i} \right] \frac{\eta_i}{a^2}, \quad (5.24)$$

whilst the change in radial gradient is given by $\varphi_r^h = r \kappa_\theta^h$, and the radial- and circumferential bending moments become:

$$m_r^h = D \sum_{i=1}^n \left[1 - \rho^{2i} \right] \frac{\eta_i}{a^2} \quad \text{and} \quad m_\theta^h = D \sum_{i=1}^n \left[1 - \frac{1 + \nu + 2\nu i}{1 + 2i + \nu} \rho^{2i} \right] \frac{\eta_i}{a^2}. \quad (5.25)$$

This higher-order approach ensures that the bending moment vanishes at the edge by using additional terms in the series of the deflection field. Hence, even for a single degree of freedom, η_1 , the curvatures show a quadratic variation in ρ .

Remark 5.1: Note the difference to uniform curvature approaches, *e.g.* in [39], where the curvatures take a constant value throughout the shell. Since the presented method is later also compared to UC approaches, it shall be pointed out that a UC approach can be obtained by setting $w = \rho^2 w_M$ without any further manipulations to satisfy the boundary conditions. In such an approach, the midpoint deflection, $w_M = \eta_1$, serves as a single degree of freedom.

Clamped subset (w^c):

A common approach for a clamped deflection field [54, 122] considers a full cosine wave, which is here approximated by a polynomial expression:

$$w^c = (1 - \rho^2)^2 w_M^c. \quad (5.26)$$

According to Eqn (5.5), the corresponding change in gradient and curvatures reads:

$$\varphi_r^c = 4\rho(1 - \rho^2) \frac{w_M^c}{a}, \quad \kappa_r^c = 4(3\rho^2 - 1) \frac{w_M^c}{a^2} \quad \text{and} \quad \kappa_\theta^c = 4(\rho^2 - 1) \frac{w_M^c}{a^2}. \quad (5.27)$$

From Eqn (5.6) follows that the expressions for both bending moments,

$$m_r^c = 4D(\rho^2(3 + \nu) - \nu - 1) \frac{w_M^c}{a^2} \quad \text{and} \quad m_\theta^c = 4D(\rho^2(1 + 3\nu) - \nu - 1) \frac{w_M^c}{a^2}, \quad (5.28)$$

are generally nonzero at the edge ($\rho = 1$). Note also that the two conditions concerning the deflection in Eqn (5.16e) are satisfied for arbitrary values of the midpoint deflection w_M^c in the clamped deflection field.

Resulting deflection field (w):

Now, the z -component of the resulting shape is described by the sum of all displacement components, $w^0 + w^h + w^c$, but the relation between the hinged and clamped

deflection field still needs to be established. Since only the former contributes to a change of gradient at the edge, the expression of φ_r can easily be found:

$$\varphi_r \Big|_{\rho=1} = \sum_{i=1}^n \left[\frac{1}{1+\nu} - \frac{2i}{1+2i+\nu} \right] \frac{\eta_i}{a}. \quad (5.29)$$

The hinged subset's edge is free to rotate ($m_r = 0$ at $\rho = 1$), and hence, the bending moment is solely evoked by the clamped part in Eqn (5.28):

$$m_r \Big|_{\rho=1} = -8D \frac{w_M^c}{a^2}. \quad (5.30)$$

In order to enforce the compatibility of the hinged and clamped deformation modes, these two expressions are substituted into the rotational spring equation, Eqn (5.15b), which eventually gives the clamped subset's midpoint deflection as a function of the n degrees of freedom, η_i :

$$w_M^c = -\frac{k_\varphi a^2}{8D} \varphi_r \Big|_{\rho=1} = \frac{k_\varphi a}{8D} \sum_{i=1}^n \left[\frac{-1}{1+\nu} + \frac{2i}{1+2i+\nu} \right] \eta_i. \quad (5.31)$$

For a vanishing spring stiffness, $k_\varphi = 0$, the clamped contribution vanishes; for k_φ tending to infinity, the edge rotation takes a very small value, but it is not allowed to vanish because the solution is calculated in terms of the hinged degrees of freedom. The consequences of this procedure are addressed in §5.3.

Remark 5.2: The clamped mode's deflection field variation in ρ is always of order four, *cf.* Eqn (5.26), while the corresponding order of the hinged mode in Eqn (5.23), $2n + 2$, increases with n . Both deflection fields were separated in order to maintain an intuitive perspective on the deformation modes that also facilitates the use of a subset of the solution in simplified one-term approaches; however, it is not strictly required, since the variational formulation ensures an optimised solution of the specified shape functions nevertheless. Since the clamped subset is of fourth order, it can also be represented by any other polynomial that does not impose the particular shape a priori.

Bending-stretching interaction

In order to calculate the Gaussian curvature, the curvatures changes, $\kappa_r = \kappa_r^h + \kappa_r^c$ and $\kappa_\theta = \kappa_\theta^h + \kappa_\theta^c$, are substituted into Eqn (5.10). Because these expressions become rather

convoluted with increasing order, the reader is referred to the appendix where the values for κ_r , κ_θ , g and the corresponding α_i terms of Eqn (5.13) are presented for a three degrees-of-freedom model with dual spring-supported edge; lower-order models can straightforwardly be derived from these expressions by setting ‘unused’ degrees of freedom to zero. Since the initial curvatures also affect g , the α_i terms are given separately for the two differing initial shapes stated in Eqn (5.21a) and Eqn (5.21b). For instance, the curvatures for a hinged ($k_\varphi = 0$), initially uniformly curved cap ($\kappa_r^0 = \kappa_\theta^0 = 2w_M^0/a^2$) with a single degree of freedom ($n = 1$) are equal to

$$\kappa_r = \frac{1}{a^2} \left[\frac{w_M^0}{2} + \eta_1 \left(\frac{1}{\nu+1} - \frac{3\rho^2}{\nu+3} \right) \right] \quad \text{and} \quad \kappa_\theta = \frac{1}{a^2} \left[\frac{w_M^0}{2} + \eta_1 \left(\frac{1}{\nu+1} - \frac{\rho^2}{\nu+3} \right) \right], \quad (5.32)$$

which both vary quadratically in ρ . The corresponding change in Gaussian curvature,

$$g = \frac{1}{a^4} \left[\frac{w_M^0}{2} + \eta_1 \left(\frac{1}{\nu+1} - \frac{3\rho^2}{\nu+3} \right) \right] \left[\frac{w_M^0}{2} + \eta_1 \left(\frac{1}{\nu+1} - \frac{\rho^2}{\nu+3} \right) \right] - \left(\frac{w_M^0}{2a^2} \right)^2, \quad (5.33)$$

is of fourth order. For the chosen series in Eqn (5.23), the upper bound of summation in Eqn (5.13) is $4n$, but since all variations of g in ρ are of even order, only the following $2n + 1$ out of $4n + 1$ terms of α_i are nonzero:

$$\alpha_0 = \frac{(2\eta_1 + (1 + \nu)w_M^0)^2}{4a^4(1 + \nu)^2}, \quad \alpha_2 = -\frac{2\eta_1(2\eta_1 + (1 + \nu)w_M^0)}{a^4(\nu + 1)(\nu + 3)}, \quad \alpha_4 = \frac{3\eta_1^2}{a^4(\nu + 3)^2}. \quad (5.34)$$

Note that in this particular case it follows from Eqn (5.31) with $k_\varphi = 0$ that $w_M^c = 0$, as expected.

In-plane stretching

Substituting the values of the previous equation into Eqn (5.14) gives the Airy stress function, from which all in-plane stresses are derived via Eqn (5.7):

$$\begin{aligned} \sigma_r &= E \sum_{i=0}^{2p-4} \frac{\alpha_i \rho^{i+2} a^2}{(i+2)^2(i+4)} + C_1 + \frac{C_2}{a^2 \rho^2} + C_3 [\log(\rho) + \log(a)], \\ \sigma_\theta &= E \sum_{i=0}^{2p-4} \frac{\alpha_i (i+3) \rho^{i+2} a^2}{(i+2)^2(i+4)} + C_1 - \frac{C_2}{a^2 \rho^2} + C_3 [1 + \log(\rho) + \log(a)]. \end{aligned} \quad (5.35)$$

In order to restrict the stretching energy to finite values, the constants C_2 and C_3 are set to zero and consequently Eqn (5.35) simplifies to

$$\sigma_r = \sigma_{pr} + C_1 \quad \text{and} \quad \sigma_\theta = \sigma_{p\theta} + C_1, \quad (5.36)$$

where σ_{pr} and $\sigma_{p\theta}$ denote the summation terms of the particular solution that contain α_i . It is easy to prove that these expressions satisfy the condition $\sigma_r = \sigma_\theta$ at the centre of the plate, which is consistent with the requirement of $u|_{\rho=0} = 0$. The remaining constant, C_1 , is employed to satisfy the compatibility equation of the linear elastic in-plane spring. Since $u = r\varepsilon_\theta$, the radial displacement reads:

$$u = \frac{r}{E} (\sigma_{p\theta} - \nu \sigma_{pr} + (1 - \nu) C_1). \quad (5.37)$$

It follows from substituting u and σ_r from Eqn (5.36) into the extensional spring relationship, Eqn (5.15a), and setting $\rho = 1$, that

$$C_1 = - \frac{E t \sigma_{pr} + k_u a (\sigma_{p\theta} - \nu \sigma_{pr})}{E t + k_u a (1 - \nu)} \Big|_{\rho=1}. \quad (5.38)$$

For the limit of a vanishing or infinite stiffness, this expression simplifies to

$$C_1 = -\sigma_{pr} \Big|_{\rho=1} \quad \text{for } k_u = 0 \quad \text{or} \quad C_1 = -\frac{E}{a} u_p \Big|_{\rho=1} = -\frac{\sigma_{p\theta} - \nu \sigma_{pr}}{1 - \nu} \Big|_{\rho=1} \quad \text{for } k_u \rightarrow \infty, \quad (5.39)$$

respectively. The appropriate expression for C_1 can be substituted into the equations for the stresses and strains, in order to calculate and then minimise the strain energy.

5.2.2 Initially Curved Shells with Annular Planform

The methodology can readily be extended to shells of an annular planform with an outer and inner radius of a and b , respectively. Inspiration is taken from the bending deformation of a Kirchhoff–Love plate to find a suitable estimate for the deflection field: the compatibility of geometrically linear deformations requires $D\nabla^4 w = 0$ in the absence of load, and the rotationally symmetric solution to this homogeneous biharmonic problem reads:

$$A_1 \rho^2 + (A_2 + A_3 \rho^2) \log(\rho) + A_4. \quad (5.40)$$

The latter two terms were energetically incompatible for closed shells but provide now additional terms that inspire the deflection field of the alternative load-free configuration. The series expansion of the log-term at an arbitrary point $0 \leq \rho_i \leq 1$,

$$\log \rho_i + \sum_{n=1}^{\infty} \frac{(-1)^{n-1} (\rho - \rho_i)^n}{n \rho_i^n}, \quad (5.41)$$

suggests that a simple polynomial series is a suitable approximation, and thus, the trial function of the deflection field with η_i degrees of freedom is chosen as:

$$w = A_0 + A_1 \rho + A_2 \rho^2 + A_3 \rho^3 + \eta_1 \rho^4 + \eta_2 \rho^5 + \eta_3 \rho^6. \quad (5.42)$$

Note that the series now allows for exponents of odd order, which include a conical deformation mode with a linear gradient. In general, it is straightforward to consider the logarithmic terms without the series expansion to satisfy the boundary conditions. In this case, the same supplementary linear polynomial terms related to $\eta_1 - \eta_3$ are chosen as additional degrees of freedom and the obtained results are virtually indistinguishable. The polynomial series, however, is computationally slightly more efficient and thus the method of choice. The four constants, A_i , are used to satisfy the four boundary conditions that are here assumed to be a hinged outer edge in combination with a free inner edge that require:

$$\begin{aligned} w = 0 \quad \text{and} \quad m_r = 0 \quad \text{at } \rho = 1 \\ q_r = 0 \quad \text{and} \quad m_r = 0 \quad \text{at } \rho = b/a; \end{aligned} \quad (5.43)$$

the solution is given in the appendix. If we wish to consider different support conditions, any of the cases in Eqn. (5.16) can be substituted for these expressions. This possibility is not systematically explored here, since the focus is on investigating the topological difference between closed and planform annular shells, and thus, the study of additional parameters is omitted. After calculating the bending moments and the change in Gaussian curvature as before in Eqn. (5.6) and (5.10), respectively, a geometric compatible stress function has to be found. In the case of annuli with rotationally symmetric deformation, it is beneficial to manipulate the compatibility equation to reduce the number of arising constants. By substituting $u' = (r\epsilon_\theta)'$, the radial displacement is eradicated from the nonlinear strain definitions in Eqn (5.2). The remaining quantities are expressed in terms of stresses by using the material law; a further substi-

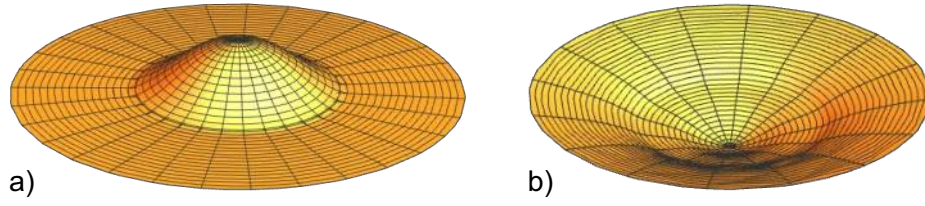


Figure 5.4: Example of a coupled shell: (a) A flat annulus with vertical supports at the *inner* edge is rigidly connected to a central doubly curved shell. (b) Strongly non-uniformly curved inverted shape.

tution that uses the Airy stress function according to Eqn (5.7) eventually leads to:

$$-r \frac{d^3 \Phi}{dr^3} - \frac{d^2 \Phi}{dr^2} + \frac{1}{r} \frac{d\Phi}{dr} = \frac{E}{2} \left[\left(\frac{d(w^0 + w)}{dr} \right)^2 - \left(\frac{dw_0}{dr} \right)^2 \right] \quad (5.44)$$

The full solution (given in the appendix) contains two terms related to constants of integration, $C_1 \rho^2$ and $C_2 \log[\rho a]$, which ensure that the in-plane boundary conditions according to Eqn (5.15a) are satisfied at the inner and outer edge. For instance, an outer boundary on rollers in combination with an inner free edge gives:

$$C_1 = \frac{a^2 b^2 \left(\frac{A_1^2}{4} \log\left(\frac{a}{b}\right) - \sigma_r^h \Big|_{r=a} + \sigma_r^h \Big|_{r=b} \right)}{a^2 - b^2} \quad (5.45)$$

and $C_2 = \frac{A_1^2 \left(b^2 \log(b) - a^2 \log(a) \right) + 4a^2 \sigma_r^h \Big|_{r=a} - 4b^2 \sigma_r^h \Big|_{r=b}}{4(a^2 - b^2)}.$

After substituting these values, the energy functional solely depends on the degrees of freedoms and the known geometric and material parameters, and thus, stable equilibria can be identified by energy minimisation.

5.2.3 Interaction of Two Shells

The established models shall now be combined to analyse the interaction of connected shells; an example is shown in Fig. 5.4. For each segment, it is required to define a separate set of shape functions since a common set is in general not capable of describing the response of both parts accurately. The initial shapes are given by two functions, w_1^0 and w_2^0 , that are defined on the interval $0 \leq r \leq c$ and $c \leq r \leq a$, respectively, where a denotes the planform radius of the outer shell and c the radial coordinate at which the shells are linked. The segments can generally have different geometric and

material parameters, but at their linkage they have to fulfil mutual coupling conditions. The equilibria of the radial bending moment, the shear force and the radial in-plane stresses require in the absence of other forces at the linkage:

$$m_{r1} = m_{r2} \quad , \quad q_{r1} = q_{r2} \quad \text{and} \quad \sigma_{r1} = \sigma_{r2} \quad \text{at } r = c \quad , \quad (5.46)$$

where indices 1 and 2 refer to the outer and inner shell, respectively. In practical applications, connections do not allow a relative displacement of one shell to another, from which follows:

$$w_1 = w_2 \quad \text{and} \quad u_{r1} = u_{r2} \quad \text{at } r = c \quad . \quad (5.47)$$

Additionally, in rigidly connected structures, the changes in gradients are equal:

$$\varphi_{r1} = \varphi_{r2} \quad \text{at } r = c \quad . \quad (5.48)$$

In view of the choice of the shape function, it has to be considered, that the number of degrees of freedom is still limited to four at maximum – but now this limit concerns the sum of both subsets. Thus less elaborated approaches compared to the previous examples are used. In order to avoid a potential loss of accuracy for the outer shell with annular planform, the original terms of the linear solution in Eqn (5.40) are employed rather than its Taylor series approximation in Eqn (5.41). Hence, the resulting deflection field reads:

$$w_1 = \log(\rho_c)A_1 + \log(\rho_c)\rho_c^2 A_2 + (1 - \rho_c^2)\eta_1 \quad , \quad (5.49)$$

where the dimensionless coordinate $\rho_c = r/c$ is represented by ρ_c . For the inner closed shell, a polynomial series,

$$w_2 = (1 - \rho_c^2)A_3 + (1 - \rho_c^4)A_4 + (1 - \rho_c^6)\eta_2 + (1 - \rho_c^8)\eta_3 \quad , \quad (5.50)$$

is assumed without the loss of generality since it is also capable of transferring a bending moment and modelling a clamped deformation mode, as mentioned in remark 5.2. It may be possible to consider an additional, fourth degree of freedom, but it will later be shown that the accuracy of the employed function is entirely satisfactory. Both functions already incorporate the requirement of equal transversal displacements at

the connection point, $\rho_c = 1$, and the remaining constants, A_i , are employed to satisfy the out-of-plane boundary conditions specified in Eqn (5.46) and Eqn (5.48) as well as the familiar conditions at the outer edge..

The coupling with the in-plane properties is established as before via Eqn (5.44) to obtain a separate Airy stress function for each segment according to the respective method described in §5.2.1 for closed shells and §5.2.2 for planform annuli. Whilst a single constant arises for the central part, two constants of integration exist for the outer, annular shell. This number matches with the three in-plane boundary conditions: two in-plane coupling conditions arise from Eqn (5.46) and Eqn (5.47) to ensure equilibrium and displacement compatibility, respectively, and a third equation considers a spring-supported outer edge via $k_u u = -t\sigma_r$ at $r = a$. Thus, all constants can be determined straightforwardly. With the known constants, the energy minimising procedure is then conducted as before to identify stable configurations.

5.2.4 Simplification to a Beam Model

Similar to cylindrical shells that can be described by the same set of differential equations as a beam on an elastic foundation, the hoop stiffness of rotationally symmetric shallow shells resembles an elastic nonlinear bedding. Thus, a simplified version of the developed shell model can be applied to beams by setting the hoop components to zero. The compatibility condition is drastically simplified since the complex geometric interaction of shells simplifies to a boundary value problem.

By assuming the same series with n degrees of freedom as in §5.2.1, the radial curvatures can be calculated as before to obtain the bending energy per unit width, which now reads:

$$\Pi_B = \pi \int_0^a \kappa_r m_r dr + \pi a k_\varphi \varphi_r^2 \Big|_{\rho=1} . \quad (5.51)$$

The absence of circumferential curvatures gives $K = g = 0$ and thus the compatibility equation (5.12) simplifies to a homogeneous biharmonic problem of $\nabla^4 \Phi = 0$. The solution gives $\Phi = \frac{1}{2} C_1 r^2$ with a corresponding constant radial stress, $\sigma_r = C_1$, which result in a stretching energy per unit width of

$$\Pi_S = \pi \frac{a t}{E} C_1^2 + \pi a k_u u^2 \Big|_{\rho=1} . \quad (5.52)$$

The value of the radial force is determined by using Eqn (5.15a) that becomes $-C_1 t = k_u u$. For roller supports, where $k_u = 0$, no in-plane stresses arise, and thus, a stretching barrier that could prevent the structure from snapping back is absent in this case.

5.3 Results

The result section is arranged as follows: first, details of the finite element simulation which are used as a reference solution are given. The predictions of the presented method are then compared to the linear theories of the previous chapter and available nonlinear results in literature, for which the simplest example of a centrally fixed shell is discussed in §5.3.2. It follows an analysis of the influence of horizontal spring supports on the bistable response of a uniformly curved cap in §5.3.3. In §5.3.4, the versatility of the presented methodology is demonstrated by analysing a fully spring-supported shell with a *nonuniformly* curved shape. Hereafter, the suitability of the annular model is evaluated in §5.3.5, where the influence of in-plane support conditions as well as the size of the central hole are quantified. Finally, §5.3.6 considers two cases of initially stress-free connected shells: firstly, a cap that is rigidly linked to a flat annulus of the same thickness and material is analysed; second, a hinge is added to a uniformly curved cap to model a local thickness variation that enriches the number of possible solutions.

Remark 5.3: For a moderate compaction of notation, the following dimensionless parameters are used:

$$\omega = \frac{w}{t} \quad , \quad S = \frac{\sigma}{Et} \quad , \quad M = \frac{m}{Et^3} \quad , \quad k_U = \frac{k_u a}{Et} \quad \text{and} \quad k_\phi = \frac{k_\phi a}{Et^3}. \quad (5.53)$$

5.3.1 Finite Element Modelling

The finite element simulations in this section were conducted with the commercial package *ABAQUS* [123]. The decisive argument to prefer *ABAQUS* to *LS-DYNA* – with which the reference solutions in the previous section were computed – was the user-friendly Python [124] interaction of the former programme. This facilitated the realisation of extensive parameter studies that serve as reference solution; note that the inversion process of shallower shells is less sensitive to specific solver configurations,

which allowed the calculation of reliable results. In order to identify critical geometric parameters for the bistable inversion, such as the critical initial rise of a cap required for bistable inversion, ω_M^{0*} , a Python algorithm successively approximates this value in nested intervals as illustrated in Fig. 5.5: after specifying a range that confines the solution space of the desired parameter as input, the algorithm uses the arithmetic mean between the two values at which the transition from monostability to bistability occurs in order to obtain a better approximation of the threshold. This procedure is updated in each step and repeated until the range of uncertainty becomes smaller than a specified tolerance of 0.25 %; the mean value of the interval is regarded as the critical geometric parameter, ω_M^{0*} .

For analysis, a quasi-static implicit dynamic time integration scheme is used to provide a stable numerical environment after static stability is lost. Only one quarter of the shell was modelled, with biaxial symmetry applied to over 600 S8R elements and the following parameters (specified in SI units): $E = 10^7$, $t = 0.01$, $a = 1$, and density equal to 10^{-5} ; see [125] for details. Mesh refinement of randomly picked samples did not lead to any changes in the critical properties.

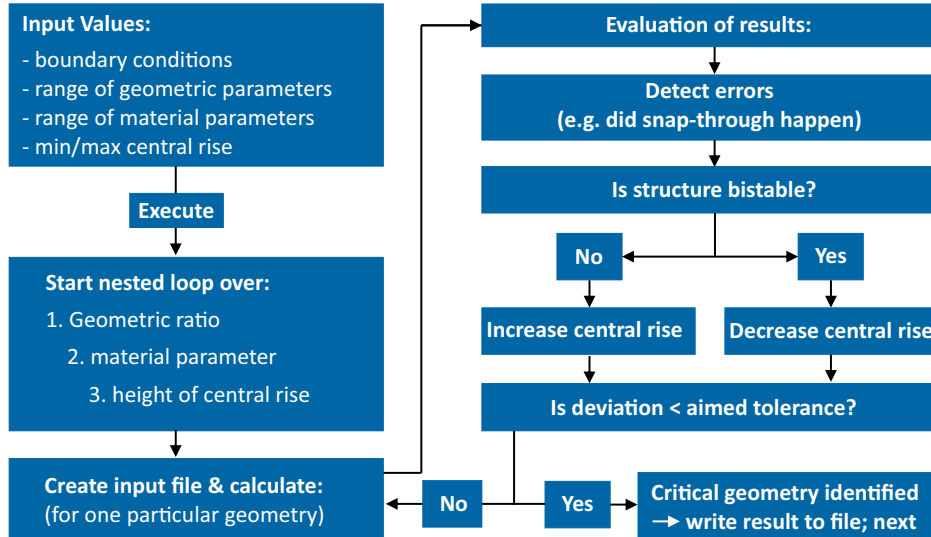


Figure 5.5: Schematic overview of overseeing python script to automatise iterative finite element simulations with the aim of finding the critical shape parameters for which bistable inversion becomes possible.

5.3.2 Centrally Fixed Examples

Centrally fixed shells and their simply supported equivalents are discussed next. First, the performance of the nonlinear approach is evaluated in the area where linear theories began to fail, and hereafter, the suitability of the presented approach is compared to other geometrically nonlinear approaches from literature.

Overcoming the Limitations of Linear Theory

As shown in the previous chapter, linear shell theory provides an excellent agreement for deep, thin shells, but struggles when these become shallow or very thick. Whilst the performance was reasonably accurate for shells with $\alpha = 20^\circ$, $a = 1$, $\nu = 0.45$ and $t \leq 0.1$, see Fig. 4.9 and Fig. 4.10, significant deviations were observed when the thickness was further increased. In this case, the solution transitioned from a rapidly damped out edge perturbation to a long wave problem that affects the entire shell. The maximum value of $t = 0.033$ was chosen, since the edge effect in even thicker shells becomes so pronounced that it causes a reversion; hence, those shells do not possess an alternative stable equilibrium state. The same shells are now analysed with the derived geometrically nonlinear shallow shell approach, see Fig. 5.6. For all thickness ratios, the inverted shapes in Fig. 5.6(a) are in good agreement with the finite element results. A closer look at the corresponding normalised out-of-plane deviations from the mirror-symmetric shape in Fig. 5.6(b) reveals that examples with ($t \geq 0.2$), in which the linear theory previously failed, are now accurately captured by the analytical model with three degrees of freedom. With regards to the slight remaining deviations, it shall be mentioned that the quality of the results is expected to increase with a decreasing total angle since the non-shallow angle of 20° introduces an additional error due to the rotationally noninvariant strain formulation of the FvK equations.

Comparison to Nonlinear Approaches in Literature

Since linear approaches failed due to nonlinear effects that sharply increase in the proximity of the critical value at which bistable inversion becomes possible, predictions of this limit are analysed in detail; note that henceforth all stability thresholds are denoted by an asterisk. The dimensionless threshold of the initial central rise, ω_M^{0*} , at which a shell is on the brink of possessing an alternative stable equilibrium configuration is shown in Fig. 5.7 as a function of the Poisson's ratio. The span of the

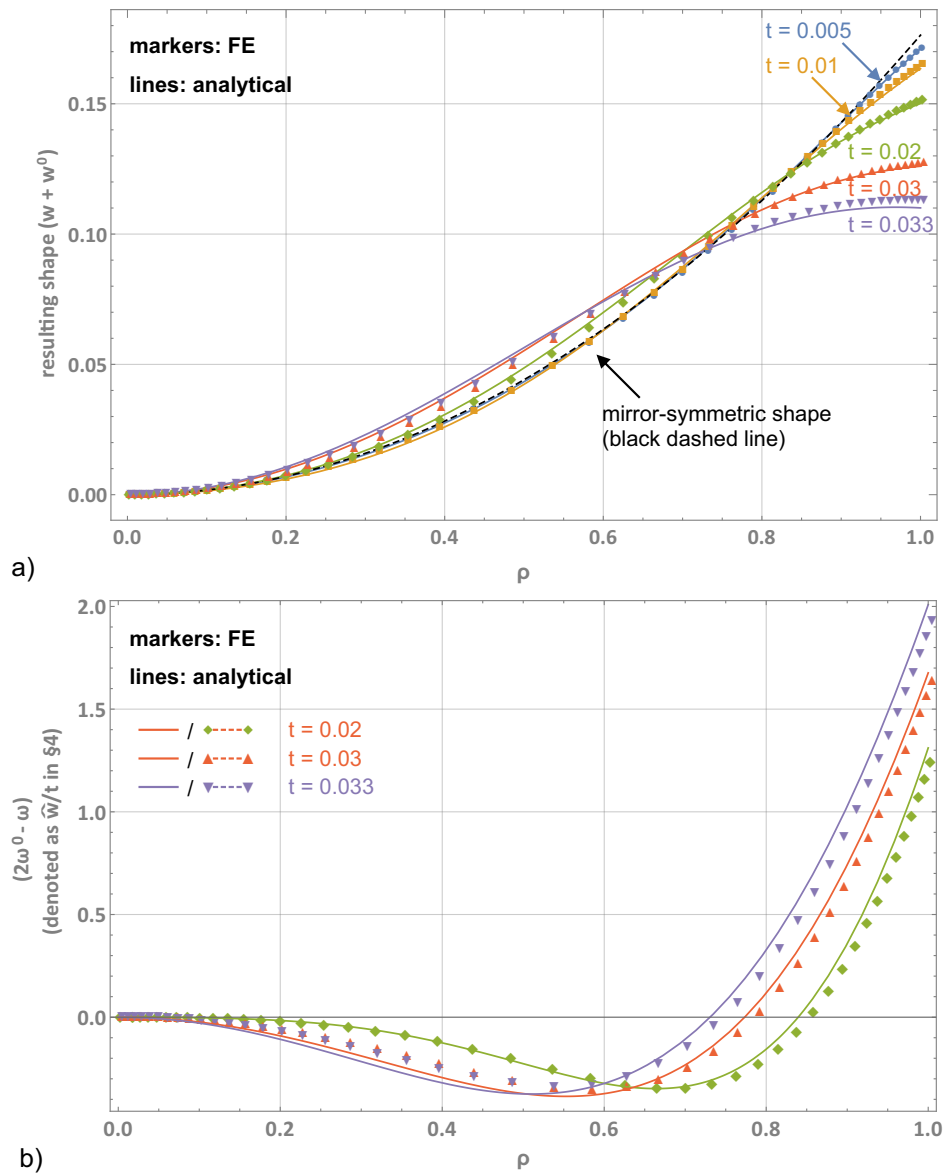


Figure 5.6: Comparison of analytical predictions (lines) and FE results (markers). (a) Inverted shape of a shell with $\alpha = 20^\circ$, $a = 1$, $\nu = 0.45$ and varying thickness; (b) corresponding normalised transversal deviations from mirror-symmetric shape, $2\omega^0 - \omega$ for $t \geq 0.2$. Note the different notation compared to §4, where w^0 denoted the dimensionless deflection towards the mirror-symmetric shape, whereas it refers to the initial configuration here.

abscissa, $(-1 \leq \nu \leq 0.5)$, covers the whole range of theoretically admissible values for isotropic materials. The threshold is independent of the only other material parameter, E , since the bending-to-stretching energy ratio of homogeneous shells is not affected by the Young's modulus. Figure 5.7(a) first compares results from previous studies to finite elements for the sake of revision before the predictions of the presen-

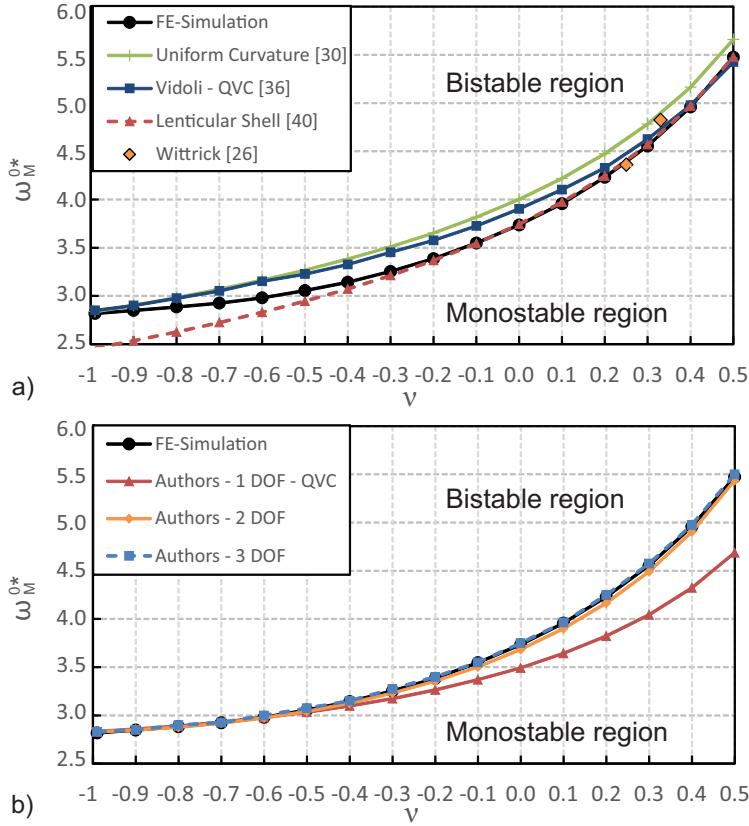


Figure 5.7: Dimensionless critical initial midpoint deflection, ω_M^{0*} , for bistable inversion of a shallow spherical cap with respect to the Poisson's ratio, ν . (a) Comparison of different approaches from key studies; (b) current models with up to three degrees of freedom [29].

ted method are disclosed in Fig. 5.7(b). All results depicted in Figs 5.7(a) and (b) yield the same rising trend in ω_M^{0*} with the Poisson's ratio. The effect is mainly caused by the increasing edge moment that scales with $1/(1 - \nu)$: the term arises since the Poisson's effect amplifies the bending moment via $1 + \nu$, while the bending rigidity is proportional to $1/(1 - \nu^2)$. It follows that shells made from materials with $\nu = 0.5$ are the least likely to show a bistable inversion, but an initial height-to-thickness ratio of at least six guarantees bistable inversion in all cases. Considering that the reversion process is driven by an edge effect, the methodology of uniform curvature approaches, which neglects precisely such an effect, may seem paradox at first glance. However, since the equilibrium equations are satisfied on average, its predictions are reasonably accurate, see *e.g.* Seffen & McMahon [39]. Wittrick *et al.* [35] employ a slightly different UC approach and deduce that the height must exceed $\omega_M^{0*} = 4.82$ for $\nu = 1/3$ and $\omega_M^{0*} = 4.36$ for $\nu = 1/4$. The reason for including these simpler UC models is that

it produces results surprisingly close the FE trend, and in fact, they yield a *better* approximation of the critical geometry than the presented QVC model with quadratically varying (Gaussian) curvature (QVC) for $\nu > 0$. Similarly, the QVC model of Vidoli [45] in Fig. 5.7(a) shows a better approximation of the FE solution in this range of ν , but the presented QVC approach in Fig. 5.7(b) is superior for auxetic materials that possess by definition a negative ratio. The results of Mansfield [56] are also presented in Fig. 5.7(a), even though the solution concerns a slightly different problem of a lenticular shell with tapering thickness that is subjected to a uniformly imposed curvature. The particular thickness profile allows him to find an elegant closed-form solution of $(\omega_M^{0*})^2 = 4(14 + 2\nu)/(1 - \nu)$ that is consistent with the support conditions, and astonishingly, it predicts the critical initial deflection precisely ($\pm 0.39\%$) for $\nu \geq 0$, but for negative Poisson's ratios the deviations rise up to 12.8%.

Although not plotted again in Fig. 5.7(b), the results of UC approaches of Vidoli [45] and Seffen & McMahon [39] are identical to the current case using $w = (1 - \rho^2) w_M$ where $(\omega_M^{0*})^2 = 16/(1 - \nu)$. The approaches depicted in Fig. 5.7(b) all satisfy the boundary conditions exactly, and more interestingly, the presented single degree-of-freedom QVC solution, which was obtained with *Mathematica* [115], takes the form:

$$(\omega_M^{0*})^2 = \frac{160 \left[-9\nu^5 - 211\nu^4 - 1986\nu^3 - 9486\nu^2 - 23221\nu - 23583 \right]}{27\nu^7 + 691\nu^6 + 7527\nu^5 + 43967\nu^4 + 138001\nu^3 + 184089\nu^2 - 64915\nu - 309387} \quad (5.54)$$

The equivalent expression for two- and three degrees of freedom are not compactly expressed, as noted before. When the number of degrees of freedom is increased to three, the obtained approximation of ω_M^{0*} is better than any other found so far in literature; it shows a maximum deviation of 0.67% from the FE results in Fig. 5.7(b) for all values of ν . Since the stability thresholds only concerns the bending-to-stretching energy *ratio*, its correct prediction does not necessarily imply that a model captures the local variations of strains and stresses accurately. An analysis of the latter, given in Fig. 5.8(a) and (b) for bending and in-plane stresses, respectively, shows that the presented QVC approach yields better results for the stress resultants than UC approaches, and similarly, its approximation of the inverted shape is more accurate (not depicted here). This is relevant since the presented QVC model's predictions of the stability threshold are *less* accurate for $\nu \gtrless 0$, which highlights that the close accuracy of the UC model is

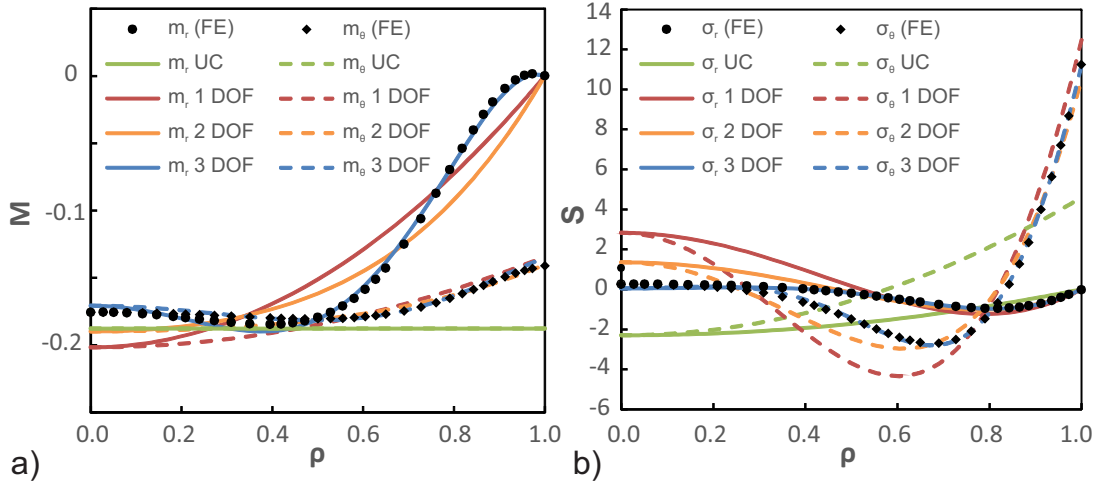


Figure 5.8: Stress resultants in the inverted configuration for models with a varying number of degrees of freedom: normalised bending stresses ($M = m/[Et^3]$) and in-plane stress resultants ($S = \sigma/[Et]$) in (a) and (b), respectively [78].

fortuitous to some extent. The solution quality successively improves with an increasing number of degrees of freedom, and the results for both, bending as well as in-plane stresses, obtained by models with three degrees-of-freedom are virtually identical to FE values.

5.3.3 Spherical Cap with Extensional Spring Supports

In a further example, the effects of extensional in-plane springs on the bistable threshold are analysed. The Poisson's ratio is first set to be 0.5 because this correlates to the *worst* case in Fig. 5.7 in terms of the accuracy of the presented QVC model for a roller-supported cap. The performance of this model in the present case is indicated in Fig. 5.9 along with uniform curvature predictions (*cf.* remark 5.2) With both approaches, closed-form solutions of the critical bistable height, ω_M^{0*} , have been obtained, and the less complex but more accurate UC solution reads as:

$$\left(\omega_M^{0*}\right)^2 = \frac{16}{1-\nu} \cdot \frac{1 + (1-\nu)k_U}{1 + (7-\nu)k_U}, \quad (5.55)$$

which converges to the solution in Eqn (3.4) of Seffen & McMahon [39] for $k_U = 0$, and to $16/(7-\nu)$ when $k_U \rightarrow \infty$. The predictions from using two- and three degrees of freedom are also plotted and are almost identical to the FE solutions with maximum absolute deviations of 0.78% and 0.73%, respectively.

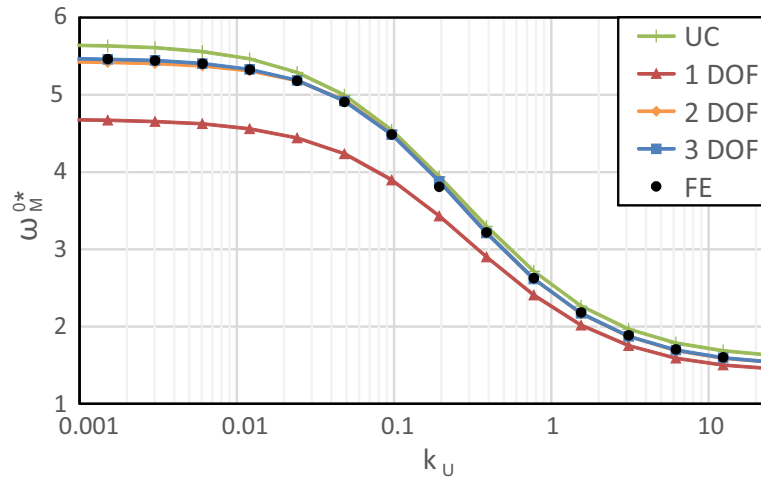


Figure 5.9: Dimensionless critical initial midpoint deflection, ω_M^{0*} , for bistability of a shallow spherical cap supported on extensional springs of stiffness k_U with $\nu = 0.5$ [29].

For small values of k_U , in-plane displacements of the outer edge are largely unrestricted, and the edge conditions resemble roller supports, Eqn (5.16b). The most accurate prediction of the associated critical height is 5.5 times the thickness, which matches that in Fig. 5.7. The critical height continuously decreases as k_U increases, and moreover, at $k_U \approx 1$ the bistable threshold, ω_M^{0*} , falls below its previous minimum value of 2.8 in Fig. 5.7 for the *lowest* Poisson's ratio value: by increasing the spring stiffness, the critical height can be smaller than that of the first case in view of promoting bistability. Once the dimensionless spring stiffness exceeds the value of 10, only little variation in the stability threshold is observed; this value corresponds to an equivalent spring stiffness of at least $10Et/a$ acting on the circumferential length of $2\pi a$. The lowest values of $\omega_M^{0*} = 1.5$ is concomitant with $k_U \rightarrow \infty$, for which the in-plane boundary displacement is entirely restricted, and thus, the caps supports are virtually fixed-pinned, as specified in Eqn (5.16d).

Note that this tendency is independent of the particular value of the Poisson's ratio, since an increasing in-plane stiffness favoured bistable inversions in all cases, see Fig. 5.10(a), where a similar accuracy as before is provided by using a three degrees-of-freedom model. The variation in critical height is now plotted as a 'landscape' with respect to ν and to k_U , and the graph of Fig. 5.9 corresponds to the line of $\nu = 0.5$ in the back of the diagram. The discrete contours in Fig. 5.10(b) allow values of ω_M^{0*} to be read more accurately; alternatively, the formula in Eqn (5.55) provides an approximation within an accuracy of 8% by comparison.

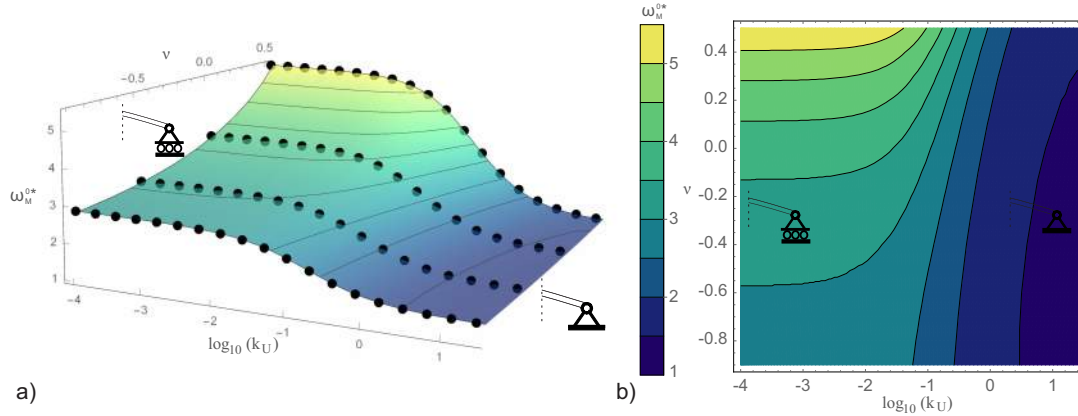


Figure 5.10: Dimensionless critical initial midpoint deflection w_M^{0*} for bistability of a shallow spherical cap supported on extensional springs. (a) Comparison of FE results with analytical model using three polynomial degrees of freedom: w_M^{0*} vs spring-stiffness, $\log(k_U)$, and Poisson's ratio, v . Dots indicate results from FE simulations, which virtually 'float' on the surface such is the accuracy of correlation, and lines are contour intervals of w_M^{0*} of 0.5. When k_U is large, the cap's edge tends towards being a fixed-pinned support, as shown, and when k_U is very small, the rim is virtually roller-supported. (b) Top view with discrete colouring between contours [29].

The landscape-plot employs the same range for k_U as Fig. 5.9, and similarly, little variation in w_M^{0*} is observed beyond $k_U = 10$. The logarithmic scale of the spring stiffness allows us to infer robustly the asymptotic performances and increases in addition the figure's conciseness. For the roller-supported case ($k_U \rightarrow 0$), the variation with Poisson's ratio is the most distinct, and for each particular value of v , the bistable threshold is the largest. The fact that the influence of the Poisson's effect becomes less pronounced with increasing k_U suggests that bistability is more and more dominated by geometrical effects. The assisting effect of the spring stiffness on bistable behaviour is not surprising from what is known about the inversion of a simpler structure: a curved *beam* [68]. Whilst beams with an initial rise of $w_M^0 \geq 1.1$ are bistable if their ends are horizontally immovable, they are always monostable if one end is unsupported; however, bistability can be restored by connecting both ends by a horizontal spring of sufficient stiffness, and the beam's critical initial rise decreases with increasing spring stiffness. Whilst the qualitative trend was predictable, the current approach *quantifies* these tendencies for shells: depending on the Poisson's ratio, the critical initial height for a roller-supported cap must be between two- and four times larger than that of a fixed-pinned cap.

Out of interest in the inversion of other geometric shapes, the FE algorithm was employed to conduct separate parameter studies of shells with rhomboidal and elliptical planforms with aspect ratios of up to 7:1. Their initial shape was given by a bi-directional sinusoidal profile of a half-wave, and hence, their entire boundary curve lies in a plane. When the edge is fixed-pinned, the variations of the critical height for bistable inversion were remarkably small: for both types of shell, the value varied between $1.45 < \omega_M^{0*} < 2$ provided that $\nu > 0$ for the rhombuses and independently of ν for the ellipses. Interestingly, this range shows a close resemblance to the results of fixed-pinned shells with circular platform, see Fig. 5.10, which suggests a universal height for bistability of around two thicknesses for this type of boundary connection irrespective of the planform shape.

5.3.4 Dual Spring-Supported Nonuniformly Curved Shell

Since neither the initial shape nor the deformation field have uniform curvature, recall Eqn (5.21b), UC approaches are no longer suitable. As discussed in the beginning of the chapter, see Fig. 5.1, the presence of rotational springs introduces extra complexity by causing a nonuniform deformation field. A moderate value of $k_U = 1$ is chosen to estimate the number of required degrees of freedom, and the predictions for a varying stiffness of $10^{-3} < k_\phi < 100$ are compared to FE results in Fig. 5.11. Again, a logarithmic abscissa was used to include the asymptotic limits in the analysis: for the smallest values of k_ϕ in this range, the outer edge approximates a hinged edge and no significant variations are observed if the value is further decreased; similarly, larger values resemble a clamped boundary condition and ω_M^{0*} reaches an apparent upper bound.

Whilst models with one or two degrees of freedom turn out to be suitable for a moderate stiffness of $k_\phi < 1$, the error in ω_M^{0*} increases considerably through its further increase. Thus, at least three degrees-of-freedom are required to achieve a good approximation ($< 2\%$) of the FE predictions. In order to analyse the combined effect of extensional and rotational spring stiffnesses on the bistability threshold, a landscape plot is given in Fig. 5.12 for a fixed value of the Poisson's ratio, $\nu = 0.3$.

Note that the direction of the axes for k_U and k_ϕ has been reversed in Fig. 5.12(a) for a more open perspective of the solution landscape, and that larger values of k_U have been used compared to previous figures in order to reveal the relevant variation. A discrete

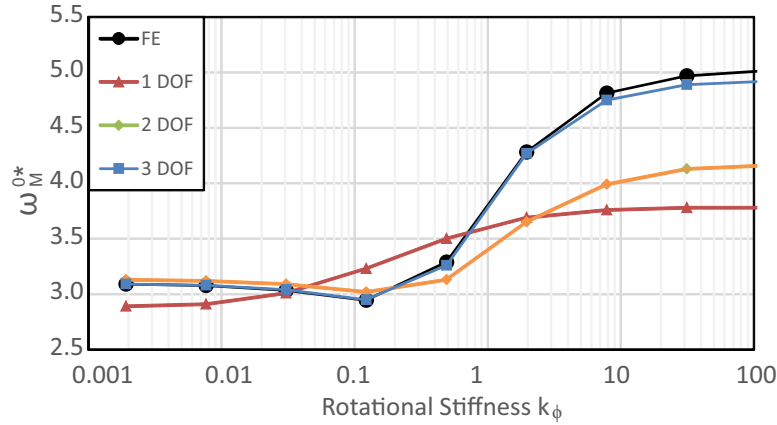


Figure 5.11: Dimensionless critical initial midpoint deflection ω_M^{0*} of a nonuniformly curved shell, Eqn (5.21b), supported on extensional (k_U) and rotational (k_ϕ) springs. Convergence to FE results occurs when the number of degrees of freedom is increased, for $k_U = 1$ and $\nu = 0.3$ [29].

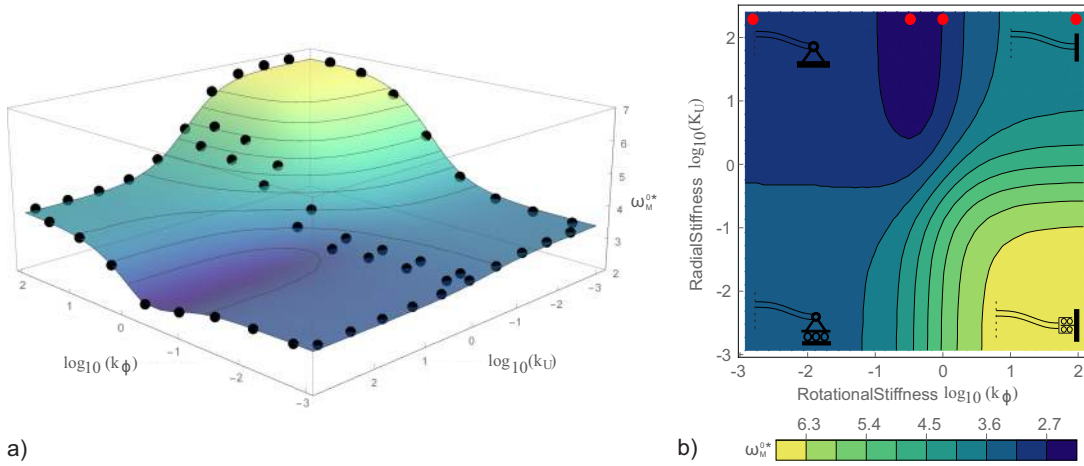


Figure 5.12: Dimensionless critical initial midpoint deflection ω_M^{0*} for a nonuniformly curved shell supported on extensional (k_U) and rotational (k_ϕ) springs. (a) Comparison of FE results (dots) with analytical model using three degrees of freedom, with $\nu = 0.3$ [29]. (b) Top view of the same plot with discrete colouring and dots indicating the asymptotic support conditions for extreme values of spring stiffnesses. Red dots indicate four representative points for which the mode shapes are further analysed.

contour plot is also given in Fig. 5.12(b) where the asymptotic support conditions are also indicated in the four corners of the plot. In the sense of in-plane vs rotational freedoms, these are fixed-fixed (k_U & $k_\phi \rightarrow \infty$), fixed-free ($k_U \rightarrow \infty$, $k_\phi \rightarrow 0$), free-fixed ($k_U \rightarrow 0$, $k_\phi \rightarrow \infty$) and free-free (k_U & $k_\phi \rightarrow 0$). The landscape topography shows apparent nonlinear variations, albeit the linear nature of the spring equations.

Interestingly, a similar trend with respect to k_U as in the previous example is observed, despite the different initial shape and the newly added rotational supports: by resisting in-plane edge displacements, bistability is promoted. In opposition to this, a rotational spring tends to revert the shell by definition since a radial edge bending moment in the sense of the initial shape is exerted. So, by reducing the applied moment by decreasing k_ϕ , a stable inversion is facilitated. Such a qualitative explanation, however, is an oversimplification and might easily miss the anomalous ‘dimple’ in the stability landscape diagram that is observed for moderate values of k_ϕ in combination with large values of k_U . Importantly, the *lowest* value of the critical height is in fact encountered for a nonzero value of k_ϕ (≈ 0.4), which suggests that a moderate rotational spring stiffness can actually engender bistability; this value of k_ϕ is equivalent to a spring stiffness of $4.37D/a$.

Analysis of the Stability Diagram’s Anomaly

A closer inspection of the corresponding inverted shapes shall reveal the driving factor of the anomaly. For the purpose of analysis, four representative shapes calculated with a three degree-of-freedom model with $k_U \rightarrow \infty$ and a rotational spring stiffness of $k_\phi = 0.001, 0.4, 1$ and 100 are plotted; note that the red dots in the stability landscape diagram of Fig. 5.12(b) indicate these positions, which denote: (1) the fixed-pinned case, (2) the particular value at which the minimum is encountered, (3) a supercritical value, and (4) the virtually clamped case, respectively. Fig. 5.13(a) shows the corresponding normalised inverted configurations of shells at the brink of bistability ($\omega_M^0 = \omega_M^{0*}$) so that the slightest reduction in height would cause a reversion; since the value of the initial rise varies, the shapes are normalised by the initial midpoint deflection.

It is conspicuous, that the clamped inverted shape qualitatively resembles the mirror-symmetric shape, while the hinged inversion is concave and approximately uniformly curved. At the minimum, only little variations from the hinged mode shape are observed, and a corresponding sub-critical point in between is not depicted, since barely any difference is observed. However, increasing k_ϕ beyond the position of the ‘minimum’ causes rapid changes of inverted shape: the shape becomes strongly curved, an inflexion point is formed, and concavity is lost. Hence, it begins to resemble a mirror image of the initial shape. The shape transition is reasonable, since an increased stiffness against rotation at the edge, causes a shift of the deflections towards the centre. By

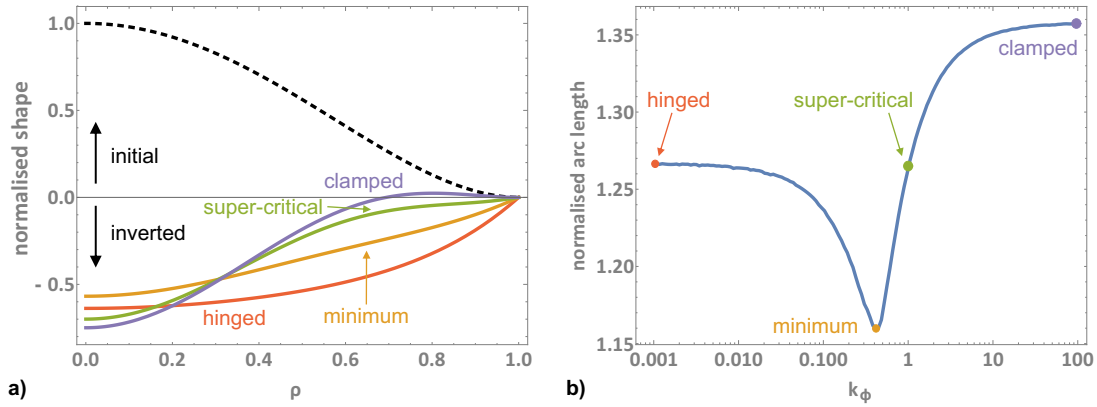


Figure 5.13: (a) Normalised inverted shapes, $(\omega^0 + \omega)/\omega_M^0$, for shells with critical initial geometries ($\omega_M^0 = \omega_M^{0*}$) and different rotational stiffnesses; the black dashed line denotes the normalised initial shape, ω^0/ω_M^0 , whose shape is identical for all cases. The terms ‘hinged’, ‘minimum’, ‘super-critical’ and ‘clamped’ refer to the spring stiffnesses indicated in (b), where the corresponding arc length of normalised inverted shapes is plotted over the dimensionless rotational spring stiffness. The depicted values relate to the topmost row in Fig. 5.12(b).

considering the arc length of the inverted shapes, see Fig. 5.13(b), it can be shown that the intermediate range, at which the minimum occurs, increases the stretching barrier; the related displacement functions were normalised via the initial midpoint displacement to ensure comparability: the shortest arc length is observed for $k_\phi = 0.40$, which is precisely within the plateau in the region of $0.32 \leq k_\phi \leq 0.42$, for which the smallest value of $\omega_M^{0*} = 2.40$ is observed.

In order to find out if a similar behaviour is observed in simpler structures, a beam model, which can be obtained by only considering a section of the shell and neglecting circumferential quantities, has been employed, see §5.2.4. The corresponding stability diagram in Fig. 5.14(a) is plotted for a horizontally immovable edge with varying rotational stiffness. The critical height for bistability is lower in all cases, when it is compared directly to the shell version. In beams, a similar ‘dimple’ is present, but in contrast to shells it constitutes only a *local* minimum. As before, it is associated with a mode transition of the inverted shape; see Fig. 5.14(b), where the two extreme cases ($k_\phi = 0.001$ and $k_\phi = 100$), the local minimum ($k_\phi = 0.6$) and a super-critical shape ($k_\phi = 1.5$) are depicted. The general response to an increasing rotational stiffness resembles the previous case where an edge rotation is avoided by increased central deformations, but unlike shells, the mode shape of inverted hinged beams displays a central dimple that indicates a barely deformed central region. This shape is energetically favourable, since most of the rotation focusses at the edge without any bending resist-

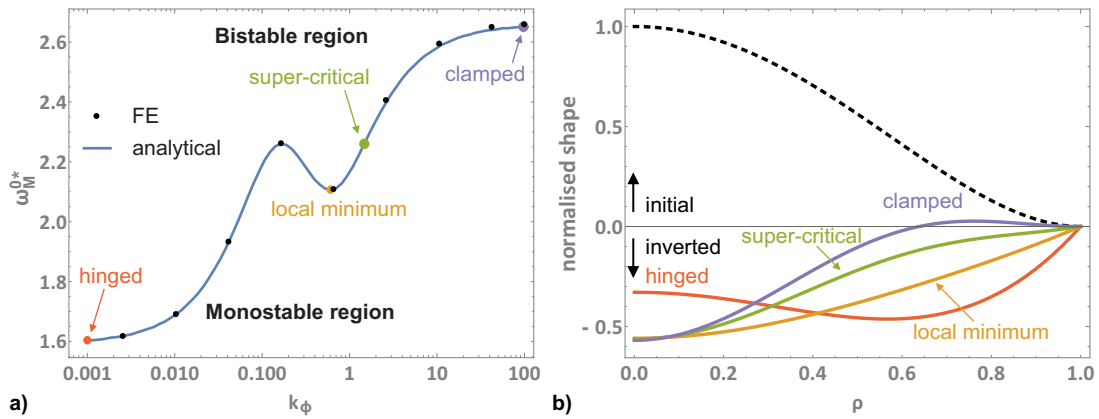


Figure 5.14: (a) Dimensionless critical initial midpoint deflection, ω_M^{0*} , for a nonuniformly curved beam with horizontally immovable edges ($k_U \rightarrow \infty$) over dimensionless rotational spring stiffness, k_ϕ . Comparison of FE results (black dots) with analytical model using three degrees of freedom. (b) Normalised initial shape, ω^0/ω_M^0 , and corresponding inverted shapes, $(\omega^0 + \omega)/\omega_M^0$, of a beam for particular values of the spring stiffness indicated in (a).

ance, but in contrast to shells, an additional inflexion point does not cause a complex bending-stretching interaction. With increasing rotational spring stiffness, the shape becomes approximately uniformly curved in the region of the local minimum, before the deformation focusses further in the centre at the supercritical state that closely resembles the inverted shape of the fully clamped case.

In conclusion, it was shown that the mode transition, which is also observed in beams, explains the phenomena partially, but the global minimum is a unique feature of shells caused by the highly nonlinear interaction between bending and stretching.

Accuracy of the Clamped Solution

Because the deflection field comprises a clamped as well as a hinged deformation mode, an ideal clamped support cannot be captured outright because the hinged mode is inherently coupled to the overall solution. An ideal clamp can only be *approached* by setting K_ϕ to a very large finite value. In the earlier derivation, the total strain energy, Π , depends on K_ϕ 's fourth power (whilst K_U evinces a quadratic relation), which compounds further the effect that large values of K_ϕ can have upon the numerical solution procedure, especially when solving for the eigenvalues of the Hessian matrix, Eqn (5.20). A sensible limit for K_ϕ should be correlated to the range of numerical floating-point precision of the particular software package. Basic packages employ a double precision analysis which covers 16 decimal places, so setting $0 < K_\phi^4 < 10^{16}$

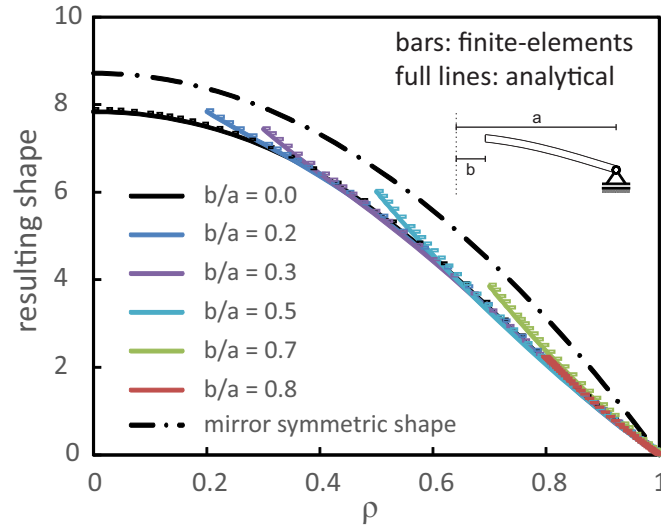


Figure 5.15: Inverted shapes of a shell with annular planform: comparison between analytical results (full lines) and FE simulations for differing hole sizes and Poisson's ratio; all shells possess an outer radius, $a = 1$ with $a/t = 1/200$ and uniform initial curvature of $\kappa_r^0 a^2/t = \kappa_\theta^0 a^2/t = 17.43$.;

should not produce inaccuracies. Here, the general analysis software package Mathematica [115] was employed, which can express much higher precision levels, and the results up to $K_\phi \leq 10^4$ were found to be indistinguishable from those of Sobota & Seffen [78] who deal with a clamped support shell from the outset. Hence, a modification towards a numerically slightly more robust methodology is possible but not required here, and thus, a perspective with a direct physical interpretation was chosen, see also remark 5.2.

5.3.5 Extension for Shells with Annular Planform

Another manipulation of the support conditions concerns the inner edge of a shell. Whilst examples in literature mainly focussed on continuous shells, the effects of central holes are not well understood. The inverted shapes of shells with annular planform are shown in Fig. 5.15, where analytical predictions with three degrees of freedom (lines) are in excellent agreement with finite element simulation (bars); the dash-dotted line indicates the mirror-symmetric shape as an orientation. The figure illustrates the changing response when a central hole of $b/a = 0.2$ is created and successively enlarged up to a value of $b/a = 0.8$. The initial height of $\omega_M^0 = 8.7$ was chosen in such a way that all analysed cases are bistable.

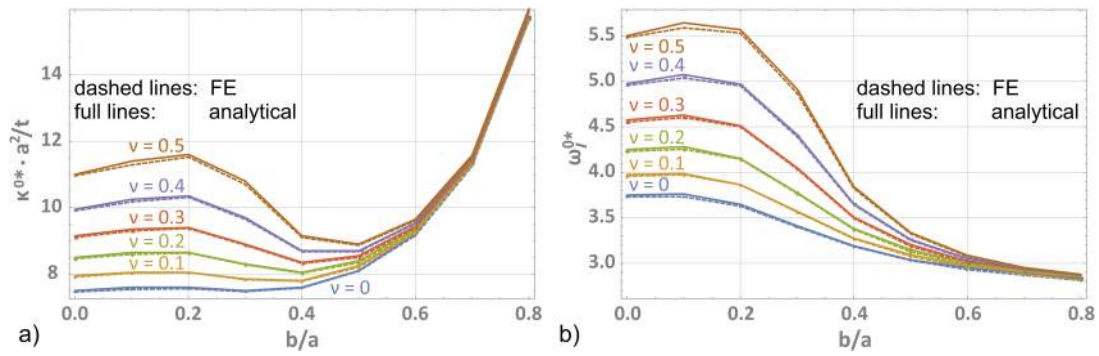


Figure 5.16: (a) Critical initial curvature for bistability, κ^{0*} , for differing Poisson's ratios and hole sizes, b/a . Analytical results with three degrees of freedom (full lines) are compared to FE results. (b) Same threshold as a function of the critical initial height of the inner edge, ω_I^{0*} .

By cutting a hole, the value of ω_M^0 becomes less representative as it describes an *imaginary* height of a shell before the hole was created. Since several publications, *e.g.* [39, 45, 71, 72], express the bistable threshold in terms of critical curvatures, Fig. 5.16(a) employs the same notation. While it was mainly used due to its suitability to describe uniformly curved shallow caps, where the simple relation $2\omega_M^0 = \kappa_r^0 \cdot a^2/t$ holds, it is less meaningful in the novel context of nonuniformly curved shells discussed in the previous section, §5.3.4. It can be seen that shells with large holes ($b/a > 0.7$) require a higher initial *curvature*, and it follows that the decisive case which required an ‘imaginary initial height’ of $\omega_M^0 = 8.7$ possesses the largest hole size of $b/a = 0.8$. However, if the same stability threshold is plotted against the initial height of the inner edge, $\omega_I^{0*} = \omega_M^{0*} \cdot [1 - (b/a)^2]$, see Fig. 5.16(b), it becomes apparent that creating a hole allows the production of bistable shells of a smaller physical height. Thus, the required curvature in (a) primarily increases because the hole reduces the shell's height.

The diminishing influence of the only relevant material parameter, ν , with increasing hole sizes is caused by a transition towards a beam-like behaviour. This is illustrated in Fig. 5.17(a)-(c), where in-plane stresses (black, left axis) and bending moments (blue, right axis) are shown for small, moderate and large holes with $b/a = 0.2, 0.5$ and 0.8 , respectively. Whilst the radial in-plane stresses always have a minor influence once a hole is present, the radial bending moments still affect shells with $b/a = 0.2$ and 0.5 but virtually vanish if the hole is large. Thus, the latter case is entirely governed by the circumferential response, and the Poisson's effect becomes negligible. The excellent

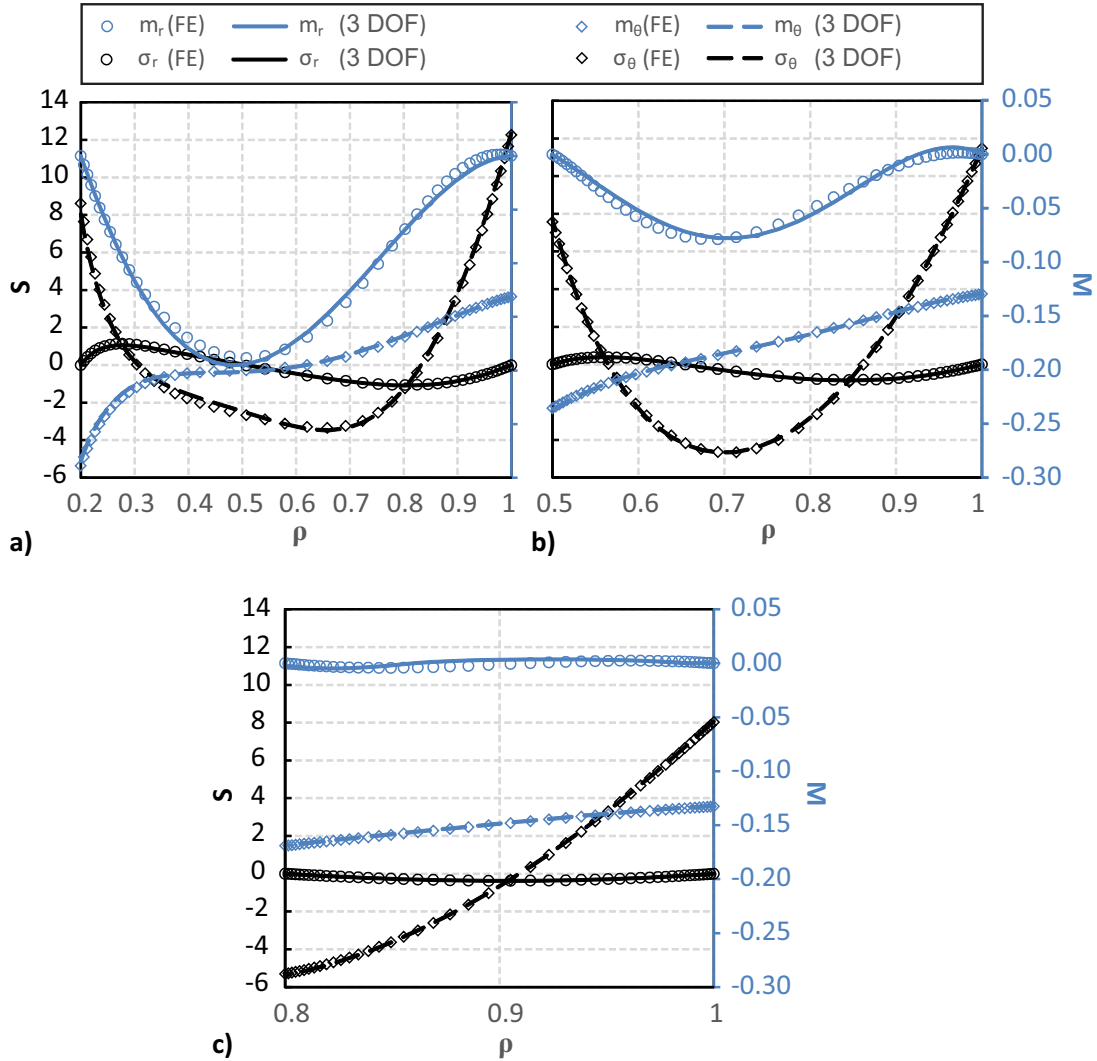


Figure 5.17: Comparison of analytical predictions with FE results: stress resultants for inverted uniformly curved shells with annular planform ($\omega^0 = 8.7$, $a/t = 200$, $\nu = 0.1$) with different ratios of inner/outer radius $b/a = 0.2$ (a), 0.5 (b), and 0.8 (c). The left axis refers to in-plane stress resultants (black) and the right axis to bending moments (blue); each ordinate has the same range in all plots; thus, the adjacent axes were omitted in (a)-(b).

agreement of the analytical predictions and FE results further underline the suitability of the model presented here.

Fixed-pinned shells with annular planform (not shown) require at most half of the height of their roller-supported counterparts to be bistable. In this case, the results of the analytical model with three degrees of freedom showed an even better agreement with finite element reference solutions than roller-supported shells. The bistable threshold, ω_l^{0*} , is less affected by variations of the hole size (reduction $< 10\%$ from

closed shell to $b/a = 0.8$), and the influence of the Poisson's ratio on ω_l^{0*} was similarly small as in fixed-pinned caps (5 % between $\nu = 0$ and $\nu = 0.5$), *cf.* the right boundary in Fig. 5.10(b). The reason for this behaviour is examined in detail in §6, where a polar-orthotropic material behaviour is employed to analyse the interaction of radial and hoop-stresses in isolation.

5.3.6 Multishell Coupling

The following two examples combine the previous results of uniform curved shells with circular and annular planform in order to model two shells that are connected at their edge. First, a nonuniformly curved shell with a geometry of the fully spring-supported case, see §5.3.4 or Eqn (5.21b), is linked to a flat annulus of the same thickness. Second, two shells of the same curvature are connected via a hinge-line, which enriches the multistable response.

Influence of an Inverted Shell on a Neighbouring Substrate

The shape was chosen since it approximates a unit cell of bistable ‘morphing metal’ arrays in Fig. 3.8 from [79] where bistable shells are arranged periodically on a substrate. Whilst the global behaviour of such arrays was described phenomenologically, a theoretical framework to quantify involved stability thresholds and energy levels is lacking. The initial shape of $w_1^0/t = (1 - \rho_c^2)^2 \omega_M^0$ and $w_2^0 = 0$ resembles a full cosine wave of wavelength $2\rho_c$ with a smooth transition to an attached annulus. Thus, the shear force condition in Eqn (5.46) is relaxed, and the constant A_4 in Eqn (5.50) is used to ensure a vanishing shear force at the outer edge of the annulus instead. This example is used as a benchmark test to measure the performance of the presented methodology with reduced order. It is challenging since a connecting edge moment is present, which was previously shown to require higher-order approaches for large values.

First, the inverted shapes of a shell with $\omega_M^0 = 4$ are considered in Fig. 5.18(a): it is conspicuous that inversions become shallower with an increasing width of the annulus, which reflects that the reverting bending moment increases, while an additional stabilising in-plane force is exerted simultaneously. Since the shape approximations as well as the stress resultants, see Fig. 5.18(b), are in fair agreement with finite element calculations, the methodology demonstrates its suitability despite using less elaborate trial functions as in the previous examples. The slight stress deviations at the centre barely

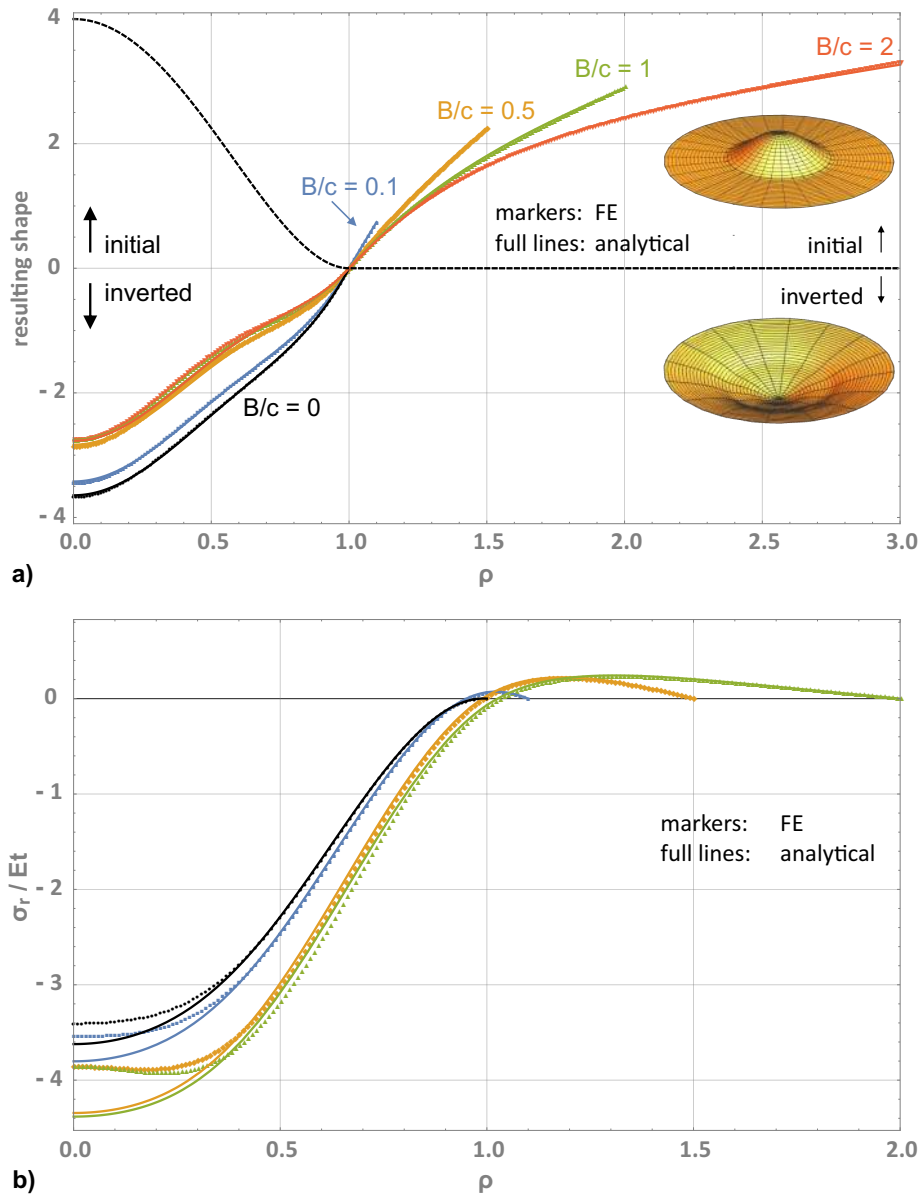


Figure 5.18: Comparison of analytical predictions (full lines) with finite element results (markers): (a) Inverted configurations of a shell with roller supports at c , an initial apex height of $4t$, a thickness of $c/t = 100$, and differing annular width between $B = 0.1c$ and $B = 2c$. (b) Corresponding radial mid-plane stress resultants in comparison to finite element results.

affect the energy functional since these are weighted by the area. Based on the previous observations in lower order approaches that allowed an accurate description of the stability threshold despite not capturing every aspect of the stress resultants precisely, *cf.* Fig. 5.7 and Fig. 5.8, the current predictions of the bistable threshold can be regarded as accurate. It is noteworthy that in this particular case, the finite element reference

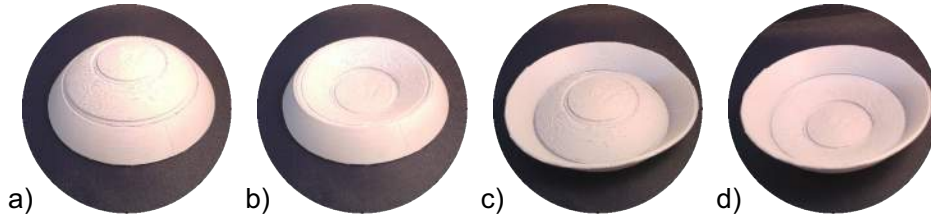


Figure 5.19: ‘Quadstable’ shell with four stable inversions due to added hinges: (a) initial configuration, (b) inner segment inverted, (c) outer segment inverted, (d) fully inverted configuration.

solutions were obtained by using a rotationally symmetric shell element to ease the modelling process, and thus, the occurrence of a nonsymmetric buckling mode cannot be excluded with absolute certainty. The analysis of the bistable threshold shows that the added annulus of a width of $0 < B < 2c$ affected the bistable threshold, ω_M^{0*} , by less than 15 %; for annular widths of more than $1.7c$, the bistable threshold approached a constant value of $\omega_M^{0*} = 3.77$. Thus, the distance that is required to avoid a significant interaction of two bistable unit cells can roughly be estimated as 3.5 times the cells radius for $\rho_c/t = 100$. A quantification of the edge layer for arbitrary ρ_c/t ratios and the consideration of noncircular planforms are problems that are crucial for application, but these shall be addressed in a separate future study. Instead, the developed model is now employed to study the effect of local thickness variations at the linkage.

Influence of Local Thickness Variations on Multistability

The second example concerns a uniformly curved shell to which local thickness variations are added, as shown in Fig. 5.19. These are realised by diminishing a narrow part’s thickness to a fifth, which reduces the flexural rigidity locally by the factor of $1/125$. Since this region is virtually free to rotate, it can be idealised as a hinge, which isolates the bending response of two shells by stopping the reverting bending moment from propagating. This enriches the solution by allowing for separate inversions of segments without significantly affecting the other parts. In the example depicted in Fig. 5.19, two hinges were added to illustrate two possible cases with regards to their location: the lower linkage allows for stable semi-inverted configurations where only one region of the shell is turned inside-out, see Fig. 5.19(b)-(c), since all segments are of sufficient size and curvature; the upper linkage, however, separates a part that is too shallow to invert in isolation, and thus, it only inverts in combination with the interme-

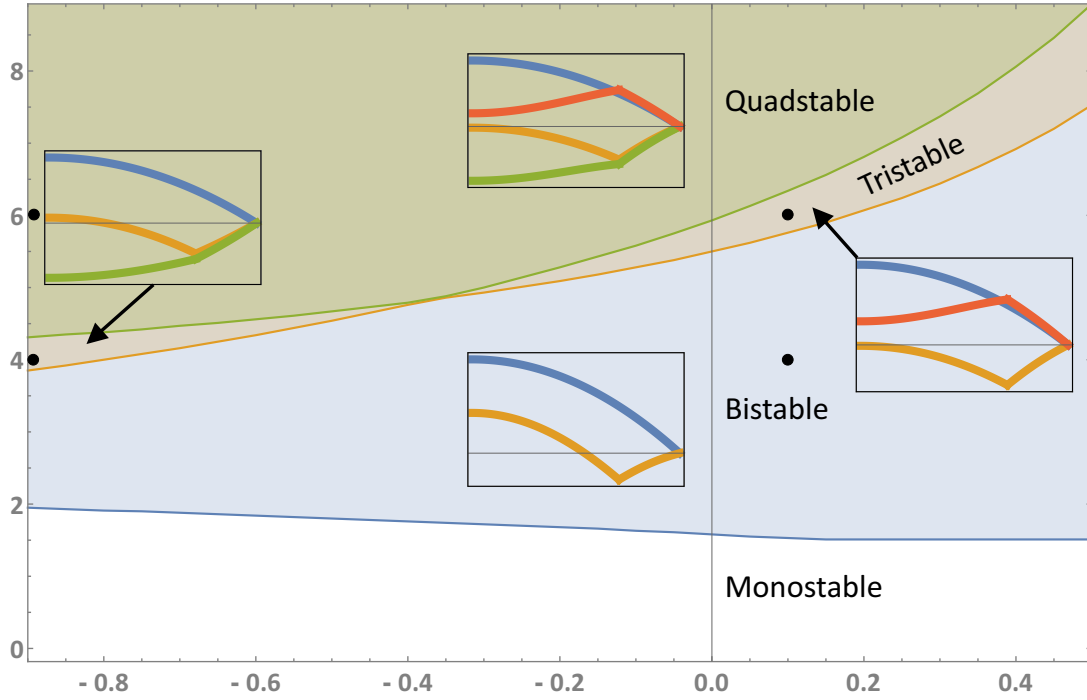


Figure 5.20: Stability diagram showing the number of possible stable configurations of a shell with a hinge-line at $c/a = \sqrt{1/2}$ as a function of the Poisson's ratio and the initial apex height; stable shapes of each region are illustrated in framed rectangles. Black dots indicate finite element results that confirmed the analytical predictions of mode shapes.

diate segments which resembles a fully connected shell. Note that in addition to the semi-inverted states of (b)-(c) a combined, full inversion is possible, see (d).

Whilst the analytical model requires equal displacements (in particular $\varphi_1 = \varphi_2$) and stress compatibility (*e.g.* $m_{r1} = m_{r2}$) at the linkage at each side of the narrow part, the idealisation neglects this condition by using a simplifying substitution: instead of modelling the strip with a separate set of basis functions, a hinge condition is employed that allows a free relative rotation, and hence, in general $\varphi_1 \neq \varphi_2$. It follows that only in-plane forces, the shear force, and a circumferential bending moment are transmitted, but a radial bending moment is avoided via an evading rotation. In order to calculate the deflection fields from Eqn (5.49) and Eqn (5.50), the two out-of-plane conditions of Eqn (5.46) are enforced, and additionally, the radial bending moment is required to vanish at the linkage ($\rho_c = 1$) and the outer edge.

The model is employed to analyse two shells that are linked via a single hinge located at $c/a = \sqrt{1/2}$. Thus, each shell segment possesses the same height of $w_M^0/2$. The stability diagram in Fig. 5.20 depicts the number of stable configurations as a function of

the critical apex height and the Poisson's ratio of a shell with fixed-pinned supports at the outer edge. As previously discussed, the bistable threshold is only slightly affected by the Poisson's ratio for such supports, *cf.* Eqn (5.55). More interestingly, the diagram shows a *triple point* at $\omega_M^{0*} \approx 4.8$ and $\nu = -0.38$ at which a direct transition from bistability to *quadstability* with four stable configurations exist. This coordinate also constitutes a point of a mode transition: whilst the isolated inversion of the outer part required the lowest initial apex height in all cases (bistable threshold, orange shape), tristable shells with $\nu < -0.38$ possess a third stable configuration in which both parts are inverted (green shape); tristable shells with $\nu > -0.38$, however, exhibit two semi-inverted configurations (drawn in orange and red). This mode transition as well as the quadstable behaviour were confirmed in FE simulations at the indicated points (dots), but an extensive FE parametric study was not conducted since it would require a high amount of tedious user interaction. Note that a simplified model, which employed separate UC models for each segment, lead to similar stability thresholds ($\approx \pm 10\%$) but it failed to predict the mode transition.

5.3.7 Limitations

The nature of the chosen nonlinear Ritz approach differs from FE analysis, and whilst some features outperform the latter, additional limitations arise: both methods can theoretically lead to 'false negatives' or to 'false positives', but the first is more likely in FE analysis, whilst the choice here *not* to linearise the work equation increases the possibility of the latter. When using FE, alternative equilibrium states can easily be missed since the linear stiffness matrix would require to evaluate an infinite number of possible combinations in static equilibrium to obtain certainty. However, because of linearisation, the problem becomes amenable to a numerical solution process even for discretisations with a large number of degrees of freedom, which allow for a high accuracy. The current method considers a nonlinear stiffness matrix, \mathbf{H} , which implies that computational efficiency is imposing a limit of a few degrees of freedom. Hence, the set of shape functions is not necessarily accurate enough. This problem can be illustrated by the example of a uniformly curved cap now clamped on its edge, where the gradient remains nonzero for all time. Although bistable behaviour was never observed in finite element simulations for a wide range of initial geometries, the theoretical analysis suggests its feasibility for an initial central rise, ω_M^0 , of more than $25t$. It can be observed in FE simulations that the radial curvature becomes highly concentrated

just before the clamped edge, which gives way to a large restoring moment despite the ‘holding’ effects of significant in-plane circumferential tension. Even though the predicted shapes were not precisely marshalled in FE simulations so that a narrow stable region may have simply been missed, it seems more likely that the presented models fail to capture the strongly curved domain next to the edge. However, simply increasing the order is not a viable solution approach because the midpoint deflections and, more importantly, deflection gradients (recall $dw/dr \ll 1$), increase beyond the limits acceptable for shallow shell behaviour and thus beyond the scope of this study.

5.4 Summary

The influence of edge effects and related support conditions on the bistable properties of shallow shells has been addressed in this chapter. For the purpose of analysis, a higher-order FvK model employing a Rayleigh Ritz approach with up to four degrees of freedom was presented. By considering additional terms in the assumed deflection field, all boundary conditions were satisfied precisely, and a relation to the in-plane response was established via Gauss Theorema Egregium before stable inversions have been identified by energy minimisation.

The suitability of this geometrically nonlinear shell model has been demonstrated for a range of problems in which the linear theory of the previous chapter has failed, since the involved normal displacements were not small. The performance was then compared to existing nonlinear approaches in literature and finite element reference solutions to highlight the superior accuracy of the approach presented here. The bistable threshold for uniformly curved shells with horizontal supports was captured in closed form and it was shown that an increasing stiffness favours a bistable response; in particular, fixed-pinned shells became in all analysed cases bistable when being at most half as shallow as their roller-supported counterparts. An additional finite element study revealed that structures with fixed-pinned supports are less affected by their geometric shape and that a wide range of different geometries becomes bistable when the initial apex height exceeds twice the thickness; thus, the obtained analytical results for a fixed-pinned cap provide a rough estimate of this threshold.

Whilst uniform curvature models were shown to be suitable to describe hinged shells, their applicability is limited by the presence of rotational spring supports and initially nonuniformly curved shells. In such cases, the response becomes more intricate

and higher-order models are required to capture the inversion process accurately. An increasing rotational stiffness has the tendency to diminish bistable responses, even though it was demonstrated for a particular case of a nonuniformly cap that a moderate rotational spring stiffness in combination with a horizontally-immovable support leads to a global minimum of the required apex height at which bistable inversion becomes possible. It was shown that the minimum is concomitant with a mode transition of the inverted shape at which its arclength is minimised. This behaviour has been compared to the inversion of bistable beams of the same profile, which displayed a similar mode transition but evinced only a *local* minimum of the stability threshold.

The shell model was then extended for shells with an annular planform. The analysis of the bistable threshold revealed that an increasing hole size favours the production of bistable shells of a smaller height that are at the same time required to possess a smaller radius of curvature.

Finally, it has been shown that ‘quadstable’ shells with four stable configurations can be manufactured by adding certain local thickness variations: these act like hinges and enable structural parts to invert in isolation since a reverting bending moment is stopped from propagating. While restricting (edge) rotations has the tendency to hinder bistable inversions, freeing it can allow for extra stable configurations. In addition, the analysis identified a point of mode transitions in the stability diagram where the order of possible inversions changes; this point constitutes simultaneously a triple point at which an infinitesimal increase of the apex height causes a transition from bistable to quadstable behaviour.

Chapter 6

Bistable Polar-Orthotropic Shells

Whilst the previous chapter elucidated the influence of outer spring supports on the bistable performance of shells, this chapter analyses how bistability is affected by variations of the *internal* stiffness of shells. Such an investigation employs a polar-orthotropic constitutive law, which allows us to increase or decrease the radial stiffness compared to its circumferential counterpart and to study each contribution in isolation.

The reason to study this rather unusual material is to obtain further insight into the governing factors of bistability, which paves the way for exploiting this characteristic more efficiently. Modifying the stiffness ratio β between circumferential and radial direction aims at the identification of stabilising and diminishing factors for bistability, which can then be applied in favourable ways. It can be realised in a simple set of table top experiments with cast silicone rubber by adding directional stiffeners, see Fig. 6.1, and the results indicate a strong variation of the way in which initially uniformly caps invert. It is notable that also the minimum height required for a bistable inversion differs significantly. Hence, it is possible to gain control over the bistable response of a shell by using appropriate stiffeners, grooves or similar structures, such as grid shells, which behave approximately polar-orthotropic in consequence of a smeared-stiffness, and the study of this particular aspect on bistability is to the best knowledge of the author completely novel.

The presented analytical model extends the approach from the previous chapter, §5, for rotationally symmetric polar-orthotropic shells that are free to rotate around the outer rim support with a variable radial spring stiffness, k_u . The more general material law requires a different set of basis functions, which are based on the geometrically linear solution of a bent plate. By employing polynomials of real powers in a Ritz

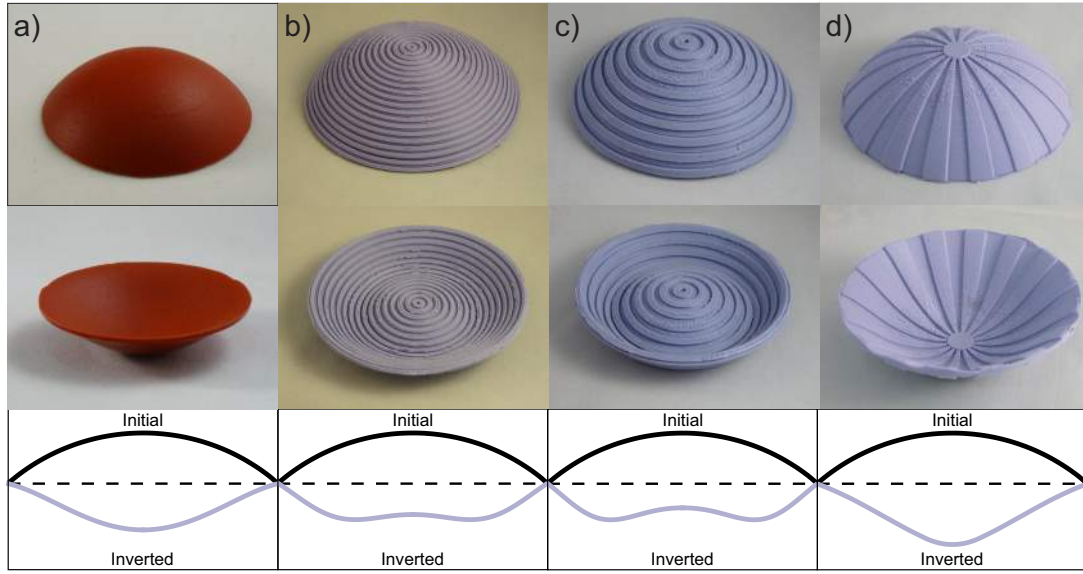


Figure 6.1: Initially stress-free shells (top), their stable inversions (middle), and a sketch of their profiles (bottom). (a) Isotropic shell with an approximately uniformly curved counterpart. (b) Circumferentially stiffened shell ($\beta > 1$), mimicking globally an orthotropic shell, since radial stresses cannot efficiently build up in the stiffened regions. The inverted configuration exhibits a central dimple, which becomes even more distinct, when the orthotropic ratio is increased, *cf.* (c). (d) Radially stiffened shell ($\beta < 1$) with a central plug due to the manufacturing process; its inversion evinces concentrated deformations at the centre.

approach, the analytical treatment is expedited, and stable inversions are found via energy minimisation.

First, this study focusses on the effects of the stiffness ratio, β , as well as the influence of additional horizontal supports on the required apex height for bistable inversion. The presented model is then drastically simplified by using a single degree of freedom to approximate the threshold of bistability in closed form. Furthermore, the stress distribution of a cap is compared to FE results and to an alternative approach inspired by a competing theory in literature, in order to emphasise the importance of a suitable set of basis functions that are capable of modelling central stress singularities precisely. Since such singularities are usually not acceptable in practical applications, the bistable behaviour of caps, in which the area around the singularity is cut out, is investigated.

In the subsequent section, the geometrically linear bending solution of a polar-orthotropic circular plate is discussed. The results inspire the choice of trial functions in the geometrically nonlinear model, given in §6.2. An extension for annular shells is

derived in §6.3 before results are presented in §6.4. The chapter is eventually summarised in §6.5.

Remark 6.1: The bistable response of polar-orthotropic shells differs from the often-studied rectilinear orthotropy, since the possible misalignment of principal strain directions and material-orientations in the latter evokes a strain-energy performance more conducive to forming extra stable equilibrium configurations; recall that in such cases one principal direction dominated so that a transition towards an alternative stable equilibrium became costly due to a high twisting rigidity. In polar-orthotropic materials however, this misalignment is not observed as long as rotational symmetry is preserved, since the absence of in-plane shear is tantamount to principal strains that align with the principal material-orientations. Hence, polar orthotropic caps are not expected to show additional stable configurations beyond bistability.

6.1 Geometrically Linear Bending of a Plate

The consideration of polar orthotropy introduces an additional parameter to the constitutive equations, which specifies the ratio of circumferential stiffness, E_θ , to radial stiffness, E_r via

$$\beta = \frac{E_\theta}{E_r}. \quad (6.1)$$

If the material law is approximated by using cross-sectional variations, *e.g.* stiffeners, different values of β in bending and stretching will arise, since flexural and in-plane rigidities scale differently with the thickness. This problem is addressed qualitatively in §6.4, but for the quantitative analysis, a unique β -value is assumed, since the focus is on gaining a fundamental understanding of effects of directional stiffness variations and furthermore, this choice avoided additional complexity in the finite element model to which the analytical results are later compared.

The Poisson's ratio is not symmetric with respect to indices, since an associated lateral contraction depends on the stiffness ratio, and their compliance requires $E_r \nu_{\theta r} = E_\theta \nu_{r\theta}$. Hence, the stiffness ratio also describes the ratio of the Poisson's effects in particular directions via $\beta = \nu_{\theta r} / \nu_{r\theta}$. By using a more succinct notation of $E = E_r$ and $\nu = \nu_{\theta r}$ within this chapter, the material tensor, \mathbf{E} , and its inverse \mathbf{E}^{-1} read:

$$\mathbf{E} = \frac{E}{1 - \nu^2/\beta} \begin{bmatrix} 1 & \nu \\ \nu & \beta \end{bmatrix} \quad \text{and} \quad \mathbf{E}^{-1} = \frac{1}{E} \begin{bmatrix} 1 & -\nu/\beta \\ -\nu/\beta & 1/\beta \end{bmatrix}. \quad (6.2)$$

These take the form of 2×2 matrices, since the constitutive equations can be written in terms of the principal directions only due to the assumed rotational symmetry. This tensor requires $\beta > \nu^2$ since it must be positive definite to ensure energetically permissible deformations. Its pre-integration in thickness direction gives the stretching and flexural rigidity matrices of $\mathbf{A} = \mathbf{E}t$ and $\mathbf{D} = \mathbf{E}t^3/12$, respectively, with $D = D_{11} = Et^3\beta/12(\beta - \nu^2)$; these relate the bending and in-plane stresses to their corresponding work conjugated strain expressions via

$$[m_r, m_\theta]^T = \mathbf{D} [\kappa_r, \kappa_\theta]^T \quad \text{and} \quad [\sigma_r, \sigma_\theta]^T = \mathbf{A} [\varepsilon_r, \varepsilon_\theta]^T, \quad (6.3)$$

respectively. In contrast to the constitutive equations, the kinematic relations and equilibrium conditions stay unchanged. Hence, the balance of moments and the vertical force,

$$q_r = \frac{dm_r}{dr} + \frac{m_r - m_\theta}{r} \quad \text{and} \quad \left(\frac{d}{dr} + \frac{1}{r} \right) q_r = -p_N, \quad (6.4)$$

respectively, can be merged into a single differential equation. By substituting the strain expressions of Eqn (5.6) for m_r and m_θ in this equation and employing furthermore the geometric relations according to Eqn (5.5) the governing differential equation for the geometrically linear bending of plates under a transversal load p_N is obtained:

$$\frac{d^4 w}{dr^4} + \frac{2}{r} \frac{d^3 w}{dr^3} - \frac{\beta}{r^2} \frac{d^2 w}{dr^2} + \frac{\beta}{r^3} \frac{dw}{dr} = \frac{p_N}{D}. \quad (6.5)$$

The solution in the absence of load ($p_N = 0$) without considering rigid body modes takes the form:

$$w_h = \begin{cases} \text{for } \beta = 1 : & A_1 r^2 + (A_2 + A_3 r^2) \log(r) \\ \text{else:} & A_1 r^{1+\sqrt{\beta}} + A_2 r^{1-\sqrt{\beta}} + A_3 r^2 \end{cases} \quad (6.6)$$

It degenerates for isotropic materials ($\beta = 1$) that have been discussed in §5.2.2 and which are thus not further investigated here. In polar-orthotropic materials the situation is more intricate, since all constants evoke some kind of singularity when $\beta < 1$. First, we calculate the curvatures according to Eqn (5.5) as well as the corresponding bending moments and shear force via Eqn (6.3) and Eqn (6.4), respectively, and then the related bending strain energy via Eqn (5.18). Since $\beta > 0$, a pure deformation mode in A_1 has finite bending energy, whereas A_2 would engender an infinite energy barrier in

closed shells and is thus not observed; in annular shells, however, even stress resultants containing terms in r raised to powers less than -1 are energetically admissible.

For A_1 the curvatures vary with r raised to $-1 + \sqrt{\beta}$, whereas A_3 causes a uniform curvature throughout the shell. Note that the first term signifies a vanishing shear force throughout the shell, whereas A_3 causes central shear-stress singularities for $\beta \neq 1$; this rather unintuitive detail is a consequence of the material law employed. The singularity of the latter would necessitate shear-deformable Reissner-Mindlin theory, but since it is energetically favourable for thin shells to evade shear deformation by flexure, the A_3 -term can be neglected. Hence, we assume the dominant deformation mode in the absence of load to be $A_1 r^{1+\sqrt{\beta}}$, despite causing bending-stress singularities at the centre for $\beta < 1$.

Admissibility of stress singularities

The governing equation suggests that stress singularities arise directly from the geometrically linear solution of a bent plate, and similarly, Woinowsky-Krieger [47] identified singularities in stretching as soon as membrane forces exist. In practice, however, elastic stresses are constrained by yielding or fracture limits, and thus, Woinowsky-Krieger as well as others [126, 127] limit the validity of their theories.

Regarding whether or not infinite stresses from singularities are ever acceptable in elasticity problems, the perspective of Barber [128, p. 142ff.] is adopted: from a mathematical point of view, they are acceptable as long as a unique and converging solution exists. While this argument may not convince the Engineering community *per se*, engineers commonly encounter and accept singularities at sharp corners and under point loads from an idealisation of geometry or the boundary conditions; here, the singularities arise directly from idealised constitutive equations. Just as there are no corners without a small fillet radius [129], perfectly polar-orthotropic materials do not exist, since fibre orientations would be undefined precisely at the singular point of $r = 0$ (cf. Fig. 6.1 (b)-(d) tantamount to a central isotropic spot). Thus, the stress definitions are predisposed for singularities. Consequently, knowing that results next to singularities are not applicable in practice, they are accepted here as long as they are energetically admissible, which requires stresses of order greater than -1 in r for closed shells.

6.2 Nonlinear Solution for Shallow Caps

In the context of polar-orthotropy, the nonlinear governing equation of equilibrium transforms similar to Eqn (6.5), but it contains the familiar additional nonlinear term that accounts for the momentum that is induced through in-plane stresses in deflected plates:

$$\frac{d^4 w}{dr^4} + \frac{2}{r} \frac{d^3 w}{dr^3} - \frac{\beta}{r^2} \frac{d^2 w}{dr^2} + \frac{\beta}{r^3} \frac{dw}{dr} = \frac{1}{D} \left[p_N + \frac{t}{r} \frac{d}{dr} \left(\frac{d\Phi}{dr} \frac{d(w + w^0)}{dr} \right) \right]. \quad (6.7)$$

The compatibility equation can be stated in terms of the Airy stress function after the following manipulations: first, by substituting $u' = (r\varepsilon_\theta)'$, the radial displacement, u , can be eliminated in the first equation of Eqn (5.2). A further substitution of ε_r and ε_θ with their corresponding stress expressions, $\sigma = A\varepsilon$, then introduces the orthotropic parameter to the compatibility equation. Eventually, the stresses are expressed through the familiar Airy stress function, see Eqn (5.7), to obtain:

$$\frac{1}{\beta} \frac{d^4 \Phi}{dr^4} + \frac{2}{\beta r} \frac{d^3 \Phi}{dr^3} - \frac{1}{r^2} \frac{d^2 \Phi}{dr^2} + \frac{1}{r^3} \frac{d\Phi}{dr} = -Eg. \quad (6.8)$$

The integration of this expression with respect to r gives, after substituting the corresponding expressions of w , for the term of the Gaussian curvature:

$$-\frac{r}{\beta} \frac{d^3 \Phi}{dr^3} - \frac{1}{\beta} \frac{d^2 \Phi}{dr^2} + \frac{1}{r} \frac{d\Phi}{dr} = \frac{1}{2} \left(\frac{d(w + w^0)}{dr} \right)^2 - \frac{1}{2} \left(\frac{dw^0}{dr} \right)^2. \quad (6.9)$$

and thus, the number of potentially relevant constants of integration reduces to two. The solution of Φ suggests that similar homogeneous terms as in (6.6) arise: the r^2 -term vanished due to the reduction of constants and, for full plates, $r^{1-\sqrt{\beta}}$ is energetically not admissible. Hence, the term $r^{1+\sqrt{\beta}}$ is the only remaining one in such a case.

Order of polynomial basis functions

In order to find alternative equilibrium configurations in shells of a shape given by w^0 , the assumption of the mode shape is crucial. However, in literature two different perspectives have been taken: while the linear deflection field, which is pointing towards singularities via Eqn (6.6), inspired some authors [130–132] to employ the non-integer deflection term, $r^{1+\sqrt{\beta}}$, others may have been influenced by the fully clamped case,

where bending-stress singularities do not occur, and chose polynomial approaches of integer powers for shells simply supported at their rim [133–135]. Some authors circumvent singularities entirely by either considering a small isotropic plug at the centre, or considering planform annuli [136–138], but here, this problem shall be addressed directly. The approach presented here takes the first perspective, and rather than avoiding the problem, such singularities are used to assess the robustness of the methodology by comparing the stress resultants to those from finite-element simulations. This grants further insight since the averaging nature of global values, such as buckling loads or natural frequencies, might yield valid results without capturing singular aspects precisely.

While the linear solution inspires only a single term of the employed trial function, further terms are required to satisfy the boundary conditions. Other nonlinear approaches, e.g. in [130], consider an additional quartic term in consequence of a uniformly applied pressure, but here any loading is absent in the inverted state: thus, there is no other reference point for the choice of mode shapes. An alternative approach might take its inspiration from shallow shell theory in §5, but more intricate Bessel functions would severely complicate to obtain closed-form solutions, and thus polynomials are the matter of choice to approximate the solution. Terms of integer power approach are not considered, since these would be equivalent to terms in Eqn (6.6) for specific β values. Consequently, the solution quality would deteriorate due to unsatisfied boundary conditions or a reduction of degrees of freedom in these particular cases. In order to address these shortcomings, the following simple series is assumed:

$$w = A_0 + A_1 \rho^{1+\sqrt{\beta}} + \eta_2 \rho^{2+\sqrt{\beta}} + \eta_3 \rho^{3+\sqrt{\beta}} + \eta_4 \rho^{4+\sqrt{\beta}} \quad (6.10)$$

with the dimensionless radius, $\rho = r/a$, as before, and, in total, five constants, A_i and η_i . The first two, A_1 and A_2 , are used to satisfy the boundary conditions of $w(\rho = 1) = 0$ and a vanishing radial bending moment at the edge, whilst the remaining constants, η_1, η_2, η_3 serve as degrees of freedom. The formulas for A_i as well as the further particulars of the derivation of the Airy stress function are given in the appendix. By considering more than one degree of freedom, some latitude is given to mitigate the penalty of using a reasonable approximation rather than the (unknown) exact function. This increases the robustness of the methodology and allows us to cover a wider range of varying parameters.

The relevant homogeneous solution of the Airy stress function, $\Phi_h = C_1 a^2 \rho^{1+\sqrt{\beta}}$ indicates that bending and stretching stresses exhibit qualitatively similar singularities at the centre. The constant C_1 is used to satisfy the boundary condition of an in-plane spring-supported edge of stiffness k_u as specified in Eqn (5.15a). As described in §5, it tends in its limits to be either a roller-supported boundary ($k_u = 0$) or a fixed-pinned edge ($k_u \rightarrow \infty$). After substituting the solution of C_1 (see appendix), the stress and strain resultants only depend on the remaining unknowns, η_1, η_2 and η_3 , and thus, the strain energy functional can be calculated and minimised according to the procedure in Eqns (5.18)-(5.20).

6.3 Nonlinear Solution for Shallow Planform Annuli

Even though annuli do not encounter central stress singularities, a thorough choice of the assumed deflection field is required. Following the same reasoning as before, the linear equilibrium solution in Eqn (6.6) is used as a part of the solution space, which now permits the usage of a second term, $A_2 \rho^{1-\sqrt{\beta}}$.

Since polynomials with negative powers are permissible now, the number of possible mode shapes increases. Choosing a similar series as in Eqn (6.10) with $\rho^{i\pm\sqrt{\beta}}$ would, in general, violate the boundary condition of $u_r = 0$ for $\nu \neq 0$, and thus a slightly different approach is employed where:

$$w = \eta_2 \rho^{1-2\sqrt{\beta}} + \eta_1 \rho^{1-\sqrt{\beta}} + A_0 + A_1 \rho^{1+\sqrt{\beta}} + A_2 \rho^{1+2\sqrt{\beta}} + A_3 \rho^{1+3\sqrt{\beta}}. \quad (6.11)$$

Four out of the six constants are used to satisfy the boundary conditions of a hinged outer edge ($r = a$) and a free inner edge ($r = b$)

$$w|_{\rho=1} = 0 \quad , \quad m_r|_{\rho=1} = 0 \quad , \quad m_r|_{\rho=b/a} = 0 \quad \text{and} \quad q_r|_{\rho=b/a} = 0, \quad (6.12)$$

leaving the system with two degrees of freedom, η_1 and η_2 ; $A_0 - A_3$ are given in the appendix. Further terms are not considered, since the increased number is simply not required in most cases and including an additional degree-of-freedom significantly deteriorates computational efficiency, since the deflection function is squared twice: once when computing the Airy stress function and the second time when calculating the stretching energy. The procedure of the preceding section can straightforwardly be extended to negative powers to compute the corresponding Airy stress

function that is compatible with the assumed deflection field. The constants of $\Phi_h = C_1 a^2 \rho^{1+\sqrt{\beta}} + C_2 a^2 \rho^{1-\sqrt{\beta}}$ are used to ensure that the free inner and outer edge conditions, $\sigma_r(b) = 0$ and Eqn (5.15a), respectively, hold; details of the calculation are given in the appendix. In order to identify alternative stable configurations, the energy minimising procedure of the previous chapter is employed.

6.4 Results

First, a quantitative analysis of stiffeners is presented in §6.4.1, before a detailed analysis of the effects of polar-orthotropic materials on the inverted shape and stress resultants is given in §6.4.2. In §6.4.3, the minimum apex height required for a stable inversion as a function of the orthotropic ratio is analysed and simplifying one-term approaches that capture this threshold in closed form are presented. The results obtained inspired to think of shells with extreme orthotropic ratios in a geometrically decoupled way and a straightforward explanation is provided by using a beam analogy in §6.4.4. Eventually the effects of central holes in §6.4.5 are analysed to demonstrate a suitable method to avoid stress singularities.

6.4.1 Qualitative Influence of Stiffeners on Bistable Inversion

In general, separate β -values for stretching, β_s , and bending, β_b , need to be considered when stiffeners are added, since the stretching rigidity relates linearly to the cross-sectional height, whereas the flexural rigidity has a cubic relation. Since the internal bending stresses always try to overcome the stretching barrier by forcing the shell back to its initial configuration, stiffeners tend to erode bistability by increasing the bending rigidity disproportionately. For a quantitative analysis, one can calculate the out-of-plane solution including the assumed deflection field using β_b , while the homogeneous terms of the Airy stress function depend on β_s . The following quantitative analysis is conducted by using a unique value in bending and stretching, $\beta = \beta_s = \beta_b$, since the aim is to analyse the effects of variations in the directional stiffness in isolation. If, however, a detailed analysis is desired, the orthotropic parameters may be approximated in view of the comparatively small width of each stiffener by only considering the stiffeners in their longitudinal direction since stresses cannot effectively build up in its orthogonal

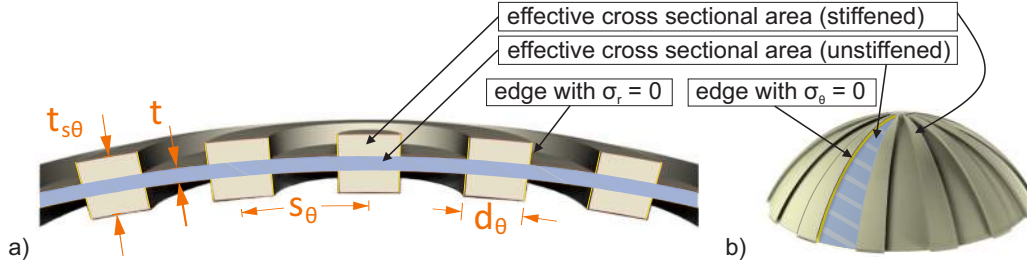


Figure 6.2: (a) Sectional view of a circumferentially stiffened shell: approximated effective areas in radial (blue hatched) and circumferential direction (beige + blue hatched). The stiffened area is neglected in radial direction, since stresses cannot evenly distribute through the stiffener's width due to the free edge boundary conditions of $\sigma_r = 0$ (yellow lines). (b) Full view of a radially stiffened shell: highlights exemplify now the effective area in circumferential direction (blue hatched) and the free edge condition $\sigma_\theta = 0$ (yellow); here, the full cross-section of ribs is only considered during the calculation of the smeared stiffness in radial direction. For these stiffeners, the nomenclature of the values t_{sr} , d_r and s_r is analogous to the one in circumferential direction, see (a).

direction (*cf.* Fig. 6.2), which leads to [15]:

$$\beta_s \approx \frac{\frac{t}{1-\nu^2} \left(1 - \frac{d_\theta}{s_\theta}\right) + t_{s\theta} \frac{d_\theta}{s_\theta}}{\frac{t}{1-\nu^2} \left(1 - \frac{d_r}{s_r}\right) + t_{sr} \frac{d_r}{s_r}} \quad \text{and} \quad \beta_b \approx \frac{\frac{t^3}{1-\nu^2} \left(1 - \frac{d_\theta}{s_\theta}\right) + t_{s\theta}^3 \frac{d_\theta}{s_\theta}}{\frac{t^3}{1-\nu^2} \left(1 - \frac{d_r}{s_r}\right) + t_{sr}^3 \frac{d_r}{s_r}}. \quad (6.13)$$

6.4.2 Quantitative Analysis:

Inverted Shapes and Corresponding Stress Resultants

Analytical (lines) and FE predictions (dots) of stable inverted configurations for pinned and roller-supported shells are depicted in Fig. 6.3(a) and (b), respectively, for the indicated values of β . The finite element simulations were conducted with *ABAQUS* [123] by employing the overseeing Python routine described in §5.3.1; see [139] for details of the numerical analysis.

All shells have the same initial height of $\omega_M^0 = 4$, which ensures that all cases in (a) exhibit bistability, where roller-supported shells of that height are only bistable for the range $0.5 < \beta < 6.1$. For $\beta < 1$, displacements are more focussed at the centre, and increasing β shifts the deformation towards the outer regions, so that shells with $\beta \gtrsim 3$ evince an inflexion point viz. a central dimple. Both responses are also observed in the stiffened shells in Fig. 6.1(d) and (b)/(c), respectively. Note that smaller β -values do not always correspond with larger central deformations, since the roller-supported

case with $\beta = 0.5$ has a decreased, yet centrally more focussed, deformation than the corresponding isotropic case. While a concentrated deformation points towards highly stressed areas, the barely deformed central region of the dimple indicates low bending stresses. Correspondingly, the resulting stresses, depicted by full lines in Fig. 6.4 for $\beta = 0.1, 0.5, 1, 5, 10$, are absent at the very centre for $\beta > 1$. These are in good agreement with FE results (dots), whereas even a *higher-order* approach of integer power as discussed in §5 (dashed line) shows slight deviations; note that lower-order integer approaches from literature that apply simpler basis functions to polar-orthotropic shells, *e.g.* [133–135], lead to less accurate results. A transition point with finite central stresses is encountered for the degenerated case of $\beta = 1$, where the integer power approach coincides with the basis functions of the presented approach in Eqn (6.10). Below this value ($\beta < 1$), FE calculations confirm induced stress singularities in bending and stretching, which are accurately captured by the presented analytical model using Eqn (6.10). It now becomes apparent that integer power approaches are inferior since they only capture singularities in stretching but not in bending, which underestimates peak stresses. The loss of accuracy cannot be overcome by increasing the number of degrees of freedom since the polynomial order does not match. A closer inspection of the central region in a doubly logarithmic plot of m_θ in Fig. 6.5 shows that the use of real powers in Eqn (6.10) accurately captures the asymptotic behaviour for $\rho \ll 1$, where the approximately linear relation in the diagram confirms the dominating influence of the $\rho^{-1+\sqrt{\beta}}$ term. This insight motivates a simplified approach which solely

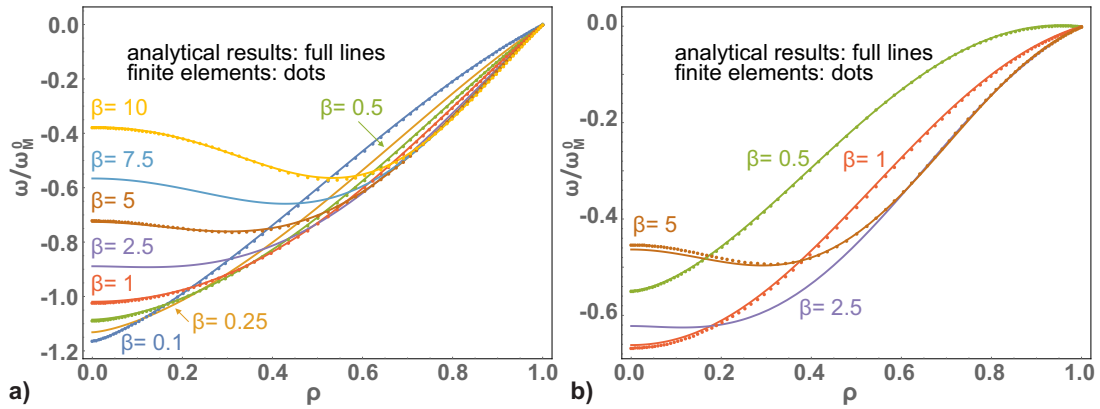


Figure 6.3: Sectional view of stable inverted shapes normalised by height of initial rise, $\omega_M^0 = 4$, for (a) fixed-pinned and (b) roller-supported edges with $0.1 \leq \beta \leq 10$ for $\nu = 0$. FE results (dots) for $\beta = 0.1, 0.5, 1, 5, 10$ are compared to analytical predictions with three degree of freedom (full lines) that are also given for intermediate values; missing results in (b) for $\beta < 0.5$ or $\beta > 6.1$ do not possess a stable inversion.

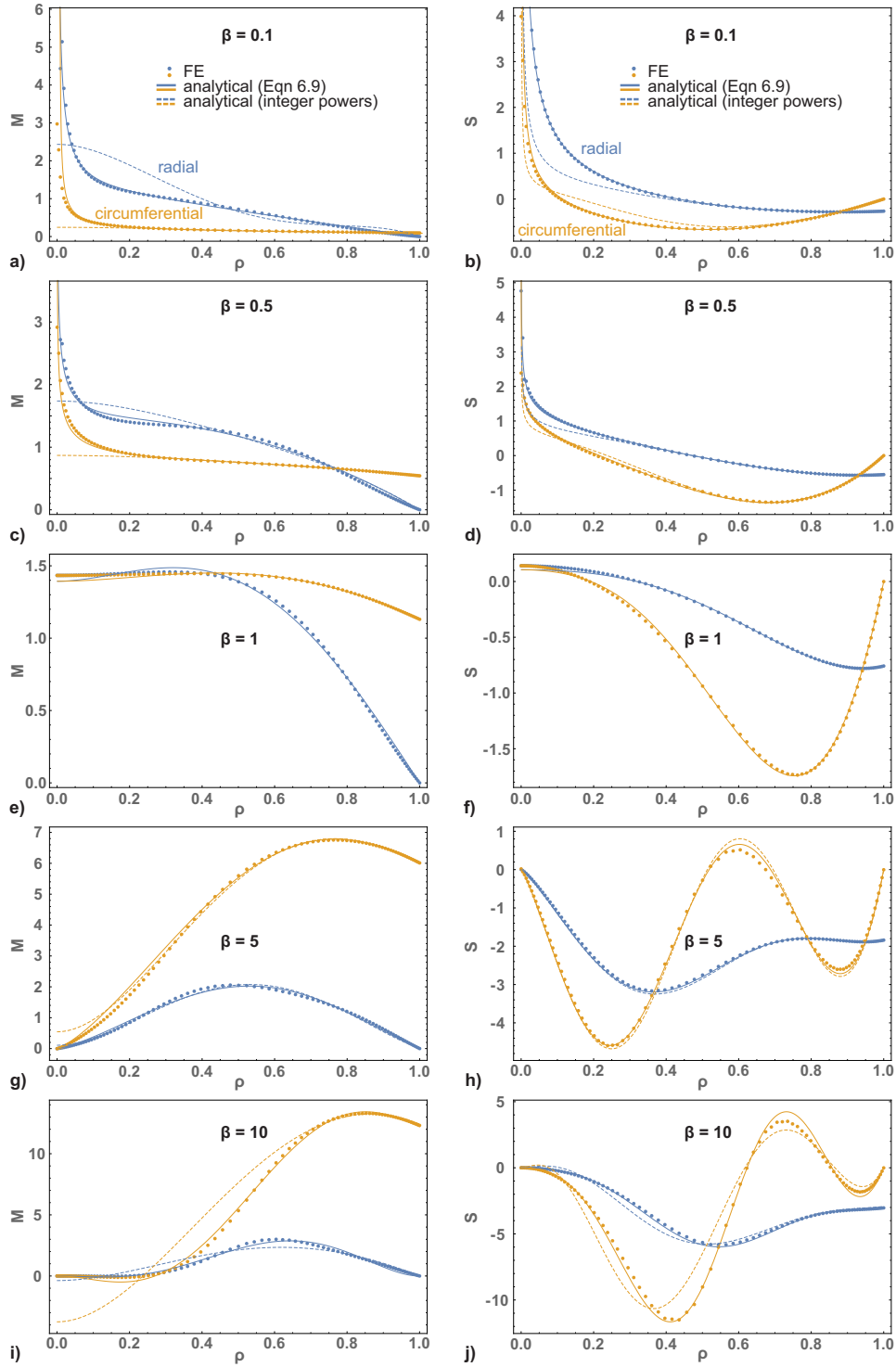


Figure 6.4: Dimensionless bending stress ($M = m/[Et^3]$, left) and membrane stress resultants ($S = \sigma/[Et^3]$, right) for differing stiffness-ratios of a fixed-pinned shell with $\omega_M^0 = 4$ and $\nu = 0$. FE values (dots) are compared to analytical predictions (full lines) according to a model with three degrees of freedom; dashed lines illustrate the shortcomings of integer-power approaches which fail to reflect the central stress singularities

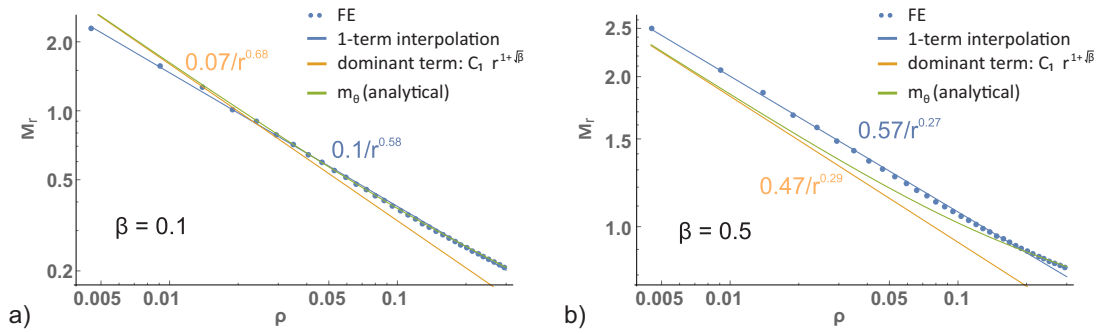


Figure 6.5: Finite element results (dots) of radial bending moments in inverted configuration on doubly logarithmic scale with linear-reciprocal regression (blue line) compared to dominant term, $C_1 \rho^{-1+\sqrt{\beta}}$, (orange) of m_θ (green) for $\beta = 0.1$ and $\beta = 0.5$ with $w_M^0 = 4t$, $\nu = 0$ and fixed-pinned edges.

depends on this term, which knowingly ignores the boundary conditions of a vanishing edge moment. While it is not expected to depict the stress resultant accurately everywhere, it can be employed to approximate the stability threshold in the following section. Insofar it can be regarded as a polar-orthotropic equivalent to the uniform curvature assumption.

6.4.3 Minimum Apex Height Required for Bistable Inversion: Refined Approaches and Simplifications

The threshold for bistable inversion in terms of the nondimensional initial apex height as a function of β is given for various choices of the deflection field in Fig. 6.6 for roller-supported (top) and pinned edges (bottom). In general, in-plane supports strongly favour bistable inversion, which confirms the observations in §5. More interestingly, the influence of the stiffness ratio differs significantly, depending on the support conditions. For a pinned edge, smaller values of β seem to generally favour bistable inversion, whilst the same values for roller-supported shells hamper and eventually erode bistable behaviour altogether. A global minimum in the latter case is found for $\beta = 3.2$, which coincides approximately with the β -ratio at which the deflection field is about to first form an inflexion point in Fig. 6.3.

In terms of computational accuracy, the results are virtually indistinguishable from FE results, with an average deviation of 0.35% whereas the FE accuracy range was set to 0.25%. The approximation is superior to results obtained by adapted lower-order models from the literature with a single degree of freedom *e.g.* by Dumir [130], which

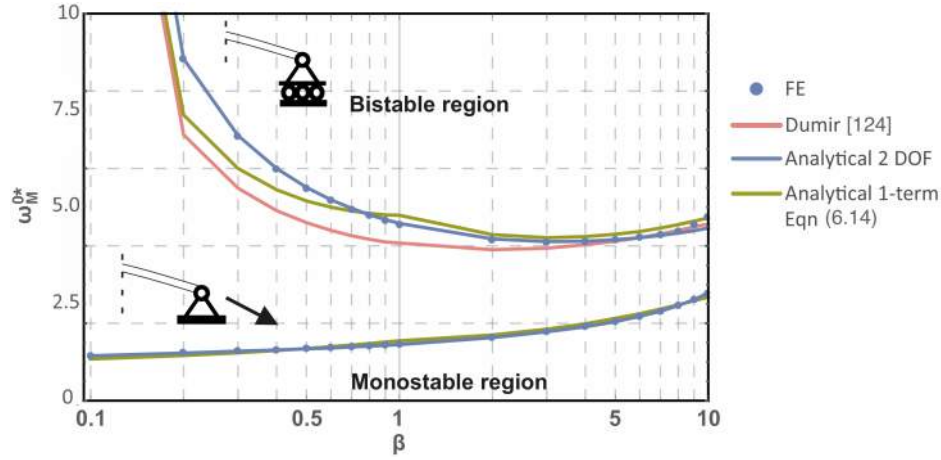


Figure 6.6: Predictions of the critical dimensionless initial apex height, ω_M^{0*} , over stiffness ratio, β , for roller-supported (top) and fixed-pinned supports (bottom) for $\nu = 0.3$. Full lines indicate analytical predictions, whilst dots represent results from FE simulations. For pinned supports only the current approach in Eqn (6.10) and the simplified one-term approach according to Eqn (6.14) are compared to FE results for the sake of clarity.

shows an average deviation of 5.2%. Closed-form solutions are found with simplifying one-term assumptions of $w = \eta_1 \rho^{1+\sqrt{\beta}}$ for $\beta < 1$ and $w = \eta_1 \rho^2$ for $\beta \geq 1$:

$$\begin{aligned}
 \left(\omega_M^{0*}\right)^2 &= \frac{(1+\sqrt{\beta})^4(2+\sqrt{\beta})(2-\nu+5\sqrt{\beta})}{3[16\beta^{3/2}+2\beta^2+\beta(20-8\nu)-(3-\nu)^2\sqrt{\beta}+2]} & \text{for } \beta < 1 \\
 \left(\omega_M^{0*}\right)^2 &= \frac{(3+\sqrt{\beta})^2(1+2\nu+\beta)}{2[\beta+6\sqrt{\beta}-\nu(\nu-6)]} & \text{for } \beta \geq 1
 \end{aligned}
 \left. \vphantom{\begin{aligned} \left(\omega_M^{0*}\right)^2 &= \frac{(1+\sqrt{\beta})^4(2+\sqrt{\beta})(2-\nu+5\sqrt{\beta})}{3[16\beta^{3/2}+2\beta^2+\beta(20-8\nu)-(3-\nu)^2\sqrt{\beta}+2]} \\ \left(\omega_M^{0*}\right)^2 &= \frac{(3+\sqrt{\beta})^2(1+2\nu+\beta)}{2[\beta+6\sqrt{\beta}-\nu(\nu-6)]} \end{aligned}} \right\} \text{pinned}$$

$$\begin{aligned}
 \left(\omega_M^{0*}\right)^2 &= \frac{(1+\sqrt{\beta})^4(2+\sqrt{\beta})}{3(\beta-\sqrt{\beta}\nu)} & \text{for } \beta < 1 \\
 \left(\omega_M^{0*}\right)^2 &= \frac{(3+\sqrt{\beta})^2(1+2\nu+\beta)}{2(\beta-\nu^2)} & \text{for } \beta \geq 1
 \end{aligned}
 \left. \vphantom{\begin{aligned} \left(\omega_M^{0*}\right)^2 &= \frac{(1+\sqrt{\beta})^4(2+\sqrt{\beta})}{3(\beta-\sqrt{\beta}\nu)} \\ \left(\omega_M^{0*}\right)^2 &= \frac{(3+\sqrt{\beta})^2(1+2\nu+\beta)}{2(\beta-\nu^2)} \end{aligned}} \right\} \text{rollers}.$$
(6.14)

These results emphasise the importance of the transition around $\beta = 1$: for small values, the deflection is governed by the homogeneous term of the linear bending solution, $\eta_1 \rho^{1+\sqrt{\beta}}$, and the singular stress field has a decisive influence on the bistable response; for $\beta > 1$, however, the averaging nature of a uniform curvature approach is suitable to predict the stability threshold for $\beta \geq 1$. This is insofar surprising, as the clearly nonuniform displacement field in Fig. 6.3 does not reflect its assumed uniform curvature and furthermore, the assumed quadratic deflection term causes shear stress singularities at the centre even for $\beta > 1$. Note that the fair agreement of the UC approach in its invalid regime (dashed line, $\beta < 1$) in the roller-supported case is coincidental and was not observed for other Poisson's ratios than $\nu \approx 0.3$.

A major finding is that the influence of the stiffness ratio differs significantly, depending on the support conditions. For a pinned edge, smaller values of β seem to generally favour bistable inversion, whilst the same values for roller-supported shells hamper and eventually completely erode bistable behaviour. A global minimum in the latter case is found for $\beta = 3.2$, which coincides approximately with the β -ratio at which the deflection field is about to first form an inflexion point in Fig. 6.3(b).

6.4.4 Beam Analogy

The influence of the boundary conditions on bistability is elucidated by considering the limits of $\beta \rightarrow \nu^2$ and $\beta \rightarrow \infty$: If $\nu = 0$ is assumed for simplicity, the circumferential stiffness tends towards zero and the first two terms of the compatibility equation, Eqn (6.8), tend to infinity in the limit of $\beta \rightarrow 0$. Hence, even large changes in Gaussian curvature do not evoke any stresses. This is reasonable, since the shell is virtually free to expand or contract in circumferential direction, and thus, the load path aligns with the stiff radial direction. Consequently, the shell's response resembles the one of symmetric beams with a wedge-planform with vanishing width at the centre, similar to the shape of a single stiffener in Fig. 6.2(b). The compatibility equation then becomes a simplified version of Eqn (6.9):

$$\sigma_r = \frac{\Phi'}{r} = \frac{1}{2} \left(\frac{d(w + w^0)}{dr} \right)^2 - \frac{1}{2} \left(\frac{dw^0}{dr} \right)^2. \quad (6.15)$$

and reflects the entirely geometric strain relation in Eqn (5.9) without hoop-interaction. The singularities arise because the area of the tapered cross section vanishes at the centre, even though the radial *force* is well defined. Interestingly, the bistable threshold of fixed-pinned shells with $\beta = 0.1$ precisely matches the threshold of fixed-pinned beams, $\omega_M^{0*} = 1.1$. The beam analogy gives a simple explanation for the observed trend in Fig. 6.6 for $\beta \ll 1$: an initially curved beam with fixed-pinned supports has a lower threshold than isotropic shells, whereas a beam on rollers does not possess an alternative stable equilibrium configuration.

This decoupled perspective also points towards ways to improve the bistable behaviour of shells in response to their particular boundary conditions. In roller-supported shells, an increase of the hoop stiffness assists the shell to form a stretching barrier required to prevent a bending recovery to the initial configuration, and an optimum value that minimises ω_M^{0*} is found to be $\beta \approx 3.2$. Hence, the bistable performance of

an isotropic shell can be improved by a moderate increase of the hoop stiffness. Interestingly, a similar trend is not observed in fixed-pinned shells that exert a contrasting influence. With respect to the hoop stiffness, it can be concluded: whilst vital in case of roller supports, it becomes redundant and even slightly hindering once a stabilising radial force is assured by an immovable support.

In the case of $\beta \rightarrow \infty$, the radial stiffness becomes negligibly small, but unlike before, the equations are not entirely decoupled, since the shell may be imagined as multiple adjacent ring beams, and thus, the radial displacements interact with circumferential strains via $\varepsilon_\theta = u/r$. This interaction ensures a certain degree of statical indeterminacy and hence, a bistable response in roller-supported shells is observed even for large values of β .

6.4.5 Bistable Inversion of Planform Annuli

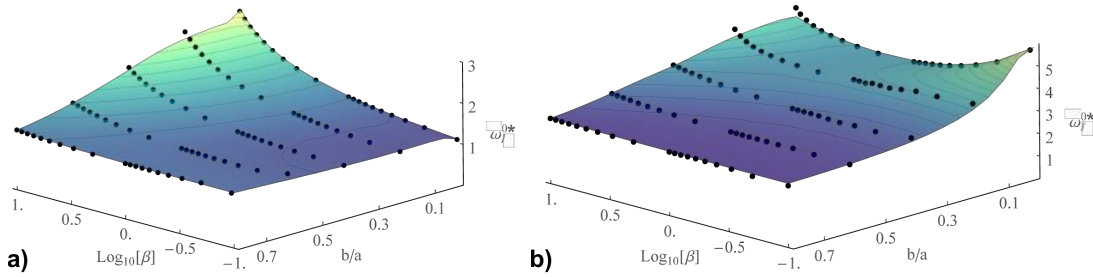


Figure 6.7: Stability map of critical initial dimensionless physical height, ω_I^{0*} , over central hole size, b/a , and stiffness ratio, β , with $\nu = 0$ for (a) fixed-pinned and (b) roller-supported edges; dots indicate FE results

The influence of a central hole on the critical minimum *physical* height required for bistable inversion, $\omega_I^{0*} = (1 - b^2/a^2)\omega_M^{0*}$, as a function of β is presented in Fig. 6.7 for (a) fixed-pinned and (b) roller-supported edges. For a more open perspective on both plots, the axes have been reversed in both plots and the values of $\log_{10}\beta$ have been plotted that cover the same range as before ($0.1 \leq \beta \leq 10$). Note that the smallest hole size calculated with annular model was $b/a = 0.05$; the results of the closed shell model have been added for $b/a = 0$ and intermediate values were linearly interpolated; hence, slight kinks are observed in the transition zone. These are owed to the slightly different choice of basis functions; for $\beta < 1$, the additional challenge to approximate local stress peaks in the proximity of a free edge boundary condition arises. The influence of the

Poisson's ratio is not studied here, since it was subject of the analysis in §5.3.5; instead, ν is set to the value at which it had the lowest influence ($\nu = 0$). Here, the focus is on the interdependency of the stiffness ratio β and the hole size, b/a , with respect to their effect on the critical height for bistable inversion, ω_I^{0*} . Note that a value of $\beta = 0.1$ is now further away from its theoretical minimal value, 0, than in the previous case, where $\beta > \nu^2 = 0.09$, and thus, it has a less hindering influence on bistability. In fixed-pinned shells, see Fig. 6.7(a), the hole size and the orthotropic ratio correlate positively with the bistable threshold. Hence, the smallest required height is found in a full plate with $\beta \rightarrow 0$. In contrast to bistable isotropic shells, creating a hole requires for small values of β a slight increase of the physical height; however, even for largest holes, the bistable threshold changes only by 12 %, and thus, stress singularities can easily be prevented by cutting a hole, or alternatively, allowing plastic deformations in the central region. In roller-supported shells, (b), with small hoop stiffness, bistability can be significantly enhanced by removing a small central region, *e.g.* a hole of $b/a = 20$ % reduces ω_I^{0*} by over 30 % for shells with $\beta = 0.1$, whilst an isotropic shell improves only by 3 % when a hole of the same size is created.

For large hole-sizes shell ($b/a > 0.5$), the structure resembles a (doubly) curved beam with abating radial stresses. Since the structure is already 'decoupled' geometrically, the radial stress components are of diminished relevance even for $\beta = 1$, and thus, the same is true for the orthotropic ratio in general; hence, results similar to the isotropic case in §5.3.5 are found.

6.5 Summary

The higher-order geometrically nonlinear Ritz approach of §5 has been extended for polar-orthotropic constitutive equations. It was employed to analyse the effects of variations of the directional stiffness via the parameter $\beta = E_\theta/E_r$. The analytical model employed an assumed deflection field that is based on the linear solution of a bent plate, and its predictions appropriately captured central stress singularities for high radial stiffnesses ($\beta < 1$). This finding has demonstrated the superiority in comparison to other analytical approaches in literature that utilise polynomial deflection fields of integer power: whilst the stability threshold can also be captured accurately by the latter, these fail to depict bending stress singularities that may constitute a decisive factor in a structure's design process.

The developed model was then employed to study how the critical apex height required for bistable inversion is affected by variations in β . While the derived higher-order approach precisely portrayed the finite element reference solution, simplified averaging single-term approaches have reasonably approximated the bistable threshold in closed form, even though they fail to predict stress resultants appropriately. A key finding is that the bistable response strongly depends on the in-plane boundary conditions. Less surprisingly, the tendency of §5 regarding the enhancement of bistability via fixed-pinned edges has been confirmed in all discussed examples. More interestingly, it was shown that the support conditions significantly affect the influence of other parameters, such as β and the hole size: in contrast to roller-supported shells, where no alternative equilibrium configurations were found for $\beta \rightarrow 0$, fixed-pinned shells showed the *lowest* required apex height. The difference is caused by a quasi-decoupling of the radial and circumferential response for very low values of the hoop stiffness, which causes the structure to evince a beam-like behaviour. The stiffness variation also elucidated the influence of the hoop stiffness on bistability: for roller supports, the presented study confirmed observations in literature [85] that identify its stabilising influence that prevents reversion. However, the opposite is true for the fixed-pinned case, where an increasing β -ratio hampers bistability. It is concluded that the circumferential stiffness is insofar stabilising as radial stresses arise from a strong coupling with a surrounding ring beam of a high stiffness. However, if radial stresses are assured by the support conditions, the hoop stiffness is a redundant feature that becomes a slight impediment. In order to circumvent stress singularities for $\beta < 1$, central holes were found to be suitable: while even large holes do not significantly increase the critical physical height of fixed-pinned shells, roller-supported ones were significantly more inclined to stay inverted once a circular hole measuring $\approx 20\%$ of the outer radius was created.

Chapter 7

Combined Actuation Methods

In this chapter, the presented analytical model is extended to explore ways to actively control shell structures. Employing actuators broadens possible areas of application by allowing engineers, for instance, to counteract external loads to minimise concomitant deformations. It is not a coincidence that nature inspired many active structures, since the sophistication of shape-changing capabilities in floral systems has a similar objective as modern multifunctional morphing structures. Leaves, for instance, grow into stiff non-Euclidean shapes of double curvature that maximise their surface area in order to optimise photosynthesis; nevertheless they are flexible enough to evade strong wind loads by rolling up rather than resisting them. Whilst leaves obtain their shape by spatially nonlinear extensional growth in direction of their mid-plane, other ‘solar-tracking’ plants, *e.g. Mimosa Pudica*, deform in bending by imposing a through-thickness strain gradient; recall Fig. 3.9. Growth, or actuation, can thus stem from in-plane or out-of-plane actions, whose interaction gives rise to a variety of solutions. In particular, well attuned, compatible actuation modes offer the theoretical possibility for large stress-free transformations, which are known as *natural growth modes* [49].

Here, a theoretical framework for making use of the synergies of both methods is developed: in-plane actuation patterns are investigated in combination with a simultaneously imposed linear through-thickness strain gradient profile, which are both free to vary locally throughout the shell’s domain. Since floral shapes are versatile and not confined to synclastic geometries – some even show repetitive undulations, see Fig. 7.1 and [140, 141] for related studies – the assumption of rotational symmetric deformations is relaxed. However, growth processes are a complex matter: the current stress state, for instance, affects not only where new material is added, but also the



Figure 7.1: Non-Euclidean geometries in nature: (a) Elliptic example of *Euphorbia characias subsp. wulfenii* with approximately rotationally symmetric outer petals. (b,c) Hyperbolic examples: saddle-shaped petals of *Bergenia ciliata* (b), and leaves of *Brachyglottis monroi* with higher wave number.

amount of cellulose fibres, which correlates with the stiffness, and additionally, juvenile leaves may grow differently than adult leaves. Such important subtleties result from millions of years of evolution and their modelling would involve a refined analysis of bio-chemical processes on smaller scales.

It is acknowledge here that nature is too sophisticated, adroit and elegant to employ solutions that are solely based on structural mechanics, and thus, the aim of this study is not to explain *why* leaves obtain a certain shape. Instead, inspiration is taken from floral growth processes to present a simplified model that mimics observed shapes. It assumes an initially flat circular plate made from an isotropic linear elastic material that is subjected to polynomial growth patterns. The imposed strains are *inelastic*, since they do not directly evoke stresses as a reaction (similar to a thermal load-case), but if such expansions or contractions are restricted either by support conditions or by an internal incompatibility, an elastic reaction arises.

Whilst the latter aspect has been analysed for growth patterns of uniform Gaussian curvature in free-standing shells, the investigation of the interaction with extensional in-plane spring supports at a shell's rim presented here is completely novel. The over-constrained environment enriches the solution and requires a refined perspective that goes beyond an analysis of a shell's internal compatibility between the bending and stretching surface. The additional displacement compatibility condition necessitates a distinction between two different in-plane actuation methods that induce non-Euclidean target geometries using a quadratic strain-field in either the radial *or*

circumferential direction. In addition, the interaction is enhanced by imposing an extra uniform constant expansion term and a radial force applied to the shell edge. Manipulations of buckling thresholds and the post-buckling behaviour within all of these specifications are analysed in detail by employing a uniform curvature approach, where in particular the conditions for natural growth modes are established.

A second novel aspect was inspired by the recent development of elaborated actuators, *e.g.* the possibility of 3D printing gels with tailored expansion coefficients [101, 102] in Fig. 3.10-3.11: these make it possible to impose arbitrary growth strains and thus also an actuation of nonuniform Gaussian curvature, which gives rise to, in particular, hyperbolic periodically varying out-of-plane target shapes. The present study investigates also an *unsupported* shell subjected to growth strains with spatial variations of higher-order polynomials. The requirements for natural growth into such hyperbolic shapes are analysed before ways to obtain similar transformations by leaf-like in-plane actuation alone are explored. The concomitant richer stability landscape that involves secondary buckling requires the employment of a higher-order model.

In the following, the, in general, non-rotationally symmetric analytical model for actuated shells is described in §7.1. The obtained results are discussed in §7.2 and compared to FE reference solutions. Finally, a summary is given in §7.3.

7.1 Analytical Model

For analysis, the same cylindrical coordinate system, (r, θ, z) , as in the previous two chapters is employed to describe an isotropic shallow shell in terms of the familiar parameters, a , t , E and ν . The consideration of the actuation parameters requires to distinguish between three different configurations as illustrated in Fig. 7.2: the initial stress-free state, Ω^0 , a *target shape* of the actuation, Ω_A , which is in general not observable except when elastic responses are absent, and finally, the resulting shape, Ω . The transition of a material point from the first to the second configuration is described via actuation-related displacements, \mathbf{u}_A , whilst elastic displacements, \mathbf{u}_E express the deformation in between the target and resulting shape; their sum, \mathbf{u} , describes the observed transformation from Ω^0 to Ω . Similarly, the total strains are expressed via the sum of both subsets, *e.g.* $\varepsilon_r = \varepsilon_{rA} + \varepsilon_{rE}$. Without the loss of generality, the initially stress-free configuration is assumed to be a flat plate, ($w^0 = 0$). The approach is never-

theless capable of considering initially curved examples by letting the shell morph into the desired shape via superposed natural growth modes, which are discussed later.

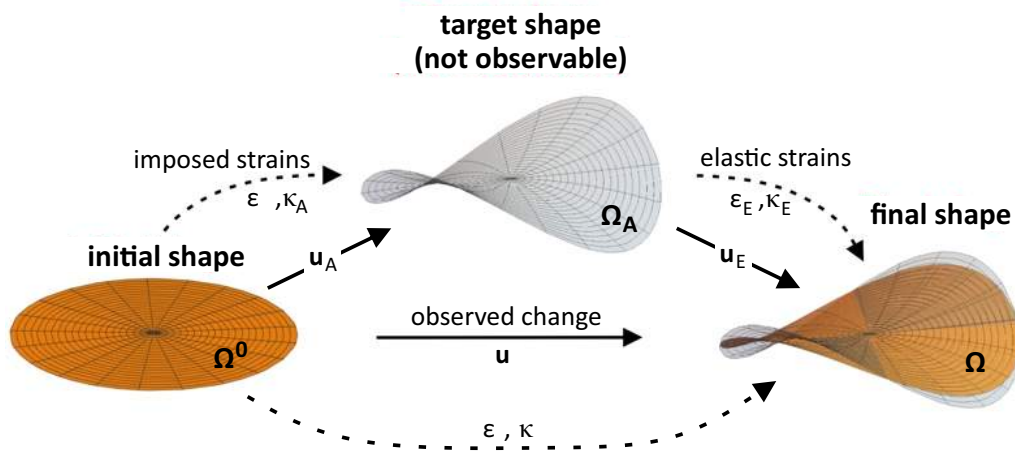


Figure 7.2: The mathematical model distinguishes between three configurations: the stress-free initial shape, Ω^0 , a target shape of the imposed actuation strains, Ω_A , and the observable resulting shape, Ω . Values with an index ‘E’ or ‘A’ refer to elastic responses or imposed values due to actuation, respectively.

Whilst rotationally symmetric deformations simplified the compatibility equation to an ordinary differential equation, the present case involves circumferential variations that require a consideration of all three nonlinear terms of the FvK strain definitions,

$$\begin{aligned} \varepsilon_r &= \frac{\partial u}{\partial r} + \frac{1}{2} \left(\frac{\partial w}{\partial r} \right)^2, & \varepsilon_\theta &= \frac{u}{r} + \frac{1}{r} \frac{\partial v}{\partial \theta} + \frac{1}{2} \left(\frac{\partial w}{r \partial \theta} \right)^2, \\ \text{and } \varepsilon_{r\theta} &= \frac{1}{2} \left(\frac{\partial u}{r \partial \theta} + \frac{\partial v}{\partial r} - \frac{v}{r} + \frac{\partial w}{r \partial \theta} \frac{\partial w}{\partial r} \right), \end{aligned} \quad (7.1)$$

where circumferential displacements are denoted by v .

In the context of combined actuation, it is convenient to think of a shell as two different surfaces: one that solely bends and another one that only stretches (recall §2.3); quantities related to one surface are denoted by a lower index ‘B’ and ‘S’, respectively. According to Calladine [18], the Gaussian curvature of the bending surface acts like a ‘*forcing term*’ on the stretching surface and vice versa. Hence, it is the incompatibility of actuation modes with respect to their change in Gaussian curvature that triggers an elastic reaction that eventually enforces compatibility of the resulting shape via $g_B = g_S$. This incompatibility is expressed by $\Delta g_A = g_{BA} - g_{SA}$, which denotes the

difference of the changes in Gaussian curvature caused by actuation. Consequently, imposed isometric deformations of one surface do not affect the counterpart, and thus do not directly evoke an elastic response; conversely, non-isometric stress-free deformations are possible when the actuation patterns of both surfaces are geared to each other. This becomes apparent, when the linear nature of the intrinsic definition of the Gaussian curvature is considered, which reads for non-axisymmetric deformations in polar coordinates [13]:

$$g_S = \frac{1}{r} \left(\frac{\partial \varepsilon_r}{\partial r} - \frac{\partial^2 (r \varepsilon_\theta)}{\partial r^2} - \frac{1}{r} \frac{\partial^2 \varepsilon_r}{\partial \theta^2} + \frac{\partial}{\partial \theta} \left(\frac{\varepsilon_{r\theta}}{r} \right) + \frac{\partial^2 \varepsilon_{r\theta}}{\partial r \partial \theta} \right). \quad (7.2)$$

The contribution of the imposed mid-plane strains, g_{SA} , and the elastic mid-plane strains, g_{SE} , can thus be calculated separately by using the same formula with corresponding substitutions, and the total value within the plane is their sum, $g_S = g_{SA} + g_{SE}$. The same does not, however, hold for its extrinsic counterpart,

$$g_B = \kappa_r \kappa_\theta - \kappa_{r\theta}^2, \quad (7.3)$$

where a nonlinear interaction of elastic and actuated values ($\kappa = \kappa_A + \kappa_E$) is caused even in initially flat shells. By rewriting the compatibility equation as

$$g_B - g_{SA} = g_{SE}, \quad (7.4)$$

the forcing term of the elastic mid-plane response can be isolated on the right-hand side. This allows the calculation of the Airy stress function in the familiar manner via $\nabla^4 \Phi = -E(g_B - g_{SA})$. While the in-plane equilibrium of the elastic stresses is given by the Airy stress function, imposed strains, *e.g.* thermal heating, do not cause an immediate response via the material law, and hence $\Phi_E = \Phi$. Note that a potential formulation exists only for the elastic response, but not in general for the imposed strains of independent magnitude and direction.

The strain energy functional of an in-plane-supported shell of stiffness k_u now includes twisting terms:

$$\begin{aligned} \Pi = \frac{1}{2} \int_0^a \int_0^{2\pi} (m_r K_{rE} + m_\theta K_{\theta E} + m_{r\theta} K_{r\theta E}) r d\theta dr + a \int_0^{2\pi} \left(\frac{k_u u^2}{2} - n_r u \right) \Big|_{\rho=1} d\theta \\ + \frac{t}{2} \int_0^a \int_0^{2\pi} (\sigma_r \varepsilon_{rE} + \sigma_\theta \varepsilon_{\theta E} + \sigma_{r\theta} \varepsilon_{r\theta E}) r d\theta dr ; \end{aligned} \quad (7.5)$$

it also considers an additional term, n_r , that describes an outward pointing radial force per unit circumference, which introduces additional complexity to the solutions by triggering an elastic reaction without need of the forcing term related to g in Eqn (7.4). The strain energy functional can be calculated in closed form for suitable sets of functions for the deflection and actuation fields, which are described next. First, the case of imposed strains with positive Gaussian curvature is considered, before anticlastic actuation patterns are discussed.

7.1.1 Growth Modes of Constant Positive g_A : Rotationally Symmetric Deflections

Positive values of g_A without circumferential variations prescribe elliptic target shapes, and here, the analysis is restricted to those with a rotationally symmetric planform. Hence, the strain definitions simplify to the familiar form of Eqn (5.2). For the out-of-plane actuation mode, a function that produces a constant Gaussian curvature throughout the shell is considered:

$$w_A = \eta_A (1 - \rho^2), \quad (7.6)$$

where η_A specifies the magnitude with the physical interpretation of the midpoint deflection. One possible way to realise such actuation pattern is via a temperature gradient through thickness, and various alternatives have been presented in §3.

For simplicity, the shape function of the actuation pattern is also assumed for the elastic deflection field, $w_E = \eta_E (1 - \rho^2)$, and thus, a uniform curvature approach is employed. This assumes that the elastic response is also rotationally symmetric, even though it has been shown that buckling in which one direction of curvature is preferred may occur in response to such a bending actuation pattern [49]. However, in the present

case, such a deformation mode is prevented by vertical edge supports and potential concomitant higher-order buckling modes are not considered here, which leaves space for future explorations.

As discussed in §5, the UC assumption drastically simplifies the problem by ignoring edge effects, whilst satisfying the equilibrium conditions on average across the shell; in return, it allows one to obtain compact closed-form solutions for the buckling threshold and the post-buckled geometry. The corresponding changes in curvatures,

$$\begin{aligned} \kappa_r &= \frac{\partial^2 w}{\partial r^2} = \frac{2}{a^2} (\eta_E + \eta_A) , \\ \kappa_\theta &= \frac{1}{r} \frac{\partial w}{\partial r} + \frac{1}{r^2} \frac{\partial^2 w}{\partial \theta^2} = \frac{2}{a^2} (\eta_E + \eta_A) \quad \text{and} \quad \kappa_{r\theta} = \frac{\partial}{\partial r} \left(\frac{1}{r} \frac{\partial w}{\partial \theta} \right) = 0 \end{aligned} \quad (7.7)$$

are constant throughout the shell. They evoke bending stresses that solely depend on elastic strain components:

$$\begin{aligned} m_r &= D (\kappa_{rE} + \nu \kappa_{\theta E}) = \frac{2}{a^2} D (1 + \nu) \eta_E , \\ m_\theta &= D (\kappa_{\theta E} + \nu \kappa_{rE}) = \frac{2}{a^2} D (1 + \nu) \eta_E \quad \text{and} \quad m_{r\theta} = D (1 - \nu) \kappa_{r\theta E} = 0 ; \end{aligned} \quad (7.8)$$

the actuation strains may later cause an elastic response in order to enforce compatibility, though.

With respect to in-plane actuation, the analytical model considers a nonlinear in-elastic strain distribution that resembles commonly encountered but simplified growth patterns in nature:

$$\varepsilon_{rA} = \epsilon_r \rho^2 + \epsilon_0 \quad , \quad \varepsilon_{\theta A} = \epsilon_\theta \rho^2 + \epsilon_0 \quad \text{and} \quad \varepsilon_{r\theta A} = 0 . \quad (7.9)$$

The first two strain-parameters ϵ_r and ϵ_θ describe an orthotropic growth process of quadratic order, and ϵ_0 denotes an additional spatially constant isotropic growth strain similar to a uniform thermal expansion; according to Eqn (7.2), their corresponding Gaussian curvature amounts to $g_{SA} = 2(\epsilon_r - 3\epsilon_\theta)/a^2$, where ϵ_0 does not appear due to its isometry. By considering rotational symmetry and substituting the strain expressions in Eqn (7.2) with equivalent stresses before using $\sigma_r = 1/r \cdot \partial \Phi / \partial r$ and $\sigma_\theta = \partial^2 \Phi / \partial r^2$, the compatibility equation in Eqn (7.4) can be rewritten as:

$$g_B - g_{SA} = -\frac{1}{E} \left(\frac{\partial^4 \Phi}{\partial r^4} + \frac{2}{r} \frac{\partial^3 \Phi}{\partial r^3} - \frac{1}{r^2} \frac{\partial^2 \Phi}{\partial r^2} + \frac{1}{r^3} \frac{\partial \Phi}{\partial r} \right) . \quad (7.10)$$

The solution of this differential equation,

$$\Phi = \frac{E\rho^4}{32} \left(a^2(\epsilon_r - 3\epsilon_\theta) - 2(\eta_E + \eta_A)^2 \right) + C_1\rho^2, \quad (7.11)$$

possesses a constant of integration that is used to satisfy the boundary condition in Fig. 7.3: in order to guarantee a compatible radial displacement u at $\rho = 1$ with an in-plane spring of stiffness, k_u , and an outward pointing radial force per unit circumference, n_r , at the edge, the following condition must hold:

$$k_u u|_{\rho=1} = -t \sigma_r|_{\rho=1} + n_r. \quad (7.12)$$

The strain energy functional depends after this substitution solely on the only remaining unknown, η_E , and equilibrium configurations are determined by $\partial\Pi/\partial\eta_E = 0$. Their stability depends on the sign of $\partial^2\Pi/\partial\eta_E^2$, which changes at the resulting buckling-thresholds, as discussed in §7.2 in terms of the chosen actuation parameters as well as the boundary parameters.

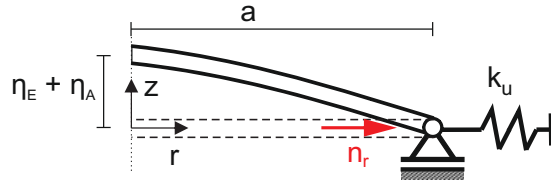


Figure 7.3: Rotationally symmetric spring-supported boundary with radial force acting on the shell edge.

7.1.2 Higher-Order Growth Modes Including $g < 0$

Actuation patterns

Actuation patterns that impose negative Gaussian curvature offer a richer behaviour that includes symmetry breaking buckling and more elaborate approaches are required. Inspired by wavy shapes of leaves, that result from in-plane growth, a simplified polynomial growth pattern is considered:

$$\epsilon_{rA} = \epsilon_{\theta A} = \epsilon \rho^m \quad \text{and} \quad \epsilon_{r\theta A} = 0, \quad (7.13)$$

where $m \geq 2$. The support conditions now also resemble floral systems in which a leaf is rigidly connected to the stem at a single point. Since gravity is not considered here, the fixed point can be assumed without a loss of generality at the plate's centre for the sake of simplicity. In contrast to the previous case, vertical supports are absent, and thus, the assumption of rotational symmetry is relaxed. Even though it would not significantly complicate the analytical methodology, isolated horizontal supports are not considered, since these are neither present in plants nor are these easily realisable in engineering applications.

Without them, the distinction between expansions in circumferential and radial direction is not required, since the only relevant parameter is the forcing term of the imposed Gaussian curvature of $g_{SA} = -\epsilon m^2 \rho^{-2+m}/a^2$. This actuation mode can be thought of as a locally nonuniform thermal in-plane expansion across the shell's domain. One way to realise such a pattern has been demonstrated in 3D printed disks made from swelling gels with a variable thermal expansion coefficient, in which a uniform heating causes nonuniform expansions [101, 102], see also §3.3. The target shapes can either be elliptic or hyperbolic when cooled ($\epsilon < 0$) or heated ($\epsilon > 0$), respectively. The latter case imposes an excess in circumferential expansions and induces periodic 'wavy' shapes.

The out-of-plane actuation pattern is chosen in such a way that it is capable of imposing a polynomial pattern of Gaussian curvature that matches the one evoked by the in-plane actuators in Eqn (7.13). However, finding the analytical expression for a shape for an arbitrary function of the Gaussian curvature is in general a nontrivial inverse problem. For polynomials however, it is straightforward to obtain the function via the following procedure: the simplest example of an anticlastic structure is a saddle, which is described by a pure twist that is given by $\rho^2 \cos(2\theta)$ in polar coordinates. By considering a generalisation of this case, $w_A = \eta_A \rho^i \cos(j\theta)$, all curvatures can be calculated according to Eqn (7.7) and Eqn (7.3). It can be shown that the Gaussian curvature does not vary in circumferential direction for $j = \pm i$, for which it takes a polynomial form: $g = -(i-1)^2 i^2 \eta_A^2 \rho^{2i-4}/a^4$. Thus, the actuation pattern is chosen to be

$$w_A = \eta_A \rho^i \cos(i\theta), \quad (7.14)$$

where continuity at $w_A(\theta = 0) = w(\theta = 2\pi)$ as well as the differentiability of w is guaranteed by choosing i as an integer greater than one. The realisation of such actuation patterns has to the knowledge of the author not been shown in practice, yet, but the

3D-printing method of Klein *et al.* [101] could be extended to introduce through thickness variations of the thermal expansion coefficient via a layered setup that accounts for such a periodic variation across the shell's domain.

Shape functions

A more elaborate deflection field is required here since the absence of rotational symmetry requires not only the radial bending moment, but also the twisting moment to vanish at the edge. The latter, however, is known to influence (bi-)stability thresholds significantly. In order to choose a set of shape functions that can adapt to several target shapes, anticlastic as well as synclastic functions, w_{g-} and w_{g+} , respectively, are considered as part of the elastic displacement field, $w_E = w_{g+} + w_{g-}$. Suitable choices for hyperbolic geometries are obtained by extending the actuation shape in Eqn (7.14) with a polynomial series of $(1 + C_1\rho^2 + C_2\rho^4)$ and determining the constants via the boundary conditions in order to obtain:

$$w_{g-} = \eta_i \rho^i \cdot \cos(i\theta) \left(1 - 2 \left(1 - \frac{2(3+i)}{3+3\nu+4i+i^2} \right) \rho^2 + \frac{1-3\nu-i^2}{3+3\nu+4i+i^2} \rho^4 \right), \quad (7.15)$$

with an integer $i > 1$ as before. By neglecting the circumferential variations in the same trial function, appropriate elliptic shape functions are found:

$$w_{g+} = \eta_0 \rho^2 + \eta_1 \rho^4 - \left(\frac{\eta_0(1+\nu) + \eta_1 2(3+\nu)}{3(5+\nu)} \right) \rho^4, \quad (7.16)$$

where two degrees of freedom, η_0 and η_1 arise, since the twisting condition is satisfied automatically. Since the approach is limited to only a few degrees of freedom, only the first two functions of w_{g-} are considered, see Fig. 7.4; higher-order one-term approaches may be used though to calculate the response in particular modes with a wave numbers greater than three.

Coupling with in-plane stretching

Even though the Gaussian curvature of each mode in isolation is constant in circumferential direction, the geometrically nonlinear mode interaction, *cf.* Eqn (7.3), introduces such variations nevertheless. In order to determine the corresponding stress function, a solution for a the general case of $\nabla^4 \Phi = \rho^i \cos(j\theta)$ without the requirement of $i = j$ is

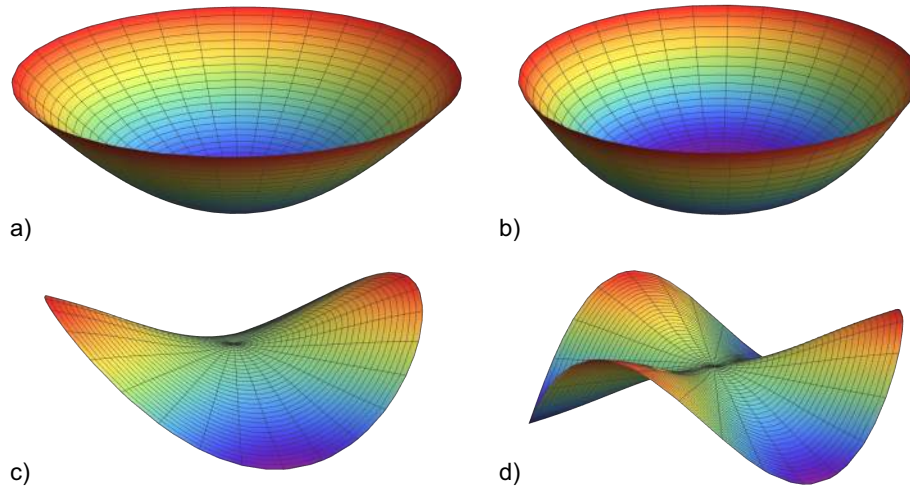


Figure 7.4: Elliptic (top) and anticlastic mode shapes (bottom): (a) and (b) illustrate a pure deformation of η_0 and η_1 according to Eqn (7.16), respectively, while the (c) and (d) show considered mode shapes of Eqn (7.15) with wave number of $i = 2$ and $i = 3$; colour indicates vertical displacement.

constructed. The terms of Gaussian curvature are sorted in a matrix, \mathbf{g}_{mn} , with respect to their polynomial order and wave number to apply a series solution: Michell [142] showed that the solution to the homogeneous problem, $\nabla^4 \Phi = 0$, gives

$$\begin{aligned}
 \Phi_h = & A_0 \log(\rho) + B_0 \rho^2 \log(\rho - 1) + C_0 \rho^2 + D_0 \theta \\
 & + \left(A_1 \rho + B_1 \rho^{-1} + B'_1 \theta \rho + C_1 \rho^3 + D_1 \rho \log(\rho) \right) \cos(\theta) \\
 & + \left(E_1 \rho + F_1 \rho^{-1} + F'_1 \theta \rho + G_1 \rho^3 + H_1 \rho \log(\rho) \right) \sin(\theta) \\
 & + \sum_{n=2}^{\infty} \left(A_n \rho^n + B_n \rho^{-n} + C_n \rho^{n+2} + D_n \rho^{-n+2} \right) \cos(n\theta) \\
 & + \sum_{n=2}^{\infty} \left(E_n \rho^n + F_n \rho^{-n} + G_n \rho^{n+2} + H_n \rho^{-n+2} \right) \sin(n\theta).
 \end{aligned} \tag{7.17}$$

This solution extends the rotationally symmetric case – where only A_0, B_0, C_0 arose – by similar terms that vary with θ . In the case of a closed cap, exponents ≤ 1 are energetically not permissible, and are thus ignored; the same holds for all components that contain $\log(\rho)$ -terms or depend on θ outside of a trigonometric function. The constants A_1 and E_1 are irrelevant since they do not evoke any stresses. Thus, the

homogeneous solution simplifies to:

$$\begin{aligned} \Phi_h = & C_0 \rho^2 + C_1 \rho^3 \cos(\theta) + G_1 \rho^3 \sin(\theta) \\ & + \sum_{n=2}^{\infty} (A_n \rho^n + C_n \rho^{n+2}) \cos(n\theta) + \sum_{n=2}^{\infty} (E_n \rho^n + G_n \rho^{n+2}) \sin(n\theta). \end{aligned} \quad (7.18)$$

The particular solution is constructed by representing the stress function as a Fourier series,

$$\Phi(\rho, \theta) = \sum_{n=-\infty}^{\infty} \Phi(\rho)_n \cos(n\theta), \quad (7.19)$$

where $\Phi(\rho)$ is a function in ρ only, while the circumferential variation is expressed through the summation term. Trying to find a solution to a single non-homogeneous term $\nabla^4 \Phi(\rho)_n \cos(n\theta) = \rho^i \cos(j\theta)$ then gives:

$$\begin{aligned} \Phi(\rho)_n = & \frac{\rho^{i+4}}{(-i+n-4)(-i+n-2)(i+n+2)(i+n+4)} \\ & + A_n \rho^n + B_n \rho^{-n} + C_n \rho^{n+2} + D_n \rho^{-n+2}, \end{aligned} \quad (7.20)$$

which is only a valid function in ρ for coinciding wave lengths, $j = n$. Note that the constants arising in this solution recover the infinite series part of the Michell [142] solution in Eqn (7.18). For the chosen basis functions, the singularity for $\pm n = i + 2$ and $\pm n = i + 4$ are not relevant. However, the singularity can easily be removed and the solutions,

$$\begin{aligned} \Phi(\rho)_n = & \frac{\rho^{i+4}(2(i+2)(i+3)\log(\rho) - i(i+7) - 11)}{16(i+2)^2(i+3)^2} \quad \text{for } \pm n = i + 2, \\ \text{and } \Phi(\rho)_n = & \frac{\rho^{i+4}(2(i+3)(i+4)\log(\rho) + i(i+5) + 5)}{16(i+3)^2(i+4)^2} \quad \text{for } \pm n = i + 4, \end{aligned} \quad (7.21)$$

show that the interaction of such modes would cause an infinite stretching energy due to the log-term.

The presented solution set is employed to relate a corresponding stress term to each entry in the coefficient matrix of the Gaussian curvature, g_{ij} , in which squared trigonometric entries are prevented by using the power reduction identities of $\cos^2(\theta) = [1 + \cos(2\theta)]/2$ and $\sin^2(\theta) = [1 - \cos(2\theta)]/2$. Despite the arbitrary choice to use a Fourier series with cos-terms, it is required to also consider the constants of

integration containing sin-terms, $E_n - H_n$, since these are needed in some cases to account for twisting terms that have a sinusoidal component due to the application of a power reduction identity. Thus, a complete solution for $\Phi(\rho, \theta)$ can be calculated, and the stress resultants are derived from it via:

$$\sigma_r = \frac{1}{r} \frac{\partial \Phi}{\partial r} + \frac{1}{r^2} \frac{\partial^2 \Phi}{\partial \theta^2}, \quad \sigma_\theta = \frac{\partial^2 \Phi}{\partial r^2} \quad \text{and} \quad \sigma_{r\theta} = -\frac{\partial}{\partial r} \left(\frac{1}{r} \frac{\partial \Phi}{\partial \theta} \right). \quad (7.22)$$

The constants of integration are employed to satisfy the in-plane boundary conditions of $\sigma_r = \sigma_{r\theta} = 0$ at $\rho = 1$. By sorting the stress terms with respect to their polynomial order and wave number before enforcing the outer edge condition on each subset, a unique and contradiction-free solution for all constants is found; their expressions are given in detail in the appendix. With these, the strain energy functional can be calculated, which allows the identification of stable configurations via energy minimisation as before.

7.2 Results

First, details about the FE reference simulations are described in §7.2.1. The solution is then compared to analytical predictions of synclastic actuation patterns in §7.2.2, before anticlastic cases are considered in §7.2.3. Each section emphasises the possibility of stress-free transformations via natural growth as well as the possible ways of in-plane actuation alone, where a shape change is evoked by accumulated internal stresses that ultimately trigger buckling.

7.2.1 Finite Element Modelling

In order to evaluate the suitability of the presented method, the results are compared to finite element simulations conducted with the commercial software *ABAQUS* [123]. The quasi-static, implicit calculation uses a default time integration scheme with a free, quad-dominated mesh using over 1000 quadratic S8R elements for the disk, with $a = 1$, $t = 0.01$, $E = 10^7$, $\nu = 0$, and a density of $2.58 \cdot 10^{-4}$; all values refer to SI units. A small imperfection with an amplitude of $t/1000$ consisting of the first ten eigenvalues was prescribed, in order to seed out-of-plane buckling modes. The analysis required to specify a very small growth increment step of $\Delta\epsilon = 0.01t^2/a^2$ to ensure

that bifurcation points are captured accurately. The growth strains were modelled as a spatially nonuniform thermal expansion in a material with polar-orthotropic thermal expansion coefficients.

7.2.2 Synclastic Cases ($g > 0$)

First, several examples of growth modes with positive imposed Gaussian curvature are discussed: natural growth modes, for which the problem simplifies to an entirely geometric one, are considered before the buckling behaviour of an initially flat plate under various in-plane actuations is analysed.

Synclastic Natural Growth

By combining in-plane and out-of-plane actuation methods, it is possible to create ‘deformed’, stress-free non-Euclidean shapes. The geometric nature of this problem requires to find compatible actuation patterns in which the stretching and bending surface deform in compatible ways; if $g_{SA} - g_{BA} = 0$, the forcing term becomes zero, and no elastic deformations are required. However, in the present over-constrained problem, the support conditions may introduce an additional source of elastic in-plane deformations, and thus, an additional in-plane compatibility equation arises that allows – if satisfied – for stress-free growth modes even in cases where out-of-plane actuation according to Eqn (7.6) imposes Gaussian curvature.

One way to determine the in-plane parameters, ϵ_r , ϵ_θ and ϵ_0 , is to declare two of them as additional degrees of freedom, and to minimize the energy by ensuring that all eigenvalues of the stiffness matrix are positive. More intuitively, the in-plane stresses, σ_r and σ_θ , can be set to zero, which provides two required equations to determine ϵ_r and ϵ_θ as:

$$\epsilon_r = \frac{2\eta_A^2}{a^2} + \frac{3n_r}{k_u a} - 3\epsilon_0 \quad \text{and} \quad \epsilon_\theta = \frac{n_r}{k_u a} - \epsilon_0. \quad (7.23)$$

The coinciding results impose a Gaussian curvature $g_{BA} = g_{SA} = 4\eta_A^2/a^4$ without elastic components ($\eta_E = 0$) and cause a central out-of-plane displacement of η_A . Natural growth modes in roller-supported shells are possible if $n_r = 0$, since $k_u = 0$ causes a singular expression otherwise. If a spring is present, it balances the external radial force via a resulting radial edge displacement of $u = n_r/k_u$, whereas the change

due to the quadratic terms, ϵ_r and ϵ_θ , is compensated by a thermal expansion of ϵ_0 that prevents an additional edge displacement; all values are limited by the underlying assumption of small strains, which requires for instance a sufficiently stiff spring if an edge force is present. Fixed-pinned shells are a particular case of spring-supported shells, in which the radial force does not affect the response any more; all other values stay unchanged. For all support cases, natural growth can be achieved by using radially quadratic variations of the actuated strain only via $\epsilon_{rA} = 2(\rho \eta_A/a)^2$ and $\epsilon_{\theta A} = 0$, when other influencing factors are absent ($n_r = \epsilon_0 = 0$).

Note that these shells become bistable, once the out-of-plane displacement exceeds $\eta_A^2 = 16t^2/(1-\nu)$ for roller-supported shells or $\eta_A^2 = 16t^2(1-\nu)/(7-\nu)$ for fixed-pinned shells; for details about these thresholds, see §5.

Synclastic Buckling due to In-Plane Actuation

If growth modes are not compatible, stresses arise and these will ultimately lead to buckling: whilst it is energetically favourable to first deform in plane, at a certain threshold, out-of-plane deformations avoid additional stretching. In the following study of the post-buckling behaviour of an initially stress-free disk, the interaction of the in-plane actuation parameters ϵ_r , ϵ_θ and ϵ_0 (see Eqn (7.9)) and additional boundary conditions, n_r and k_u (Eqn (7.12)) is emphasized.

Buckling due to radial force and constant expansion ($\epsilon_r = \epsilon_\theta = \eta_A = 0 \rightarrow g_A = 0$):

Before cases with induced Gaussian curvature, g_A , are analysed, the buckling thresholds of a radial force and a constant expansion is discussed to evaluate the suitability of the presented approach. From the stability criterion, $\partial^2 \Pi / \partial \eta_E^2 = 0$, the critical radial load is derived:

$$(n_r)_{cr} = \epsilon_0 k_u a - \frac{k_u t^2}{3a} - \frac{Et^3}{3a^2(1-\nu)}. \quad (7.24)$$

In the limiting cases of roller supports ($k_u = 0$) and pinned supports ($k_u \rightarrow \infty$), this simplifies to

$$(n_r)_{cr} = -\frac{Et^3}{3a^2(1-\nu)} \quad \text{or} \quad (\epsilon_0)_{cr} = \frac{t^2}{3a^2}, \quad (7.25)$$

respectively. The uniform thermal expansion, ϵ_0 , drops out in the first case since the imposed deformation is compatible ($g_A = 0$) and there is no support reaction in response to a radial displacement u ; in the second case, the radial force does not affect

the strain energy equation anymore since $u = 0$. For $\nu = 0$, the result of $n_{cr} = 3.33$ differs from the finite element result of $n_{cr} = 2.85$ by 16 % and provides a competitive and even slightly superior accuracy compared to ‘exact’ approaches using Bessel functions [48], where n_{cr} is found to be 3.5.

After buckling, the midpoint deflection becomes

$$\eta_E = \pm 2a \sqrt{-3 \frac{n_r - (n_r)_{cr}}{Et + k_u a(7 - \nu)}} \quad \text{with} \quad \lim_{k_u \rightarrow \infty} \eta_E = \pm 2a \sqrt{3 \frac{\epsilon_0 - (\epsilon_0)_{cr}}{7 - \nu}}; \quad (7.26)$$

the square root term is positive, since n_r is negative and has a larger magnitude than $(n_r)_{cr}$. These structures are also bistable in their post-buckled state, because they can be inverted to precisely form their mirrored shape; each shape is separated by an energy barrier commensurate with snap-through buckling.

Buckling due to imposed in-plane strains ($\eta_A = 0$):

In a more general case, additional in-plane actuations are considered, which impose a non-Euclidean shape via $g_{SA} = 2(\epsilon_r - 3\epsilon_\theta)/a^2$. Using the previous solution, a buckling threshold, g_{SA}^* , at which out-of-plane deformations begin, is found:

$$g_{SA}^* = \frac{16}{a^4} \frac{Et^3/(1 - \nu) + t^2 k_u a - 3k_u a^3(\epsilon_\theta + \epsilon_0) + 3n_r a^2}{Et + k_u a(7 - \nu)}; \quad (7.27)$$

it simplifies to

$$\begin{aligned} g_{SA}^* &= \frac{16}{a^2} \left[\frac{t^2}{a^2(1 - \nu)} + \frac{3n_r}{Et} \right] \quad \text{for } k_u = 0 \\ \text{and} \quad g_{SA}^* &= \frac{16}{a^2} \frac{t^2 - 3a^2(\epsilon_\theta + \epsilon_0)}{a^2(7 - \nu)} \quad \text{for } k_u \rightarrow \infty. \end{aligned} \quad (7.28)$$

The corresponding post-buckled midpoint deflection takes a particularly compact form of

$$\eta_E = \pm \frac{a^2}{2} \sqrt{g_{SA} - g_{SA}^*}, \quad (7.29)$$

where the \pm sign indicates a mirror-symmetric bistable response in either the up or down direction. For the simple case of $k_u = n_r = \epsilon_0 = \epsilon_\theta = 0$, a buckling limit of $g_{SA}^* = 16t^2/(1 - \nu)a^4$ and a post buckled shape that is identical to the finding of [49] is obtained. For other values of k_u , the shape differs only by the buckling threshold, g_{SA}^* in Eqn (7.27).

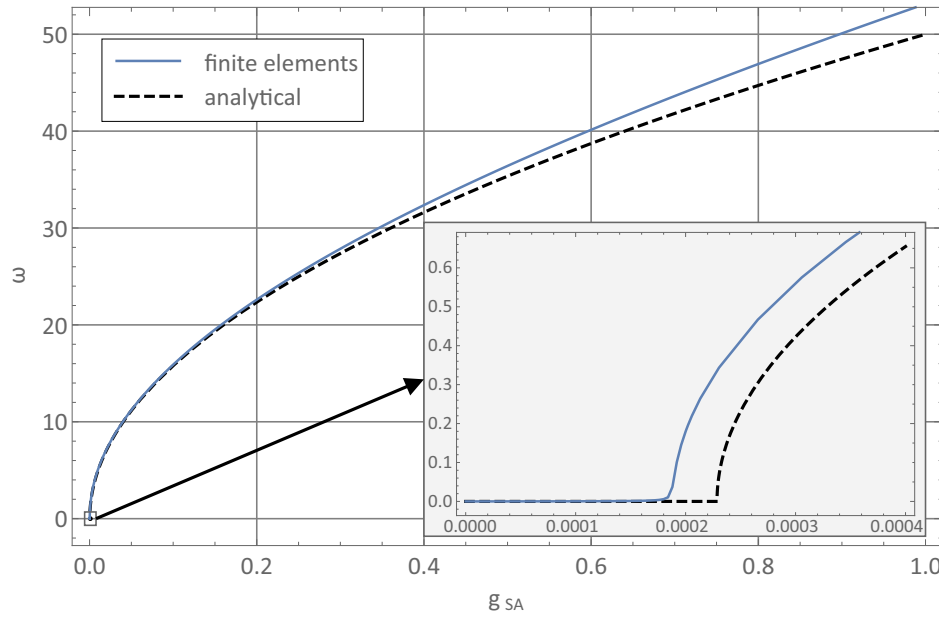


Figure 7.5: Disk subjected to a radially quadratically varying temperature field with $\epsilon_r = \epsilon_\theta = -\epsilon_0$: FE results (full line) with $a/t = 100$ compared to analytical model (dashed line). The results are in excellent agreement with up to $\omega = 50$. The inset-figure shows the buckling threshold in close-up.

The predictions for the midpoint deflection are compared to finite element results in Fig. 7.5 for $k_u \rightarrow \infty$ and, interestingly, they show an excellent agreement far beyond the limits of shallow shell theory, up to a value of $50t$, equal to one half of the shell's planform radius. Such an excellent agreement, however, cannot be explained without overlapping effects from several assumption that cancel out each other. The most relevant assumptions in this context are: (1) a small strain assumption, whilst the imposed in-plane strains for $g_{SA} = 1$ amount to 21 %; (2) the strain energy is calculated on the initial configuration, even though the surface area changed by 15 %; (3) the derivation employed only nonlinear displacement components of the transversal components and is thus not invariant under rotation, but the outer edge rotates up to 60° ; (4) the condition of a vanishing edge moment is neglected by the uniform curvature approach. Hence, further investigations are required to shed more light into the governing factors.

7.2.3 Anticlastic Cases ($g < 0$)

Relaxing rotational symmetry offers an interesting variety of achievable hyperbolic geometries. In contrast to elliptic geometries ($g > 0$), the asymmetry of hyperbolic geometries ($g < 0$) leads to out-of-plane shapes described by periodic ‘waves’. In order to make this nontrivial problem amenable to an analytical solution procedure, only case of free plates without boundary supports are considered.

Higher-Order Natural Growth Modes Without Rotational Symmetry

For the considered polynomial growth patterns of order m according to Eqn (7.13), a matching out-of-plane actuation growth pattern with wave number i as described in Eqn (7.14) is found by setting $g_{BA} = g_{SA}$. If elastic deformations are absent, $g_B = g_{BA}$, and thus, the natural growth mode can be found by comparison of coefficients via:

$$-(i-1)^2 i^2 \eta_A^2 \rho^{2i-4} / a^4 = -\epsilon m^2 r^{-2+m} / a^m. \quad (7.30)$$

Matching orders require $i = m/2 + 1$ or equivalently $m = 2(i-1)$ to cause a compatible deflected shape of:

$$w = \eta_A \rho^i \cdot \cos(i\theta) \quad \text{with } i > 1 \quad \text{and} \quad i \in \mathbb{N}. \quad (7.31)$$

The corresponding in-plane actuation strains in Eqn (7.13) prevent an elastic response if they take the value:

$$\varepsilon_{rA} = \varepsilon_{\theta A} = \left(\frac{(2+m)\eta_A}{4a} \rho^{i-1} \right)^2 \quad \text{and} \quad \varepsilon_{r\theta A} = 0. \quad (7.32)$$

The squared term arises due to the nonlinear influence of the out-of-plane displacement on the in-plane strains and ultimately requires in-plane actuation modes of even order for natural growth modes. The latter wave number is restricted to integers due to compatibility in closed shells. As a result, an additional wave can be formed as soon as the polynomial order of in-plane actuation strains is increased by two.

Anticlastic Buckling

Since out-of-plane actuation modes ($\eta_A \neq 0$) complicate the manufacturing process due to their circumferential variations, it appears tempting to control the wave number by solely using a rotationally symmetric in-plane actuation mode of $\varepsilon_{rA} = \varepsilon_{\theta A} = \varepsilon \rho^m$.

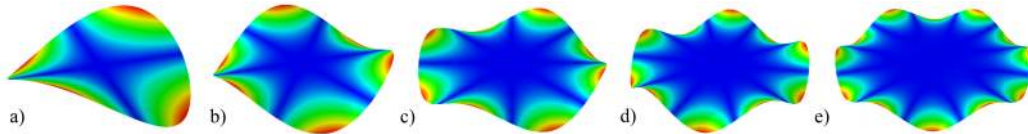


Figure 7.6: Magnitude of displacements according to FE results analysing the post-buckled shape of very thin disks with $a/t = 1000$ subjected to grow strains proportional to ρ^2 (a), ρ^4 (b), ρ^6 (c), ρ^8 (d), and ρ^{10} (e). Increasing powers in the grow strain polynomial correlate with the wave number in the post-buckled shape via $\rho^{i/2+1}$ giving i waves.

Finite element simulations in Fig. 7.6 confirmed that imposing solely in-plane strains, ε_{rA} and $\varepsilon_{\theta A}$, of order ρ^{2i-2} without stipulating out-of-plane actuation modes results in stable configuration with i waves if a transition to such a shape was marshalled. However, entirely in-plane actuated shells do not straightforwardly deform into those shapes, since buckling into shapes of lower wave number occurs first. This becomes apparent, when a polynomial in-plane growth strain of order m is considered and a simplified shape function of a single mode of order i of the form $w_E = \rho^i \cos(i\theta)$ is taken into account: in order to obtain a compact estimate of the buckling threshold, the boundary conditions are ignored here for the moment, so that the buckling threshold of imposed in-plane strains according to Eqn (7.13) reads:

$$\epsilon \geq \frac{5i(m+2)(m+2i)t^2}{48m(1+\nu)}. \quad (7.33)$$

Since i is an integer greater than one, this value is lowest for $i = 2$ for any polynomial, and thus, an initially flat plate will – independently of the growth strain's order, m – first buckle into a saddle. This result is reasonable since it aligns with the scaling law of the energies: whilst the stretching energy scales with $\Pi_S \propto E t a^2 \epsilon^2$, the bending energy is proportional to $\Pi_B \propto E t^3 \epsilon$; thus, at a certain threshold, ϵ^* , that scales with the slenderness, t^2/a^2 , bending becomes favourable to stretching – and hence, the shell buckles. Responses of lower wave numbers, however, that consequently include less

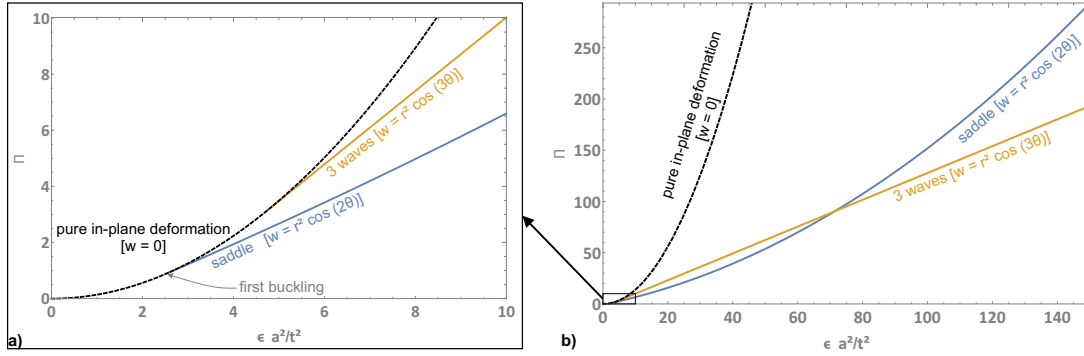


Figure 7.7: Strain energy predictions of simplified one-term models over dimensionless actuation parameter $\epsilon \cdot a^2/t^2$ for an actuation strain of $\epsilon_{rA} = \epsilon_{\theta A} = \epsilon \rho^4$ that prescribes a target shape with three waves: pure stretching response (dashed), compared to mode with two waves (blue) and three waves (orange). A close up of (b) is depicted in (a). Buckling into a saddle shape is energetically favourable for small ϵ , while shapes with three waves that resemble the target geometry become energetically favourable for larger values of the imposed strain.

Table 7.1: Buckling threshold for in-plane actuation strains of differing orders: comparison of analytical predictions to FE results.

Order	Dimensionless buckling threshold $\epsilon^* \cdot a^2/t^2$		
	FE	Analytical	Deviation [%]
ρ^2	3.19	3.03	5.01
ρ^4	3.28	3.28	0.00
ρ^6	3.74	3.84	2.80
ρ^8	4.25	4.49	5.60
$\rho^2 + \frac{1}{4}\rho^4 + \frac{1}{8}\rho^8$	2.92	1.96	32.9

bending, become energetically favourable at an earlier point; see the energy plot for different mode shapes in Fig. 7.7 for an illustration.

The values for the buckling threshold in Eqn (7.33) were obtained by a simplified approach that neglected the vanishing edge moments. They deviate by approximately 25 % from the finite element results for polynomial orders between 2 and 8. The employed higher-order model with shape functions specified in Eqn (7.15) has a significantly improved accuracy, which is listed in Tab. 7.1. Since nature does not necessarily restrict itself to polynomials with a single term, the model additionally considered a more intricate, arbitrarily chosen polynomial actuation pattern of $\epsilon_{rA} = \epsilon_{\theta A} = \rho^2 + \frac{1}{4}\rho^4 + \frac{1}{8}\rho^8$, which combines multiple terms of different order to illustrate the versatility of the presented approach: whilst the finite element reference solution shows that the buckling threshold differs by almost a third, the deflection field,

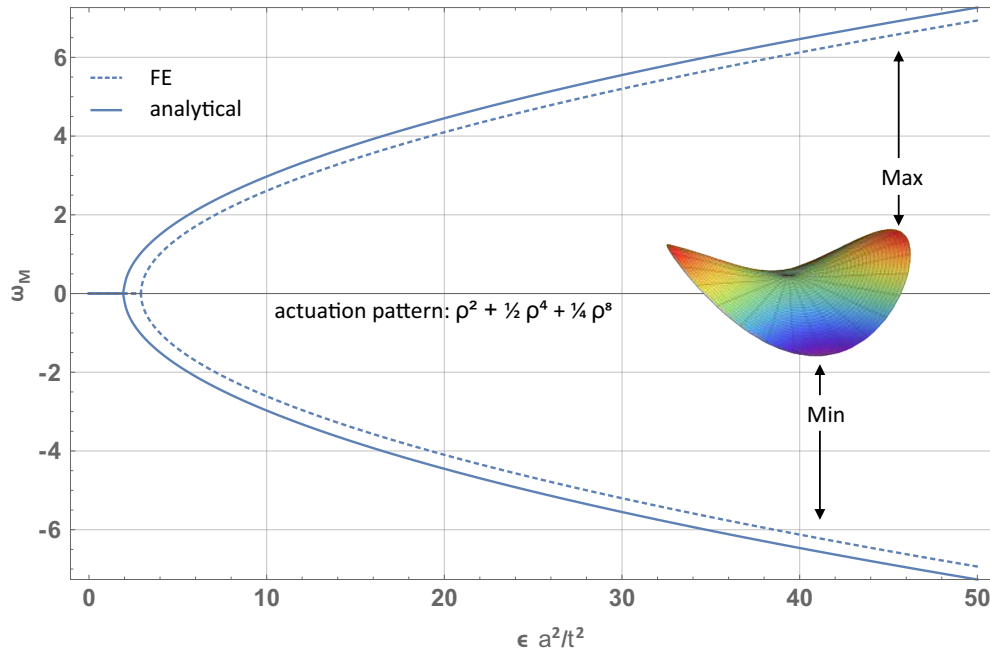


Figure 7.8: Dimensionless midpoint deflection over dimensionless in-plane strain actuation parameter, $\epsilon \cdot a^2/t^2 \propto g_{SA}$ for a polynomial actuation pattern.

depicted in Fig. 7.8, is approximated well; the difference in ϵ^* however, causes an offset that remains.

Secondary buckling modes:

Since all considered shells buckle into a saddle first, the question arises, if a shape that evinces the wave number of the target shape will actually be achieved due to a further increase of the actuation strain for orders of $m \geq 4$, or if the saddle stabilises itself and prevents the required additional buckling transition. As an example, let us consider an initially flat plate that is subjected to a constantly increasing in-plane actuation strain of $\epsilon_{rA} = \epsilon_{\theta A} = \epsilon \rho^4$ that corresponds to a target shape with three waves. The corresponding minima and maxima of the displacement curve for $\omega_M \leq 20$ are shown in Fig. 7.9(a) as a function of ϵ , where full lines indicate analytical predictions that are compared to FE simulations (dashed lines). The finite element reference solution was obtained by preventing the radial rotation at one outer node, since the shell is neutrally stable otherwise and would allow for circumferential wave propagations in the post-buckled state; for the analytical model, the mirror-symmetric buckling modes were omitted for the sake of clarity.

Before the existing deviations between the two methods are discussed, the qualitative buckling behaviour, which is captured consistently by both methods and depicted

in Fig. 7.9(b), is described: the initially flat plate first buckles into a saddle and a secondary bifurcation is observed at a significantly larger value of ϵ . However, instead of increasing the wave number, the additional instability causes the saddle to develop a dominant direction of curvature via a deformation mode that is approximately cylindrical. This form of symmetry breaking buckling is a known effect in out-of-plane actuated shells [49], but it has to the knowledge of the author not been modelled in in-plane actuated shells. The reason for this buckling is that the Gaussian curvature of the deformed configuration evinces a significant mismatch with the target configuration, and thus, additional stretching as well as bending stresses arise; the latter eventually induce the second instability. According to the presented analytical method, an additional configuration with three waves becomes stable at $\epsilon = 8.9t^2/a^2$, but its strain energy is higher, and thus, no mode transition is expected in the framework of shallow shell theory with $\omega_M \lesssim 20$. Finite element simulations confirmed the existence and stability of the additional mode, but as expected it required to marshal the transition by applying a temporary external load.

Whilst FE reference simulations and the analytical model are qualitatively concurring, the quantitative predictions of the secondary buckling threshold are not satisfying in the latter case since they show significant differences. These are partially caused by existing deviations in the post-buckled shape and the buckling-sensitivity of shells. It is well-known that imperfections as small as $t/10$ can cause significant reductions of the buckling threshold, and here, the discrepancy between FE simulations and the analytical model at the point of the secondary buckling is of the order of the thickness. This suggests that more elaborate shape functions are required to accurately approximate the post-buckled shape.

The results demonstrate that the presented approach and FE method complement each other in growth problems: first, the estimates of the buckling threshold obtained by the higher-order model are vital to estimate the growth increment size required in finite element simulations. If it was chosen too high, *e.g.* a value as small as $\Delta\epsilon = 0.1t^2/a^2$ in the considered example, the correct bifurcation point is missed in a transient analysis. Note that an arc-length method would require a user-defined subroutine in *ABAQUS*, in which the load-proportionality factor is substituted by a *growth proportionality factor*. Second, the knowledge about the target shape allows us to understand the structural behaviour and interpret the observed results. Lastly, and most importantly, the ‘hidden’ alternative stable configuration with three waves would have

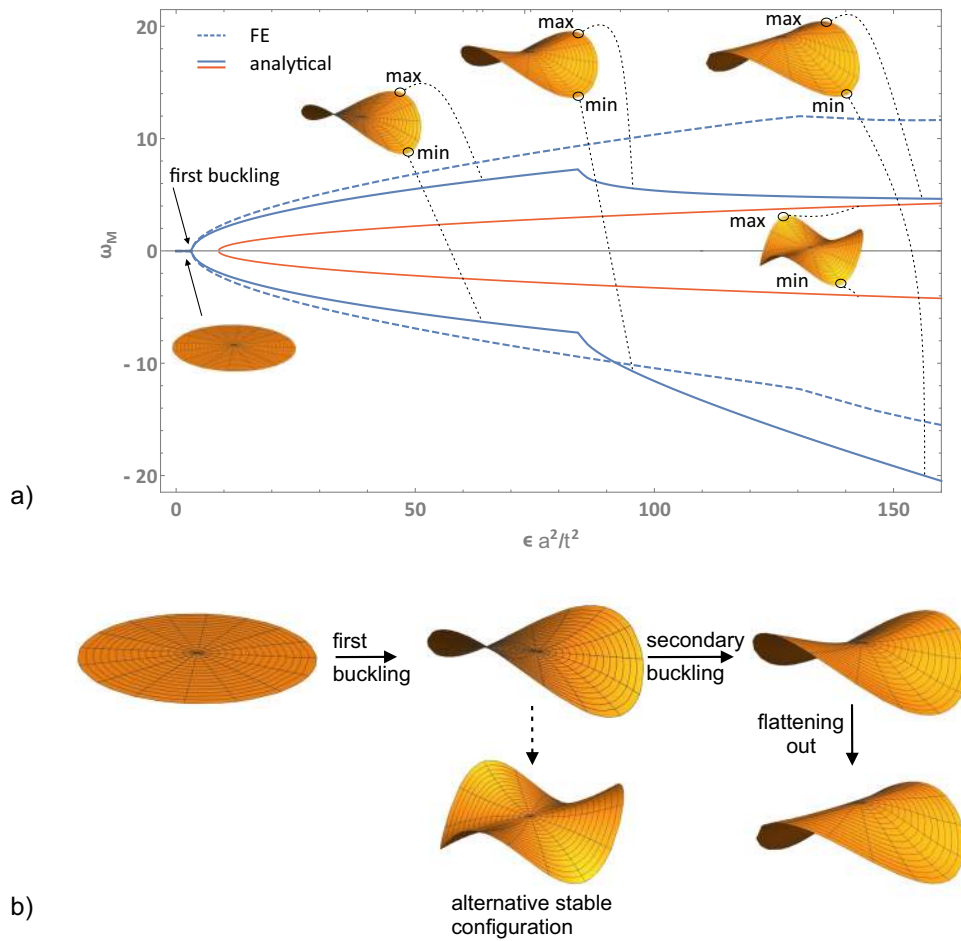


Figure 7.9: (a) Deflection over growth parameter: the shell buckles first into a saddle before a secondary buckling occurs. Additional stable configurations with three waves exist and show the lowest amplitude. (b) Illustration of the buckling behaviour: solid arrows show the observed response in the absence of load, while dashed arrows show load-free stable configurations that are separated by an additional energy barrier.

easily been missed in FE simulations since a load that closely resembles the target shape is required to foster the transition. The analytical predictions were crucial in order to prove the existence of such a state since they pointed towards this result and provided an estimate of the threshold of stabilisation.

7.3 Summary

A shallow shell model for differential actuation patterns that mimic simplified nonlinear growth patterns in floral systems was presented. In a first step, a Ritz approach

assuming uniform curvature was employed. In order to analyse the interaction of actuation methods on their post-buckling behaviour, a three-parameter in-plane actuation mode, a uniform out-of-plane actuation mode, an additional radial force on the boundary as well as horizontal supports with variable stiffness were considered. The predictions of the buckling thresholds and post-buckled shapes were found to be in good agreement with available data in literature as well as FE results, for which some predictions showed an excellent fit even far beyond the limits of shallow shell theory. It was demonstrated that natural growth modes, in which no stresses arise, are achievable in the presence of horizontal supports by combining in-plane with out-of-plane actuation modes. In particular, it sufficed to employ a single in-plane actuation parameter that imposes only radial growth strains with a quadratic variation to match a uniformly applied out-of-plane actuation.

In order to analyse hyperbolic shape transformations, the assumption of rotational symmetry was then relaxed and a centrally fixed shell was considered. First, it was demonstrated that natural growth modes with circumferential variations of $\cos \pi n$ exist, if the imposed deformation is matched by a polynomial in-plane actuation patterns that only vary radially by an even order of $2n - 2$. In a subsequent step, the response of shells to an isolated in-plane actuation was investigated: when subjected to anticlastic actuation patterns, shells are forced to buckle into a saddle-shape first, even when the target shape possesses more than two waves. In such cases, a second instability was observed, but instead of transforming towards a higher wave number, shells buckled in a symmetry-breaking manner that caused a flattening out via a cylindrical deformation mode.

Whilst a transition towards a shape of the target shape's wave number was not achieved directly through in-plane actuation alone, such a stable shape was predicted by the analytical model and its existence was confirmed in FE simulations; however, the transition had to be marshalled to observe it. This finding emphasises the synergistic relation between the developed analytical model and numerical approaches: the qualitative predictions, which evinced remaining quantitative discrepancies, captured the qualitative behaviour appropriately, and thus, it was possible to confirm and refine the analytical predictions; without those, however, tedious numerical parameter studies that might nevertheless easily miss a certain feature are required. So, while the first provides insight into the structural behaviour with a certain degree of uncertainty, the latter can be employed for the purpose of reassurance.

Chapter 8

Conclusions and Future Work

This dissertation investigated the bistable behaviour of shells in the presence of additional support conditions and aimed at gaining further insight into the promoting and eschewing factors of bistability by employing a (semi-)analytical methodology. For deep spherical or cylindrical shells, it was shown that geometrically linear theories are suitable to describe their inversion. Since only small deviations from an idealised mirror-symmetric post-buckled shape are evoked through an edge effect of a vanishing bending moment, accurate predictions were obtained. However, for shallower and thicker shells, more elaborate approaches that consider geometric nonlinearities are required, which constituted the main focus of this dissertation.

In the framework of the Föppl-von Kármán plate theory, a novel semi-analytical Ritz approach was derived with the aim to get hold of relevant aspects via closed-form solutions. The assumption of a polynomial deflection field contained up to four degrees of freedom and satisfied all boundary conditions strongly – in contrast to simplifying uniform curvature approaches. The relation between out-of-plane bending and in-plane stretching was established via Gauss Theorema Egregium and stable configurations were identified via energy minimisation. The analysis focussed on three particular aspects for which the interaction with the support conditions were studied.

First, a macro-element for isotropic, homogeneous and rotationally symmetric shallow shells was developed by considering extensional in-plane springs as well as rotational springs at the outer rim. The familiar clamped or hinged boundary conditions were approximated via the limits of the respective spring stiffness, and intermediate values allowed investigations of the transition between these extreme states. It was demonstrated that the superior accuracy of the employed approach with a higher-order

deflection field is required to investigate (initially) nonuniformly curved shells as well as more intricate deformations that result from clamped edges. In all studied examples, it was found that an increased in-plane stiffness promotes bistable inversions, whereas the influence of rotational springs was multi-faceted. Whilst in general, an increased resistance against rotation has a hindering effect, an intermediate stiffness value may cause a mode transition that is in fact stabilising bistable inversions.

Another boundary condition – the one of a free inner edge – was then imposed by cutting a hole into a cap. It was found that these have a beneficial effect, since bistable shells of a smaller physical height can be produced. In a further step, the developed macro-element was employed to study the interaction of shells. It has been shown that shells with at least four stable configurations can be manufactured by adding hinges that enable structural parts to invert in isolation by stopping bending from propagating. So, while restricting edge rotations has the tendency to hinder bistable inversions, freeing them can allow for extra stable configurations and widen the space for further structural manipulations.

Second, variations of the internal directional stiffness of shells were analysed. The constitutive equations were aligned with the rotational symmetry of the concerned structure and a polar-orthotropic material law was considered that has not been studied in the context of bistability before. Based on the linear solution for plate bending, the approach presented here was extended to include deflection terms that capture stress singularities in bending as well as stretching that arise if the radial stiffness exceeds the circumferential one. A detailed investigation of the stress resultants and a comparison to finite element reference solutions confirmed the validity of this assumption and demonstrated the superiority of the approach compared to existing nonlinear shallow shell models. An analysis of the interaction between the support conditions and the orthotropic parameter elucidated a strong coupling with respect to the bistable performance: in contrast to roller-supported shells, where no alternative equilibrium configurations were found for a very small circumferential stiffness, fixed-pinned shells showed the lowest required apex height for such materials. The difference is engendered by a quasi-decoupling of the radial and circumferential response for very low values of the hoop stiffness, which causes the structure to evince a beam-like behaviour. The analysis of stiffness variations pointed towards a new perspective on the influence of the hoop stiffness with respect to bistability. Whilst the circumferential rigidity is usually perceived as a promoting factor in free-standing shells, an contradicting trend was observed here in fixed-pinned caps. It was found that the circumferential stiffness is only

insofar stabilising as it evokes radial in-plane stresses through a strong ring beam effect, but if radial stresses are assured by horizontally-immovable supports, it becomes a redundant feature that is even a slight impediment. It was then demonstrated that stress-singularities can straightforwardly be avoided by creating a central hole in the centre of the shell. Whilst the bistable performance of fixed-pinned shells was barely affected by such a cut, roller-supported ones showed a significant stabilisation and were more likely to stay inverted.

Finally, the analytical model was extended by considering imposed in-plane stretching as well as out-of-plane bending strains. These had non-Euclidean target metrics due to spatially nonlinear varying actuation patterns. Additional horizontal supports required a refined perspective of the actuation parameters, so that the interaction of six parameters in total was investigated. When all of them are fine tuned in a compatible way, it becomes possible to evoke non-Euclidean shape transformations without changes of the strain energy known as ‘natural growth modes’. In particular, it was found that imposing only two actuation parameters allowed initially flat plates the stress-free transformation into the target shape of a cap even when horizontal supports are present. In a final example, the assumption of rotational symmetry was relaxed in exchange for the simpler supports conditions of a free-standing shell: by considering more elaborated growth patterns, it was found that natural growth into anticlastic target shapes with n sinusoidal waves is possible, if the out-of-plane actuation pattern is matched by a particularly simple pattern of imposed in-plane strains, which is a polynomial of order $2(n - 1)$ in r without circumferential variations. The result inspired the analysis of a shell’s response to such an in-plane actuation of order m in isolation: it was demonstrated that independently of the order, all shells buckle into a saddle-shape first, even though actuation strains of order $m \geq 4$ have a target shape with a higher wave number. A further increase of such growth strains caused a secondary buckling, but instead of increasing the wave number, an approximately cylindrical deformation mode was observed. Interestingly, an additional, ‘hidden’ stable mode with a matching wave number was identified, but it could not be observed without arranging a transition via a temporary applied external load. Whilst the qualitative behaviour was accurately captured by the presented analytical model, quantitative differences of the secondary buckling threshold indicated that an even more elaborated approach can further increase the accuracy. The results highlighted the importance of analytical approaches, since they point towards results that might easily be missed otherwise. Insofar, the syn-

ergistic nature with finite element simulations was demonstrated: while the first give inspiration in the design stage, the latter is used for validation and a refined analysis.

The derived shallow shell model is capable of adapting to various requirements in shape-changing structures and can be applied as a macro-element in future studies. It might in particular inspire further investigations of array applications of bistable unit cells as in ‘morphing metal’, *cf.* Fig. 3.8. The new understanding of the influence of support conditions on the inversion of doubly curved shapes allows one to decide where simpler beam structures suffice, and where shells provide indispensable components. A possible application involves morphing solids, where multiple arrays with bistable unit cells are stacked in thickness direction. By collapsing one layer into an approximately mirror-symmetric shape, it would become possible to produce, for instance, façades with adaptable thermal isolation properties, or novel meta-materials with a multistable ‘memory effect’. Prototypes with beam-like structures were produced during this research project and serve as a proof of concept, but the employment of shells might offer a richer and an even more robust design space in the future.

Bibliography

- [1] Vogel, S. *Von Grashalmen und Hochhäusern: [mechanische Schöpfungen in Natur und Technik]* (Wiley-VCH, 2000).
- [2] Pierau, B. & Kiehl, J. Widerstands- und Ausweichprinzip: Vergleich zweier Entwurfsmethoden für Tunnelbauten in quellfähigem Gebirge. *Taschenbuch für den Tunnelbau* **1997**, 226–247 (1996).
- [3] Gatto, A., Mattioni, F. & Friswell, M. Experimental investigation of bistable winglets to enhance aircraft wing lift takeoff capability. *Journal of Aircraft* **46**, 647–655 (2009).
- [4] Forterre, Y., Skotheim, J. M., Dumais, J. & Mahadevan, L. How the Venus Flytrap snaps. *Nature* **433**, 421–425 (2005).
- [5] Smith, M., Yanega, G. & Ruina, A. Elastic instability model of rapid beak closure in hummingbirds. *Journal of theoretical biology* **282**, 41–51 (2011).
- [6] Potyrailo, R. A. *et al.* Towards outperforming conventional sensor arrays with fabricated individual photonic vapour sensors inspired by Morpho butterflies. *Nature communications* **6**, 1–12 (2015).
- [7] Kostovski, G., Mitchell, A., Holland, A. & Austin, M. Sidewall corrugation lithography: Bulk fabrication of ordered nanowires, nanoribbons, and nanorings. *Applied Physics Letters* **92**, 223109 (2008).
- [8] Mertens, J. Plasmonic gold rings, gold discs and stretch-tuneable plasmonic elastomer films. Tech. rep., University of Cambridge (2012). [unpublished].
- [9] Coulais, C. As the extension, so the twist. *Science* **358**, 994–995 (2017).
- [10] Timoshenko, S. *History of strength of materials: with a brief account of the history of theory of elasticity and theory of structures* (Courier Corporation, 1983).
- [11] Spivak, M. D. *A comprehensive introduction to differential geometry* (Publish or perish, 1970).
- [12] Zeidler, E. *Nonlinear functional analysis and its applications: III: variational methods and optimization* (Springer Science & Business Media, 2013).
- [13] Calladine, C. R. *Theory of shell structures* (Cambridge University Press, 1983).
- [14] Love, A. E. H. The small free vibrations and deformation of a thin elastic shell. *Philosophical Transactions of the Royal Society of London A* 491–546 (1888).
- [15] Ventsel, E. & Krauthammer, T. *Thin plates and shells* (Marcel Dekker New York, 2001).
- [16] von Kármán, T. Festigkeitsprobleme im Maschinenbau. *Encyclopädie der mathematischen Wissenschaften* **4** (1910).
- [17] Föppl, A. *Vorlesungen über Technische Mechanik*, vol. 5 (BG Teubner, 1907).

- [18] Calladine, C. R. The static–geometric analogy in the equations of thin shell structures. In *Mathematical Proceedings of the Cambridge Philosophical Society*, vol. 82, 335–351 (Cambridge University Press, 1977).
- [19] Chladni, E. F. F. *Die Akustik* (Breitkopf & Härtel, 1830).
- [20] Meleshko, V. Selected topics in the history of the two-dimensional biharmonic problem. *Applied Mechanics Reviews* **56**, 33–85 (2003).
- [21] Voigt, W. Bemerkung zu dem Problem der transversalen Schwingungen rechteckiger Platten. *Nachrichten von der Königl. Gesellschaft der Wissenschaften und der Georg-Augusts-Universität zu Göttingen* **1893**, 225–230 (1893).
- [22] Strutt, J. W. & Rayleigh, B. The theory of sound, vol. 1 (1877).
- [23] Ritz, W. Theorie der Transversalschwingungen einer quadratischen Platte mit freien Rändern. *Annalen der Physik* **333**, 737–786 (1909).
- [24] Way, S. Bending of circular plates with large deflection. *Trans. ASME* **56**, 627 (1934).
- [25] Berger, H. M. *A new approach to the analysis of large deflections of plates*. Ph.D. thesis, California Institute of Technology (1954).
- [26] Banerjee, B. & Datta, S. A new approach to an analysis of large deflections of thin elastic plates. *International Journal of Non-Linear Mechanics* **16**, 47–52 (1981).
- [27] Sinharay, G. & Banerjee, B. A new approach to large deflection analyses of spherical and cylindrical shells. *Journal of applied mechanics* **52**, 872–876 (1985).
- [28] Guest, S. D. & Pellegrino, S. Analytical models for bistable cylindrical shells. *Proceedings of the Royal Society of London A* **462**, 839–854 (2006).
- [29] Sobota, P. M. & Seffen, K. A. Effects of boundary conditions on bistable behaviour in axisymmetrical shallow shells. *Proceedings of the Royal Society of London A* **473**, 20170230 (2017).
- [30] Timoshenko, S. & Goodier, J. Theory of elasticity. *New York* **412**, 108 (1951).
- [31] Koiter, W. A consistent first approximation in the general theory of thin elastic shells. *Theory of thin elastic shells* 12–33 (1960).
- [32] Anh, V. T. T., Hong Cong, P., Huy Bich, D. & Duc, N. D. On the linear stability of eccentrically stiffened functionally graded annular spherical shell on elastic foundations. *Advanced Composite Materials* **25**, 525–540 (2016).
- [33] Anh, V. T. T. & Duc, N. D. The nonlinear stability of axisymmetric functionally graded material annular spherical shells under thermo-mechanical load. *Mechanics of Advanced Materials and Structures* **23**, 1421–1429 (2016).
- [34] Duc, N. D., Quang, V. D. & Anh, V. T. T. The nonlinear dynamic and vibration of the S-FGM shallow spherical shells resting on an elastic foundations including temperature effects. *International Journal of Mechanical Sciences* **123**, 54–63 (2017).
- [35] Wittrick, W., Myers, D. & Blunden, W. Stability of a bimetallic disk. *The Quarterly Journal of Mechanics and Applied Mathematics* **6**, 15–31 (1953).
- [36] Freund, L. Some elementary connections between curvature and mismatch strain in compositionally graded thin films. *Journal of the Mechanics and Physics of Solids* **44**, 723–736 (1996).

- [37] Hyer, M. W. Calculations of the room-temperature shapes of unsymmetric laminates. *Journal of Composite Materials* **15**, 296–310 (1981).
- [38] Kebabze, E., Guest, S. D. & Pellegrino, S. Bistable prestressed shell structures. *International Journal of Solids and Structures* **41**, 2801–2820 (2004).
- [39] Seffen, K. A. & McMahon, R. A. Heating of a uniform wafer disk. *International Journal of Mechanical Sciences* **49**, 230–238 (2007).
- [40] Vidoli, S. & Maurini, C. Tristability of thin orthotropic shells with uniform initial curvature. *Proceedings of the Royal Society of London A* **464**, 2949–2966 (2008).
- [41] Coburn, B. H., Pirrera, A., Weaver, P. M. & Vidoli, S. Tristability of an orthotropic doubly curved shell. *Composite Structures* **96**, 446–454 (2013).
- [42] Seffen, K. A. & Guest, S. D. Prestressed morphing bistable and neutrally stable shells. *Journal of Applied Mechanics* **78**, 011002 (2011).
- [43] Guest, S. D., Kebabze, E. & Pellegrino, S. A zero-stiffness elastic shell structure. *Journal of Mechanics of Materials and Structures* **6**, 203–212 (2011).
- [44] Eckstein, E., Pirrera, A. & Weaver, P. Multi-mode morphing using initially curved composite plates. *Composite Structures* **109**, 240–245 (2014).
- [45] Vidoli, S. Discrete approximations of the Föppl–von Kármán shell model: from coarse to more refined models. *International Journal of Solids and Structures* **50**, 1241–1252 (2013).
- [46] Chen, Z. *et al.* Nonlinear geometric effects in mechanical bistable morphing structures. *Physical review letters* **109**, 114302 (2012).
- [47] Woinowsky-Krieger, S. Über die Beulsicherheit von Kreisplatten mit kreiszylindrischer Aelotropie. *Archive of Applied Mechanics* **26**, 129–133 (1958).
- [48] Najafizadeh, M. & Eslami, M. Buckling analysis of circular plates of functionally graded materials under uniform radial compression. *International Journal of Mechanical Sciences* **44**, 2479–2493 (2002).
- [49] Seffen, K. A. & Maurini, C. Growth and shape control of disks by bending and extension. *Journal of the Mechanics and Physics of Solids* **61**, 190–204 (2013).
- [50] Arrieta, A., Hagedorn, P., Erturk, A. & Inman, D. A piezoelectric bistable plate for nonlinear broadband energy harvesting. *Applied Physics Letters* **97**, 104102 (2010).
- [51] Betts, D. N., Kim, H. A., Bowen, C. R. & Inman, D. Optimal configurations of bistable piezo-composites for energy harvesting. *Applied Physics Letters* **100**, 114104 (2012).
- [52] Hamouche, W., Maurini, C., Vidoli, S. & Vincenti, A. Multi-parameter actuation of a neutrally stable shell: a flexible gear-less motor. *Proceedings of the Royal Society of London A* **473**, 20170364 (2017).
- [53] Kim, H. A., Betts, D. N., T. Salo, A. I. & Bowen, C. R. Shape memory alloy-piezoelectric active structures for reversible actuation of bistable composites. *AIAA Journal* **48**, 1265–1268 (2010).
- [54] Timoshenko, S. & Woinowsky-Krieger, S. *Theory of plates and shells*, vol. 2 (McGraw-hill New York, 1959).
- [55] Seffen, K. A. Morphing bistable orthotropic elliptical shallow shells. *Proceedings of the Royal Society of London A* **463**, 67–83 (2007).

- [56] Mansfield, E. H. Bending, buckling and curling of a heated elliptical plate. *Proceedings of the Royal Society of London A* **288**, 396–417 (1965).
- [57] Gomez, M., Moulton, D. E. & Vella, D. The shallow shell approach to Pogorelov's problem and the breakdown of 'mirror buckling'. *Proceedings of the Royal Society of London A* **472**, 20150732 (2016).
- [58] Pogorelov, A. V. *Bendings of surfaces and stability of shells*, vol. 72 (American Mathematical Soc., 1988).
- [59] Taffetani, M., Jiang, X., Holmes, D. P. & Vella, D. Static bistability of spherical caps. *Proceedings of the Royal Society of London A* **474**, 20170910 (2018).
- [60] Brinkmeyer, A., Santer, M., Pirrera, A. & Weaver, P. Pseudo-bistable self-actuated domes for morphing applications. *International Journal of Solids and Structures* **49**, 1077–1087 (2012).
- [61] Walker, M. G. & Seffen, K. A. Bistable behaviour of creased thin metallic strips. *Proceedings of the International Association for Shell and Spatial Structures (IASS)* (2017).
- [62] Pirrera, A., Avitabile, D. & Weaver, P. Bistable plates for morphing structures: a refined analytical approach with high-order polynomials. *International Journal of Solids and Structures* **47**, 3412–3425 (2010).
- [63] Pirrera, A., Avitabile, D. & Weaver, P. On the thermally induced bistability of composite cylindrical shells for morphing structures. *International Journal of Solids and Structures* **49**, 685–700 (2012).
- [64] Daton-Lovett, A. An extendible member. *Patent Cooperation Treaty application PCT/GB97/00839* (1996).
- [65] Brinkmeyer, A., Pellegrino, S. & Weaver, P. M. Effects of long-term stowage on the deployment of bistable tape springs. *Journal of Applied Mechanics* **83**, 011008 (2016).
- [66] Diaconu, C. G., Weaver, P. M. & Mattioni, F. Concepts for morphing airfoil sections using bi-stable laminated composite structures. *Thin-Walled Structures* **46**, 689–701 (2008).
- [67] Chun, I. S., Challa, A., Derickson, B., Hsia, K. J. & Li, X. Geometry effect on the strain-induced self-rolling of semiconductor membranes. *Nano letters* **10**, 3927–3932 (2010).
- [68] Timoshenko, S. *Theory of elastic stability*, (2nd edition) (McGraw-Hill Education, 1963).
- [69] Qiu, J., Lang, J. H. & Slocum, A. H. A centrally-clamped parallel-beam bistable MEMS mechanism. In *14th IEEE International Conference on Micro Electro Mechanical Systems*, 353–356 (2001).
- [70] Brunetti, M., Vincenti, A. & Vidoli, S. A class of morphing shell structures satisfying clamped boundary conditions. *International Journal of Solids and Structures* (2015).
- [71] Brunetti, M., Kloda, L., Romeo, F. & Warminski, J. Multistable cantilever shells: Analytical prediction, numerical simulation and experimental validation. *Composites Science and Technology* **165**, 397–410 (2018).
- [72] Hamouche, W., Maurini, C., Vincenti, A. & Vidoli, S. Basic criteria to design and produce multistable shells. *Meccanica* (2016).

- [73] Schenk, M. & Guest, S. D. On zero stiffness. *Proceedings of the Institution of Mechanical Engineers, Part C: Journal of Mechanical Engineering Science* **228**, 1701–1714 (2014).
- [74] Lachenal, X., Daynes, S. & Weaver, P. A zero torsional stiffness twist morphing blade as a wind turbine load alleviation device. *Smart Materials and Structures* **22**, 065016 (2013).
- [75] Daynes, S., Lachenal, X. & Weaver, P. M. Concept for morphing airfoil with zero torsional stiffness. *Thin-Walled Structures* **94**, 129–134 (2015).
- [76] Lachenal, X., Weaver, P. & Daynes, S. Multi-stable composite twisting structure for morphing applications. *Proceedings of the Royal Society of London A* **468**, 1230–1251 (2012).
- [77] Lachenal, X., Daynes, S. & Weaver, P. M. A non-linear stiffness composite twisting I-beam. *Journal of Intelligent Material Systems and Structures* **25**, 744–754 (2014).
- [78] Sobota, P. M. & Seffen, K. A. Multistable slit caps. *Proceedings of the International Association for Shell and Spatial Structures (IASS)* (2016). “Spatial Structures in the 21st Century”, Tokyo, Japan, Madrid, Spain: IASS.
- [79] Seffen, K. Mechanical memory metal: a novel material for developing morphing engineering structures. *Scripta materialia* **55**, 411–414 (2006).
- [80] Lienhard, J., Alpermann, H., Gengnagel, C. & Knippers, J. Active bending, a review on structures where bending is used as a self-formation process. *International Journal of Space Structures* **28**, 187–196 (2013).
- [81] Neuhäuser, S., Haase, W., Weickgenannt, M. & Sawodny, O. Adaptive Tragwerke—Aktuelle Forschungen im Ultraleichtbau. *Stahlbau* **82**, 428–437 (2013).
- [82] Senatore, G., Duffour, P. & Winslow, P. Energy and Cost Assessment of Adaptive Structures: Case Studies. *Journal of Structural Engineering* **144**, 04018107 (2018).
- [83] Schultz, M. R. & Hyer, M. W. Snap-through of unsymmetric cross-ply laminates using piezoceramic actuators. *Journal of Intelligent Material Systems and Structures* **14**, 795–814 (2003).
- [84] Kwak, M. K., Heo, S. & Jeong, M. Dynamic modelling and active vibration controller design for a cylindrical shell equipped with piezoelectric sensors and actuators. *Journal of Sound and Vibration* **321**, 510–524 (2009).
- [85] Seffen, K. A. Curling of a Heated Annulus. *Journal of Applied Mechanics* **83**, 021005 (2016).
- [86] Nerl, M. S. Periodic correlated magnetic actuator systems and methods of use thereof (2012). US Patent App. 13/178,816.
- [87] Fullerton, L. W. & Roberts, M. D. Correlated magnetic harness and method for using the correlated magnetic harness (2010). US Patent 7,821,367.
- [88] Seffen, K. A. & Vidoli, S. Eversion of bistable shells under magnetic actuation: a model of nonlinear shapes. *Smart Materials and Structures* **25**, 065010 (2016).
- [89] Cao, W., Cudney, H. H. & Waser, R. Smart materials and structures. *Proceedings of the National Academy of Sciences* **96**, 8330–8331 (1999).
- [90] Sack, F. D. Plant gravity sensing. In *International review of cytology*, vol. 127, 193–252 (Elsevier, 1991).

- [91] Monshausen, G. B., Swanson, S. J. & Gilroy, S. Touch sensing and thigmotropism. *Plant Tropisms*. Blackwell, Ames, IA 91–122 (2008).
- [92] Lonsdale, D. *Principles of tree hazard assessment and management*. (Stationery Office Ltd, Publications Centre, 1999).
- [93] Kappel, R. Zugseile in der Natur. *Ph.D. thesis, Universität Karlsruhe* (2007).
- [94] Charpentier, V. *et al.* Kinematic amplification strategies in plants and engineering. *Smart Materials and Structures* **26**, 063002 (2017).
- [95] Reyssat, E. & Mahadevan, L. Hygromorphs: from pine cones to biomimetic bilayers. *Journal of the Royal Society Interface* **6**, 951–957 (2009).
- [96] Nguyen, V. Q., Ahmed, A. S. & Ramanujan, R. V. Morphing soft magnetic composites. *Advanced Materials* **24**, 4041–4054 (2012).
- [97] Schleicher, S., Lienhard, J., Poppinga, S., Speck, T. & Knippers, J. A methodology for transferring principles of plant movements to elastic systems in architecture. *Computer-Aided Design* **60**, 105–117 (2015).
- [98] Zarzar, L. D., Kim, P. & Aizenberg, J. Bio-inspired design of submerged hydrogel-actuated polymer microstructures operating in response to pH. *Advanced materials* **23**, 1442–1446 (2011).
- [99] Johnson, B., Beebe, D. & Crone, W. Effects of swelling on the mechanical properties of a pH-sensitive hydrogel for use in microfluidic devices. *Materials Science and Engineering: C* **24**, 575–581 (2004).
- [100] Na, J.-H., Bende, N. P., Bae, J., Santangelo, C. D. & Hayward, R. C. Grayscale gel lithography for programmed buckling of non-Euclidean hydrogel plates. *Soft matter* **12**, 4985–4990 (2016).
- [101] Klein, Y., Efrati, E. & Sharon, E. Shaping of elastic sheets by prescription of non-Euclidean metrics. *Science* **315**, 1116–1120 (2007).
- [102] Gladman, A. S., Matsumoto, E. A., Nuzzo, R. G., Mahadevan, L. & Lewis, J. A. Biomimetic 4D printing. *Nature materials* **15**, 413 (2016).
- [103] Siefert, E., Bico, J., Reyssat, E. & Roman, B. Baromorphs-Dynamically controlled bio-inspired shape-morphing. *Bulletin of the American Physical Society* (2018).
- [104] Siéfert, E., Reyssat, E., Bico, J. & Roman, B. Bio-inspired pneumatic shape-morphing elastomers. *Nature materials* **1** (2018).
- [105] Geymonat, G. & Leger, A. Nonlinear spherical caps and associated plate and membrane problems. *Journal of elasticity* **57**, 171–200 (1999).
- [106] Haughton, D. & Chen, Y.-C. On the eversion of incompressible elastic spherical shells. *Zeitschrift für angewandte Mathematik und Physik ZAMP* **50**, 312–326 (1999).
- [107] Mandal, P. & Calladine, C. R. Buckling of thin cylindrical shells under axial compression. *International Journal of Solids and Structures* **37**, 4509–4525 (2000).
- [108] Zoelly, R. *Über ein Knickungsproblem an der Kugelschale*. Ph.D. thesis, ETH Zurich (1915).
- [109] Hutchinson, J. W. Imperfection sensitivity of externally pressurized spherical shells. *Journal of Applied Mechanics* **34**, 49–55 (1967).

- [110] Calladine, C. R. Understanding imperfection-sensitivity in the buckling of thin-walled shells. *Thin-Walled Structures* **23**, 215–235 (1995).
- [111] Hutchinson, J. W. Buckling of spherical shells revisited. *Proceedings of the Royal Society of London A* **472**, 20160577 (2016).
- [112] Meissner, E. Über Elastizität und Festigkeit dünner Schalen. *Vierteljahrschrift der Naturforschenden Gesellschaft in Zürich* **60** (1915).
- [113] Stodola, A. *Die Dampfturbinen* (Julius Springer, 1910).
- [114] Reissner, H. *Muller-Breslau-Festschrift* (1912).
- [115] Wolfram Research, Inc. *Mathematica* (Wolfram Research, Inc., Champaign, Illinois, 2016), 10.4 edn.
- [116] Meijer, C. *On the G-function* (North-Holland, 1946).
- [117] Gravina, P. B. J. *Theorie und Berechnung der Rotationsschalen* (Springer-Verlag, 1961).
- [118] Blumenthal, O. Über die Genauigkeit der Wurzeln linearer Gleichungen. *Zeitschrift für Mathematik und Physik* **62**, 359–362 (1914).
- [119] Geckeler, J. Über die Festigkeit achsensymmetrischer Schalen, Forschungsarbeiten auf dem Gebiet des Ingenieurwesens, Heft 276 (1926).
- [120] Hallquist, J. O. *et al.* LS-DYNA keyword user's manual. *Livermore Software Technology Corporation* **970**, 299–800 (2007).
- [121] Hilber, H. M., Hughes, T. J. & Taylor, R. L. Improved numerical dissipation for time integration algorithms in structural dynamics. *Earthquake Engineering & Structural Dynamics* **5**, 283–292 (1977).
- [122] Zhang, Y. Large deflection of clamped circular plate and accuracy of its approximate analytical solutions. *Science China Physics, Mechanics & Astronomy* **59**, 1–11 (2016).
- [123] Hibbit, Karlsson & Sorensen. *ABAQUS/Standard User's Manual, Version 6.14*, vol. 1 (Hibbit, Karlsson & Sorensen, 2014).
- [124] Van Rossum, G. & Drake, F. L. *The Python Language Reference Manual* (Network Theory Ltd., 2011).
- [125] Sobota, P. M. & Seffen, K. A. Figshare repository containing Abaqus calculations (2017). URL <https://figshare.com/s/10f43228745c412a810f>.
- [126] Pandalai, K. & Patel, S. A. Buckling of orthotropic circular plates. *The Aeronautical Journal* **69**, 279–280 (1965).
- [127] Swamidas, A. & Kunukasseril, V. X. Buckling of orthotropic circular plates. *AIAA Journal* **11**, 1633–1636 (1973).
- [128] Barber, J. R. *Elasticity* (Springer, 1992).
- [129] Mattheck, C. *Warum alles kaputt geht - Form und Versagen in Natur und Technik* (Forschungszentrum Karlsruhe, 2003).
- [130] Dumir, P. Nonlinear axisymmetric response of orthotropic thin spherical caps on elastic foundations. *International Journal of Mechanical Sciences* **27**, 751–760 (1985).

- [131] Gupta, U. & Ansari, A. Asymmetric vibrations and elastic stability of polar orthotropic circular plates of linearly varying profile. *Journal of Sound and Vibration* **215**, 231–250 (1998).
- [132] Nie, G., Chan, C., Yao, J. & He, X. Asymptotic solution for nonlinear buckling of orthotropic shells on elastic foundation. *AIAA journal* **47**, 1772–1783 (2009).
- [133] Gupta, U., Lal, R. & Jain, S. Effect of elastic foundation on axisymmetric vibrations of polar orthotropic circular plates of variable thickness. *Journal of Sound and Vibration* **139**, 503–513 (1990).
- [134] Gutierrez, R., Romanelli, E. & Laura, P. Vibrations and elastic stability of thin circular plates with variable profile. *Journal of sound and vibration* **195**, 391–399 (1996).
- [135] Akour, S. N. & Nayfeh, J. F. Nonlinear dynamics of polar-orthotropic circular plates. *International Journal of Structural Stability and Dynamics* **6**, 253–268 (2006).
- [136] Uthgenannt, E. & Brand, R. Postbuckling of orthotropic annular plates. *ASME Journal of Applied Mechanics* **40**, 559–564 (1973).
- [137] Ramaiah, G. & Vijayakumar, K. Buckling of polar orthotropic annular plates under uniform internal pressure. *AIAA Journal* **12**, 1045–1050 (1974).
- [138] Nath, Y. & Jain, R. Orthotropic annular shells on elastic foundations. *Journal of engineering mechanics* **111**, 1242–1256 (1985).
- [139] Sobota, P. M. & Seffen, K. A. Figshare repository containing Abaqus calculations (2018). URL <https://figshare.com/s/795cc51bfc95e2cf5fa1>.
- [140] Audoly, B. & Boudaoud, A. Self-similar structures near boundaries in strained systems. *Physical review letters* **91**, 086105 (2003).
- [141] Roman, B. & Pocheau, A. Buckling cascade of thin plates: Forms, constraints and similarity. *EPL (Europhysics Letters)* **46**, 602 (1999).
- [142] Michell, J. On the direct determination of stress in an elastic solid, with application to the theory of plates. *Proceedings of the London Mathematical Society* **1**, 100–124 (1899).

Appendix A

Isotropic Nonlinear Shell Model

Closed shells

For a n degree-of-freedom model, the current radial and circumferential curvatures, κ_r and κ_θ , respectively, read:

$$\begin{aligned}\kappa_r &= \kappa_r^0 + \kappa_r^h + \kappa_r^c \\ &= \kappa_r^0 + \sum_{i=1}^n \left[\frac{1}{1+\nu} - \frac{1+2i}{1+2i+\nu} \rho^{2i} \right] \frac{\eta_i}{a^2} - 4(3\rho^2 - 1) \frac{K_\varphi a}{8D} \sum_{i=1}^n \left[\frac{1}{1+\nu} - \frac{2i}{1+2i+\nu} \right] \frac{\eta_i}{a^2}, \\ \kappa_\theta &= \kappa_\theta^0 + \kappa_\theta^h + \kappa_\theta^c \\ &= \kappa_\theta^0 + \sum_{i=1}^n \left[\frac{1}{1+\nu} - \frac{1}{1+2i+\nu} \rho^{2i} \right] \frac{\eta_i}{a^2} - 4(\rho^2 - 1) \frac{K_\varphi a}{8D} \sum_{i=1}^n \left[\frac{1}{1+\nu} - \frac{2i}{1+2i+\nu} \right] \frac{\eta_i}{a^2},\end{aligned}\tag{A.1}$$

where the initial values κ_r^0 and κ_θ^0 follow from Eqn (5.21). The change in Gaussian curvature according to Eqn (5.10) is found to be:

$$\begin{aligned}g &= \left[\kappa_r^0 + \sum_{i=1}^n \left[\frac{1}{1+\nu} - \frac{1+2i}{1+2i+\nu} \rho^{2i} \right] \frac{\eta_i}{a^2} - 4(3\rho^2 - 1) \frac{w_M^c}{a^2} \right] \times \\ &\quad \left[\kappa_\theta^0 + \sum_{i=1}^n \left[\frac{1}{1+\nu} - \frac{1}{1+2i+\nu} \rho^{2i} \right] \frac{\eta_i}{a^2} - 4(\rho^2 - 1) \frac{w_M^c}{a^2} \right] - \kappa_r^0 \kappa_\theta^0,\end{aligned}\tag{A.2}$$

where w_M^c is defined in Eqn (5.31). The corresponding α_i -terms for Eqn (5.13), where $2p - 4 = 4n$, for three degrees of freedom and a uniformly curved initial shape [c.f. Eqn (5.21a)] read:

$$\begin{aligned}
\alpha_0 &= \frac{\left(2(\eta_1 + \eta_2 + \eta_3 + 4(\nu + 1)w_M^c) + (\nu + 1)w_M^0\right)^2}{4a^4(\nu + 1)^2}, \\
\alpha_2 &= -\frac{2\left[\eta_1 + 4(\nu + 3)w_M^c\right]\left[2(\eta_1 + \eta_2 + \eta_3 + 4(\nu + 1)w_M^c) + (\nu + 1)w_M^0\right]}{a^4(\nu + 1)(\nu + 3)}, \\
\alpha_4 &= \frac{3}{a^4}\left(\frac{8\eta_1 w_M^c}{\nu + 3} - \frac{8\eta_2 w_M^c}{\nu + 5} + 16w_M^{2c} + \frac{\eta_1^2}{(\nu + 3)^2} - \frac{2\eta_2(\eta_1 + \eta_2 + \eta_3)}{(\nu + 1)(\nu + 5)} - \frac{\eta_2 w_M^0}{\nu + 5}\right), \\
\alpha_6 &= \frac{4}{a^4}\left(\frac{8\eta_2 w_M^c}{\nu + 5} - \frac{8\eta_3 w_M^c}{\nu + 7} + \frac{2\eta_1 \eta_2}{\nu^2 + 8\nu + 15} - \frac{2\eta_3(\eta_1 + \eta_2 + \eta_3)}{(\nu + 1)(\nu + 7)} - \frac{\eta_3 w_M^0}{\nu + 7}\right), \\
\alpha_8 &= \frac{5}{2a^4}\left(\frac{4\eta_3(4(\nu + 3)w_M^c + \eta_1)}{(\nu + 3)(\nu + 7)} + \frac{2\eta_2^2}{(\nu + 5)^2}\right), \\
\alpha_{10} &= \frac{1}{a^4}\frac{12\eta_2 \eta_3}{(\nu + 5)(\nu + 7)}, \quad \alpha_{12} = \frac{1}{a^4}\frac{7\eta_3^2}{(\nu + 7)^2}, \quad \alpha_1 = \alpha_3 = \alpha_5 = \alpha_7 = \alpha_9 = \alpha_{11} = 0.
\end{aligned} \tag{A.3}$$

For non-uniformly curved initial shapes defined in Eqn (5.21b), the corresponding α -terms of a model with three degrees of freedom are calculated to be:

$$\begin{aligned}
\alpha_0 &= \frac{\left(4(\nu + 1)w_M^c + \eta_1 + \eta_2 + \eta_3 + 4(\nu + 1)w_M^0\right)^2}{a^4(\nu + 1)^2}, \\
\alpha_2 &= -\frac{4\left(4(\nu + 3)w_M^c + \eta_1 + 4(\nu + 3)w_M^0\right)\left(4(\nu + 1)w_M^c + \eta_1 + \eta_2 + \eta_3 + 4(\nu + 1)w_M^0\right)}{a^4(\nu + 1)(\nu + 3)}, \\
\alpha_4 &= \frac{3}{2a^4}\left(\frac{16\eta_1(w_M^c + w_M^0)}{\nu + 3} + \eta_2\left[\frac{(\eta_1 + \eta_2 + \eta_3 - 16(w_M^0 + w_M^c))}{\nu + 5} - \frac{(\eta_1 + \eta_2 + \eta_3)}{\nu + 1}\right] \right. \\
&\quad \left. + 32(w_M^c + w_M^0)^2 + \frac{2\eta_1^2}{(\nu + 3)^2}\right), \\
\alpha_6 &= \frac{8}{a^4}\left(\frac{4\eta_2 w_M^c}{\nu + 5} - \frac{4\eta_3 w_M^c}{\nu + 7} + \frac{\eta_1 \eta_2}{\nu^2 + 8\nu + 15} - \frac{\eta_3(\eta_1 + \eta_2 + \eta_3)}{(\nu + 1)(\nu + 7)} + \frac{4\eta_2 w_M^0}{\nu + 5} - \frac{4\eta_3 w_M^0}{\nu + 7}\right), \\
\alpha_8 &= \frac{5}{2a^4}\left(\frac{4\eta_3(4(\nu + 3)w_M^c + \eta_1 + 4(\nu + 3)w_M^0)}{(\nu + 3)(\nu + 7)} + \frac{2\eta_2^2}{(\nu + 5)^2}\right), \\
\alpha_{10} &= \frac{1}{a^4}\frac{12\eta_2 \eta_3}{(\nu + 5)(\nu + 7)}, \quad \alpha_{12} = \frac{1}{a^4}\frac{7\eta_3^2}{(\nu + 7)^2}, \quad \alpha_1 = \alpha_3 = \alpha_5 = \alpha_7 = \alpha_9 = \alpha_{11} = 0.
\end{aligned} \tag{A.4}$$

Annular Shells

Constants A_i for an initially uniformly curved shell with annular planform and a deflection field according to Eqn (5.42) subjected to boundary conditions as specified in Eqn (5.43):

$$\begin{aligned}
 A_0 &= -(A_1 + A_2 + A_3 + \eta_1 + \eta_2 + \eta_3) \\
 A_1 &= -\frac{2A_2(1 + \nu) + 3A_3(2 + \nu) + 4\eta_1\nu + 5\eta_2\nu + 6\eta_3(5 + \nu) + 12\eta_1 + 20\eta_2}{\nu} \\
 A_2 &= -\left[3a^3A_3(2 + \nu)(a + b) + 4a^2\eta_1(3 + \nu)(a^2 + ab + b^2) + 5a\eta_2(4 + \nu)(a + b) \right. \\
 &\quad \cdot (a^2 + b^2) + 6\eta_3(5 + \nu)(a^4 + a^3b + a^2b^2 + ab^3 + b^4) \left. \right] \left/ \left[2a^4(1 + \nu) \right] \right. \\
 A_3 &= -\left[4a^2\eta_1((a^2 + ab)(3 + \nu) - 8b^2\nu) + 5a\eta_2((a^3 + a^2b + ab^2)(4 + \nu) - 15b^3\nu) \right. \\
 &\quad \left. + 6\eta_3((a^4 + a^3b + a^2b^2 + ab^3)(5 + \nu) - 24b^4\nu) \right] \left/ \left[3a^3(a(2 + \nu) - 3b\nu) \right] \right.
 \end{aligned} \tag{A.5}$$

It is convenient to write the solution to Eqn (5.44) in form of a series:

$$\begin{aligned}
 \frac{\Phi}{E} &= -\frac{1}{72}\xi_1\rho^2(9\xi_1(\log(a\rho) - 1) + 16w_M^0\rho) - \sum_{i=2}^6 \frac{i\xi_1\xi_i\rho^{i+1}}{(i-1)(i+1)^2} \\
 &\quad - \frac{1}{10} \sum_{i=2}^6 \sum_{j=2}^6 \xi_i\rho^i \left(\frac{4w_M^0\rho^2}{(i+2)^2} + \frac{5ij\xi_j\rho^j}{(i+j-2)(i+j)^2} \right) + C_1\rho^2 + C_2 \log[\rho a],
 \end{aligned} \tag{A.6}$$

where the following substitution was employed in order to allow for a compact notation: $A_1 = \xi_1$, $A_2 = \xi_2$, $A_3 = \xi_3$, $\eta_1 = \xi_4$, $\eta_2 = \xi_5$, $\eta_3 = \xi_6$.

Appendix B

Polar-Orthotropic Nonlinear Shell Model

Closed Cap

In order to satisfy the boundary conditions of $w(a) = 0$, $m_r(a) = 0$, substitute the following values in Eqn. (6.10).

$$\begin{aligned} A_0 &= -a^{1+\sqrt{\beta}} (\eta_1 + a\eta_2 + a^2\eta_3 + a^3\eta_4) \\ A_4 &= \frac{\eta_1 a(1 + \sqrt{\beta})(\sqrt{\beta} + \nu) + \eta_2 a^2(2 + \sqrt{\beta})(1 + \sqrt{\beta} + \nu) + \eta_3 a^3(3 + \sqrt{\beta})(2 + \sqrt{\beta} + \nu)}{-a^4(4 + \sqrt{\beta})(3 + \sqrt{\beta} + \nu)} \end{aligned} \quad (B.1)$$

Using the compatibility Eqn (6.9), the Airy stress function, $\Phi = \Phi_p + \Phi_h$, can be expressed in terms of the η constants as:

$$\begin{aligned} \Phi_p &= \frac{E\beta}{2} \sum_{i=1}^4 \sum_{j=1}^4 (\sqrt{\beta} + i) \eta_i \rho^{\sqrt{\beta}+i} \left[\frac{4w_M^0 \rho^2 \delta_{ij}}{(i+1)(\sqrt{\beta} + i + 2)(2\sqrt{\beta} + i + 1)} \right. \\ &\quad \left. + \frac{(\sqrt{\beta} + j) \eta_j \rho^{\sqrt{\beta}+j}}{(\sqrt{\beta} + i + j - 1)(2\sqrt{\beta} + i + j)(3\sqrt{\beta} + i + j - 1)} \right] \end{aligned} \quad (B.2)$$

where δ_{ij} denotes the Kronecker delta.

Denoting the stresses arising from the particular solution, Φ_p , with σ_{ar} and $\sigma_{a\theta}$, the remaining constant takes the value:

$$C_1 = - \frac{\sigma_{pr} (\nu k_u a + \beta E) - k_u a \sigma_{p\theta}}{(\sqrt{\beta} + 1) [k_u a (\nu - \sqrt{\beta}) + \beta E]} \Big|_{\rho=1}, \quad (\text{B.3})$$

which simplifies to

$$\begin{aligned} C_1 &= \frac{-\sigma_{pr}}{1 + \sqrt{\beta}} \Big|_{\rho=1} && \text{for } k_u = 0 \\ &&& \text{(rollers)} \\ \text{and } C_1 &= - \frac{\sigma_{p\theta} - \nu \sigma_{pr}}{(1 + \sqrt{\beta})(\sqrt{\beta} - \nu)} \Big|_{\rho=1} && \text{for } k_u \rightarrow \infty \\ &&& \text{(fixed pins)} \end{aligned} \quad (\text{B.4})$$

Annulus

First, substitute $\eta_2 = \xi_{-2}, \eta_1 = \xi_{-1}, A_0 = \xi_0, A_1 = \xi_1, A_2 = \xi_2$ and $A_3 = \xi_3$ for the constants in Eqn (6.11). In order to satisfy the boundary conditions of $w(a) = 0$, $m_r(a) = 0$, $m_r(b) = 0$ and $q_r(b) = 0$ then substitute the following values one after another.

$$\begin{aligned} \xi_0 &= -(\xi_{-2} + \xi_{-1} + \xi_1 + \xi_2 + \xi_3) \\ \xi_3 &= \frac{b^{-5} \sqrt{\beta} (3\xi_{-2}(2\sqrt{\beta} - 1)a^5 \sqrt{\beta} - 3\xi_2(2\sqrt{\beta} + 1)a \sqrt{\beta} b^4 \sqrt{\beta})}{8(3\sqrt{\beta} + 1)} \\ \xi_2 &= \left[-8b^5 \sqrt{\beta} (\xi_{-2}(4\beta + \nu - 2(\nu + 1)\sqrt{\beta}) + \xi_{-1}(\beta + \nu - (\nu + 1)\sqrt{\beta}) + \xi_1(\beta + \nu + \nu\sqrt{\beta} + \sqrt{\beta})) - 3\xi_{-2}(2\sqrt{\beta} - 1)a^5 \sqrt{\beta}(\nu + 3\sqrt{\beta}) \right] / \left[b^4 \sqrt{\beta} ((2\sqrt{\beta} + 1)(8b \sqrt{\beta}(\nu + 2\sqrt{\beta}) - 3a \sqrt{\beta}(\nu + 3\sqrt{\beta}))) \right] \\ \xi_1 &= \left[a^3 \sqrt{\beta} b \sqrt{\beta} (\xi_{-2} (-28\beta^{3/2} + \beta(14 - 6\nu) + \nu(-5\nu + 10\nu\sqrt{\beta} + 3\sqrt{\beta})) + 3\xi_{-1} (3\beta^{3/2} - \beta(2\nu + 3) + \nu(\nu - \nu\sqrt{\beta} + 2\sqrt{\beta})) - 12\xi_{-2} a^4 \sqrt{\beta} (\sqrt{\beta} - 2\beta)(\nu + 3\sqrt{\beta}) + a \sqrt{\beta} (-b^3 \sqrt{\beta}) (5\nu + 7\sqrt{\beta}) (\xi_{-2}(4\beta + \nu - 2(\nu + 1)\sqrt{\beta}) + \xi_{-1}(\beta + \nu - (\nu + 1)\sqrt{\beta})) - (5\nu + 7\sqrt{\beta}) ((ab)^2 \sqrt{\beta} + b^4 \sqrt{\beta}) (\xi_{-2}(4\beta + \nu - 2(\nu + 1)\sqrt{\beta}) + \xi_{-1}(\beta + \nu - (\nu + 1)\sqrt{\beta})) \right] / \left[b^3 \sqrt{\beta} ((\sqrt{\beta} + 1)(\nu + \sqrt{\beta})(b \sqrt{\beta}(5\nu + 7\sqrt{\beta}) - 3a \sqrt{\beta}(\nu + 3\sqrt{\beta}))) \right] \end{aligned} \quad (\text{B.5})$$

Then use the same substitution to calculate the Airy stress function in terms of the remaining two degrees of freedom, ξ_{-2} and ξ_{-1} :

$$\begin{aligned} \Phi'_p = & -\frac{E\beta}{2a} \sum_{i=-2}^3 \sum_{j=-2}^3 (1+i\sqrt{\beta}) \rho^{1+i\sqrt{\beta}} \xi_i \left[\frac{4w_M^0 \rho \delta_{ij}}{(2+\sqrt{\beta}+i\sqrt{\beta})(2+(i-1)\sqrt{\beta})} \right. \\ & \left. + \frac{(1+j\sqrt{\beta}) \rho^j \xi_j (1-\delta_{-ij})}{(1+(i+j-1)\sqrt{\beta})(1+(1+i+j)\sqrt{\beta})} \right] (1-\delta_{i0})(1-\delta_{j0}) \end{aligned} \quad (\text{B.6})$$

Constants for annulus with $k_u \rightarrow 0$ (roller supports):

$$C_1 = \frac{\sigma_{pr|\rho=1} - \left(\frac{b}{a}\right)^{1+\sqrt{\beta}} \sigma_{pr|\rho=b/a}}{(1+\sqrt{\beta}) \left[\left(\frac{b}{a}\right)^{2\sqrt{\beta}} - 1 \right]}, \quad C_2 = -\frac{\left(\frac{b}{a}\right)^{\sqrt{\beta}} \left[\left(\frac{b}{a}\right)^{\sqrt{\beta}} \sigma_{pr|\rho=1} - \frac{b}{a} \sigma_{pr|\rho=b/a} \right]}{(1+\sqrt{\beta}) \left[\left(\frac{b}{a}\right)^{2\sqrt{\beta}} - 1 \right]} \quad (\text{B.7})$$

Constants for annulus with $k_u \rightarrow \infty$ (fixed pins):

$$\begin{aligned} C_1 = & \frac{a^{1+\sqrt{\beta}} (\nu \sigma_{pr}(a) - \sigma_{p\theta}(a)) - b^{1+\sqrt{\beta}} (\sqrt{\beta} + \nu) \sigma_{pr}(b)}{(\sqrt{\beta} + 1) (a^{2\sqrt{\beta}} (\sqrt{\beta} - \nu) + b^{2\sqrt{\beta}} (\sqrt{\beta} + \nu))} \\ C_2 = & \frac{a^{\sqrt{\beta}} b^{\sqrt{\beta}} (ba^{\sqrt{\beta}} (\sqrt{\beta} - \nu) \sigma_{pr}(b) + ab^{\sqrt{\beta}} [\nu \sigma_{pr}(a) - \sigma_{p\theta}(a)])}{(\sqrt{\beta} - 1) [a^{2\sqrt{\beta}} (\sqrt{\beta} - \nu) + b^{2\sqrt{\beta}} (\sqrt{\beta} + \nu)]} \end{aligned} \quad (\text{B.8})$$

Appendix C

Actuation

The constants of integration for a nonlinear shell model of an initially flat plate are given in the following. The shell is subjected to a polynomial in-plane actuation pattern of order m according to Eqn (7.13). The deflection field possesses four degrees of freedom: the first two, η_0 and η_1 , according to Eqn (7.16) relate to synclastic modes, whilst the latter two, η_2 and η_3 as specified in Eqn (7.14), arise in anticlastic modes shapes with wave numbers of 2 and 3, respectively.

$$\begin{aligned} C_0 &= \frac{24}{1440} \left[\left(11\eta_0^2 + \frac{4(\eta_0 + \eta_1)(3\eta_0 + 2\eta_1)}{5 + \nu} + \frac{16(\eta_0 + \eta_1)^2}{(5 + \nu)^2} + 8\eta_0\eta_1 + 2\eta_1^2 \right) \right. \\ &\quad \left. - 16\eta_2^2 \frac{304 + 3\nu(19 + \nu)}{(5 + \nu)^2} - 3\eta_3^2 \frac{272\nu(73 + 12\nu) + 40787}{(15 + 8\nu)^2} \right] + \frac{\epsilon}{m + 2} \\ C_1 &= -16\eta_2\eta_3 \frac{4\nu(7413 + 716\nu) + 62785}{45045(5 + \nu)(15 + 8\nu)}, \quad A_4 = \eta_2^2 \frac{\nu(182 + 59\nu) + 235}{3360(5 + \nu)^2} \\ C_4 &= -\eta_2^2 \frac{\nu(146 + 47\nu) + 155}{840(5 + \nu)^2}, \quad A_5 = 16\eta_2\eta_3 \frac{8\nu(194957 + 51622\nu) + 1628035}{3828825(5 + \nu)(15 + 8\nu)} \\ C_5 &= 16\eta_2\eta_3 \frac{4\nu(97795 + 25916\nu) + 339281}{765765(5 + \nu)(15 + 8\nu)} \\ A_6 &= -\eta_3^2 \frac{16\nu(9775 + 3748\nu) + 42825}{11520(15 + 8\nu)^2}, \quad C_6 = \eta_3^2 \frac{16\nu(9649 + 5772\nu) + 61195}{10752(15 + 8\nu)^2} \\ E_2 &= \eta_2 \frac{\eta_0 [\nu(132 + 17\nu) + 255] + \eta_1 [\nu(136 + 13\nu) + 375]}{210(5 + \nu)^2} \end{aligned}$$

$$\begin{aligned}
G_2 &= -\eta_2 \frac{\eta_0 [\nu(1118 + 153\nu) + 1805] + 2\eta_1 [\nu(479 + 48\nu) + 1215]}{315(5 + \nu)^2} \\
E_3 &= 32\eta_3 \frac{5\eta_0 [20\nu(327 + 44\nu) + 9209] + \eta_1 [8\nu(2603 + 298\nu) + 37065]}{135135(5 + \nu)(15 + 8\nu)} \\
G_3 &= \frac{32\eta_3 [\eta_0(16\nu(328 + 53\nu) + 11225) - \eta_1 [4\nu(8047 + 1060\nu) + 48755)]}{45045(5 + \nu)(15 + 8\nu)}
\end{aligned} \tag{C.1}$$